Fourier-Transform Rheology applied on homopolymer melts of different architectures - Experiments and finite element simulations

Dem Fachbereich Maschinenbau
an der Technischen Universität Darmstadt
zur
Erlangung des Grades eines Doktor-Ingenieurs (Dr.-Ing.)
eingereichte

Dissertation

vorgelegt von

Dipl.-Ing Iakovos A. Vittorias

aus Rhodos

Die vorliegende Arbeit wurde in der Zeit von November 2003 bis Oktober 2006
am Max-Planck-Institut für Polymerforschung und an der Technische Universität Darmstadt
unter der Betreuung von Herrn Prof. Dr. M. Wilhelm angefertigt.

Berichterstatter: Prof. Dr. M. Wilhelm
Mitberichterstatter: Prof. Dr. C. Friedrich
Tag der Einreichung: 30.10.06
Tag der mündlichen Prüfung: 21.12.06

To my family

“Give me where to stand and I will move the earth”
-Archimedes

Contents

Chapter 1

Introduction

1.1 General

The word "polymer" originates from the greek word "$\pi o \lambda \upsilon$ " (= much, a lot) and "$\mu \epsilon \rho o s$" (= part) and refers to a substance made by many parts ("$\pi o \lambda \upsilon \mu \epsilon \rho \epsilon s$"). Polymers are macromolecules that can be found in nature as pure organic (e.g. cellulose, enzymes, natural rubber) or partly inorganic substances (e.g. sulfur-based or silicon-based polymers). Macromolecules can also be synthetically produced (e.g. polyethylene, polystyrene, polypropylene, polyesters). In the year 2005 the production of polymers was more than 250 Mtones / year [Gröhn 06] and it is estimated that today more than 50% of the chemical engineers in the world work in the field of polymers [Griskey 95]. The polymer processing industry is developed and still growing, in parallel to the polymer production. A more practical separation of the different types of polymer related industries would be: production, compounding, processing and final product formation.

One could roughly categorize polymer materials according to production quantity into: mass production, or "commodity" polymers (e.g. polyethylene, polystyrene, polypropylene), technical polymers (e.g. polyamides, epoxy-resins) and special polymers (e.g. polymethylmethacrylate, teflon). According to their mechanical-thermal behaviour, e.g. during heating, there are three categories, namely: thermoplastics, thermosets and elastomers [Young 91]. This work is focused on thermoplastics, however the methods presented could be easily applied on the other two polymer types. Thermoplastics are materials like polyethylene (PE), polystyrene (PS) and polypropylene (PP), that gain plasticity and can be formed and processed under heat and pressure. This phenomenon is reversible and takes place without any chemical change. Materials belonging in this category can be melted and dissolved in solvents. The macromolecules of a thermoplastic material can have different architectures (topology), such as linear, short-chain branched (SCB), long-chain branched (LCB), star-like, H-like or pom-poms (see Fig. 1.1). Thermoplastics are produced in large quantities in comparison with

other polymeric materials. Because of their special properties and low price, thermoplastics have numerous technical and consumer applications. About 3/4 of the world polymer production consists of thermoplastics and within this 3/4 from that production belongs to polyolefines (PE, PP) and polystyrene (PS). Typical prices for polyolefines are approximately 1-2 EURO/kg.

Polystyrene was developed in laboratories and was produced in pilot-plant scale during 1920 -1930. It was considered a technical polymer until 1950 and afterwards was put into mass production. Some of its applications are in technical consumer parts and polymer foams.

Polyethylene was discovered and developed during 1930 -1940 and until 1945 it was considered a special polymer and was produced in small quantities. After 1955 it moved to mass production. In 1933, eight grams of polyethylene were recovered by the study of ethylene polymerization and after 6 years, in 1939, the polyethylene production increased to 100 tones/year, due to its crucial importance in the war, since it was an ideal material for radar cable insulation [Morawetz 85]. Nowdays, it is the most widely produced polymer with over 60 Mtones/year of worldwide production. It can be found in sheets, pipes, packaging and consumer products. In similar applications one can find PP, which however was developed in a laboratory scale during 1955-1960 and was put in large industrial production after 1965 [Peacock 00].

The molecular structure, as well as the macromolecular architecture and morphology of these materials is strongly correlated with their characteristic chemical, physical and processing properties. The particular structure of each macromolecule depends on the production method (mechanism, technique, polymerization conditions etc.). For the final use of a polymer in an application field, one has to take economic criteria into consideration, such as cost of the specific polymer in comparison with other competing polymeric or non-polymeric materials, processing cost, raw materials cost etc. In a reverse manner, based on an application field, the polymer must posses some desired properties. The “unusual” properties of several polymers in comparison with traditional materials (metals, ceramic etc.) satisfy the technological needs of our time and lead to a broad use in numerous industrial applications. However, today’s technology sets constantly new demands on polymer properties, such as:

- balance between stiffness and elasticity (substitution of metals with polymers, e.g. in mass transport vehicles)
- thermal stability at high temperatures (e.g. motor-engine parts)
- membrane formation and applications
- optical properties and electrical conductivity (e.g. screens, electronics)
- low price
- low density
- processing ability, easy to shape and form (e.g. for blow-molding, film production etc.)

It is obvious that the more specific the application of a polymer is, the larger the demand

for special designed properties. The desired new and optimized properties can concern polymers that are used as raw materials, or are needed for final product design. In any case, there is always a strong demand on the development and optimization of numerous characterization techniques, in order to detect and quantify desired material characteristics. Among the techiques undertaken to characterize polymers, especially close to their final use, are mechanical tests. One of these methods is rheology, which is defined as the science of deformation and flow of matter.

1.2 Motivation

The main subject of this dissertation is the detection and quantification of branched structures in polymer melts via FT-Rheology and the study of their rheological behaviour at large deformations. Thus, it is necessary to introduce rheology as a research field and in especially dynamic oscillatory shear. The concepts behind FT-Rheology as a method to quantify the non-linear regime, along with information about the investigated material types are also provided. This brief theoretical background is presented in the introduction chapter.

In chapter 2, the experimental method and the flow modelling method are presented in detail. The experimental setup is described along with short descriptions of methods additionally used. These complementary utilized methods are correlated with FT-Rheology and can contribute to the correct interpretation of the derived non-linear rheological quantities. A general description of the finite element method is additionally presented. There is a focus in the specific model used withing this work, as well as in the numerical scheme and problem setup of a LAOS flow simulation.

A large part of this work is related to industrial samples. However, one needs to validate methods by applying it initially to simple and known materials before expanding to complex systems. Hence, FT-Rheology and LAOS simulations are initially used to characterize model systems of known simple architecture (linear), or well-characterized samples of complex topology (anionically synthesized polystyrene combs). These systems are mainly monodisperse. Furthermore, because of the synthesis type, it is accepted that the polystyrene linear samples do not contain any side-chains. Large amplitude oscillatory shear flow simulations are applied to study the non-linear behaviour of polystyrene comb melts and solutions, previously measured and characterized via FT-Rheology [Höfl 06]. The specific samples have been extensively investigated and their topology was determined, with respect to the number of side-arms per backbone and the arm and backbone length. The results of this part are presented in chapter 3. The Pom-pom model introduced in chapter 2 in its DCPP formulation (Double-Convected-Pom-pom), is used as a constitutive equation to predict the LAOS flow of the above materials.

Chapter 4 deals with the expansion of FT-Rheology and LAOS to industrial samples of complex or unknown topology and specifically industrial linear, SCB, LCB polyethylenes,

as well as polyethylene blends of linear and LCB components. The experimental results are compared with finite element simulations. Information acquired from ^{13}C melt-state nuclear magnetic resonance (NMR), gel-permeation chromatography (GPC) and elongational rheology are also taken into consideration and used complementary to FT-Rheology. Predictions of LAOS flow and non-linear behaviour of linear and LCB PE and a parameter sensitivity analysis for the non-linear rheological response under LAOS, concerning the molecular architecture parameters of the DCPP model, are presented.

A major issue in polymer melt flow is the occurring instabilities that take place during a non-linear flow of a polymer melt. Wall slip, stick-slip, sharkskin effect, melt distortion in capillary flows and edge fracture, meniscus distortions and wall slip in plate-plate geometries are very important phenomena. Such occurring instabilities are found to significantly influence the non-linearities, as quantified via FT-Rheology. Thus, chapter 5 is devoted in the detection, monitoring and quantification of flow instabilities on LAOS and capillary flow of polymer melts via FT-Rheology. This behaviour is modelled and the appearing non-linearities and flow distortions are correlated to molecular weight, molecular weight distribution and topology.

Chapter 6 is the conclusive one. A summary of the presented results and the current research status is stated. It is accompanied with proposals for future work and improvements of the method, as well as possible further applications.

1.3 Polymer synthesis and architecture

The importance of polymer architecture for designing tailor-made properties and optimizing the process-ability of the material was fully understood in the last decades and it is still an ongoing problem for chemists, rheologists and polymer engineers [Gahleitner 01, McLeish 97, Münstedt 98, Trinkle 02]. Over the last two decades the crucial role of topology has been supported by the remarkable contrast in rheological behaviour of polymer melts, where e.g. homopolymers have different architectures [McLeish 97]. Concerning commercial materials, the effort is most prominent in explaining the radically different processing behaviour of long-chain branched polyethylenes, i.e. LCB PE, from linear. However, by studying small quantities of tailored monodisperse materials with a well-defined topology (typically anionically synthesized polystyrenes, polyisoprenes and polybutadienes), one can obtain a better insight in the polymer dynamics. Hence, the relation between polymer architecture and rheological behaviour, as well as processing properties, can be elucidated [McLeish 97]. The properties of a produced macromolecular system are a consequence of the synthesis method that was undertaken. Thus, one has to understand the mechanism of chain formation and control the polymerization with a specific way in order to get to the desired molecular structure and connectivity.

There are several different types of polymerization with the two major kinetic schemes being the step-wise (or step-growth) and the chain polymerization. The first type refers to the polymerization where the polymer chains grow by reactions that can occur between any two molecular species, in a step-wise manner, e.g. polycondensation reactions. In chain polymerization (e.g. radical polymerization) the macromolecule grows by reaction of the monomer with a reactive end-group of the growing chain. A common mechanism for the chain polymerization can be subdivided into: initiation, propagation and termination steps [Young 91]. The free-radical polymerization belongs in this category. In this synthesis route the initiation takes place when an initiator molecule decomposes into two radicals via photolysis, thermal initiation or irradiation. The polymer chains can prematurely be terminated either by recombination of two macro-radicals or by disproportionation. Additionally, chain transfer can occur, which results in the formation of branches [Young 91]. If ionic species are used for the initiation then the polymerization is called ionic. There are two types of ionic polymerization, the cationic and the anionic. During the propagation the active center of the growing chain is transfered from its last unit to a newly bonded monomer. The last step, the termination, occurs when the active center is saturated and not by a reaction between two ionic active centers because they are of similar charge and hence repel each other. In cationic type, termination occurs either by unimolecular rearrangement of the ion pair or by chain transfer. Chain transfer to monomer often contributes significantly in this step. Additionally, chain transfer to solvent, reactive impurities and polymer may take place. The latter results in the formation of branched species. In the anionic polymerization there is an absence of inherent termination process, in contrast to free-radical and cationic polymerization. Termination by ion-pair rearrangement is highly unfavourable, due to the required elimination of a hydride ion. The used counter-ions have no tendency to combine with the carbanionic active centers to form non-reactive covalent bonds. Thus, in the absence of chain transfer the macromolecule grows as long as monomer is available. These kind of polymerizations where the polymers permanently retain their active centers are called “living” and are widely and successfully used in order to produce polymers with narrow molecular weight distribution and with well defined topologies. Several polymerization methods are presented below, which are relevant to the present work.

1.3.1 Anionic polymerization

Anionic polymerization is a common polymerization method and it is widely used [Young 91]. The initiator is usually an alkali metal (or alkaline earth metal) and the active center in a propagating chain is negatively charged. In the propagation step, the initiator has no tendency to combine with the carbanionic active centers, because they exist in differently dissociated and therefore differently active ion-pair states [Hadjichristid 00, Roovers 79b, Young 91]. Thus, the monomers are completely converted into macromolecules. The number

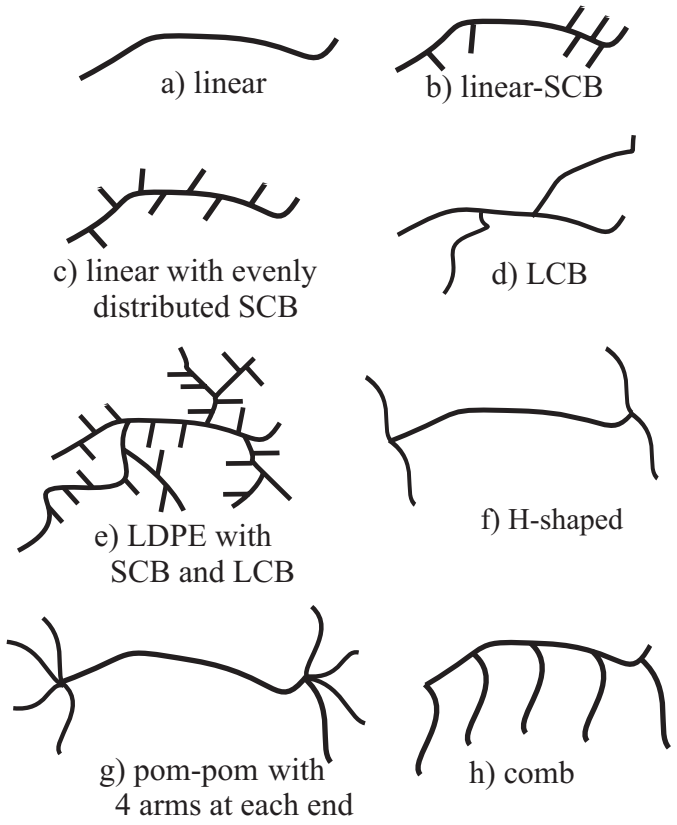

Figure 1.1: *Typical chain structures for polyolefines and polystyrene.*

of reactive centers built in the initiation process remains constant and these species can even be active for a considerable time. By the addition of monomer, the "living" chains will continue to grow. The advantage of this particular method is the capability to synthesize e.g. block copolymers, by addition of different monomers. Anionic polymerization can also be used to obtain polymers of defined architecture such as: stars, H-shaped, graft, combs, pom-poms etc. As mentioned above, this polymerization type allows the production of polymers with very narrow molecular weight distribution. Linear polystyrenes and polystyrene combs of defined arm number and length investigated within this work, are produced by this method.

1.3.2 Ziegler-Natta method

The method of anionic polymerization has several chemical drawbacks, i.e. it is restricted only to specific monomers. Ethylene and propylene can be polymerized via coordination. In 1953 Ziegler prepared polyethylene using aluminium alkyl compounds and transition metal halides [Ziegler 55]. Natta foresaw the potential of this method and slightly modified Ziegler's catalyst to produce stereoregular polymers, with the most prominent example being polypropylene [Natta 60].

The Ziegler-Natta method was one of the developments that contributed significantly in the effort to control the kinetics and obtain products with narrower molecular weight distributions in a free-radical polymerization. Conventional Ziegler-Natta catalysts have a variety of active sites with different chemical natures and characteristics regarding comonomer incorporation and stereostructure. Their preparation involves reactive compounds (commonly halides of e.g. Ti, V, Cr, Zr) with organometallic compounds (e.g. alkyls, aryls or hydrids) of Al, Mg, Li. The catalysts are heterogeneous and their activity is strongly affected by the components and the method used for their preparation. Although millions of tones of polymers are produced every year by this method, the mechanism is not yet fully understood and clarified.

1.3.3 Metallocene catalysts

The last decades a revolutionary method has been developed to improve the product tacticity and to control the molecular weight distribution. It is based on the use of soluble stereoregular catalysts known as metallocene catalysts [Pino 80]. In contrast to Ziegler-Natta, metallocene catalysts have identical characteristics for each active site, allowing the synthesis of a much more homogeneous polymer structure [Hamielec 96]. Thus, stereoregular polymers can be produced and metallocenes solve basic problems of the Ziegler-Natta synthesis. The catalyst is composed by a metal (active center, commonly Zr, Ti, Hf, Sc, Th or Nd, Yb, Y, Lu, Sm), a co-catalyst or ion of opposite charge (the most commonly used is methylalumoxane, MAO) and a ligand for the complex creation (e.g. cyclopentadienyl). The size and orientation of the ligands define the direction for the incoming monomers. Thus, the monomers react only when they are specifically oriented, resulting to a tactic polymer, in other words a macromolecule with a specific spatial arrangement of side-chains.

As mentioned above, the metallocene-catalysts can produce stereoregular polymers of narrow distribution, which would have desired mechanical properties. Some applications are in the production of ultra-high-molecular weight polyethylene, UHMWPE M_w = 6,000,000 g/mol) used in hip implants or bullet-proof vests, or linear polyethylenes (mLLDPE).

1.3.4 Polymer topologies

In fig. 1.1 schematic representations of typical polymer architectures are depicted. Polymer structure a) is a linear HDPE, with no SCB and this allows its crystallinity to be as high as 70%. The SCB can be incorporated as a comonomer or can be formed by the catalyst. The polymers of type b) can be linear low density polyethylenes (LLDPE), with relatively broad

molecular weight distribution and short-chain branches. Materials of type c) can be produced by single-side catalyst technology that enables an even distribution of side chains along the backbone and a better control of molecular weight. Polymers with an architecture like d) contain long-chain branches (LCB), but no SCB. Type e) architectures can be metallocene low density polyethylenes (mLDPE) which contain LCB randomly grafted in the backbone chain and in other branches and can have a maximum of 50% crystallinity. The last three types: f), g) and h), are model topologies and mainly produced in a laboratory scale by anionic polymerization (e.g. monodisperse polystyrene).

The main goal of this thesis is to detect structures like the above in polystyrene and industrial polyethylene, quantify the branching degree and correlate the topology of the macromolecules with their non-linear rheological behaviour as analyzed and quantified via Fourier-Transform Rheology. The experimental results are correlated to flow simulations.

1.4 Polymer rheology

In several polymerization techniques and especially in industrial production, it is not always possible to accurately control the product characteristics, i.e. the molecular weight, molecular weight distribution and macromolecular structure. All materials possess specific structures at the molecular, crystal or macroscopic level which are involved in flow phenomena of interest [Tanner 00]. For this reason, rheological and mechanical methods are developed and used. One advantage of such techniques is that the mechanical deformation of a material under compression, elongation or shear is extremely sensitive to the material morphology, chain size and topology.

Rheology is defined as the science of deformation and flow of matter [Tanner 00]. The principal theoretical concepts are kinematics dealing with geometrical aspects of deformation and flow, conservation laws related to forces, stresses and energy interchanges and constitutive relations serving as a link between motion and forces. Over the years, rheology has been established as a scientific method to perform quality control on polymers used as raw material, consistency monitoring and troubleshooting of products, “fingerprinting” of different structures, new material development, product performance prediction, design and optimization of processes. Rheology is the bridge between molecular structure and processing ability, as well as product performance. Rheological methods are developed and used as an important link in the so-called “chain of knowledge” on polymer mechanical properties and their correlation with processing features [Gahleitner 01].

1.4.1 Viscoelastic models

Generally, rheology can give information about the viscosity and the modulus of a material, in simple words how hard or soft it is and what are it's deformation and flow properties [Larson 99]. Since rheology has a wide range of applications, there are several methods that belong in this field, with the more applied being extensional rheology, steady-shear and oscillatory shear. The latter method is the one mainly undertaken in the present work, hence the introduction will focus on this particular type of flow.

The word "viscoelastic" corresponds to a material with both viscous (fluid-like) and elastic properties (solid-like). The two different ideal states of a viscous fluid and an elastic solid can be described by linear model systems and for the specific case of shear flow.

- Ideal solids, which are elastic and obey the Hooke's law:

$$\sigma = G\gamma \tag{1.1}$$

where σ is the stress (force per area), G is the shear-modulus (a material dependent proportionality constant) and γ is the deformation, or strain. The deformation is defined as x/d, where x is the displacement of the studied body and d a characteristic length scale of the flow. As an example, in an extending rod, x, is the length of the extended part and d is equal to the initial length. For a fluid sheared between two parallel plates with the one moving with velocity $v = dx/dt$, where x is the displacement of the moving plate and d corresponds to the distance between the two plates.

One can imagine a spring, which is extended with an angular velocity (radial frequency) ω and a strain amplitude γ_0 (fig. 1.2 and 1.3) and relaxes back to the starting position [Macosko 94].

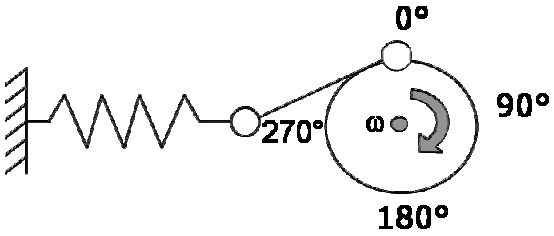

Figure 1.2: *Ideal elastic behaviour of a spring.*

If we assume that the deformation is sinusoidal then:

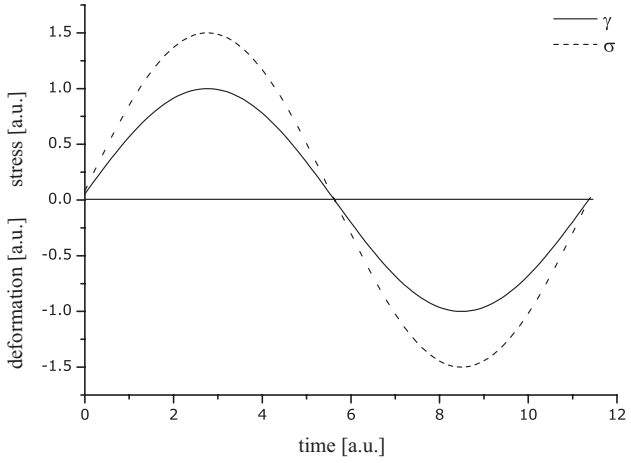

Figure 1.3: *Deformation as a function of time for ideal-elastic behaviour.*

$$\gamma = \gamma_0 \sin(\omega t) \tag{1.2}$$

For the shear stress, σ, we have:

$$\sigma = G\gamma_0 \sin(\omega t) \tag{1.3}$$

In fig. 1.3 it is shown that stress and deformation are sinusoidal and in phase. This model is assumed to describe ideal solid materials.

- Ideal fluids obey the Newton's law:

$$\sigma = \eta\dot{\gamma} \tag{1.4}$$

The stress σ depends linearly on the shear-rate, $\dot{\gamma} = d\gamma/dt$, which is the time derivative of γ. The proportionality constant here is the viscosity, η. To model this behaviour, one can use a damper in vessel or so-called dash-pot (fig. 1.4).

If the movement is the same as for the spring, then the deformation is as follows:

$$\dot{\gamma} = \frac{d\gamma}{dt} = \gamma_0\omega \cos(\omega t) \tag{1.5}$$

and the shear stress

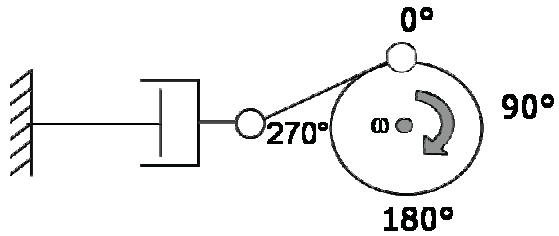

Figure 1.4: *Ideal viscous material described by a damper in a vessel filled with a viscous fluid.*

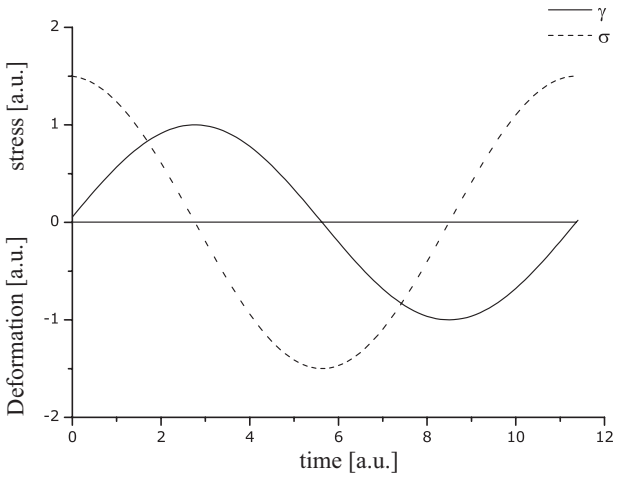

Figure 1.5: *Deformation as a function of time for an ideal viscous material.*

$$\sigma = \eta\gamma_0\omega\cos(\omega t). \tag{1.6}$$

In this case, the shear stress is $\delta = 90^\circ$ out of phase in relation to the deformation (fig. 1.5). This can be obtained from eq. 1.6 and models an ideal viscous liquid-like behaviour:

$$\sigma = \eta\gamma_0\omega\sin(\omega t + \delta), \delta = 90^\circ \tag{1.7}$$

The physical meaning and the difference between the two models is that, in the Hookean spring the given energy is stored in the system, while in the Newtonian damper an energy dissipation takes place. In other words, the spring “remembers” it’s initial state and returns to it, while the damper moves in an irreversible manner.

The above situations are ideal and can only approximate a real material. Every solid material does not react only with a pure elastic manner, but also with a certain viscous behaviour. The opposite argument stands for fluids, where the non-pure viscous behaviour is coupled with an elastic part. In order to approximate better the viscoelastic behaviour of real

materials, models are developed from combinations of the above mentioned basic elements (spring and dash-pot). The simplest cases are the Kevin-Voigt-Model, where the spring and the damper are parallel connected (for solids with some viscous part) and the Maxwell-Model (for fluids with some elastic part), where the two basic parts are connected in a row. The total stress, σ, for the Kelvin-Voigt and the total strain, γ, for the Maxwell, respectively, are added [Tanner 00]. The resulting phase lag between stress and deformation is $0° < \delta < 90°$. One can of course combine the two basic elements in more complicated ways to achieve a better approach of the real behaviour of viscoelastic materials at small deformation amplitudes.

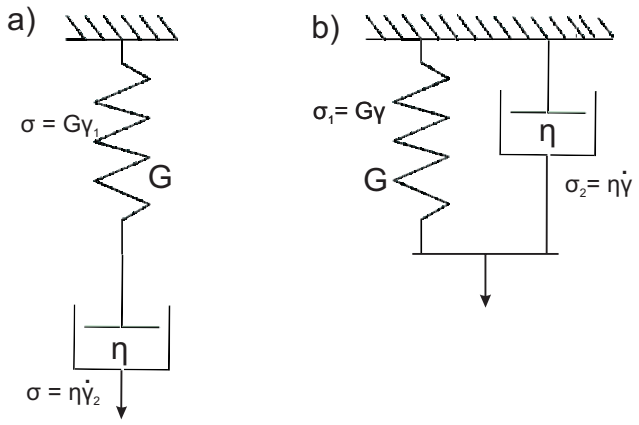

Figure 1.6: *a) Maxwell model with the elastic and viscous elements in a row. The total strain is:* $\gamma = \gamma_1 + \gamma_2$. *b) Kelvin-Voigt model with the two elements in parallel connection. The total stress is:* $\sigma = \sigma_1 + \sigma_2$.

1.4.2 Dynamic oscillatory shear for viscoelastic materials

With the use of dynamic oscillatory shear measurements, it is possible to gain complex rheological information from viscoelastic materials, since the excitation frequency and the temperature can be varied over a wide range. The sample is deformed in a periodic sinusoidal manner and the material response is recorded. This response is a shear stress with a phase lag in relation with the deformation, i.e. the shear strain. The mathematical description of the deformation is as follows:

$$\gamma(t) = \gamma_0 \sin(\omega t) \tag{1.8}$$

and for the resulting stress we have:

$$\sigma(t) = \sigma_0 \sin(\omega t + \delta) \tag{1.9}$$

The complex modulus as a function of excitation frequency is defined as:

$$G^*(\omega) = \frac{\sigma^*}{\gamma^*} = G'(\omega) + iG''(\omega) \tag{1.10}$$

hence, the total stress is:

$$\sigma(t) = G'(\omega)\gamma_0 \sin(\omega t) + G''(\omega)\gamma_0 \cos(\omega t) \tag{1.11}$$

The first term on the right side of the equation which includes $G'(\omega)$ is in phase with the deformation and the term with the $G''(\omega)$ proportionality is out of phase. The quantity $G'(\omega)$ describes the elastic part of the response and is called the storage modulus. Respectively the $G''(\omega)$ is the loss modulus and stands for the viscous part of the stress response. The two moduli are related through:

$$\tan\delta = \frac{G''(\omega)}{G'(\omega)} \tag{1.12}$$

where tan δ is the loss tangent. If tan $\delta > 1$ the sample mainly "flows" (behaves fluid-like) and if tan $\delta < 1$ the sample has a dominant solid-like (elastic) behaviour. The loss tangent is in contrast to the moduli $G'(\omega)$ and $G''(\omega)$, an intensive quantity and can be measured with a high reproducibility. Errors, e.g. due to sample loading or preparation, are compensated to a large degree for $\tan\delta$. Thus, it is frequently used in the industry. It must be noted that eq. 1.11 is valid only for small strain amplitudes, γ_0. In other words only for the linear viscoelastic regime, where the viscosity is independent of shear-rate or strain amplitude.

The complex dynamic viscosity can be derived from the complex modulus [Tanner 00]:

$$\eta^* = \frac{G^*}{i\omega} \tag{1.13}$$

Equation 1.12 can be written as:

$$\tan\delta = \frac{G''(\omega)}{G'(\omega)} = \frac{\eta'(\omega)}{\eta''(\omega)} \tag{1.14}$$

For a large number of monodisperse homopolymer melts above the glass transition and solutions of homopolymers, the shear-rate dependent viscosity is approximately equal to the frequency dependent complex viscosity $\eta(\dot{\gamma})$ [Cox 58]:

$$|\eta^*(\omega)| = \eta(\dot{\gamma}) \tag{1.15}$$

This is an empirical observation, known as the Cox-Merz-rule [Cox 58]. It is widely applied in industry, in order to estimate shear moduli from viscoelastic data, especially if time-temperature superposition can be applied (see paragraph 1.4.3). However, it is invalid for complex systems, e.g. block-copolymers, liquid crystals, or gels and generally this empirical rule needs first to be established for each system.

For entangled, linear, monodisperse polymer melts (with no solvent), the frequency-dependent moduli G' and G'' have characteristic dependencies (see Fig. 1.7). Using the Maxwell model, at low frequencies the proportionalities: $G' \propto \omega^2$ and $G'' \propto \omega^1$ can be obtained. This is summarized as follows [Tanner 00] (for a detailed analysis see paragraph C in Appendix):

$$G'(\omega) = G\frac{\omega^2\tau^2}{1+\omega^2\tau^2} \tag{1.16}$$

and

$$G''(\omega) = G\frac{\omega\tau}{1+\omega^2\tau^2}. \tag{1.17}$$

where τ is a characteristic relaxation time for the dash-pot, G is the modulus for which $\tau = \eta/G$. Equations 1.16 and 1.17 correspond to a dominantly Hookean behaviour when $G' >> G''$ and to a dominantly Newtonian behaviour for $G'' >> G'$. The elastic modulus, G', at the low frequency range can be negligible in comparison to G'', hence this regime is called also "Newtonian" or "flow region" and corresponds to $\omega << 1/\tau_d$ in fig. 1.7.

Figure 1.7 depicts the resulting frequency dependent G', G'' and complex viscosity, derived from an oscillatory shear measurement at a specific reference temperature. In the zone where $\omega << 1/\tau_d = 1/\tau$ (flow region) the complex viscosity, $|\eta^*(\omega)|$, is independent of ω, because of the linear relation between G'' and ω (eq. 1.13). The specific material behaviour

approximates that of a viscous fluid. At higher frequencies there is a crossover between $G'(\omega)$ and $G''(\omega)$ at $\omega = 1/\tau_d$ and above this crossover frequency the regime is called the "rubbery plateau". The inverse of this above mentioned frequency is the longest characteristic relaxation time of the material, τ_d, and can be considered as the relaxation of a polymer chain via reptation movements [deGennes 71]. In the rubbery zone the material has a dominant elastic behaviour and one can extract a plateau modulus, G_N^0. It can be calculated from the value of $G'(\omega)$ at the lower frequency where tan δ has a minimum (see Appendix D).

When studying polymer materials, the molecular weight between entanglements, M_e can be derived from the plateau modulus. The probed length scale in this frequency range corresponds to the chain length between entanglements [Fetters 94, Ward 04]:

$$M_e = \frac{\rho RT}{G_N^0} \tag{1.18}$$

where ρ is the density, R is the universal gas constant and T is the absolute temperature. The extend of the plateau zone depends on the molecular weight of the polymer. The time-scale in this regime corresponds to the Rouse time, τ_R, where macromolecules relax through segmental "Rouse-like" movements [Larson 99].

At higher frequencies or reduced temperatures, a second moduli crossover point is

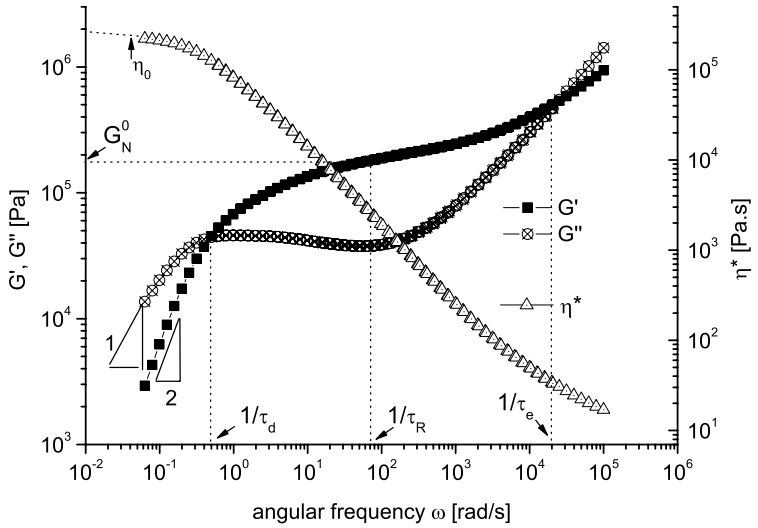

Figure 1.7: *Typical G', G'' and absolute complex viscosity $|\eta^*|$ as a function of frequency, for a linear monodisperse polystyrene melt of 330 kg/mol.*

observed, at $\omega = 1/\tau_e = 2\times10^{-4}$ rad/s in fig. 1.7. This inverse crossover frequency corresponds

to the entanglement characteristic time, τ_e. This is the transition zone towards the glassy plateau, that describes the relaxation process of chain segments. The moduli curves in this zone have higher slopes as in the flow region. At even higher frequencies one can see a third crossover point, which is not easy to reach experimentally (not shown in fig. 1.7). This third crossover point at very high frequencies corresponds to the inverse of a segmental motion characteristic time, τ_s, and for $\omega > 1/\tau_s$ the glass plateau follows. In this area every chain movement is "frozen" and one approaches the glass transition temperature, T_g. The probed length scale here has typical polymer glass dimensions, of the order of 2-3 nm [Ward 04]. Typical moduli values for this process are around 10^9 Pa.

1.4.3 Time-temperature superposition (TTS)

Figure 1.7 is a typical graph representing the frequency-dependent shear moduli. However, these moduli could not have been experimentally measured in the presented frequency range, which covers almost seven decades. This plot of the viscoelastic properties represents a "mastercurve" which can be obtained for a wide range of frequencies (typically 6-10 decades) with the time-temperature superposition method (TTS). According to this semi-empirical method, the internal mobility of the material is higher when the temperature increases. Hence, a temperature increase corresponds to a decrease on the time-scale of the chain movement. Taking advantage of this fact, we can measure at different temperatures for the same frequency range and horizontally shift (with respect to frequency) the resulting curves to a mastercurve, by using a shift factor for the frequency axis, a_T, which follows the eq. 1.19. The mastercurve will correspond to the wider frequency range. The reference temperature is where $a_T = 1$. This is valid of course when no phase transition takes place in the measured temperature range. A relation for this superposition is given by the Williams-Landel-Ferry (WLF) equation [Williams 55]:

$$\log a_T = -\frac{C_1(T - T_0)}{C_2 + (T - T_0)} \tag{1.19}$$

where T_0 is the reference temperature typically between T_g and T_g + 100 °C, where T_g is the glass-transition temperature [Ward 04]. Parameters C_1 and C_2 are material constants. An example of a TTS can be seen in fig. 1.8. In fig. 1.8 the frequency sweeps performed at different temperatures are depicted. The resulting curves are shifted using eq. 1.19 and the mastercurve shown in fig. 1.7 can be obtained. The horizontal shift-factor, a_T, is shown in fig. 1.9. In this example, the reference temperature is 180 °C and for this temperature: $a_T = 1$. A small vertical shift factor, b_T, can also be utilized to compensate for density differences and is given by:

$$b_T = \frac{\rho T}{\rho_0 T_0)} \tag{1.20}$$

where T_0 is the reference temperature and ρ_0 is the density at T_0.

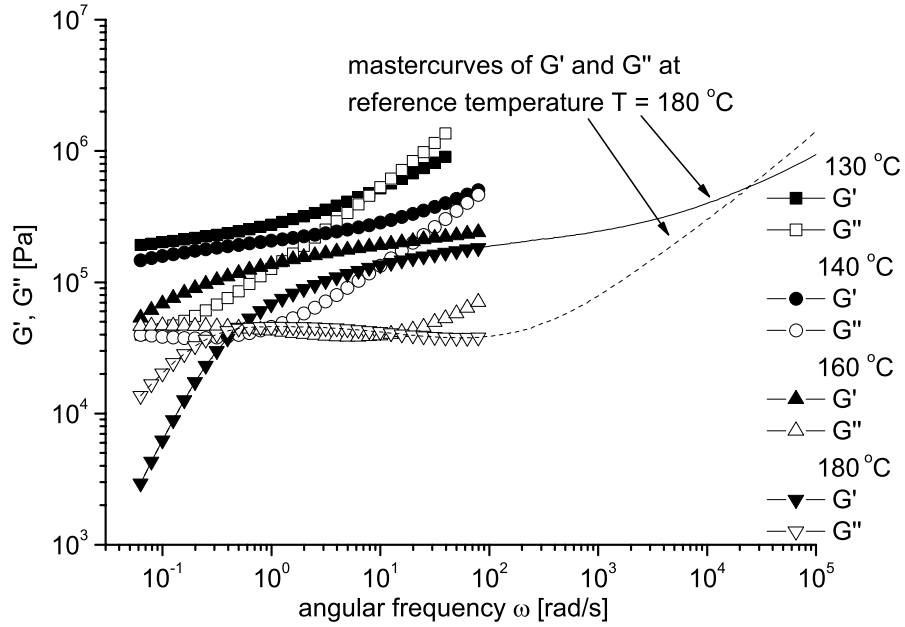

Figure 1.8: *Four frequency sweep measurements at different temperatures. The sample is a linear polystyrene melt with molecular weight M_w = 330 kg/mol. The solid and the dashed lines represent the resulting mastercurve after applying TTS with a reference temperature T = 180°C.*

1.4.4 Pipkin diagram

For the purpose of this work, the Deborah number, *De*, must be introduced. It is a dimensionless number and defines the ratio of the relaxation time of the material, τ, to the characteristic time of the deformation, t:

$$De = \frac{\tau}{t} = \tau\omega \tag{1.21}$$

In literature for oscillatory shear one can find the Deborah number defined as: $De = \tau\omega\gamma_0$. However, within this work the definition of eq. 1.21 is used. The deformation amplitude,

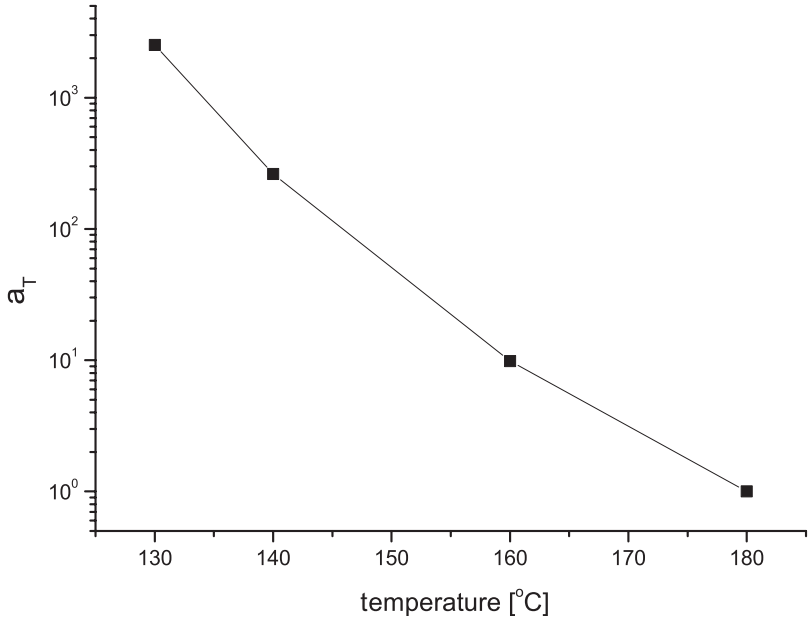

Figure 1.9: *The WLF-shift factors for the frequency sweep measurements of fig. 1.8. The constants are* $C_1 = 5.52$ *and* $C_2 = 131.2$ *and the reference temperature is 180°C.*

γ_0, is an important quantity. By increasing γ_0 one moves from the linear to the non-linear rheological regime. High Deborah numbers ($De >> 1$) correspond to an elastic response of the material, while a viscous response can be observed at $De << 1$. At intermediate Deborah numbers $De \approx 1$, viscoelastic behaviour is observed. The relation between frequency, strain amplitude and the resulting polymer behaviour can be illustrated in the so-called Pipkin-Diagram, presented in fig. 1.10.

From the Pipkin diagram, one can conclude that polymers for $De << 1$ and low deformation amplitudes behave rheologically similar to Newtonian fluids. For very high *De* the material behaviour approaches a Hookean solid. For $De \approx 1$, the viscoelastic character is probed and for low or high deformation amplitudes the process is in the linear or non-linear regime, where the viscosity is shear-rate-independent or shear-rate-dependent, respectively. In this region of intermediate *De* the relaxation time and the deformation time are of the same order of magnitude.

Many rheological processes and the majority of the industrial polymer processing takes place in the non-linear viscoelastic regime. Thus, it is important to investigate and understand the flow phenomena that occur in this non-Newtonian region. The classical rheological experiments are not adequate because they do not provide enough information about the non-linear behaviour of a material. One useful technique that shows a great potential towards studying the non-linear regime, is Fourier-transform Rheology (FT-Rheology) [Giacomin 98, Krieger 73, Wilhelm 98], which is the method mainly undertaken in the present thesis. FT-Rheology will be discussed in paragraph 1.5.

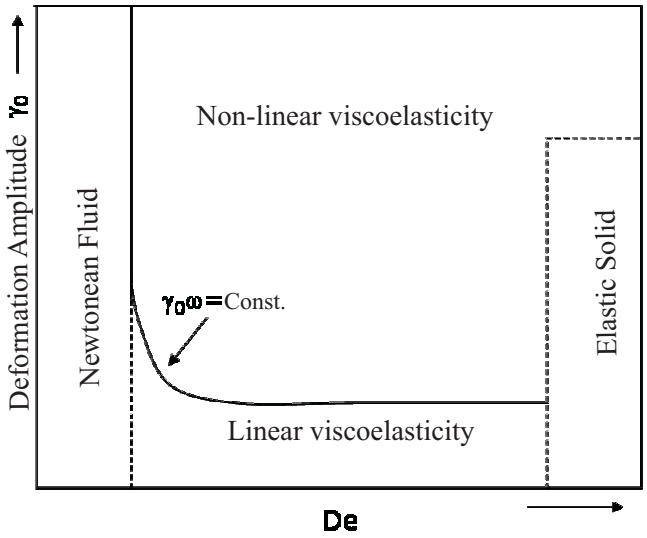

Figure 1.10: *Pipkin-Diagram.*

1.4.5 Polymer stress relaxation-tube model-reptation model

Polymer chains that have a molecular weight larger than a specific value create temporary entanglements by "chain overlapping". The longer the chain is, the more entanglements a polymer will possess. These temporary junctions influence the relaxation behaviour of the polymer under mechanical deformation (e.g. shear or elongation). This is because entanglements act as physical obstacles in the free movement of the chain. Considering a single chain, these topological constraints present a boundary on the normal to the chain direction. Thus, the situation can be described as a "tube" created from the neighbouring chains that are entangled with the considered chain and act as a wall that prevents free chain movement to the normal direction, illustrated in fig. 1.11, [deGennes 71, Doi 79].

Linear homopolymers have a characteristic molecular weight, M_c, and an entanglement molecular weight, M_e. The first one corresponds to the average chain length above which the creation of entanglements increases the viscosity significantly. After this critical length, the relation between zero-shear viscosity, η_0, and molecular weight is not linear, but can be described by: $\eta_0 \propto M^{3.4}$, for $M > M_c$ [Larson 99]. The second characteristic molecular weight, M_e, corresponds to the chain length between two entanglements and can be rheologically determined (see paragraph 1.4.2).

Taking the "tube" picture into consideration, the reptation model was proposed by de Gennes, in order to describe the viscoelasticity and the diffusion in concentrated polymer solutions and melts, accompanied by the tube-theory of Doi and Edwards [deGennes 71, Doi 78a, Doi 78b, Doi 78c, Doi 79]. In this model, the chain is able to move only in a con-

fined space, due to the entanglements with neighbouring chains, as illustrated in fig. 1.11. The polymer chain can reptate along this tube. The tube diameter can be interpreted as the end-to-end distance of an entanglement strand of N_e monomers and is given as $\alpha_{tube} \approx bN_e^{1/2}$, where b is the monomer size and N_e the number of monomers in an entanglement strand. The product of α_{tube} with the average number of entanglement strands per chain, N/N_e, provides the average countour lenght of the chain primitive path, $\langle L \rangle$ [Rubinstein 03]. After a specific time, the chain will manage to reptate out of the original tube and will confine itself into a new tube. The chain relaxation process in a tube can be described as a diffusion of its contour length. The curvilinear diffusion coefficient, D, that describes the motion of the chain along the tube, is simply the Rouse diffusion coefficient of the chain [Rubinstein 03] and is given by the Einstein equation (1.22).

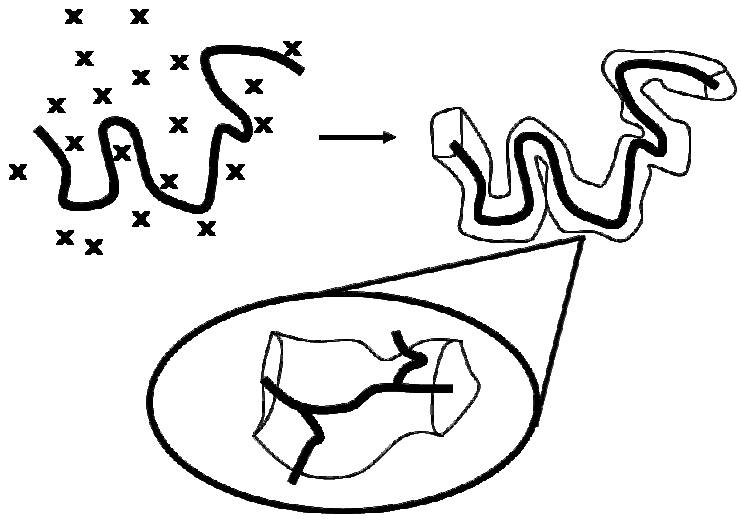

Figure 1.11: *The Reptation model. The movement of a polymer chain is confined by the entanglements with the neighbouring chains (x). The situation can be simulated by a tube. For topological complicated materials additional entanglements (permanent) are considered, which effectively influence the tube dimensions and the chain relaxation within the tube.*

$$D = \frac{kT}{N\xi} \propto \frac{1}{M} \tag{1.22}$$

In the above equation, k is the Boltzman constant, T is the absolute temperature, N is the number of chain-segment and ξ is the friction coefficient of the single monomer. This is valid for an entangled chain moving through a tube.

In order for the chain to diffuse from its original tube of length $\langle L \rangle$, a time equal to the reptation time, τ_d, is needed and expressed as:

$$\tau_d \simeq \frac{l^2}{D} \tag{1.23}$$

where l is the contour-length of the chain. Thus, one can derive a relation between the longest relaxation time, τ_d, and the molecular weight:

$$\tau_d \propto \xi N^3 \propto M^3 \tag{1.24}$$

This model is not an exact description of the reality, due to the assumption of having only one moving chain while the other macromolecules are in a fixed position. This is the reason for the difference on the power of molecular weight, M, found experimentally, where $\tau_d \sim M^{3.4}$, from the theoretically predicted value of 3 from de Gennes [Larson 99]. The same relation can be obtained for the viscosity, $\eta_0(M_w)$, which is an extremely important rheological fact, since it explicitly correlates molecular wight with an experimentally determined bulk rheological material property.

Within this work, polymer systemscontaining SCB and LCB are investigated . If these side-chains are relatively short (unentangled) they do not affect the reptation of the backbone chain throughout the tube. However, if the side-chain has a molecular weight larger than the entanglement molecular weight, then these branches are considered as effective topological constrains for the chain backbone and result in a more complex relaxation process for the material (and a different relation between η_0 and M_w).

1.4.6 Non-linearities in polymer rheology

As depicted in the Pipkin diagram in fig. 1.10, in principle all viscoelastic materials can exhibit non-linearities for the whole range of *De* numbers, as long as the strain amplitude is large enough. When a molecular conformation departs significantly from equilibrium due to flow characteristics, even for negligible inertia effects, non-linearities arise [Marrucci 94]. The amount of non-linearity and the character of the non-linear rheological behaviour is a result from both flow characteristics and material properties. For example, large deformations are combined with specific relaxation mechanisms for solutions or entangled chains (branched or linear), or other material properties that can introduce non-linearities in the flow, e.g. structure formation or destruction.

In linear viscoelasticity once the relaxation function of the polymer is known, deformation and flow can be predicted, although only as long as the response of the material remains in the linear regime (small γ_0). When the deformation is such that the material state is different from the equilibrium, a non-linear response is observed. This is the most likely case in industrial processes (e.g. involving film blowing, blow molding, extrusion, etc.). The

non-linear viscoelasticity cannot be simply described by a single material function, due to the fact that the stress is also a function of the deformation history. Some examples of non-linear rheological behaviour in polymers are given below.

- Shear thinning in entangled systems of flexible polymers, like melts or concentrated solutions. This process can be described by the reptation theory of de Gennes [deGennes 71] and the tube model of Doi and Edwards [Doi 78b, Doi 78c, Doi 79]. In particular, when the polymer is subjected in shear flow, the tube is oriented in the shear direction, with an orientation depending on the shear-rate. This causes a loss in the proportionality between stress growth and $\dot{\gamma}$, i.e. a decrease in viscosity. By a further increase of $\dot{\gamma}$, the system can become unstable. Marrucci [Marrucci 94] stated that polydispersity broadens the relaxation spectrum, introduces additional relaxation mechanisms, such as constrain-release [Graessley 82], and thus makes the discrimination of the different dynamic processes harder to achieve.

- Shear thinning in liquid crystalline polymers. This mechanism can be explained in a similar manner as above, however the critical shear rate where the shear thinning takes place can be significantly lower. It has been proposed that it results from the progressive formation of a nematic phase, with increasing shear-rate [Marrucci 94].

- Shear thickening. It is an unusual case for polymers, however it is observed in complex systems, such as ionomers in non-polar solvents, where the ions tend to segregate into clusters. Large viscosities can then be seen, resulting from the formation of networks whose junctions are ion aggregates [Marrucci 93, Marrucci 94].

1.5 Fourier-Transform rheology

As mentioned above, the majority of industrial processes takes place in the non-linear regime, where large and time-dependent deformations are involved. Hence, the linearity between excitation and rheological response is not valid. Another example of a process in the non-linear regime is the application of a sinusoidal strain with a large amplitude. The resulting stress response will not be a pure sinusoidal signal with a phase lag, but rather a periodic signal that cannot be fully described by a single sinus function (see fig. 1.12). Therefore, one of the goals in rheology is to understand, model and predict the non-linear behaviour of polymers under these types of deformations, i.e. where linear viscoelastic theory cannot be applied.

The method of FT-Rheology has been proposed as a useful tool to investigate

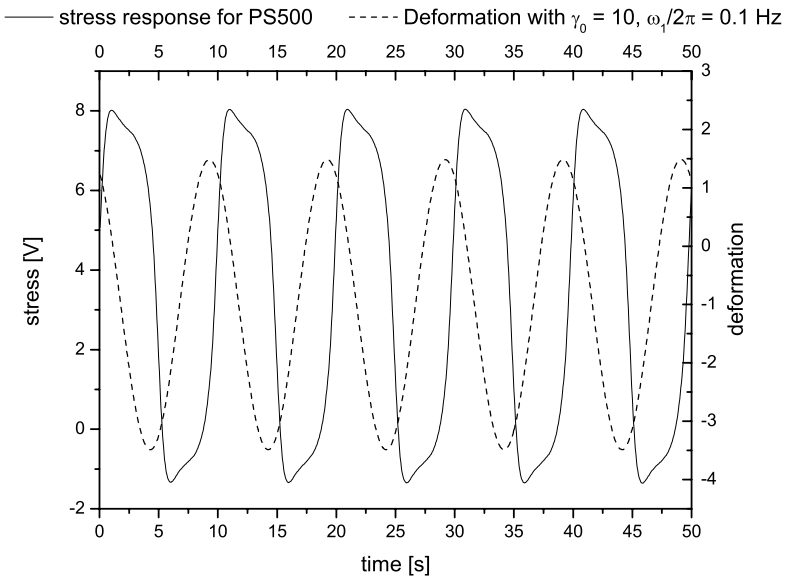

Figure 1.12: *Applied deformation and recorded shear stress response, for a linear PS with 500 kg/mol under LAOS.*

the non-linear regime in polymers, combined with large amplitude oscillatory shear experiments (LAOS) [Giacomin 98, Krieger 73, Neidhöfer 01, Wilhelm 98, Wilhelm 00, Wilhelm 02]. Large strain amplitudes are needed to provoke the material non-linear behaviour. Similar experiments have been performed in the past [Krieger 73], mainly using sliding plate geometries. However, because of hardware and software limitations the accuracy of the measurements was low and the data analysis tedious. The FT-Rheology as applied within this work, is much more sensitive and accurate, while still being simple from a hardware point of view [Wilhelm 99, Dusschoten 01]. As a method it has been successfully used to study polymer colloidal dispersions in combination with optical methods [Klein 05] and for investigation of polymer melts and solutions with different topologies ([Höfl 06, Neidhöfer 03b, Neidhöfer 03a, Neidhöfer 04, Vittorias 06]. Leblanc [Leblanc 03] used FT-Rheology to study gum elastomers and rubbers. FT-Rheology has also been used to characterize linear polystyrene solutions, by Neidhöfer et al. [Neidhöfer 03a]. Experimental results were combined with simulation of LAOS flow with the Giesekus constitutive model. The analysis of the Fourier spectrum of the stress response, i.e. the relative intensity $I_{n/1}$ and the phase Φ_n oh the higher harmonics, allowed distinguishing different topologies of polystyrene solution, where small amplitude oscillatory shear (SAOS) and non-linear step-shear measurements had failed to discriminate between them [Neidhöfer 04]. In particular, the use of the relative phase of the third harmonic, Φ_3, over a broad range of applied frequencies was investigated. The differences between linear and star-shaped architectures

were found to be more pronounced for Deborah (*De*) numbers varying between 0.3 and 30.

1.5.1 Fourier-transformation

This mathematical transformation is named after the mathematician and physicist Jean Baptiste Joseph Fourier (1768 - 1830). Fourier-transformations (FT) have a broad application in many science fields, e.g. in NMR- and IR-Spectroscopy [Ernst 90, Kauppinen 01, Schmidt-Rohr 94]. One can describe a continuous, integrable, periodic function, $f(t)$, in a series of trigonometrical functions, the Fourier-series [Bartsch 74, Ramirez 85, Zachmann 94]:

$$f(t) = \sum_{k=0}^{\infty} (A_k \cos \omega_k t + B_k \sin \omega_k t) \tag{1.25}$$

where $\omega_k = \frac{2\pi k}{T}$ are the frequencies and T are the periods of $f(t)$. The Fourier coefficients (amplitudes) are calculated as follows:

$$A_k = \frac{2}{T} \int_0^T f(t) \cos \omega_k t dt \tag{1.26}$$

$$B_k = \frac{2}{T} \int_0^T f(t) \sin \omega_k t dt \tag{1.27}$$

If they are expressed in a complex way and the Euler formula is used we obtain:

$$f(t) = \sum_{k=-\infty}^{\infty} C_k \exp \{i\omega_k t\} \tag{1.28}$$

where the coefficient C_k is:

$$C_k = \frac{1}{T} \int_0^T f(t) \exp \{-i\omega_k t\} \, dt \tag{1.29}$$

Allowing a period $T \to \infty$, then the Fourier-Integral is derived:

$$f(t) = \frac{1}{2\pi} \int_{-\infty}^{\infty} F(\omega) \exp\{i\omega t\}\, dt \tag{1.30}$$

which can easily be reversibly transformed:

$$F(\omega) = \int_{-\infty}^{\infty} f(t) \exp\{-i\omega t\}\, dt \tag{1.31}$$

The prefactor $\frac{1}{2\pi}$ can vary, dependently on conventions. The complex function, $F(\omega)$, can be expressed by a real and an imaginary part, or in the form of an amplitude and a phase:

$$F(\omega) = F_{re}(\omega) + iF_{im}(\omega) = A(\omega) \exp\{iP(\omega)\} \tag{1.32}$$

where $F_{re}(\omega)$ is the absorption part and $F_{im}(\omega)$ is the dispersion part. Then the amplitude spectrum is given by:

$$\mid A(\omega) \mid = \sqrt{F_{re}(\omega)^2 + F_{im}(\omega)^2} \tag{1.33}$$

and the phase spectrum:

$$P(\omega) = \arctan(F_{re}(\omega)/F_{im}(\omega)) \tag{1.34}$$

The dependence between these components can be presented in a Polar diagram (Fig. 1.13).

A very important feature of the FT is it's linearity.

$$af(t) + bg(t) \overset{FT}{\longleftrightarrow} aF(\omega) + bF(\omega) \tag{1.35}$$

The superposition of more than one signal in the time domain, will be through FT transformed into a superposition of frequencies in the frequency domain. Hence, for a periodic response signal of an oscillation, one can calculate the corresponding frequencies in the time signal and analyse them in respect to their amplitude and phase.

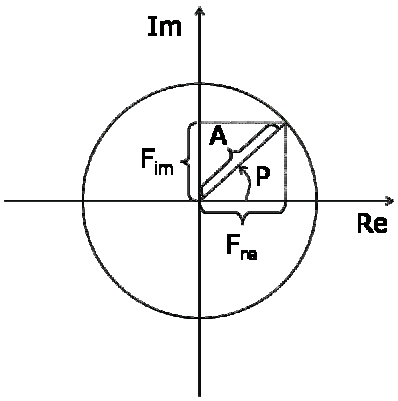

Figure 1.13: *Polar diagram of a complex number $z = Re + iIm$. The quantity A corresponds to the amplitude and P to the phase spectrum, at a fixed frequency ω_1.*

1.5.2 Fourier-transformation in rheology

With the application of FT-Rheology, resulting stress signals, such as the one depicted in fig. 1.12, can be analyzed and the non-linear rheological behaviour of a material under LAOS can be quantified. For the FT-Rheology a half-side, discrete, complex Fourier-transformation is implemented, in order to be able to analyze phases and magnitudes of the resulting FT-spectrum derived from the stress time signal. Half-sided means that the space between the integration limits in eq. 1.30 and 1.31 is reduced to the half, i.e. $0 \leq t < \infty$. A FT is inherently complex. Hence, even from a real signal in the time domain, $f(t)$, one obtains a complex spectrum, $F(\omega)$, with a real and an imaginary part. In the majority of LAOS experiments, the time data are acquired not continuous but in a discrete way and with a specific time interval between two successive points, called the dwelling time, t_{dw}. These N discrete time data are acquired with a k-bit analog-to-digital converter (ADC card). This device has $2^k - 1$ discretization in the y-dimension [Wilhelm 99, Wilhelm 02]. High values of k allow the detection of smaller intensities of a signal, where an ADC card with less available bits would fail. Thus, the signal-to-noise ratio (S/N) can be significantly increased [Skoog 96]. In this work a 16-bit ADC card is utilized. The dwelling time, t_{dw}, is the same for the whole time domain or acquisition time, hence $t_{aq} = t_{dw}N$. From N real (or complex) time data via the Fourier-Transformation we obtain N complex points in a discrete spectrum. The spectral width is defined by the highest measurable frequency, the Nyquist-frequency, and is given by:

$$\frac{\omega_{max}}{2\pi} = \nu_{max} = \frac{1}{2t_{dw}} \tag{1.36}$$

The spectral resolution, in other words the frequency difference between successive points in the spectrum is:

$$\Delta\nu = \frac{1}{t_{aq}} \tag{1.37}$$

An increase of t_{aq} reduces the line width and increases the S/N, which is defined as the ratio of the amplitude of the highest peak to the average of the noise level. The oscillations result in broad peaks in the FT-spectrum, hence the acquisition time must be large enough to achieve a high sensitivity and narrow peaks [Wilhelm 99]. This dependence can be seen in fig. 1.14. An optimum acquisition and dwelling time should be used, with respect to the peak width, measurement time and data file size. An extremely large acquisition time would not improve the peak width substantially, since there are factors, such as experimental inaccuracies and hardware limitations, which result to an additional line broadening. Typically 5 to 50 cycles of the excitation frequency are acquired.

Data averaging of the spectra can increase the sensitivity significantly. The S/N increases with the square root of the number of spectra added, n.

$$S/N \propto \sqrt{n} \tag{1.38}$$

This method of FT and data acquisition is used to measure the intensity of harmonics with a higher accuracy, however phase information may be lost in case only magnitude spectra are simply added without triggered time data acquisition.

In order to improve the S/N ratio and also to be able to measure data at very low torques "oversampling" can be applied [Dusschoten 01]. This technique increases the sensitivity of measurements in the linear and in the non-linear regime, by a factor of 3 to 10, for standard rheometers. The raw data are acquired with the highest possible sampling rate, in other words much more points than the minimum number needed to fully characterize the signal. A large number of points between t and $t + \Delta t$ is averaged and we obtain a signal value for $t + 0.5\Delta t$. Data acquired with the use of "oversampling" have a significantly higher S/N. A typical oversampling of 100 to 3000 is applied within this work, depending on the excitation frequency (see chapter 2).

1.5.3 Principles of FT-Rheology

Fourier-Transform-Rheology is a theoretically and experimentally simple and robust method used to investigate and quantify time-dependent non-linear flow phenomena. In the following paragraph, the basic theoretical aspects of the high-sensitivity FT-Rheology are presented by the example of the dynamic oscillatory shear [Wilhelm 98, Wilhelm 02].

The force balance of a system of mass, m, viscosity, η, and elastic modulus, k, which is

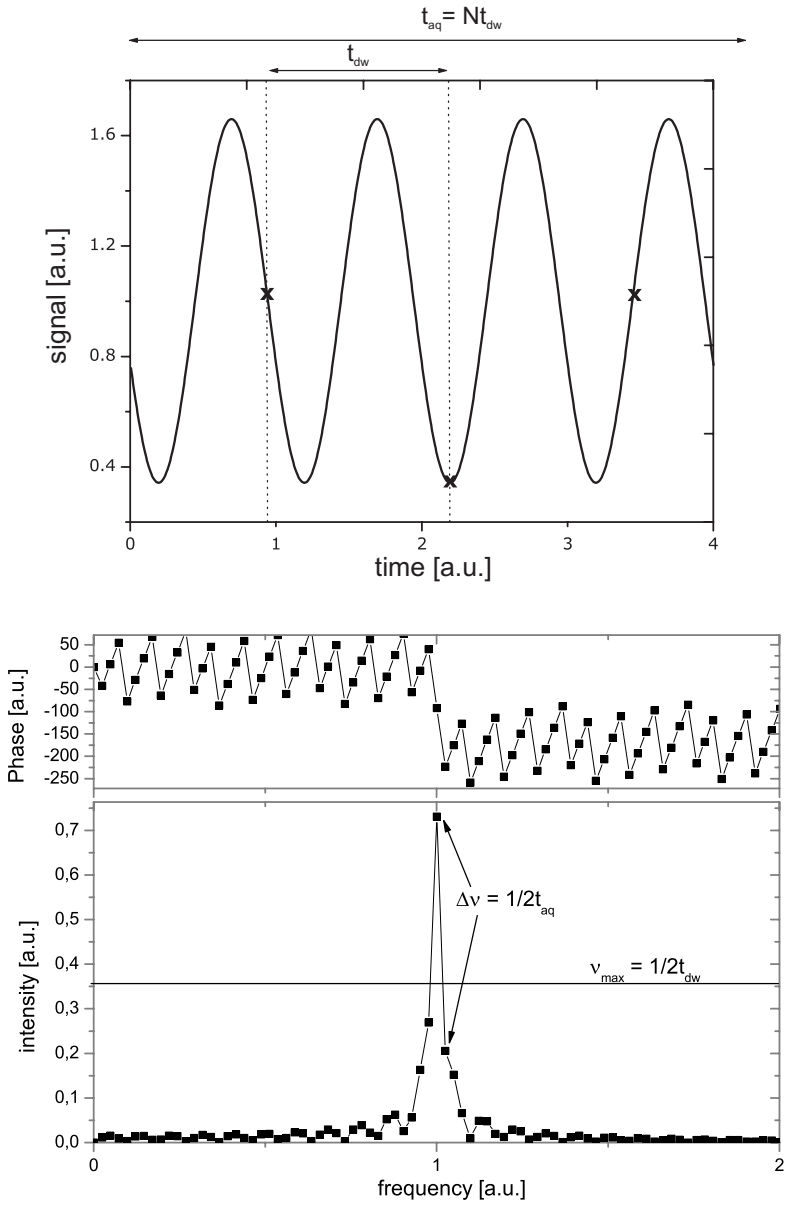

Figure 1.14: *Basic scheme of a discrete Fourier-Transformation. The time data are shown in the upper part and below analyzed with respect to amplitudes and phases. The dwelling time t_{dw} limits the spectral width ν_{max} and the acquisition time, t_{aq} limits the spectral resolution, $\Delta\nu$ [Wilhelm 99].*

excited with a simple oscillatory movement of frequency, $\omega_1/2\pi$, is given by a simple linear differential equation of the following archeotype:

$$m\ddot{\gamma} + \eta\dot{\gamma} + k\gamma = A_0 \exp\{i\omega_1 t\} \tag{1.39}$$

The three left terms correspond to the kinematic, viscous and elastic part of the force applied to the system. The mathematical expression for a deformation, γ, for constant η in equation 1.39 is a simple harmonic function:

$$\gamma(t) = \gamma_0 \exp\{i(\omega_1 t + \delta)\} \tag{1.40}$$

where $\omega_1/2\pi$ is the excitation frequency and δ the characteristic phase lag. As already mentioned, the viscosity is given by the equation $\sigma = \eta\dot{\gamma}$ (Newton's law). For a Newtonian material the viscosity, η, is always constant and shear-rate independent. If the material is non-Newtonian, η is a function of time and shear-rate in the non-linear regime, $\eta = \eta(\dot{\gamma}, t)$. If the shear is in a periodic steady state (constant strain amplitude and excitation frequency), η will be dependent only on the applied strain deformation. Furthermore, the viscosity will not depend on the direction of the shear: $\eta = \eta(\dot{\gamma}) = \eta(-\dot{\gamma}) = \eta(\mid \dot{\gamma} \mid)$. Under these assumptions, the viscosity can be expressed with a Taylor expansion of the absolute value of the shear-rate:

$$\eta(\mid \dot{\gamma} \mid)) = \eta_0 + a \mid \dot{\gamma} \mid + b \mid \dot{\gamma} \mid^2 + ... \tag{1.41}$$

For oscillatory shear the shear-strain (or deformation), γ, is:

$$\gamma = \gamma_0 \sin(\omega_1 t) \tag{1.42}$$

and the shear-rate, $\mid \dot{\gamma} \mid$, is the product of the shear-strain:

$$\mid \dot{\gamma} \mid = \omega_1 \gamma_0 \mid \cos(\omega_1 t) \mid \tag{1.43}$$

The shear-rate, $\mid \dot{\gamma} \mid$, is expressed as a Fourier-series, in order to derive the time-dependency as a sum of the harmonics [Ramirez 85]:

$$\begin{aligned} \mid \dot{\gamma} \mid &= \omega_1 \gamma_0 \left(\frac{2}{\pi} + \frac{4}{\pi} \left(\frac{\cos(2\omega_1 t)}{1 \cdot 3} - \frac{\cos(4\omega_1 t)}{1 \cdot 5} + \frac{\cos(6\omega_1 t)}{1 \cdot 7} \pm ... \right) \right) \\ &\propto a' + b' \cos(2\omega_1 t) + c' \cos(4\omega_1 t) + ... \end{aligned} \tag{1.44}$$

The absolute value of the cosine function is repeated every $180°$. Thus, in eq. 1.44 we find only even multiples of the first harmonic in ω_1. Equations 1.41 and 1.44 are introduced into the Newton's law:

$$\begin{aligned}
\sigma &\propto \eta\dot{\gamma} \\
&\propto (\eta_0 + a \mid \dot{\gamma} \mid + b \mid \dot{\gamma} \mid^2 + ...)\cos(\omega_1 t) \\
&\propto (\eta_0 + a(a' + b'\cos(2\omega_1 t) + c'\cos(4\omega_1 t) + ... \\
&\quad + b(a' + b'\cos(2\omega_1 t) + c'\cos(4\omega_1 t) + ...)^2 ...)\cos(\omega_1 t) \\
&\propto (a'' + b''\cos(2\omega_1 t) + c''\cos(4\omega_1 t) + ...)\cos(\omega_1 t)
\end{aligned} \tag{1.45}$$

From the application of the trigonometric additions theorem we obtain a sum of even harmonics. When this result is multiplied with the cosine part ($cos(\omega_1 t)$) for the shear excitation, the result is a sum of odd harmonics. Hence, one can rearrange eq. 1.45:

$$\sigma \propto a_1\cos(\omega_1 t) + a_3\cos(3\omega_1 t) + a_5\cos(5\omega_1 t) + ... \tag{1.46}$$

where a_i are complex coefficients. The different frequencies are analysed via a Fourier transformation of the response signal. A frequency spectrum with the first harmonic in excitation frequency, $\omega_1/2\pi$, and the harmonics at odd multiples is obtained. Each odd peak ($3\omega_1, 5\omega_1 ...$) can be quantified by the intensity, I_n, and the phase ϕ_n. In FT-Rheology these quantities are used as parameters to characterize the non-linear behaviour of materials.

The non-linearity in a material can be quantified by the ratio of the higher harmonics to the first, $I_{n/1} = \frac{I(n\omega_1)}{I(\omega_1)}$. The relative intensity $I_{n/1}$ has the advantage of being more reproducible, because through this normalization errors originating e.g. from variations in sample preparation, are minimized. The characteristic form of the LAOS stress signal is then quantitatively described by the relative contribution of the higher harmonics to the periodic response. The first odd harmonic that appears above the noise level is at a frequency of $3\omega_1/2\pi$. It has the highest relative intensity, $I_{3/1}$, in comparison with the other odd harmonics, which have an exponential decreasing intensity and appear when larger deformations are applied in the material at $5\omega_1/2\pi$, $7\omega_1/2\pi$, ...etc. Hence, the study of the FT-spectrum is in this work limited to the 3^{rd} higher harmonic contribution of the stress response during a LAOS for polymer melts, in respect to its relative intensity and phase. For other classes of materials, e.g. dispersions, a large number of higher harmonics can be detected with significant intensity [Kallus 01]. An empirical equation that describes the relative intensity of the 3^{rd} harmonic, $I_{3/1}$, as a function of γ_0 for a specific ω_1 with a sigmoidal curve can have

the following form [Wilhelm 02]:

$$I_{3/1}(\gamma_0) = A\left(1 - \frac{1}{1 + (B\gamma_0)^C}\right) \tag{1.47}$$

where *A* is the plateau $I_{3/1}$ for very large γ_0 and has typical values of 0.2 ± 0.1 for the studied polystyrene and polyethylene melts. Parameter *B* is the inverse critical strain amplitude. For $\gamma_0 = \frac{1}{B}$ we have $I_{3/1} = \frac{A}{2}$. Finally parameter *C* is the slope of $\log(I_{3/1})$ plotted against $\log(\gamma_0)$ for small strain amplitudes and has a theoretical value of 1.7 to 2 [Pearson 82]. Experimentally it is found to be between 1.7 and 2.5 [Neidhöfer 03b, Vittorias 06].

The empirical equation 1.47 requires available data from a broad range of strain amplitudes. In order to have a realistic value for parameter *C*, one needs enough data at low γ_0 (e.g. for polymer melts $0.1 < \gamma_0 < 2$). Parameter *A* can be estimated by fitting $I_{3/1}$ at very large strain amplitudes (for PE and PS typically: $\gamma_0 > 7$). However, these limits are not always experimentally reachable. This makes the analysis of a non-linearity plateau problematic. However, one can take only data corresponding to $\gamma_0 <$ 2-3 into account and use an equation which approximates eq. 1.47 at low and medium γ_0, by expanding it in a Taylor series as follows:

$$\begin{aligned} I_{3/1}(\gamma_0) &= A\left(1 - \frac{1}{1 + (B\gamma_0)^C}\right) = & (1.48)\\ &= A(1 - (1 - (B\gamma_0)^C - ((B\gamma_0)^C)^2 - ((B\gamma_0)^C)^3 - ...)) = \\ &= A((B\gamma_0)^C + ((B\gamma_0)^C)^2 + ((B\gamma_0)^C)^3 + ...) & (1.49) \end{aligned}$$

If one considers only the first term of the Taylor expansion, the expression derived is the following:

$$I_{3/1}(\gamma_0) \cong A((B\gamma_0)^C) = AB^C(\gamma_0^C) \tag{1.50}$$

where we substitute AB^C with a new parameter *D*, thus the non-linearity can be quantified via $I_{3/1}$ as a function of strain amplitude, γ_0, for low and medium amplitude oscillatory shear:

$$I_{3/1}(\gamma_0) = D\gamma_0^C \tag{1.51}$$

The loss of symmetry in the time response signal can be characterized and quantified by the relative phase of the higher harmonics. A linear pure sinusoidal signal would be mirror-symmetric in its maximum and minimum. This mirror-symmetry is lost when the maximum

and minimum are shifted or "bended", e.g. fig.1.12. In order to analyze the resulting higher harmonics with respect to the relative phases, eq. 1.46 is reformed for a response signal as follows:

$$\sigma(t) = I_1 \cos(\omega_1 t + \phi_1) + I_3 \cos(3\omega_1 t + \phi_3) + I_5 \cos(5\omega_1 t + \phi_5) + ... \tag{1.52}$$

The absolute value of the phases of the higher harmonics is shifted with the phase of the first harmonic in order to obtain comparable data [Neidhöfer 03b]. The time domain data are shifted by a factor of $-\frac{\phi_1}{\omega_1}$ and t is substituted by $t' - \frac{\phi_1}{\omega_1}$. Hence, we obtain the expression:

$$\begin{aligned} \sigma(t' - \frac{\phi_1}{\omega_1}) &= I_1 \cos(\omega_1(t' - \frac{\phi_1}{\omega_1}) + \phi_1) + I_3 \cos(3\omega_1(t' - \frac{\phi_1}{\omega_1}) + \phi_3) + ... \\ &= I_1 \cos(\omega_1 t') + I_3 \cos(3\omega_1 t' + (\phi_3 - 3\phi_1)) + ... \end{aligned} \tag{1.53}$$

Consequently, the definition of the relative phase difference with respect to the phase of the first harmonic is:

$$\Phi_n := \phi_n - n\phi_1 \tag{1.54}$$

An example of how the relative phase of the higher harmonics affects the response signal from a LAOS experiment is shown in fig. 1.15.

It has been suggested that the phase of the 3^{rd} harmonic can be related to strain-hardening or strain-softening [Neidhöfer 03b]. An extremely shear-thinning material has a response signal out-of-phase with respect to the main cosine function ($\Phi_3 = 180°$). The opposite is found for a material exhibiting extreme shear-thickening, namely a signal with both terms in-phase ($\Phi_3 = 0° = 360°$). For all values of Φ_3 smaller than $180°$ the maxima and minima of the resulting response signals are shifted to the left and for $\Phi_3 > 180°$ are shifted to the right (mirror-symmetry distortion). This suggestion demonstrates the potential of Φ_3 as a parameter to characterize materials in the non-linear regime [Höfl 06, Neidhöfer 04, Vittorias 06].

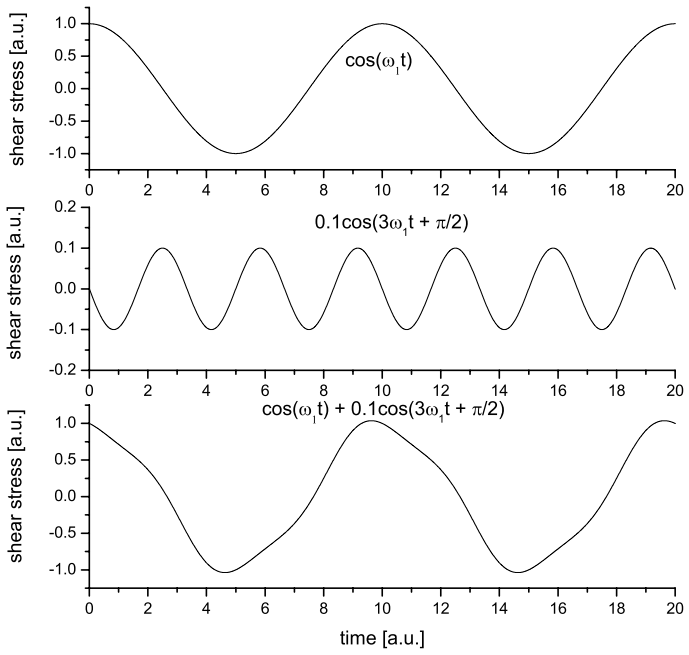

Figure 1.15: *Time-dependent response signal. A cosine term with the excitation frequency (corresponding to the first harmonic) and a term corresponding to the third harmonic are added [Neidhöfer 03a].*

1.5.4 Application of FT-Rheology on polymer systems of different topologies

One application of FT-Rheology was the characterization of anionically synthesized linear and star-shaped polystyrene solutions, as well as polystyrene combs [Höfl 06, Neidhöfer 03b, Neidhöfer 03a, Neidhöfer 04]. Polymers with linear chains were compared to materials with 3-arm and 4-arm star topologies, that had similar rheological behaviour in the linear regime. The investigation of this systems with FT-Rheology and the use of $I_{3/1}$ and Φ_3 provided a higher sensitivity in detecting topological differences in polymers. Additionally the non-linear parameters like Φ_3 as a function of Deborah number, De, were successfully used to discriminated between linear and star polymers in the non-linear rheological behaviour. Experimental FT-Rheology was subsequently applied to PS comb structures in solutions and melts and revealed their differences in the resulting non-linearities during LAOS flow.

1.6 Numerical simulations

Computational fluid dynamics is a major tool for the analysis, design and optimization of industrial flow processes. In the polymer processing field there is a wide range of operations,

such as extrusion, blow molding, film blowing, coating, mixing etc. Thus, there is a need for a detailed analysis of the special features and conditions of each non-Newtonian flow type [Nassehi 02].

The core of every computational analysis is the numerical method used. This determines its accuracy, reliability, speed and computation cost. Within this work the finite element method is utilized. This particular method was initially developed by structural engineers, for the numerical modelling of solid-mechanical problems. However, it has quickly expanded in all types of flow and in all material fields (gases, liquids, Newtonian and non-Newtonian fluids, elastic solids, multi-phase flows) and it is established as a powerful technique to solve fluid flow and heat transfer problems [Nassehi 02]. It is a geometrically flexible method and thus selected for the analysis of problems with complex geometrical domains.

Within this work we focus on modelling the behaviour of a viscoelastic material (polymer melt) in a simple parallel-plate geometry under LAOS. This domain consists of two parallel plates with the upper plate moving periodically with a fixed frequency, ω_1, (corresponding to the excitation frequency in the rheometer) and a fixed strain amplitude, γ_0 (corresponding to the applied strain amplitude in the LAOS experiment). The complexity in the specific problem is introduced not in the flow field but in the material properties. The model used to describe the polymer melt is a complex differential constitutive model and contains parameters related to the molecular architecture. Hence, it is interesting to investigate if the non-linear behaviour of polymer melts with different topologies under LAOS can be predicted numerically and if the model itself captures the features of the deformed material, compared to experimental results.

Generally, a non-Newtonian flow problem consists of the formulation of the mathematical system to describe the process. This systems involves the equations that describe the conservation of mass, energy and momentum. Additionally the flow properties are provided by means of a constitutive equation. Finally, the specific boundary conditions of the problem are given and the formulated mathematical problem is solved via a computer based numerical technique.

A well established solution process for industrially relevant problems is the utilization of a finite element package to carry out the calculations and present the results in a consistent and clear way.

1.6.1 Finite element method

Mathematical models of polymer flow involve generally non-linear partial differential equations and cannot be solved analytically. Therefore, these equation sets are solved numerically. The finite element method is a numerical technique for solving problems which can be described by partial differential equations. The investigated flow domain is represented as an assembly of finite elements. The nodal values of a physical field in each element determine

approximating functions and a continuous physical problem is transformed into a discretized finite element problem with the nodal values as unknown.

The elements in which the domain is discretized (domain discretization) can be two-dimensional or three-dimensional and can be of various shapes (rectangular, triangular, hexagonal, combination of triangular and rectangular, etc.) and sizes. The nodes are located on the boundary lines of the elements and can also be inside an element. The boundary nodes act as junction points between the elements of a finite element mesh. They are geometrical sub-regions and do not represent fluid body parts. The consequence of the discretization is that the unknown functions of the physical quantities (velocity, pressure, stress) are represented in each element by interpolation functions. The value for a continuous function, *f*, is then approximately interpolated by the position, *x*, and geometrical functions, called shape functions. A simple example for a one-dimensional linear element is given in fig. 1.16 and in fig. 1.17 an example of a bi-linear rectangular element is depicted.

Figure 1.16: *A one-dimensional linear element*

For the element in fig. 1.16, the continuous function can be approximated by the shape functions as follows:

$$\tilde{f}_x = f_A \frac{l-x}{l} + f_B \frac{x}{l} \tag{1.55}$$

If the element is rectangular the approximated function can be expressed as:

$$\tilde{f} = \alpha_1 + \alpha_2 x + \alpha_3 y + \alpha_4 y \tag{1.56}$$

where *x* is the position in the horizontal axis, *y* is the position in the vertical axis and α_n are the shape functions.

The element's shape and node positions can be more complicated and the shape functions can also be more elaborated than polynomial expressions, e.g. products of selected polynomials that give desired function variations in element edges.

The finite element method has a great geometrical flexibility and can cope effectively with various types of boundary conditions. However, there are some setbacks in

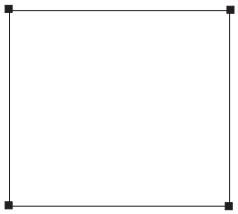

Figure 1.17: *Bi-linear rectangular element with four nodes*

this method, namely the computational cost, especially for the case of three-dimensional finite element simulations. Rational approximations may be used in order to overcome such drawbacks. More details about the finite element method can be found elsewhere [Crochet 92, Nassehi 02, Polyflow 03].

Chapter 2

Experimental setup and flow modeling

In the present chapter, a detailed description of the experimental setup is presented. Furthermore, the undertaken numerical simulation method is introduced along with the rheological constitutive models that are studied within this thesis.

2.1 Experimental setup

The experimental setup consists of the rheometers utilized for measuring linear viscoelastic properties of polymer melts and applying LAOS at a broad range of excitation frequencies and strain amplitudes. Additionally, there is a brief description of the hardware used for ^{13}C melt-state NMR measurements.

2.1.1 Equipment for dynamic oscillatory shear experiments

Rheological measurements are undertaken on a TA Instruments ARES Rheometer and an Alpha Technologies RPA2000 (rubber process analyzer). Both rheometers belong to the category of rotational strain-controlled rheometers and can perform dynamic mechanical measurements of high viscous materials. In these devices, the sample is loaded between two parallel plates, or a cone of a small angle (typically 0.2 rad) and a plate or between two cones. The experiment consists of measuring with a force transducer the torque applied from the studied material on the upper plate of the rheometer, while the lower plate is driven by a motor in an oscillatory movement of a specific frequency and amplitude. The term strain-controlled (CR) refers to the working principal of such an apparatus. The applied deformation is

defined by setting the excitation frequency and the amplitude of the oscillatory movement, thus controlling the strain applied in the investigated material. The stress response of the material under deformation is recorded and analyzed. Instruments in which stress is defined and controlled are called stress-controlled rheometers (CS). Generally strain-controlled rheometers have insignificant inertia effects, can apply higher shear-rates and have a wider torque detection range. However, they are much more expensive.

The ARES rheometer is designed to perform measurements of high viscosity materials, i.e. polymer melts and solutions of high molecular weight. Viscoelastic properties of PE and PS samples in the linear regime are measured with this rheometer, namely: $G'(\omega)$, $G''(\omega)$, tan δ and the complex viscosity $|\eta^*(\omega)|$. This instrument is equipped with a 1KFRTN1 torque transducer detecting torques ranging from 4×10^{-7} Nm to 0.1 Nm. Parallel plate geometry of 13 mm diameter is mainly used. With this radius we are able to carry out measurements for strains up to 3 while keeping the resulting torque within the transducer's limits. However, plates of 8 mm and 25 mm diameter are also utilized. The samples under investigation are high molecular weight melts. This makes the use of cone-plate geometry with the advantage of a uniform strain field problematic in many cases. The utilization of parallel plates with a non-uniform strain field, leads to decreased measured values of relative intensity of the 3^{rd} harmonic by a factor of 0.75, as described by Wilhelm et al. [Wilhelm 99].

For measurements on the ARES rheometer, melt sample disks of 13 mm diameter and 1 mm thickness are pressed, at 150 °C and 20 bars in a Weber hydraulic press under vacuum. All measurements are performed under a nitrogen atmosphere to prevent sample oxidation.

The ARES rheometer is a commercial widely used device and is considered to be

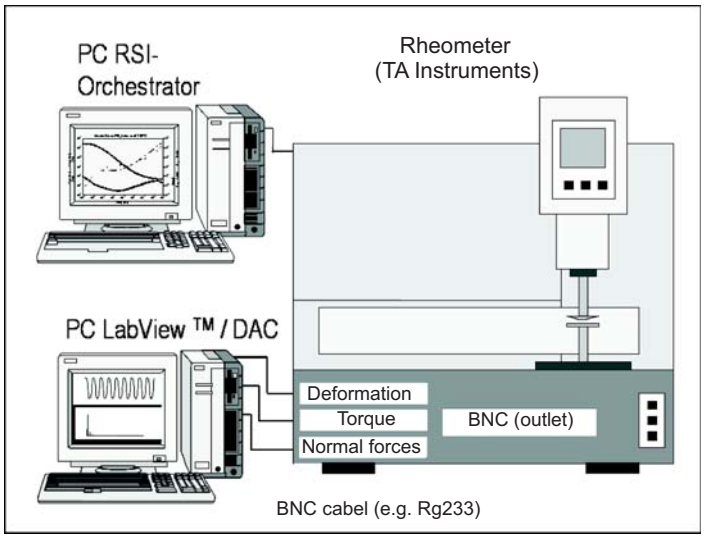

Figure 2.1: *Setup for FT-Rheology. A custom-made LabVIEW routine is used to acquire the raw data of deformation and torque from the rheometer.*

sensitive and reliable. However the utilized open-rim geometry presents some problems and

limitations in the LAOS application. For a strain amplitude larger than specific critical values (which depend on the excitation frequency and the studied material) sample overflow and edge fracturing or meniscus distortions may occur. These phenomena significantly affect the accuracy of the LAOS measurements. Additionally, the maximum detected torque limit of the transducer prevents the application of very large strain amplitudes ($\gamma_0 > 3$). Thus, another device must be utilized in order to reach high deformations with minimized secondary flows and instability problems. This is achieved by using the RPA2000.

This specific rheometer is equipped with a transducer whose operating range is from 10^{-4} Nm to 5.6 Nm. The sample in this apparatus is kept in a sealed test chamber which is pressurized to about 6 MPa during the experiment. The die geometry is bi-conical with an opening half angle of 0.062 rad and with large grooves to prevent slippage. A more detailed presentation of the instrument is provided by Debbaut and Burhin [Debbaut 02] and a schematic representation of the test chamber is depicted in fig. 2.2. The detectable torque range of the RPA2000 is extended in our specific setup by a factor 5-10 in the low torque range, as described by Hilliou et al. [Hilliou 04]. Although no special sample treatment is needed for the RPA2000 apparatus, it should be noted that 3.5 g - 4 g of sample are needed for each experiment.

In both devices the excitation frequency for LAOS experiments varies between 0.01 Hz

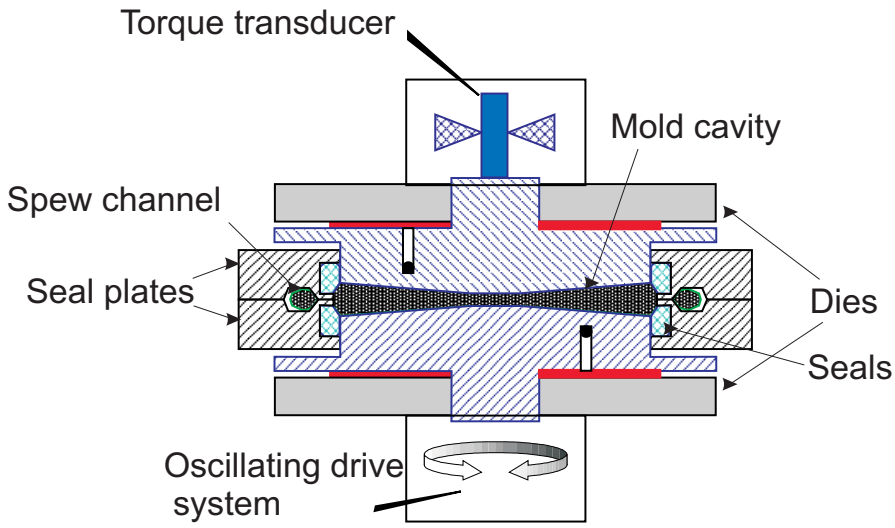

Figure 2.2: *Schematic representation of the geometry with a sealed test chamber in the RPA2000.*

and 5 Hz, and for dynamic oscillatory shear at low strain amplitudes (linear regime) it is 0.01 Hz - 15 Hz. The applied strain amplitude ranges from 0.5 to 3 in ARES and 2-10 on the RPA. The measurements are conducted at temperatures varying from 120 °C to 200 °C. It is found that the results from both rheometers are in good agreement. The deviation in measured values of tan δ, between ARES and RPA is less than 5%. However, for a better overlap of the FT-Rheology results, we have to apply a shift factor of 0.75 on the $I_{3/1}(\gamma_0)$ measured in the ARES, to compensate for the use of a parallel plate geometry in contrast to

the bi-conical die used in the RPA.

2.1.2 LAOS and FT-Rheology measurements

The specific setup for acquiring LAOS data of high sensitivity and applying FT-Rheology is presented here. This flow type is characterized by a broad range of strain amplitudes and excitation frequencies. An optimized experimental setup is demanded, that can record torque signals with a high accuracy at minimum noise.

The rheometer is kept in a rigid and mechanically stable environment to reduce the mechanical noise level. The raw torque data is externally digitised using a 16-bit analog-to-digital converter (ADC) card (PCI-MIO-16XE, National Instruments, Austin, TX) operating at sampling rates up to 100 kHz for one channel, or 50 kHz for two channels. Two channels allow the measurement and averaging (oversampling) of the shear strain and torque "on the fly" [Hilliou 04, Dusschoten 01]. A typical oversampling between 100 and 3000 raw data points is used, depending on the applied frequency and sampling rate. The analysis by FT-Rheology is carried out via custom LabVIEW routines (LabVIEW 5.1, National Instruments).

Measurements are carried out after a periodic-steady state has been reached and 5 to 50 cycles are recorded. It is generally observed that after 1-3 cycles delay there are no transient or startup effects in the signal and the rest acquired periods can be safely analyzed. The change of relative intensities and phases is negligible within more than 60 min of measurement (e.g. $I_{3/1}$ = 3% $\pm$ 0.15% and $\Phi_3 = 150^\circ \pm 5^\circ$). Measurements are repeated three times and are found to be reproducible with a typical deviation $<$ 5% of the relative intensity value and 5° of the relative phase (e.g. $I_{3/1}$ = 6% $\pm$ 0.3% and Φ_3 = 150° $\pm$ 5°).

2.1.3 ^{13}C melt-state NMR spectroscopy

In order to estimate the branching degree of polyethylenes, as discussed later in chapter 4, nuclear magnetic resonance (NMR) technique is complementary used and the outcomes are correlated to the FT-Rheology results concerning the detection and quantification of SCB and LCB.

Melt-state ^{13}C NMR is carried out on a Bruker DSX 500 dedicated solid-state NMR spectrometer operating at proton and carbon Larmor frequencies ν_H = 500.13 MHz and $\nu_{^{13}C}$ = 125.75 MHz respectively. All measurements are undertaken using a special commercial Bruker, ^{13}C-^{1}H optimised, high temperature, 7 mm magic-angle spinning (MAS) probehead with zirconia rotors and rotor caps. Nitrogen gas is used for all pneumatics to limit thermal oxidation. All measurements are conducted at $\omega_1/2\pi$= 3 kHz spinning speed and at 150 °C

sample temperature [Klimke 06].

Single pulse excitation spectra are acquired using 10 μs ^{13}C $\pi/2$ excitation pulses and π pulse-train heteronuclear dipolar decoupling. Depending on degree of branching, 4 to 21400 scans are needed to achieve a desirable signal-to-noise ratio (S/N) of 10 for the CH-branch carbon using a 2 s recycle delay and 16 dummy scans. Measurement times range from 1 min to 13 h. Short measurement times resulted from bulk state investigation, combined with short recycle delays [Pollard 04].

Branch quantification is achieved by integrating the quantitative proton-decoupled ^{13}C melt-state NMR spectra. The ratio of integrals associated with a branch site to that of the bulk backbone CH_2 sites (δ) allows direct access to the degree of branching (see Appendix E for carbon-site assingements). Although the actual CH (*) branch site is resolved, the three α-sites adjacent to this are used for branch quantification, due to their increased sensitivity.

Branches of 4 carbons in length (B_4), as well as branches containing 6 or more carbons (B_{6+}) are found within the polyethylenes investigated. The different branch lengths are identified by the chemical shifts of the carbon site adjacent to the methyl group on the branch, at 23.3 and 22.8 ppm respectively. However, these sites cannot be used for quantification due to the short recycle delays used [Pollard 04]. With the quantitative αB_4 and αB_{6+} sites, both having the same chemical shift of 34.7 ppm, only the content of branches containing 4 or more carbons (B_{4+}) can be quantified using the area of this peak:

$$B_4^+ = \frac{1/3 A_{\alpha B_4^+}}{A_\delta} = LCB_{max} = LCB + SCB(> C_4) \tag{2.1}$$

The determined degree of B_{4+} branching is then defined as the maximum possible amount of LCB in the sample. It should be noted that this is still only an approximation of the degree of B_{4+} branching within each system as correction factors cannot be applied due to the unknown length of the B_{4+} branches [Stadler 05].

2.2 Flow modelling

Flow under LAOS has been modeled in the past for polystyrene solutions [Neidhöfer 03a] and polyethylene melts using the Giesekus equation [Debbaut 02]. The FT-Rheology method was applied for both experimental measurements and simulations. This earlier work demonstrated the applicability of FT-Rheology and LAOS in combination with viscoelastic simulation. However, the Giesekus model does not include any parameter explicitly related to the molecular architecture, which could be practical for modelling polymers with branched topologies.

Finding a suitable model to describe the rheological behaviour of polymers under different types of flow is a crucial subject and a matter of intensive research in the last decades. McLeish and Larson [McLeish 98], and Inkson et al. [Inkson 99] presented a model for branched polymers consisting of constitutive equations including molecular parameters. The authors extended the tube model of Doi and Edwards [Doi 78c, Doi 79] and decoupled the structure of a branched material into an equivalent set of "pom-pom" macromolecules, with the number of arms and relaxation times as main model parameters. Rutgers et al. [Rutgers 02] had used this multi-mode Pom-pom model to simulate uniaxial extension flow of viscoelastic melts. The Double Convected Pom-pom model (DCPP) was introduced and used in the work of Clemeur et al. [Clemeur 03, Clemeur 04]. The authors predicted polyethylene melt flow for transient uniaxial extension and reverse step-strain experiments, with the linear parameters of this model as determined by fitting linear viscoelastic data. The non-linear parameters were determined by fitting transient extensional viscosity curves. Large amplitude oscillatory shear was subsequently simulated and analyzed by Lissajous plots and FT-Rheology. These results showed that the Pom-pom model could predict LAOS oscillatory shear and be combined with experimental FT-Rheology data.

The application of FT-Rheology to quantify macromolecular architecture of industrial polyethylene via simulations has also been presented by Schlatter et al. [Schlatter 05]. The resulting phases of higher harmonics where analysed following the work of Neidhöfer et al. [Neidhöfer 03a]. A differential multi-mode Pom-pom model and a modified Wagner integral model (Wagner-Stephenson) were used to simulate the FT-Rheology experiments. Predictions from both models were compared with experimental results. For this simple rheometric flow (parallel-plate geometry), the Wagner model showed generally better agreement. The Pom-pom model was able to fit the $I_{3/1}(\gamma_0)$, but it was not able to predict the whole non-linear response ($I_{3/1}(\gamma_0)$ and $\Phi_3(\gamma_0)$) for the polymers showing the highest non-linear behaviour.

To model the polymer melt flow under LAOS conditions, a viscoelastic constitutive equation is needed. Of importance are constitutive models, whose parameters can be qualitatively interpreted as the fingerprint of macromolecular attributes, e.g. M_n, M_w, PDI, and topology. We evaluate this using the Pom-pom model [McLeish 98, Inkson 99]. In particular, the DCPP formulation is selected considering previous implementations to study the flow of branched polymers [Clemeur 03, Clemeur 04].

2.2.1 Calculation domain and boundary conditions

Numerical simulations are performed using the commercial finite element package POLYFLOW [Crochet 92, Polyflow 03], primarily designed for the analysis of industrial flows dominated by nonlinear viscous phenomena and viscoelastic effects. The specific flow under investigation is a LAOS flow of a viscoelastic material. In the LAOS flow type, materials undergo a simple periodic shear deformation of a large amplitude. The experimental

flow geometry is relatively simple. It consists of two parallel disks with a typical diameter of 13 mm and a small gap distance (typically 1 mm). The material is loaded between the plates and deformed in a periodic fashion, as the lower plate oscillates driven by the rheometer motor with an angular frequency, ω_1, and an amplitude, γ_0. Hence, the approach by Debbaut and Burhin can be followed [Debbaut 02].

The calculation domain is a square of length, *L*, and we monitor the stress response in the fluid element sheared under periodic conditions. In order to simulate this flow with an acceptable computational cost, we are obliged to accept some simplifications and approximations. The flow domain is reduced into a two-dimensional rectangular geometry with a plane symmetry applied. The dimensions are reduced in a 1×1 domain. In other words, it is assumed that the deformation of a small part of the polymer is the same as for the whole polymer mass under LAOS between the parallel plates. Finally, free surface and edge effects are neglected. The domain along with the boundary conditions is shown in fig. 2.3.

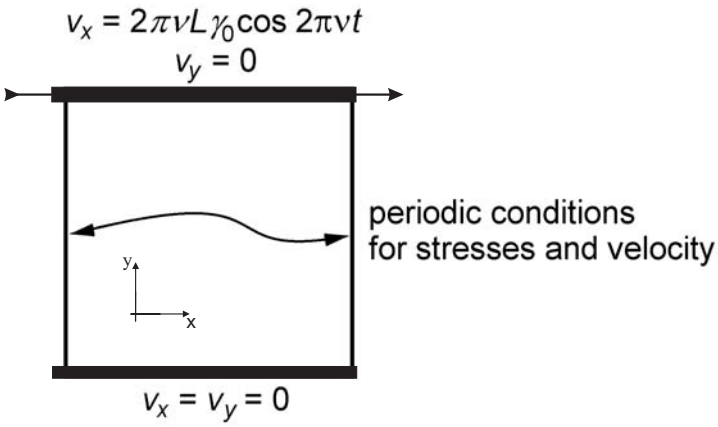

Figure 2.3: *Calculation domain and boundary conditions for LAOS simulation. Adapted from [Neidhöfer 03b].*

Vanishing velocities are imposed at the lower boundary, while the upper boundary moves with a tangential velocity, v_x:

$$v_x = L\gamma_0\omega_1 \cos(\omega_1 t) \tag{2.2}$$

This velocity boundary condition corresponds to a dynamic oscillatory shear deformation of strain amplitude γ_0 and angular frequency ω_1:

$$\gamma(t) = \gamma_0 \sin(\omega_1 t) \tag{2.3}$$

Finally, periodic conditions of translation symmetry are imposed on both vertical sides.

There are no specific limitations on γ_0 or ω_1 for LAOS flow simulations. This was also demonstrated by Debbaut and Burhin [Debbaut 02] and Vittorias et al. [Vittorias 06]. However, simulations with very low frequencies (e.g. 0.01 Hz) demand a large number of time steps. On the other hand, large amplitude oscillatory shear with very high frequencies (e.g. $\omega_1/2\pi$ = 10 Hz, with a 3^{rd} harmonic contribution at $\omega_3/2\pi$ = 30 Hz) demands decreased time steps ($<$ 0.001 s). In both cases one needs an increased calculation time.

The viscoelastic flow can be modelled by solving the basic equations, which are the following:

The incompressibility equation:

$$\bigtriangledown \cdot \bar{\mathbf{v}} = 0 \tag{2.4}$$

where $\bar{\mathbf{v}}$ is the velocity vector.

The momentum equation:

$$-\bigtriangledown p + \bigtriangledown \cdot \mathbf{T} + \mathbf{f} = \rho \bar{\mathbf{a}} \tag{2.5}$$

where *p* is the pressure, $\mathbf{T}$ is the extra-stress tensor, ρ is the density, f is the volumetric force and $\bar{\mathbf{a}}$ is the acceleration vector.

The energy equation is irrelevant for the specific case, since we are dealing with an isothermal flow. Furthermore, for viscoelastic flows the total extra-stress tensor, defined as the stress tensor without the hydrostatic pressure components, is decomposed into a viscoelastic component $\mathbf{T}_1$ and a purely-viscous component $\mathbf{T}_2$:

$$\mathbf{T} = \mathbf{T_1} + \mathbf{T_2} \tag{2.6}$$

The viscoelastic component is computed differently for each type of viscoelastic model. The purely viscous part $\mathbf{T}_2$, is an optional component within this specific simulation, usually interpreted as the solvent contribution to the stress in polymer solutions or as the stress response associated with very fast relaxation modes (e.g. short chains). It can be derived from the following equation:

$$\mathbf{T_V} = 2\eta_V \mathbf{D} \tag{2.7}$$

where **D** is the rate-of-deformation tensor and η_V is the additional Newtonian viscosity. The presence of a purely viscous component has a significant impact on mathematical properties of the equation governing viscoelastic flows and can improve the convergence of the numerical method [Polyflow 03]. For polymer melts this can also be interpreted as the stress response associated with very fast relaxation modes, approaching the effect of a solvent for the simulated macromolecules at the investigated timescale. It is interesting to recall that a suitably selected value of η_2 corrects the actual shear-rate dependent viscosity of the mainly used DCPP model, at high shear-rates, which would otherwise exhibit a non-realistic slope of -2 [Polyflow 03]. Furthermore, as mentioned before, this additional contribution can improve the stability of the numerical solver when solving complex flows.

2.2.2 Constitutive equations

There are flow phenomena in viscoelastic flows that generally cannot be predicted by classical Navier-Stokes equations, such as shear-rate dependence of viscosity, presence of normal-stresses, high resistance to elongational deformation, elasticity-associated memory effect [Nassehi 02, Polyflow 03]. In the literature, one can find a variety of equations and models that can be used to describe flows of Non-Newtonian materials.

For each viscoelastic model, a different constitutive equation is used for the calculation of $\mathbf{T_1}$. The viscoelastic extra-stress tensor is computed from a differential equation or an algebraic that involves a state variable (configuration tensor), obeying a differential equation. While in the Pom-pom model, $\mathbf{T_1}$ is algebraically derived from the configuration tensor, models of the Oldroyd type (including upper-convected Maxwell, Giesekus, e.a.) contain a differential equation written in terms of the extra stress tensor [Polyflow 03]. The Maxwell and the Giesekus constitutive equations are presented briefly below.
The general equation for computing $\mathbf{T_1}$ for Oldroyd-type models is the following:

$$g(\mathbf{T_1}) \cdot \mathbf{T_1} + \lambda \frac{\delta \mathbf{T_1}}{\delta t} = 2\eta_1 \mathbf{D} \tag{2.8}$$

where $g(\mathbf{T_1})$ is a model-defined function. Parameter λ is a model-defined relaxation time and corresponds to the time needed for the shear stress to reduce to the half of its equilibrium value when the strain-rate vanishes. High relaxation times indicate high memory retention of the flow and low λ indicate a significant memory loss. For the second case, the Newtonian flow is approached (λ = 0). Finally, η_1 is a model-defined viscosity for the viscoelastic component of $\mathbf{T}$, $\mathbf{T_1}$. The term $\frac{\delta \mathbf{T_1}}{\delta t}$ is defined as the linear combination of the lower- and

upper-convected derivatives:

$$\frac{\delta \mathbf{T_1}}{\delta t} = \frac{\xi}{2} \overset{\triangle}{\mathbf{T_1}} + (1 - \frac{\xi}{2}) \overset{\triangledown}{\mathbf{T_1}} \tag{2.9}$$

with $0 \leq \xi \leq 2$. $\overset{\triangle}{\mathbf{T_1}}$ is the lower-convected derivative of the viscoelastic extra stress defined as:

$$\overset{\triangle}{\mathbf{T_1}} = \frac{D\mathbf{T_1}}{Dt} + \mathbf{T_1} \cdot \nabla \bar{\mathbf{v}}^T + \nabla \bar{\mathbf{v}} \cdot \mathbf{T_1} \tag{2.10}$$

while $\overset{\triangledown}{\mathbf{T_1}}$ is the upper-convected derivative defined as:

$$\overset{\triangledown}{\mathbf{T_1}} = \frac{D\mathbf{T_1}}{Dt} - \mathbf{T_1} \cdot \nabla \bar{\mathbf{v}} - \nabla \bar{\mathbf{v}}^T \cdot \mathbf{T_1} \tag{2.11}$$

For a material with multiple relaxation times, $\mathbf{T_1}$ represents the sum of all viscoelastic contributions, each obeying a constitutive equation (e.g. eq. 2.8). Each viscoelastic contribution has its own material parameters (η, λ, etc.) for the model-specific function $g(\mathbf{T_1})$.

The Maxwell model is one of the simplest constitutive equations. The upper convected Maxwell model (UCMM) exhibits a constant viscosity and a quadratic first normal stress difference [Owens 02]. Due to its simplicity it is used only qualitatively, or when low amount of information is available for the studied material. For the upper-convected Maxwell model, the viscoelastic stress tensor is computed as follows:

$$\mathbf{T_1} + \lambda \overset{\triangledown}{\mathbf{T_1}} = 2\eta_1 \mathbf{D} \tag{2.12}$$

There is no purely viscous contribution, thus $\mathbf{T_1} = \mathbf{0}$.

A more complicated and widely studied model is the Giesekus constitutive equation [Neidhöfer 03b, Tanner 00]. It is considered as one of the most realistic differential constitutive models and can describe the shear thinning phenomenon. The model produces a non-quadratic first normal-stress difference as a function of shear-rate at high shear-rates

[Polyflow 03]. It can contain a purely viscous contribution (from eq. 2.7).

The Giesekus equation for $\mathbf{T_1}$ is the following:

$$(\mathbf{I} - \frac{\alpha\lambda}{\eta_1}\mathbf{T_1}) \cdot \mathbf{T_1} + \lambda \overset{\nabla}{\mathbf{T}}_{\mathbf{1}} = 2\eta_1\mathbf{D} \tag{2.13}$$

where **I** is the unit tensor and α is a non-linear material parameter controlling the shear-rate dependence of the viscosity.

The Pom-pom model which is mainly studied in this work, belongs to the type of models with the viscoelastic extra-stress tensor computed from an algebraic equation that involves a configuration tensor. It is the first constitutive model containing parameters directly related to the polymer architecture and was recently proposed by McLeish and Larson [McLeish 98]. The molecule described by the Pom-pom model contains a backbone of a specific length and *q* arms at each end (like the "pom-pom molecule" in fig. 1.1). The backbone is confined in a Doi-Edwards tube, consisting of the entangled surrounding neighbouring macromolecules. While only the backbone reptates and relaxes through orientation and stretching mechanisms inside the tube, the dangling arms at each tube-end freely relax in a much faster process, often described as "breathing modes" [McLeish 98, Inkson 99]. However, when the imposed stress is high enough the side-arms can retract in the tube. A schematic representation of a "pom-pom molecule" is shown in fig. 2.4. The concept of this model is suitable to describe flow of branched polymers. The capability of the Pom-pom model to capture simultaneously the shear-thinning character along with the extensional hardening behaviour of polyethylene is today widely acknowledged. Hence, it is mainly used for the flow simulation of long-chain branched PE [McLeish 98, Inkson 99, Rutgers 02, Clemeur 03, Clemeur 04].

Within this work, the Double-Convected-Pom-pom formulation is undertaken, which includes changes and improvements to the initial model by McLeish and Larson [McLeish 98], in order to make it more suitable for software implementation and to introduce a non-zero second normal stress difference [Clemeur 03]. Additionally, several modes of the DCPP model are used, in other words a multi-mode differential constitutive model. Hence, the total extra-stress tensor is the sum of the stress contribution from each individual mode, *i*, of the total N modes.

$$\mathbf{T} = \sum_{i=1}^{N} \mathbf{T_i} + \mathbf{T_V}. \tag{2.14}$$

where $\mathbf{T_i}$ is the viscoelastic stress component of each mode and $\mathbf{T_V}$ is the purely-viscous component (denoted as $\mathbf{T_2}$ in eq 2.6). In eq. 2.14, each mode can be interpreted as the equivalent set of "pom-pom" molecules with a range of relaxation times and arm numbers, in which the structure is decoupled [Inkson 99]. In this formulation of the DCPP model, the constitutive equation for the stress of each individual mode is as follows:

$$\mathbf{T_i} = \frac{G_i}{1-\xi_i}(3\Lambda_i^2\mathbf{S_i} - \mathbf{I}) \tag{2.15}$$

where G_i is the shear modulus, ξ_i is a non-linear parameter that enables the introduction of a non-vanishing second normal stress difference [Clemeur 03], $\mathbf{S_i}$ is the the orientation tensor, Λ_i is the stretching scalar and $\mathbf{I}$ is the unity vector. The state variables $\mathbf{S_i}$ and Λ_i can be computed from the following equations:

$$\lambda_i[(1-\frac{\xi_i}{2})\overset{\triangledown}{\mathbf{S_i}} + \frac{\xi_i}{2}\overset{\triangle}{\mathbf{S_i}}] + \lambda_i(1-\xi_i)[2\mathbf{D_i} : \mathbf{S_i}]\mathbf{S_i} + \frac{1}{\Lambda^2}[\mathbf{S_i} - \frac{\mathbf{I}}{3}] = 0 \tag{2.16}$$

$$\lambda_{si}\frac{D\mathbf{\Lambda_i}}{Dt} - \lambda_{si}(\mathbf{D_i} : \mathbf{S_i})\mathbf{\Lambda_i} + (\mathbf{\Lambda_i} - 1)e^{\frac{2(\mathbf{\Lambda_i}-1)}{q_i}} = 0. \tag{2.17}$$

where **D** is the rate-of-deformation tensor, while the symbols $\triangledown$ and $\triangle$ denote the upper- and lower-convected derivatives, respectively. Equations 2.16 and 2.17 involve additional material parameters. The parameters λ_i and λ_{si} are the characteristic relaxation times for backbone orientation and stretching mechanisms, respectively, while the parameter q_i reflects the number of arms (branches) attached at each end of the "pom-pom" backbone.

2.2.3 Identification of material parameters

The set of constitutive equations 2.14- 2.17 involves 5N+1 parameters. For each individual mode, the relaxation modulus G_i, the relaxation times for orientation and stretching mechanisms, λ_i and λ_{si}, respectively, the number of arms per backbone-end, q_i, and parameter ξ_i, have to be determined. Finally, we have the "background" viscosity, η_V.

Relaxation characteristic times, λ_i, for backbone orientation of each mode and shear moduli, G_i, are determined from experimental mastercurves of linear data $G'(\omega)$, $G''(\omega)$ and

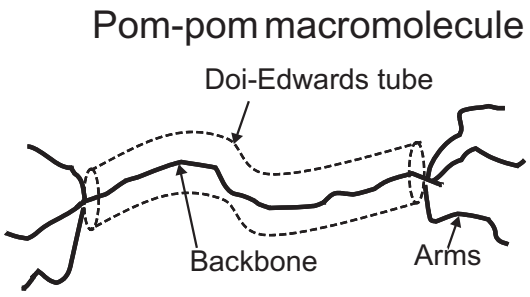

Figure 2.4: *Schematic representation of the branched macromolecule described by the Pom-pom model. In this example, the number of side-arms is q = 3. The backbone can relax while confined in the tube via orientation mechanism with characteristic time λ and via stretching with characteristic time λ_s. However, the stress relaxation is constrained by the existence of branch points.*

$|\eta^*(\omega)|$ at a reference temperature of 140 °C or 180 °C. Generally, viscoelastic flow simulations literature suggests a non-vanishing value of η_V [Polyflow 03]. The flow presently considered is characterised by a well-known kinematics and therefore, we found it more relevant to determine its value by fitting the data at high frequency. Actually, in earlier publications, Debbaut and Burhin [Debbaut 02] and Neidhöfer et al. [Neidhöfer 03b] did not add any purely Newtonian contribution to the total extra-stress tensor.

The non-linear parameter, ξ_i, does not strongly influence the oscillatory response of the model and can be physically interpreted as controlling the polymer backbone's slippage with respect to the motion of the surrounding continuum [Clemeur 04]. Following Verbeeten et al. [Verbeeten 04] and Clemeur et al. [Clemeur 04], a weak dependence of parameter ξ_i with respect to q_i is assumed:

$$\xi_i = \frac{0.2}{\log_{10} q_i + 1} \tag{2.18}$$

Utilizing this information, 4N parameters have to be considered. The ratio of the orientation relaxation times to the stretching relaxation time, λ_i/λ_{si}, is related to the number of entanglements. This ratio ranges between 2 and 10 for a typical polymer melt [McLeish 98, Inkson 99] and is given by:

$$\frac{\lambda_i}{\lambda_{si}} = \frac{4}{\pi^2} N_e \tag{2.19}$$

where N_e is the number of entanglements. The ratio λ_i/λ_{si} is kept constant for all modes ($\lambda_i/\lambda_{si} = \lambda/\lambda_s$, for i = 1, 2,...n) and is determined by adjusting model predictions to FT-Rheology experimental data, i.e. $I_{3/1}(\gamma_0, \omega)$ and $\Phi_3(\gamma_0, \omega)$. The number of branches per

backbone end, q_i, is also determined by fitting $I_{3/1}$ and Φ_3 for different strain amplitudes and frequencies. For linear polymers q_i = 1 for all modes. For branched systems, q_i is identical for all modes, or the material is handled as a blend of "pom-pom" molecules, where the number of arms increases with the relaxation time [Inkson 99]. The mode with the longest orientation relaxation time (highest seniority) has the maximum number of arms (highest priority), in agreement with Inkson et al. [Inkson 99]. Graham et al. indeed proposed that the moduli and the backbone orientation time, λ_i, should be determined from linear viscoelastic behaviour, while values for parameters λ_{si} and q_i must be obtained from non-linear flow experiments [Graham 01].

Selecting four to six modes seems to be an optimum choice for fitting the whole range of available experimental linear data, while keeping the calculation time for a single LAOS simulation within reasonable limits. It should be noted that for large numbers of modes, the parameter identification can become ill-posed [Clemeur 04, Inkson 99].

2.2.4 Time marching scheme

For the transient calculation the technique similar to that suggested by Debbaut and Burhin [Debbaut 02] and Neidhöfer et al. [Neidhöfer 03b] is used. Starting from rest state, the simulated time interval must be long enough in order to reach a steady periodic regime. At t = 0, the calculation starts with relatively large time steps (typically 1/10 of a period) for a time interval equal to 5-10 times the longest relaxation time. By doing so, the stress contributions from the modes with longest relaxation times reach the periodic steady-state flow regime. Next, the time steps are progressively decreased to properly capture contributions from the shorter relaxation modes. FT-Rheology analysis is then applied on the last periods of the resulting stress response.

Chapter 3

FT-Rheology on anionically synthesized model polystyrene

In order to validate FT-Rheology as a method to study polymers of varying architecture, one needs to apply it initially to simple model systems. The well-defined materials used within this work, consist of PS melts with known narrow molecular weight distribution. This distribution can be quantified by the weight-average molecular weight, M_w and the number-average molecular weight, M_n. The ratio between these two average quantities, M_w/M_n = PDI, is called the polydispersity index which describes the width of the distribution [Sperling 92, Young 91]. The model samples used have a typical polydispersity index, *PDI* $\leq$ 1.1. The topology of the specific PS samples is defined by the synthesis method, which in this case is anionic polymerization with and without chemical crosslinker [Neidhöfer 03a, Roovers 79b]. Due to the undertaken synthesis route, the samples with an estimated linear topology, indeed contain no side arms neither long nor short. The systematic study of these melts can reveal the factors affecting the non-linear rheological behaviour of macromolecules under LAOS and separate them from the influence of long-chain branches.

Additionally, polystyrene combs (see fig. 1.1) experimentally measured via FT-Rheology [Höfl 06], are used as model branched systems to evaluate the numerical simulations of LAOS flow using the Pom-pom model. These materials are also anionically synthesized, relatively monodisperse, with a specific known number of branches per backbone and arm-length [Höfl 06, Roovers 79b, Roovers 79a, Roovers 81, Roovers 87]. The only topological characteristic not defined is the distribution of the side-arms on the backbone. The specific comb samples have been extensively investigated in the past and the experimental study of these materials via FT-Rheology is performed and presented by Höfl [Höfl 06].

The application of FT-Rheology on polystyrene solutions of known topology (linear, 3-arm and 4-arm stars) has been a subject of investigation in the past [Neidhöfer 03b, Neidhöfer 04]. Large amplitude oscillatory shear was applied in anionically synthesized linear, 3-arm and 4-arm star polystyrenes and the resulted stress time signal

has been analyzed via FT-Rheology. For the case of linear polystyrene solutions, the experimental results where coupled with finite element simulations using the Giesekus model [Neidhöfer 03b]. The experimental investigation of the linear solutions showed no significant molecular weight dependence of the phase of the $3^r d$ harmonic, Φ_3, as a function of Deborah number, De. However, a discrimination between linear and branched topologies (star polystyrenes) was achieved via the experimental $I_{3/1}$ and Φ_3, for high De [Neidhöfer 04].

However, when one studies entangled melts the flow involves more complicated phenomena. Topological constrains, like entanglements, branches, and molecular weight have a strong influence on the melt behaviour under deformation. Additionally, flow instabilities, such as edge fracture, meniscus distortions and wall slip may occur and influence the non-linear character of the flow [Larson 92]. These phenomena may also posses a molecular weight and topology dependence and can be predicted. The recorded flow instabilities during LAOS flow are more extensively investigated in chapter 5.

3.1 Studied materials and sample preparation

A set of linear monodisperse polystyrene melts of M_w ranging from $\sim$40 kg/mol to $\sim$4,500 kg/mol are studied within this work. Additionally, polydisperse linear PS melts are measured to assess the influence of a broadened molecular weight distribution on non-linear rheological behaviour. Finally, numerical simulations for the prediction of LAOS flow are performed for a set of PS solutions and melts with well-defined branched topology.

Furthermore, binary blends are generated from low and high molecular weight linear PS and are investigated. Four binary blends of linear polystyrenes are measured. The first two consist of PS41 with PS330 in mass ratios of 32.4/62.6 and 13.8/86.2. The other two mixtures are blends of PS41 with PS750 in mass ratios of 52.2/47.8 and 19.8/80.2. The mixing is performed by dissolving the components in THF (tetrahydrofurane) at room temperature (25 °C) and subsequently evaporating the solvent. Samples are left to dry in vacuum at T = 100 °C for more than 10 days. Gel permeation chromatography measurements (GPC) confirm the presence of the pure components in the binary blend.

For measurements on the ARES rheometer, melt sample disks of 8 mm, 13 mm and 25 mm diameter and 1 mm thickness are pressed, at 150 °C and 20 bars in a Weber hydraulic press under vacuum. For sample PS330 disks of the above diameters but with a thickness of $\sim$ 2 mm are additionally prepared. The time for the melt and press procedure under vacuum generally varies between 2 h and 12 h, depending on the sample molecular weight and residual solvent concentration. The measurements are performed for disk samples finally containing no residual solvent or air bubbles. For every measurement a fresh sample is used. All experiments are performed under a nitrogen atmosphere to prevent sample oxidation. Although no special sample treatment is needed for the RPA2000 apparatus, it should be noted that 3.5 g-

4 g of sample are needed for each experiment.

Large amplitude oscillatory shear flow simulations are performed for a number of polystyrene combs. The molecular characterization, via NMR, GPC and mass spectrometry, as well as the experimental rheological and FT-Rheology results were performed by Höfl [Höfl 06]. The modelled samples are presented in Table 3.3 along with their topological characteristics.

Samples M_w-PDI	**M_w (kg/mol)**	M_w/M_n	**source**
PS41	41	1.03	MPIP
PS57	57	1.03	MPIP
PS78	78	1.03	MPIP
PS100	100	1.10	BASF
PS110	110	1.03	MPIP
PS220	220	1.05	MPIP
PS330	330	1.10	BASF
PS370	370	1.08	MPIP
PS400	400	1.11	MPIP
PS500	500	1.10	BASF
PS750	750	1.10	MPIP
PS2000	2000	1.21	MPIP
PS134_1.97	134	1.97	MPIP
PS168_2.69	168	2.69	MPIP
PS744_1.78	744	1.78	MPIP
PS4530_3	4529	2.96	MPIP

Table 3.1: *Anionically synthesized linear polystyrene samples. Weight-average molecular weight M_w and polydispersity M_w/M_n as given by GPC. The samples are referenced as PSM_w for monodisperse linear PS. The polydisperse linear PS are referenced as PSM_w_PDI.*

Samples	**PS41 wt %**	**PS330 wt %**	**PS750 wt %**
PSmix1	32.4	-	67.6
PSmix2	13.8	-	86.2
PSmix3	52.2	47.8	-
PSmix4	19.8	80.2	-

Table 3.2: *Binary blends of anionically synthesized linear polystyrene samples. The weight fraction of each component in the blends is given.*

Samples	M_b **(kg/mol)**	M_a **(kg/mol)**	N_{arms}	$M_{w,total}$ **(kg/mol)**	M_w/M_n	c **wt % in DOP**
			solutions			
PS250_41	262.8	-	-	262.8	1.08	41.0
C642	275	47	29	1630	< 1.06	33.3
C732	860	25.7	26	1530	< 1.06	23.8
C742	860	47	29	2230	< 1.06	20.7
			melts			
PSH2	46	44	4	237	-	-
C622	275	11.7	30	624	< 1.06	-
C722	860	11.7	28	1190	< 1.06	-

Table 3.3: *Modelled linear and branched polystyrenes. Estimated molecular weight of polymer backbone, M_{wb}, molecular weight of side-arms, M_{wa} and number of side-arms per backbone, total weight-average molecular weight, $M_{w,total}$ and polydispersity, M_w/M_n, as determined by GPC. Sample PS250_41 was synthesized by Neidhöfer [Neidhöfer 03b], all other samples are from Roovers [Roovers 79b] and provided by Prof. D. Vlassopoulos. The solvent used for all solutions was dioctylphthalate (DOP).*

3.2 Dynamic oscillatory shear in the linear regime, SAOS

When a sample is exposed under dynamic oscillatory shear with a small strain amplitude, γ_0 (SAOS), the rheometric flow takes place still in the linear rheological regime. As described in chapter 1, by performing frequency sweeps in different temperatures we can shift the resulted spectra and obtain a mastercurve of G', G'', tan δ and $|\eta^*(\omega)|$. Polystyrene has a strong temperature dependence concerning its rheological properties, thus allowing us to obtain mastercurves over a broad range of frequencies. Results for several linear monodisperse polystyrenes are shown in fig. 3.1 and 3.2.

The dependence of the moduli and the crossover frequency, ω_c, of G' and G'' on the molecular weight is clearly depicted. It is worth mentioning that for samples with increasing M_w, the crossover point is shifted towards lower frequencies, at a constant temperature, as expected. By performing dynamic measurements in these conditions, the behaviour of the samples in the rubbery plateau is probed. In literature, average molecular weight between entanglements, M_e, of 13-19 kg/mol for polystyrene is reported and within this work, we assume the value $M_e \approx 18$ kg/mol [Bicerano 02, Seitz 93]. Linear polystyrene melts with a high molecular weight and $M_w/M_e \geq 20$, which corresponds to an average number of entanglements per chain more than 20, show a dominant elastic character in these specific experimental conditions.

Subsequently, the binary blends, consisting of a low and a high molecular weight component, are measured with respect to their linear rheological properties. In all four blends,

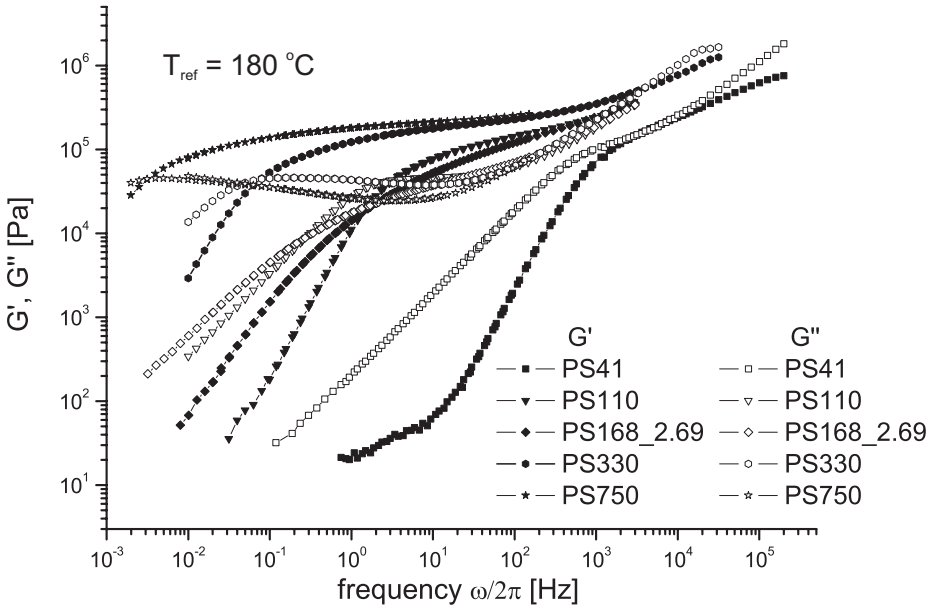

Figure 3.1: *Storage and loss moduli, G' and G'', for linear polystyrene melts. Mastercurves for a reference temperature $T = 180\,^{\circ}C$.*

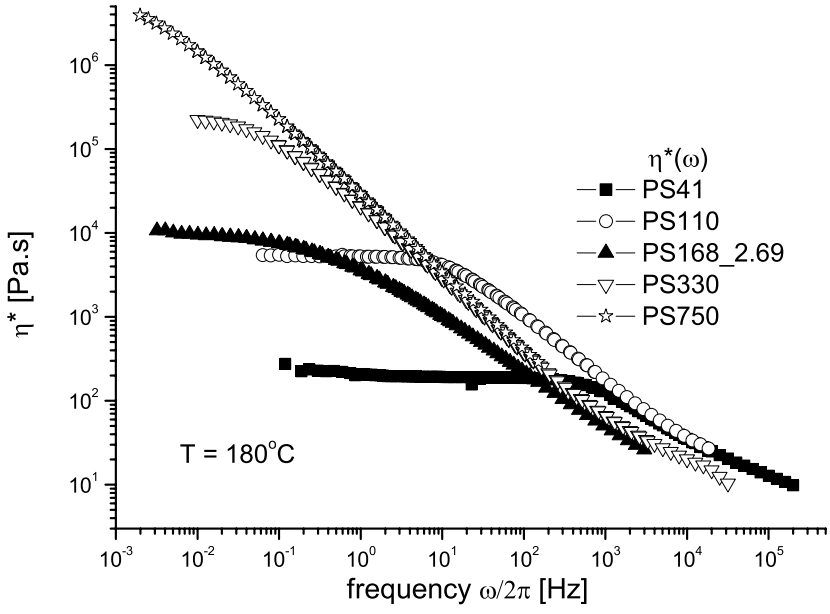

Figure 3.2: *Absolute value of the complex shear viscosity $|\,\eta^*(\omega)\,|$ for linear polystyrene melts. Mastercurves for a reference temperature $T = 180\,^{\circ}C$.*

one can clearly observe two "shoulders" in the G'' curve, one at a low frequency, $\omega_{mL}/2\pi$ and one at a higher frequency, $\omega_{mS}/2\pi$ (fig. 3.3, 3.4). According to Strunglinski et al. [Strunglinski 88], this feature is prominent in linear-linear mixtures and the two corresponding frequencies, ω_{mL} and ω_{mS}, are "fingerprints" of the relaxation of the long and short chains respectively. The same authors reported a shift of the short chain peak frequency, ω_{mS}, to lower frequencies with increasing concentration of the long-chain component. However, for samples PSmix2 and PSmix4, a suppression of the long-chain "shoulder" in ω_{mL} is observed, indicating a broadening of the relaxation spectrum of the high molecular weight components.

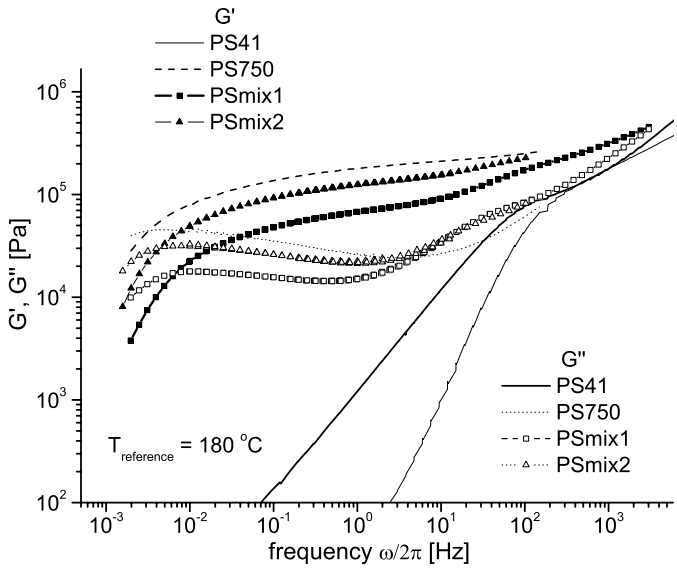

Figure 3.3: *Storage and loss moduli, G' and G'', for binary polystyrene blends PSmix1 and PSmix2 (see Table 3.2), as well as data for the linear blend components. Mastercurves for a reference temperature T = 180 °C.*

3.3 Application of LAOS and FT-Rheology

Subsequently, strain sweeps are applied with LAOS for all linear melts, at a fixed temperature, T = 180 °C and excitation frequency, $\omega_1/2\pi$ = 0.1 Hz. The resulting torque time signal is analyzed via FT-Rheology. Not all samples can be measured with the RPA2000 apparatus, due to limited available material quantity, especially for the samples synthesized at the MPIP. Thus, non-linear behaviour at very large strain amplitudes (typically $\gamma_0 \geq 2.5$) can be measured only

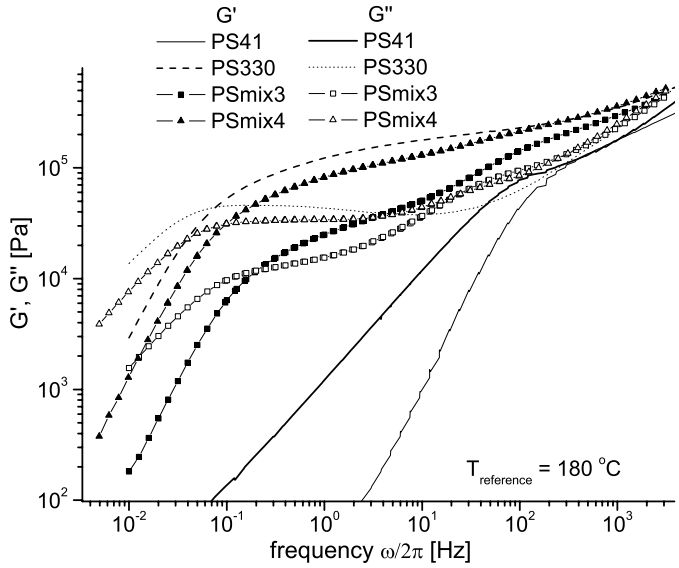

Figure 3.4: *Storage and loss moduli, G' and G'', for binary polystyrene blends PSmix3 and PSmix4 (see Table 3.2), as well as data for the linear blend components. Mastercurves for a reference temperature T = 180 °C.*

for industrial samples PS110, PS330 and PS500. Another limitation on the maximum deformation in which each sample is induced to, results from the occurrence of flow instabilities caused by wall slip, stick-slip or meniscus distortion effects. This behaviour will be studied in chapter 5. In fig. 3.5 and 3.6, a typical LAOS torque time signal and the corresponding FT-spectrum are presented.

The samples are induced in LAOS, for a typical strain amplitude range of 0.1 - 3. The resulted relative intensities of the 3^{rd} harmonic, $I_{3/1}$ and relative phases, Φ_3 are presented in fig. 3.7 for the linear monodisperse samples. For low molecular weights ($M_w < 110$ kg/mol), corresponding to a number of entanglements per chain $N_e < 6$ there is no strong dependence of the non-linearities on M_w at this temperature. A high molecular weight affects the non-linear behaviour for a $N_e > 6$ and results in higher $I_{3/1}(\gamma_0)$ and lower $\Phi_3(\gamma_0)$. A polydisperse linear melt presents higher non-linearities than a monodisperse one with similar M_w, as depicted in fig. 3.8. At large γ_0 flow instabilities are observed and the reproducibility of the results is clearly affected (see fig. 3.7 and 3.8).

For the case of the linear blends shown in fig. 3.9 and 3.10, instabilities during the LAOS flow are prominent in large amplitudes in the open-rim geometry of the ARES (typically $\gamma_0 > 1$). There is no clear correlation between the measured non-linearities and the blend composition. However, one can argue that a dilution of a high molecular weight melt with a low molecular weight component (PS41) can reduce the non-linearities and has an ef-

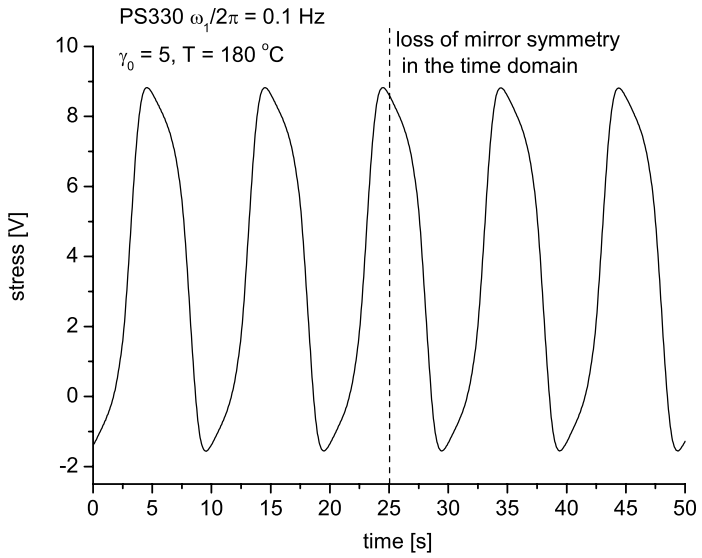

Figure 3.5: *Stress response time signal, for PS330 under LAOS with $\omega_1/2\pi$ = 0.1 Hz, γ_0 = 5 at T = 180 °C. The maximum is "tilted" to the left reflecting the loss of linearity from the rheological process.*

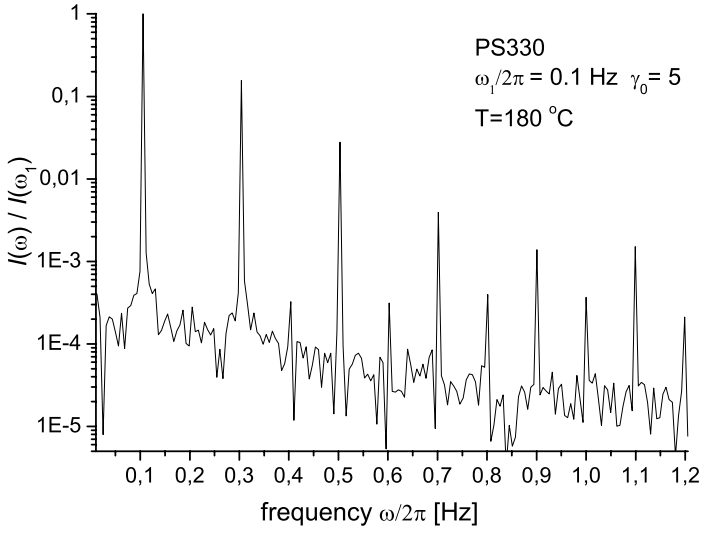

Figure 3.6: *Fourier-Transform spectrum for PS330 under LAOS with $\omega_1/2\pi$ = 0.1 Hz, γ_0 = 5 at T = 180 °C, corresponding to time data of fig. 3.5.*

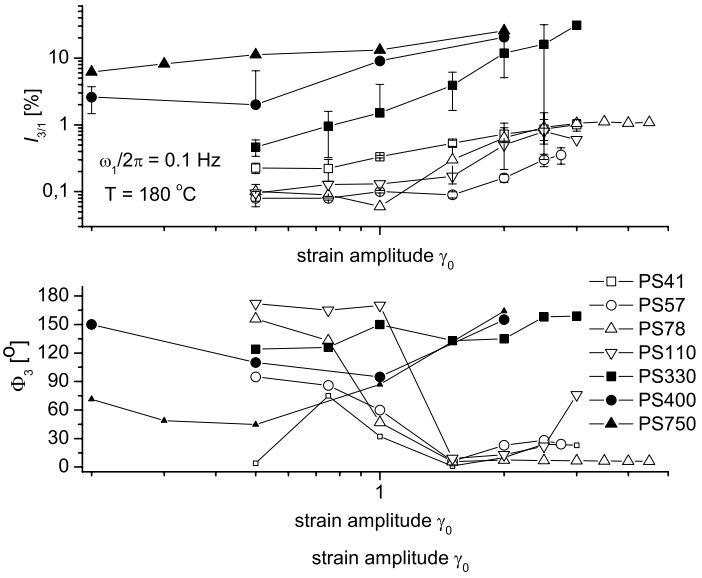

Figure 3.7: *$I_{3/1}$ and Φ_3 for linear monodisperse polystyrene melts, for LAOS with an excitation frequency of $\omega_1/2\pi$ = 0.1 Hz at T = 180 °C.*

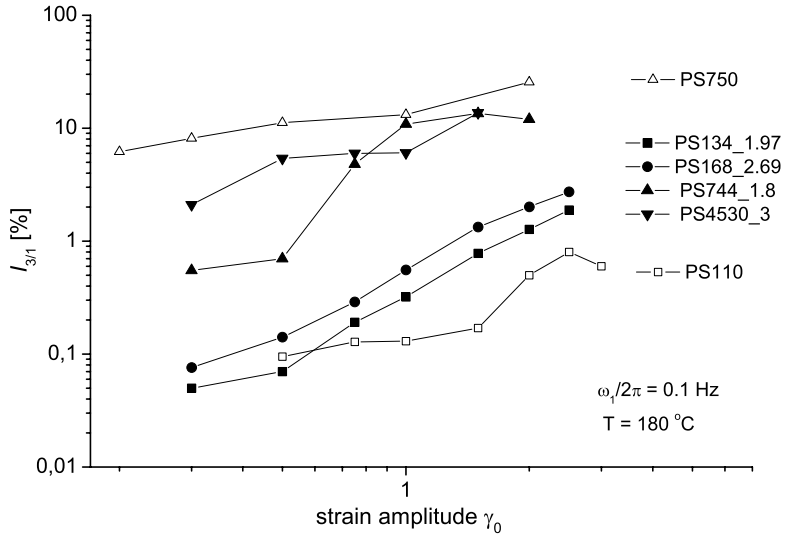

Figure 3.8: *Effect of polydispersity on $I_{3/1}$ for linear polydisperse polystyrene melts, for LAOS with an excitation frequency of $\omega_1/2\pi$ = 0.1 Hz at T = 180 °C.*

fect on the relative phase of the melt. Additionally, comparing $I_{3/1}$ and Φ_3 of the blends with the pure components, we can conclude that the non-linear behaviour is mainly the result of the presence of large macromolecules in the melt. Even for a 52/48 ratio of PS41 and PS330 (PSmix3), the $I_{3/1}$ of the blend and the relative phase is closer to that of that of the pure high M_w component (fig. 3.10).

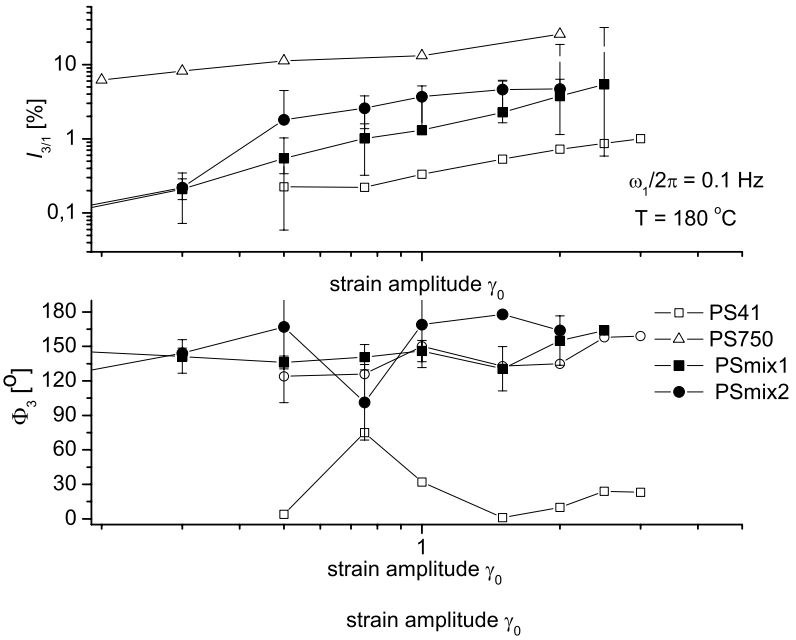

Figure 3.9: *$I_{3/1}$ and Φ_3 for binary blends of linear PS41 and PS750. LAOS with an excitation frequency of $\omega_1/2\pi$ = 0.1 Hz at T = 180 °C is applied.*

3.3.1 Effect of deformation history on non-linear rheological behaviour

As already mentioned in paragraph 3.3, for LAOS with γ_0 above a critical value, flow instabilities occur. These phenomena are experimentally detected and recorded via the FT-spectrum. Especially the appearance of even harmonics and the large increase of the odd harmonics is a clear indication of instable flow [Chen 94, Graham 95]. Representative examples of torque time signals recorded at large γ_0 are shown in fig. 3.11. The samples of PS750 in this figure are prepared in a similar way. However, small differences may exist in their deformation history during the strain sweep tests, which result in a different evolution of instabilities such as meniscus distortions and wall slip. For these large γ_0 ($\gamma_0 > \gamma_{0,critical}$) the reproducibility of $I_{3/1}$ and Φ_3 can be very low and deviations up to 50-100% of their values are recorded.

In order to derive reproducible results with minor effects from normal forces and in-

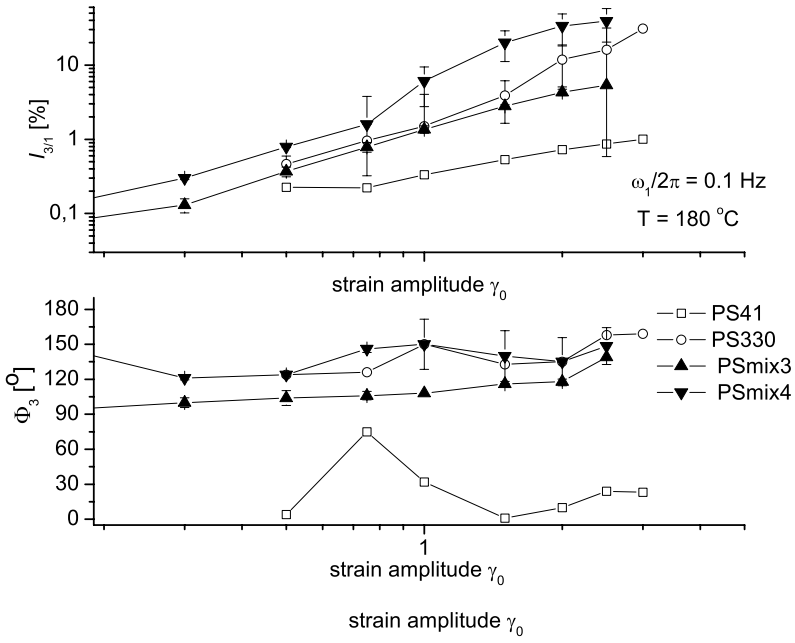

Figure 3.10: *$I_{3/1}$ and Φ_3 for binary blends of linear PS41 and PS330. Applied LAOS with an excitation frequency of $\omega_1/2\pi$ at T = 180 °C.*

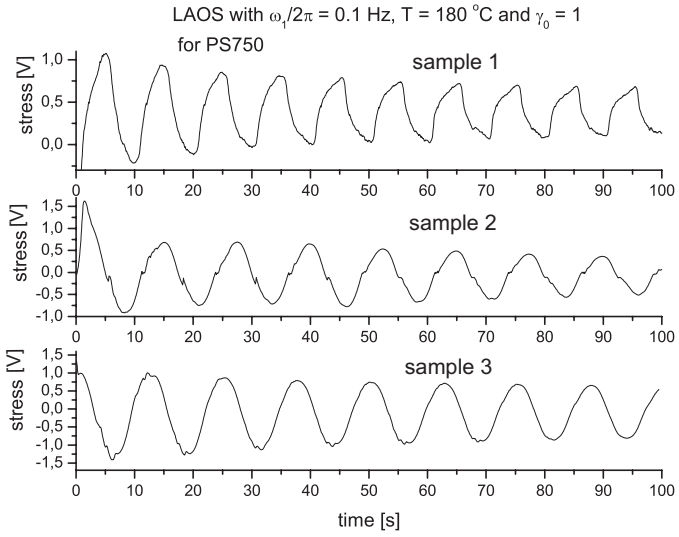

Figure 3.11: *Examples of LAOS torque time signals for three different samples of PS750, with a strain amplitude larger than the critical γ_0 for the onset of instabilities. Small changes on the deformation history result in different non-linear behaviour at large γ_0 of low reproducibility.*

stabilities, strain sweeps are performed with strain amplitudes ranging from values used for small amplitude oscillatory shear (SAOS) frequency sweep measurements (typically γ_0 = 0.1) up to $\gamma_0 \approx \gamma_{0,critical}$. This critical γ_0 corresponds to the onset of instable non-linear behaviour, as determined by the decay of the stress signal amplitude, which after 5 periods may exhibit a decrease of 10% of its value. Above this upper limit of applied strain amplitude the reproducibility of the measurements is significantly lower, the resulting LAOS signal depends strongly on the initial conditions of the experiment and the form of the stress signal (respectively the resulting FT-spectrum) is time-dependent. This critical γ_0 has a strong dependence on molecular weight and topology (see more details in chapter 5). The results for $I_{3/1}$ from three different strain sweeps for PS330 are presented in fig. 3.12 and 3.13. Each $I_{3/1}$ and Φ_3 data point is derived from analyzing 20 recorded cycles. The $I_{3/1}$ from the first strain sweeps is recored for γ_0 up to the critical value where instabilities occur, $\gamma_{0,critical}$ = 0.65. For the strain sweeps started from relatively large initial γ_0 = 0.5 with larger steps, a critical value of $\gamma_{0,critical}$ = 1.5 is observed (deviation from the predicted non-linear behaviour). Above this strain amplitude, the instabilities that occur, as well as the large normal forces (typically >1 N for a 13 mm diameter plate) result in an extreme non-linear behaviour and a loss in LAOS stress signal periodicity. The upper limit for this measurement is the maximum possible applied γ_0 in the ARES for the specific geometry and LAOS conditions. It is clear that the onset and evolution of instabilities, as reflected in the high non-linearities, depends on the previous deformation history of the polystyrene melt. For a strain sweep at a specific frequency and temperature an increased number of strain amplitude steps and deformation cycles (black points in fig. 3.12) result in a lower $\gamma_{0,critical}$. A "mastercurve" can be derived using eq. 1.47 and combining data from RPA2000 and from ARES (for $\gamma_0 < \gamma_{0,critical}$). The relative phases present an abrupt increase for strain amplitudes close to the critical values. However, if we extrapolate the phase derived from RPA to lower strain amplitudes, $\Phi_3(\gamma_0)$ data from both strain sweeps in the ARES for $\gamma_0 < \gamma_{0,critical}$, follow the same "mastercurve".

The deformation history is important for the occurrence of instabilities and extreme non-linear phenomena ($\gamma_{0,critical}$, $I_{3/1}(\gamma_0)$ and $\Phi_3(\gamma_0)$ for $\gamma_0 > \gamma_{0,critical}$). However, if the effect of the flow instabilities and normal forces can be controlled and minimized, the inherent non-linearity of linear polystyrenes will not depend on past deformation. In other words the evolution of the resulted $I_{3/1}(\gamma_0)$ and $\Phi_3(\gamma_0)$ can be independent of the past deformation on the absence of flow distortions and large normal forces. Conclusively, an optimum strain amplitude range for applying LAOS in these samples ranges from typically γ_0 = 0.07-0.1 to $\gamma_{0,critical}$ (onset of instabilities). For $\gamma_0 > \gamma_{0,critical}$ normal forces and slip phenomena have a drastic effect in the material non-linear response.

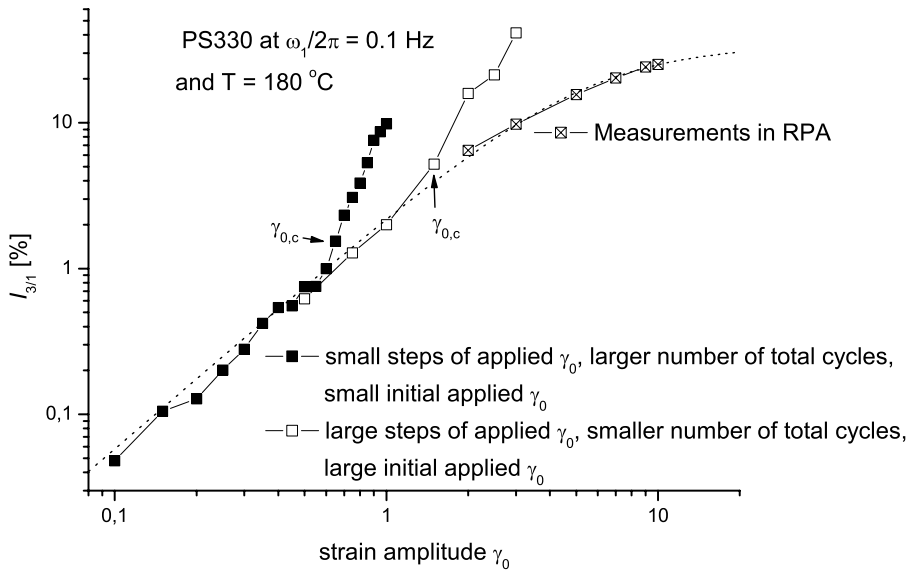

Figure 3.12: *$I_{3/1}$ of PS330 with different deformation history. The 1^{st} strain sweep (black symbols) begins with small γ_0 steps (0.05) and stops when non-linearity increases due to flow instabilities. The 2^{nd} experiment (open symbols) is with larger steps and up to the limit of applied γ_0 in the ARES. The 3^{rd} measurement is performed in the RPA apparatus. At each strain step 20 cycles are recorded. The parameters of eq. 1.47 (dashed-line) for this case are: A = 33%, B = 0.18 and C = 1.6.*

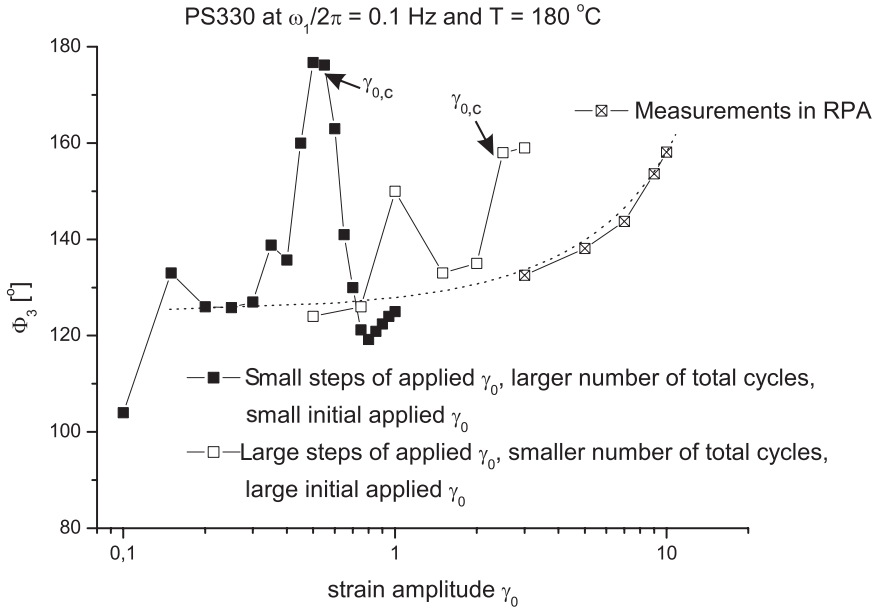

Figure 3.13: *$\Phi_3(\gamma_0)$ for strain sweeps with small and large γ_0 in the ARES and measured in the RPA. The dashed-line is an approximation of the relative phase for flow with no instabilities.*

3.3.2 Molecular weight dependence of non-linearities

In order to minimze the effects of flow instabilites on the resulting FT-Rheology data and derive the material inherent non-linearity, which depends only on material properties such as M_w and PDI, strain sweeps are applied with LAOS and FT-Rheology for all polystyrene linear melts for $\gamma_0 < \gamma_{0,critical}$ in the ARES. The resulting $I_{3/1}(\gamma_0)$ and $\Phi_3(\gamma_0)$ are depicted in fig. 3.14 and fig. 3.15, respectively. The experimental conditions for LAOS ($\omega_1/2\pi$ = 0.1 Hz and T = 180 °C) correspond to the flow region in the G' and G'' spectrum for polystyrenes with $M_w \leq$ 110 kg/mol. Larger macromolecules with $N_e > 6$ exhibit a dominant elastic rheological behaviour at T = 180 °C. The excitation frequency $\omega_1/2\pi$ = 0.1 Hz corresponds to the rubbery plateau for this sample.

There is a clear dependence of the non-linear behaviour of the melts on molecular weight (as quantified by M_w) especially for M_w higher than ∼200 kg/mol. Entanglements become an effective topological constrain in the non-linear flow of the polystyrene melts for $N_e > 10$, at the specific experimental conditions. Larger and highly entangled macromolecules induce non-linearities at smaller deformations and result in higher $I_{3/1}(\gamma_0)$. The relative phase for the linear polystyrenes, shown in fig. 3.15 posses no significant molecular weight dependence for $M_w <$ 110 kg/mol. For higher molecular weights $\Phi_3(\gamma_0)$ is between 120°-160°. However, for strain amplitudes above a specific value, the phase experience a sudden decrease and this observed $\gamma_{0,critical}$ decreases with increasing M_w. A material sheared with a strain amplitude $\gamma_{0,critical}$ responds with a stress time signal of decaying amplitude. The shape of the periodic signal is not significantly changing after some cycles, however the amplitude is decreasing (fig. 3.16). This phenomenon is discussed in detail in chapter 5. It must be noted that, measuring low molecular weight PS samples (e.g. PS41, PS57, PS78), the detected torque is very low. The noise has a significant contribution to the recorded non-linearities, even with the use of "oversampling", thus the resulting $I_{3/1}$ and Φ_3 for these cases suffer from poor accuracy (see fig. 3.14, 3.17, 3.18). In order to measure non-linearities more accurately, one must measure at $\gamma_0 > 3$, which is not possible with the current experimental setup in the ARES rheometer.

The non-linear behaviour of the polystyrene blends, quantified by FT-Rheology, is presented in fig. 3.17 and 3.18. It is observed that a dilution of a high molecular weight polystyrene melt with a linear component of a smaller M_w results in a reduction of the non-linear behaviour of the sample and a shift of the critical strain amplitude to larger values. Furthermore, when focusing in PSmix3 with a ∼50/50 weight ratio of PS41 and PS330, the $I_{3/1}(\gamma_0)$ and $\Phi_3(\gamma_0)$ are closer to the values of the pure high molecular weight component. Thus, we can conclude that the non-linear behaviour is dominantly controlled and induced from large highly entangled macromolecules. Nevertheless, the flow properties of such materials can be optimized by diluting them with short polymeric chains. These short macromolecules act in the polydisperse melt as plasticizers and can effectively reduce the occurring non-linearities.

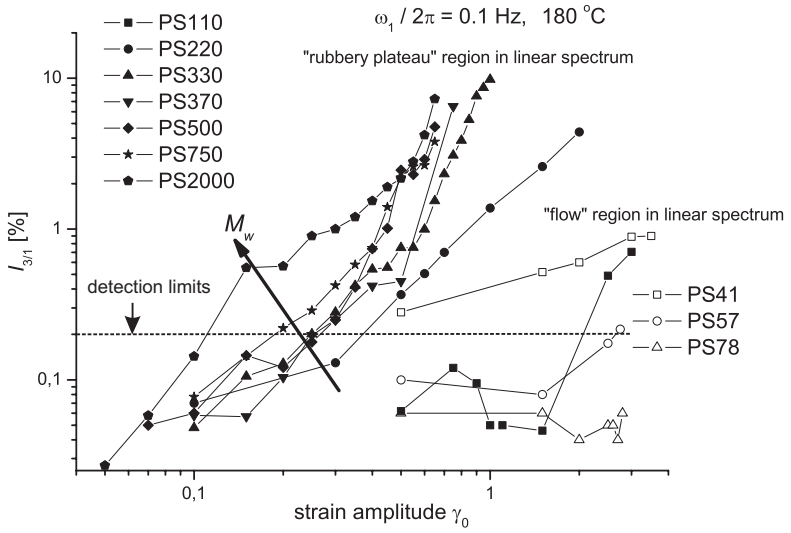

Figure 3.14: *$I_{3/1}$ at low and medium γ_0, for linear monodisperse polystyrene melts. The LAOS conditions, $\omega_1/2\pi$ = 0.1 Hz and T = 180 °C, correspond to the flow region in the linear spectrum for PS with $M_w \leq$ 110 kg/mol. For higher M_w, conditions correspond to the rubbery plateau in the linear rheological spectrum.*

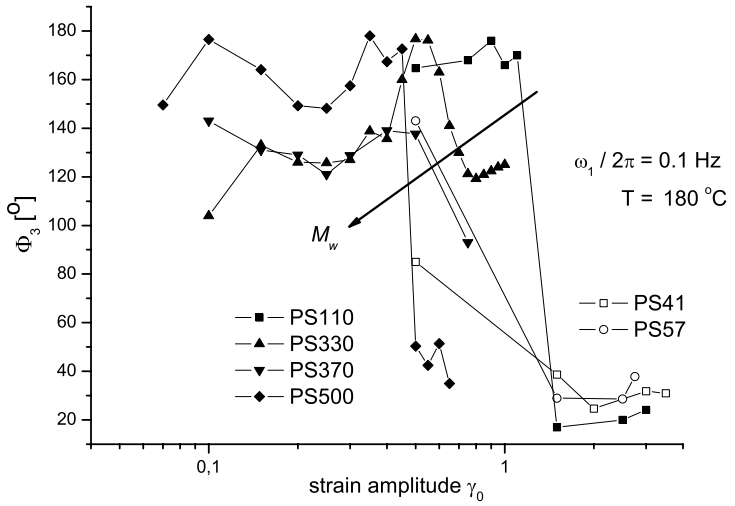

Figure 3.15: *$\Phi_3(\gamma_0)$ at low and medium γ_0, for linear monodisperse polystyrene melts. The LAOS conditions, $\omega_1/2\pi$ = 0.1 Hz and T = 180 °C, correspond to the flow region in the linear spectrum for PS with $M_w \leq$ 110 kg/mol. For higher M_w, conditions correspond to the rubbery plateau in the linear response regime.*

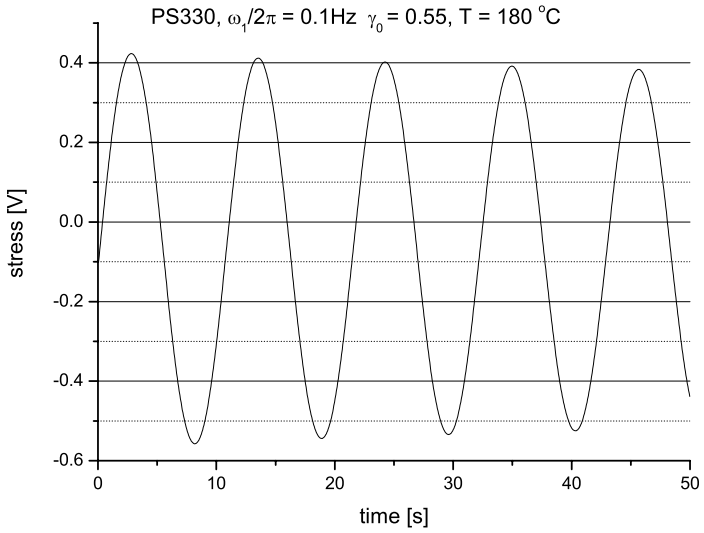

Figure 3.16: *LAOS stress signal for γ_0 larger than the critical value, where a continuous increase in $I_{3/1}(\gamma_0)$ and a decrease in $\Phi_3(\gamma_0)$ is observed.*

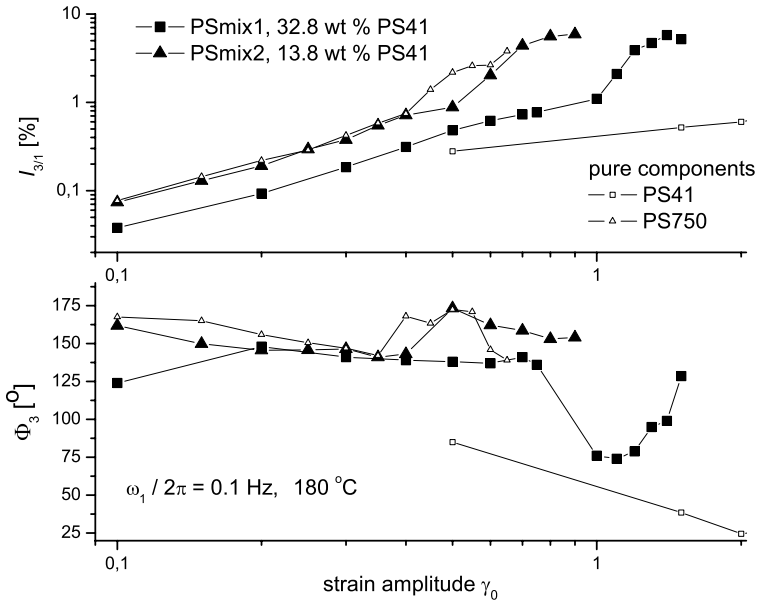

Figure 3.17: *$I_{3/1}(\gamma_0)$ and $\Phi_3(\gamma_0)$ at low and medium γ_0, for binary blends PSmix1 and PSmix2, from linear monodisperse PS41 and PS750. For the case of PS41, detection problems are encountered due to its low molecular weight and viscosity.*

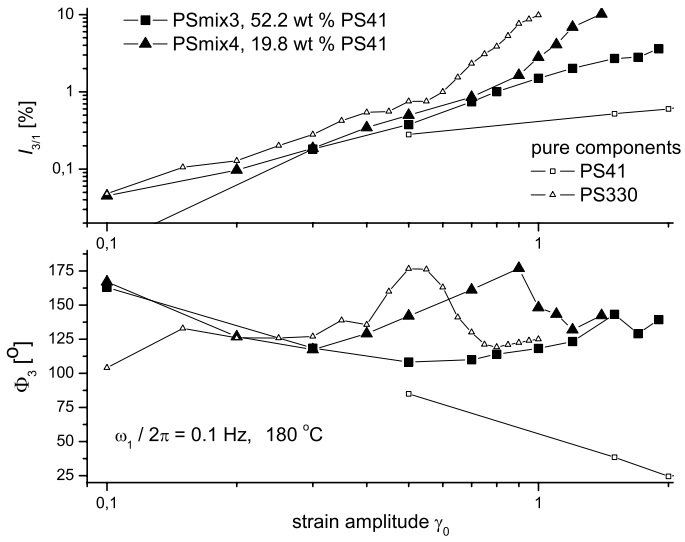

Figure 3.18: *$I_{3/1}(\gamma_0)$ and $\Phi_3(\gamma_0)$ at low and medium γ_0, for binary blends PSmix3 and PSmix4, from linear monodisperse PS41 and PS330. For the case of PS41, detection problems are encountered due to its low molecular weight and viscosity.*

3.3.3 Quantification of material non-linearity at low and medium strain amplitudes

The non-linear rheological behaviour of the linear polystyrenes is quantified via $I_{3/1}(\gamma_0)$, which can be fitted by simple empirical equations, in particular eq. 1.47 and 1.51. From the investigated PS materials only PS100, PS330 and PS500 are commercial samples and can be measured for γ_0 up to 10. The available quantity of the samples except the above is inadequate for LAOS with the RPA2000 apparatus (3.5 g - 4 g sample per measurement needed), hence their non-linearity at very large strain amplitudes of typically $\gamma_0 > 3$ is not measured. Thus, eq. 1.51 is used to fit the resulting $I_{3/1}(\gamma_0)$ at low and medium γ_0 and correlate it to M_w. Furthermore, the effects from flow instabilities on the resulting FT-spectrum are neglected in this analysis, allowing the quantification of the material inherent non-linearity. The results of parameters *D* and *C* are depicted in fig. 3.19 as a function of M_w for linear monodisperse polystyrene melts. Parameter *D* increases with increasing molecular weight, for macromolecules containing more than 6 entanglements per chain. The values of *C* depart from the theoretically predicted value and increase with increasing M_w for the highly entangled melts ($N_e > 6$).

Generally, polydispersity increases $I_{3/1}(\gamma_0)$, due to the presence of large macromolecules. This can also be seen in the parameters derived from fitting the polydisperse linear samples: PS134_1.97 (D = 0.005), PS168_2.69 (D = 0.006), PS744_1.8 (D = 0.170) compared to monodisperse samples of similar M_w, PS110 (D = 0.001) and PS750 (D = 0.158), respec-

tively. The effect of larger macromolecules is also seen in the blends: PSmix1, PSmix2, PSmix3, PSmix4 in comparison with the monodisperse pure components (PS41, PS330 and PS750). Both non-linear parameters increase by a broadening of the molecular weight distribution, due to the presence of longer macromolecules in the polydisperse melt. Parameters *D* and *C* can be decreased by a dilution of the melt with smaller chains. These macromolecules of low molecular weight and entanglement number (in this case $N_e \approx 2$) do not posses a strong inherent non-linear character and additionally torque detection problems occur that influence the measurement accuracy. However, short chains act as plasticizers, affect the relaxation and dynamics of the longer chains and tend to decrease the non-linear behaviour of the high molecular weight melts, as reflected in parameters *D* and *C*.

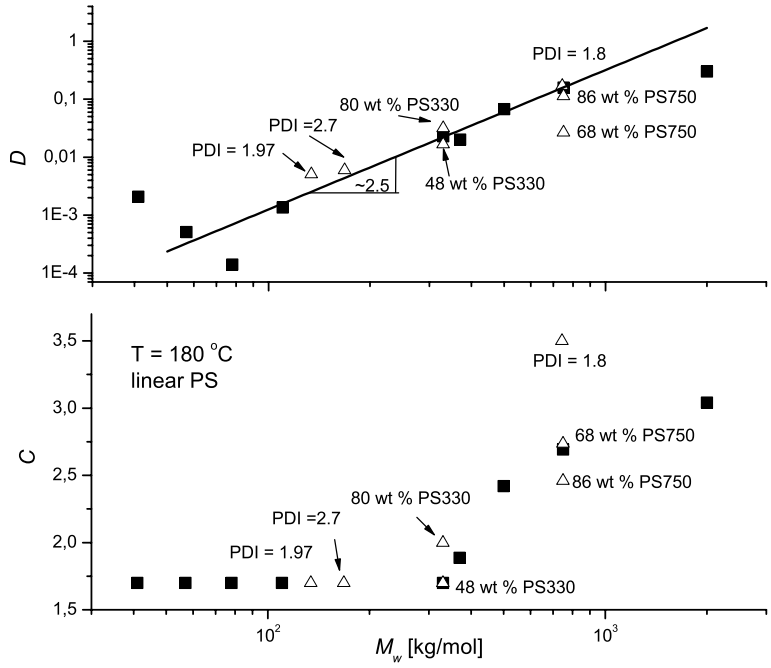

Figure 3.19: *Parameters D and C, derived from fitting $I_{3/1}(\gamma_0)$ at low and medium strain amplitudes. Open symbols correspond to polydisperse samples. For PSmix, M_w is taken from the high molecular weight component.*

From fig. 3.19 one can derive an expression for the non-linearity as a function of M_w (in kg/mol):

$$D = 1.9^{-8} M_w^{2.5} \tag{3.1}$$

The above equation fitts in a satisfactory manner non-linearities of linear monodisperse polystyrenes with medium and high molecular weights ($M_w > 100$ kg/mol). A more elaborated equation can be derived to include polydispersity effects and if possible, topological characteristics (branching content). Nevertheless, it is shown that the non-linear parameter for low and medium γ_0, D, has a general dependence on molecular weight of the form $D \propto {M_w}^a$, where a = 2-3, for linear melts.

3.4 LAOS simulations for linear and branched polystyrene melts

Large amplitude oscillatory shear flow is simulated for the polystyrene samples presented in Table 3.3. The resulting stress response is analysed in the same way as the experimental torque signals, via FT-Rheology analysis. Although the samples are not of a pom-pom topology (see fig. 1.1), we can use the DCPP model to describe the LAOS flow of these branched materials. However, it must be noted that the molecular parameters related to polymer architecture, q and λ/λ_s, must be considered as model parameters and not as realistic topological features of the studied samples. For example, a comb with 30 side-arms statistically distributed along a single backbone [Höfl 06, Roovers 79b] is not expected to be successfully modelled via with respect to its rheological properties via a pom-pom macromolecule with q = 15 (see 2.4).

Experimental measurements of linear rheological properties (G', G'', $|\eta^*(\omega)|$), as well as FT-Rheology data are reported by Höfl [Höfl 06] and Neidhöfer et al. [Neidhöfer 03b, Neidhöfer 03a]. The linear parameters of the DCPP model, i.e. the relaxation time, λ_i, and the shear modulus, G_i, of each mode are identified by fitting experimental data of G', G'' and $|\eta^*(\omega)|$. As an example, the fit of the polystyrene comb melt C642 with a 4-mode DCPP model is presented in fig. 3.20.

3.4.1 Comparison between Giesekus and DCPP model for LAOS flow

As already mentioned, the Giesekus model has been utilized in the past to model LAOS flow behaviour of polystyrene solutions [Neidhöfer 03b]. Thus, a comparison between the two models for the case of linear and branched polystyrenes would be meaningful. In previous studies [Neidhöfer 03b, Neidhöfer 03a] predicted LAOS signals were analyzed via FT-Rheology for sample PS250_41. The results from this study are compared with simulations using the DCPP model. Both multi-mode constitutive equations can describe the linear properties and fit G', G'' and $|\eta^*(\omega)|$ experimental data. The resulting $I_{3/1}(\gamma_0)$ and $\Phi_3(\gamma_0)$ of the LAOS strain sweeps simulated with both models, as well as experimental data are depicted in fig. 3.21 and 3.22. The flow modelling using both constitutive equation is according to the

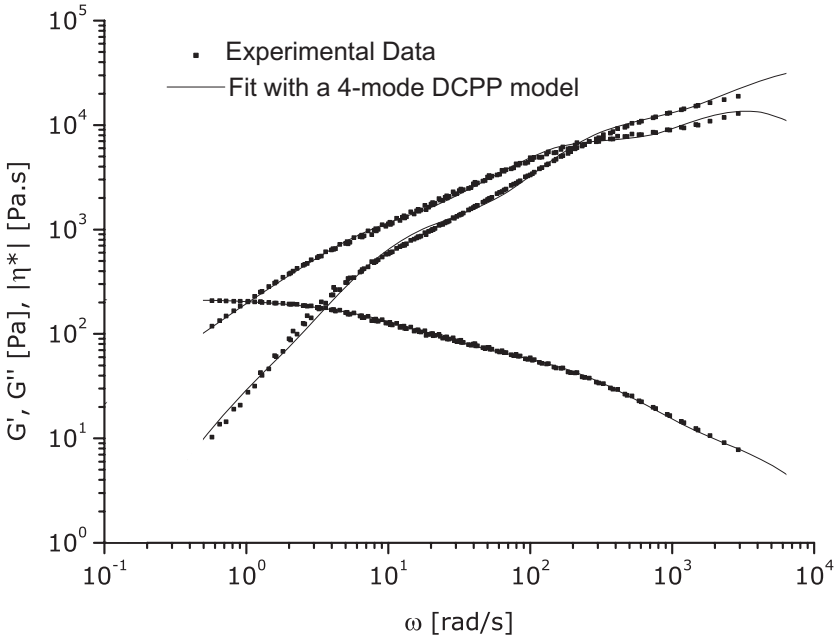

Figure 3.20: *Fit of linear rheological material properties of comb C642 solutions (see Table 3.3), by a 4-mode differential DCPP model. Experimental data for G', G'' and $|\eta^*(\omega)|$ obtained by dynamic oscillatory shear with TTS at a reference temperature T = 60°C.*

described method in chapter 2. For the Giesekus model, the non-linear parameter α is determined from the shear viscosity, as estimated by applying the Cox-Merz rule [Neidhöfer 03b]. Concerning the DCPP model, the number of arms was set to 1 for all modes ($q_i = 1$) to account for the linear topology. The ratio of λ_i/λ_{si} is generally proportional to the number of entanglements (eq. 2.19) and takes values between 2 and 10. For the specific sample Neidhöfer et al. [Neidhöfer 03b] estimates $N_e \approx 6$, thus a low value of orientation/stretch relaxation ratio, $\lambda_i/\lambda_{si} \approx 2$, is expected to best fit non-linear experimental data (see eq. 2.19). Additionally, LAOS simulations are performed for a larger ratio, λ_i/λ_{si} = 10, to estimate the effect of the parameter in the non-linear behaviour of the linear polystyrene solution, as modeled by DCPP.

The Giesekus model exhibits a good prediction of the non-linearities for the specific LAOS flow. However, it overpredicts the relative phase, especially at low strain amplitudes. The DCPP is found to correctly capture the evolution of the non-linearities and the relative phase with increasing strain amplitude. The λ_i/λ_{si} ratio must be properly adjusted for the model with q_i = 1 to fit the non-linear behaviour of a linear polystyrene solution at a broad range of deformations, with minimum deviation from experimental FT-Rheology data.

Subsequently, both models are validated with respect to their predicting capability for LAOS flow of a branched polystyrene melt, in particularly PSH2 (see Table 3.3). The specific sample is an H-shaped polystyrene melt (see fig. 1.1) and can be considered as a pom-pom with two arms at each end of the backbone. Thus, for the DCPP model, parameter q_i can

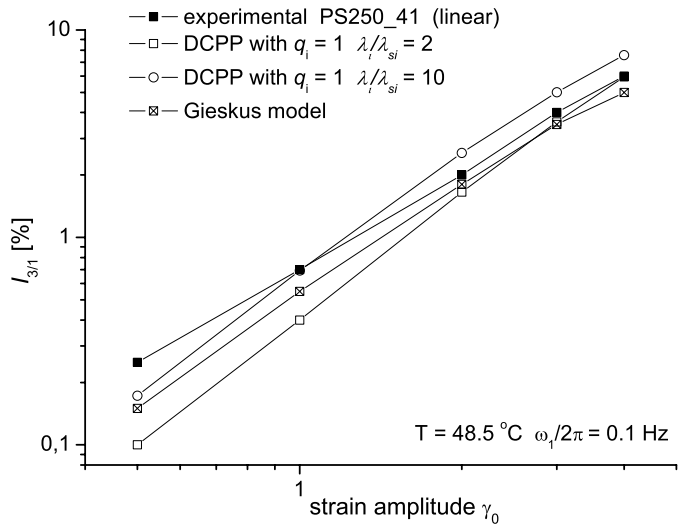

Figure 3.21: *Predicted $I_{3/1}(\gamma_0)$ for linear solution PS250_41 for LAOS with $\omega_1/2\pi$ = 0.1 Hz, at T = 48.5 °C.*

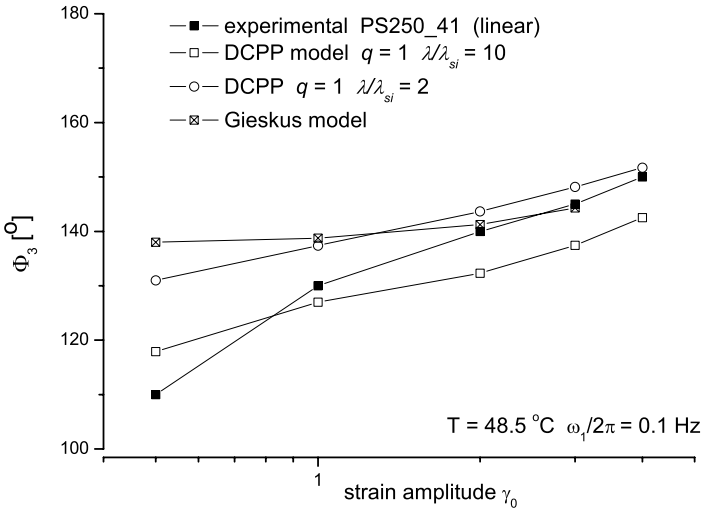

Figure 3.22: *Predicted $\Phi_3(\gamma_0)$ for linear solution PS250_41 for LAOS with $\omega_1/2\pi$ = 0.1 Hz, at T = 48.5 °C.*

be taken equal to 2. The backbone has a molecular weight corresponding to an average of N_e = 2.5 entanglements. Taking into account eq. 2.19, low λ_i/λ_{si} are expected to better fit the resulting non-linearities. This specific ratio is kept constant for all modes as illustrated in fig. 3.23. For the simulations with the multi-mode Giesekus model the same number of modes is used and the non-linear parameters, α_i, are determined by fitting the shear-rate dependent viscosity after the application of the Cox-Merz rule. Parameters for both models are given in Table 3.4.

	DCPP				Giesekus		
modes	λ_i **(s)**	G_i **(Pa)**	q_i	λ_i/λ_{si}	λ_i **(s)**	η_i **(Pa.s)**	α_i
1	1	2,008	2	1-10	1	1	0.2
2	0.1	36,122	2	1-10	0.1	100	0.63
3	0.01	80,820	2	1-10	0.01	10000	0.303
4	0.0004	283,000	2	1-10	0.0004	100000	0.2

Table 3.4: *Parameters for the multi-mode models DCPP and Giesekus. The relaxation times, λ_i, moduli, G_i, viscosity factors, η_i and non-linear parameters, α_i, where selected on the basis of linear oscillatory shear data.*

Simulation results for three different ratios of orientation to stretch characteristic times (λ_i/λ_{si}) for the DCPP are compared with those from the Giesekus model. Experimental data are also shown for the PSH2 melt in fig. 3.23. Measurements and simulations are performed at T = 180 °C.

The Giesekus model predicts lower $I_{3/1}(\gamma_0)$ and the phase Φ_3 is 10° - 20° higher than the experimental data for this PS H-shaped melt. For the DCPP model, one can clearly see the dependence of the non-linearities and phases on the relaxation mechanism. When the "pom-pom macromolecule" relaxes mainly with orientation and less via backbone stretching process, in other words when λ_i/λ_{si} is high and approaches the upper limit of 10, the non-linearities increase significantly for a large range of strain deformations.

Simulation for the same sample are also performed to couple experimental FT-Rheology data derived from a wide range of Deborah numbers. The De number is defined as in chapter 1. Within this chapter, $\lambda_T = \tau$ is the relaxation time used and corresponds to the inverse of the minimum ω where tan δ = 1. The results are presented in fig. 3.24. It is worth mentioning that the number of modes used is limited and in this case is equal to four. For a high number of DCPP modes the problem becomes ill-posed to the high number of adjustable parameters [Clemeur 04, Inkson 99]. On the other hand, if the linear spectrum covers a wide range of frequencies (for the case of PSH2 more than 8 decades) a low number of modes is not adequate to correctly fit G' and G'', for the whole range of ω. Thus, data at very high frequencies, or respectively low temperatures and respectively high *De* are poorly fitted concerning their

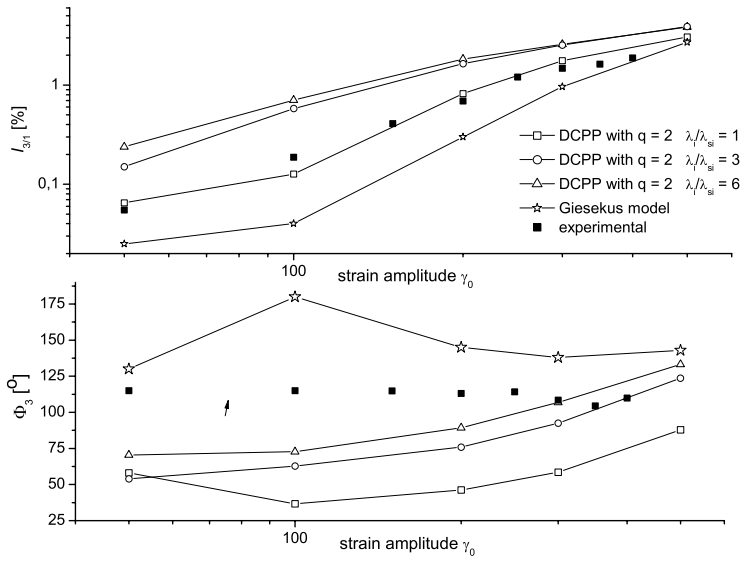

Figure 3.23: *Predicted $I_{3/1}(\gamma_0)$ and $\Phi_3(\gamma_0)$ and experimental data for H-shaped melt PSH2. LAOS performed with $\omega_1/2\pi$ = 0.1 Hz, at T = 180 °C. The ratio λ_i/λ_{si} is changed for each simulated strain sweep with the DCPP model.*

linear properties. Hence, the DCPP model predictions would fail to predict the non-linear behaviour at high *De* for this case.

3.4.2 Simulation of LAOS flow for comb-like polystyrene solutions

The effects of the branch number and branch length in the non-linear behaviour, as analyzed via FT-Rheology, can be separated and a clear estimation can be derived in the case of well-characterized branched samples. For this reason, we present results from LAOS simulations for polystyrene combs (in solution and in melt state) with a well defined architecture. Details about the studied materials as well as experimental FT-Rheology and linear rheological results are provided by Höfl [Höfl 06].

All samples are anionically synthesized, monodisperse and contain a specific number of side-arms of the same length. The synthetic route results in monodisperse molecular weight of the backbone, as well as molecular weights of each arm. Due to the excellent control of the reaction that the anionic polymerization method provides, no differences in topology between macromolecules of the same sample are expected, or other defects like branches on branches. However, with the synthetic technique presented by Roovers [Roovers 79b] and discussed also by Neidhöfer [Neidhöfer 03a] and Höfl [Höfl 06], the distribution of the side-chains along the

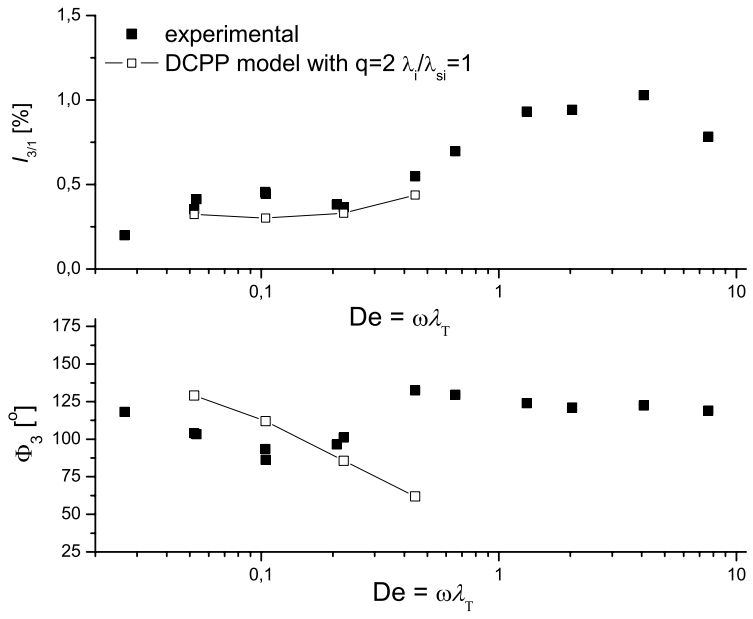

Figure 3.24: *Predicted $I_{3/1}$ and Φ_3 and experimental data as a function of Deborah number for H-shaped melt PSH2. LAOS experiments performed by Neidhöfer [Neidhöfer 03a]. In all measurements and simulations γ_0 = 1.*

backbone is unknown. In this case, these chains are grafted in a random manner on the backbone and it cannot be estimated whether there is a high density of side-arms at the backbone ends (approaching a pom-pom architecture) or a more orderly distributed branching.

The samples C642, C732 and C742 are solutions with ∼30 side-arms. Sample C642 has a shorter backbone (M_b = 275 kg/mol) in comparison with the C732 and C742 which consist of a backbone nearly three times larger (860 kg/mol). However, C642 and C742 have longer side-arms, with M_a = 47 kg/mol, almost of double length as the branches of C732 (M_a = 25.7 kg/mol). In fig. 3.25 the loss and storage moduli for the above samples, along with the fits with the DCPP multi-mode model are presented. One can clearly see the effect of a longer backbone which shifts the crossover point of G' and G'' to lower frequencies. A three times longer backbone results in an approximately 25 times decreased crossover frequency ($\omega_{crossover,C742}$ $\approx \omega_{crossover,C642}$/25). For the same backbone length and number of arms ($N_{arms} \approx 30$), a double side-arms length decreases significantly the elastic character of the linear behaviour for these combs (samples C732, C742). The PS sample with the longer backbone, for which the rubbery plateau is in the studied frequency range, no second crossover between the rubbery and the glass regime is observed. Instead, the storage and loss moduli increase in a parallel manner at very high frequencies, due to the relaxation of the side-arms. This process is faster than the relaxation of the backbone and more pronounced for C742, which has side-arms of a

higher average entanglement number, $N_e \sim 2.6$. Shorter arms are less entangled and thus less rheologically effective (for C732, $N_e \approx 1.4$). These features can be captured by the multi-mode DCPP model for the linear regime and are demonstrated by the quality of the fits for G' and G''.

In fig. 3.26 we present the experimentally derived $I_{3/1}$ as a function of *De* along with the

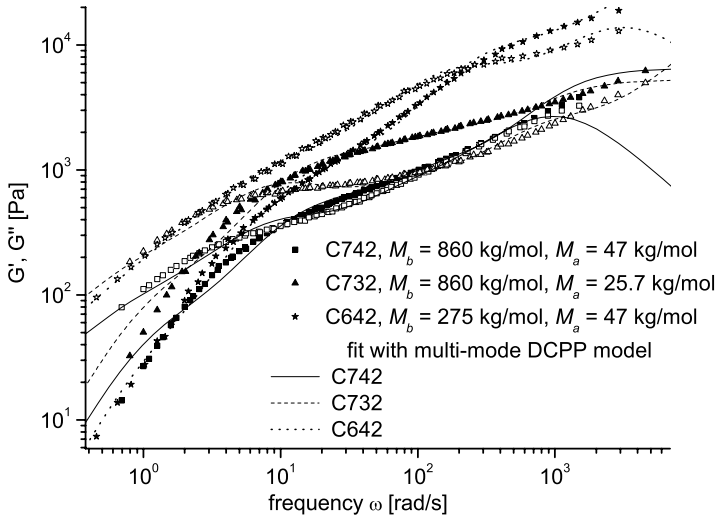

Figure 3.25: *Fit of linear rheological material properties of polystyrene comb solutions C642, C732, C742, by a 4-mode differential DCPP model. Experimental data for G', G'' and $|\eta^*(\omega)|$ obtained by dynamic oscillatory shear referenced to a temperature of T = 60°C. Experimental data from S. Höfl [Höfl 06]*

non-linearities predicted from LAOS simulations with the DCPP, for several sets of non-linear parameters, q_i and λ_i/λ_{si}. All LAOS measurements and simulations are performed under a strain amplitude of γ_0 = 1. A dependence of the non-linear behaviour on the molecular parameters of the DCPP model is found, especially for *De* < 1. The model can qualitatively predict the evolution of the non-linearities for low *De* numbers where the material has a dominant viscous character, and high *De* where the elastic behaviour is more pronounced. A minimum in $I_{3/1}$ is experimentally observed for *De* = 6 for C742, which is also predicted by the LAOS simulations (at *De* = 4). However, one can observe that generally N_{arms} is not directly equal to parameter *q* of the DCPP model. In particularly, a comb with *N* side-arms is not necessarily described successfully with a blend of "pom-pom" molecules with *q* = *N*/2 arms at each backbone end, due to the difference between real and model topology. Additionally, the use of several modes to fit experimental data for a wide range of frequencies implies polydispersity of the polystyrene macromolecules, something not consistent with the investigated material. It must be pointed out that q_i must be considered as a model parameter and correlated to branching degree. However, it should not be regarded as the exact number of branches grafted in the

backbone, since the comb structure is analyzed as being a pom-pom with different number of arms. Finally the characteristic time ratio λ_i/λ_{si}, according to eq. 2.19, should be generally low, considering the fact that the average number of entanglements per molecule is low. The samples are polymer solutions of $c \approx 30$ wt % (in DOP) [Roovers 79b].

Similar results are derived from the analysis of the relative phase, Φ_3 for the two comb solutions. For the case of C742, the DCPP model can follow the evolution of the non-linearities and the phases qualitatively better than for C732. This can be attributed in the small arm length of C732, which corresponds to a low number of entanglements and thus rheologically less effective. Considering the above, one can summarize that the DCPP can qualitatively predict the non-linear behaviour of polystyrene combs for a wide range of *De*. The differences between experimental results and simulations can be minimized by a proper parameter selection, taking into account the different concept between a solution described with a blend of "pom-pom" molecules and a monodisperse comb-like solution.

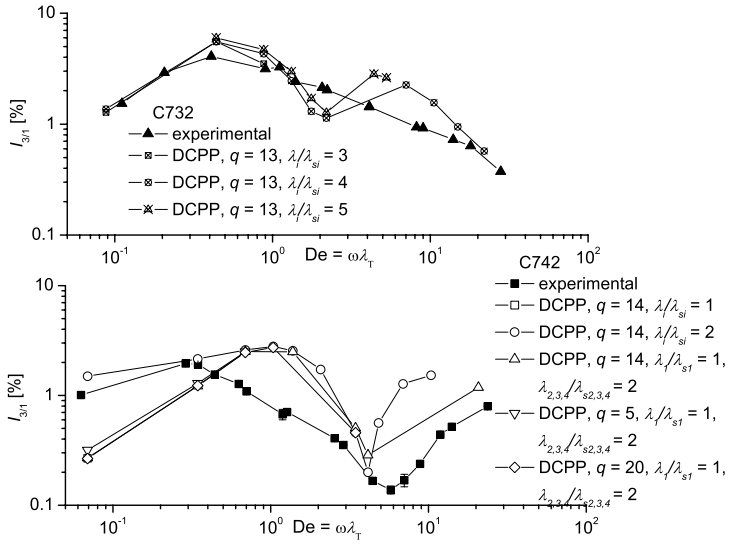

Figure 3.26: *Predicted $I_{3/1}$ and experimental data as a function of Deborah number for polystyrene comb solutions C732 and C742. Both samples have a backbone of 860 kg/mol. Sample C732 has side-chains with half the length of the side-chains in C742. LAOS experiments performed by Dr. S. Höfl [Höfl 06]. In all measurements and LAOS simulations $\gamma_0 = 1$.*

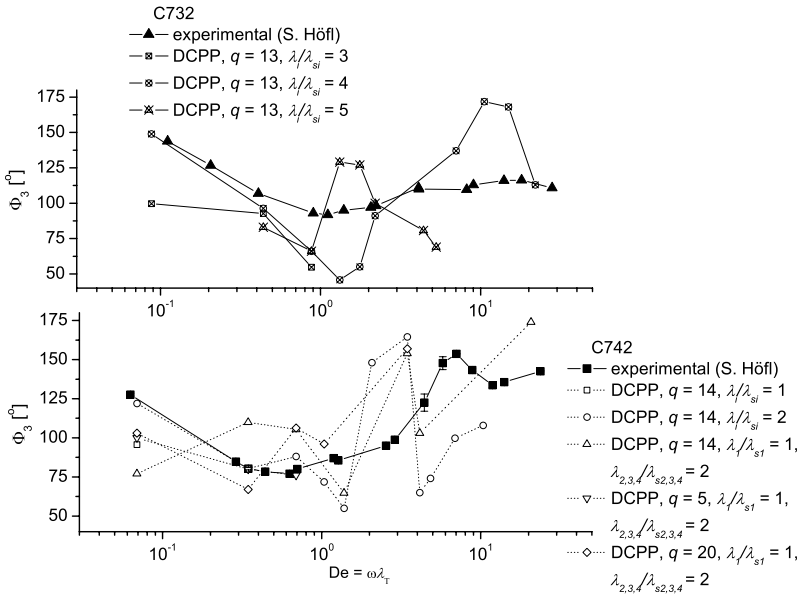

Figure 3.27: *Predicted Φ_3 and experimental data as a function of Deborah number for polystyrene comb solutions C732 and C742. Both have a backbone of 860 kg/mol. Sample C732 has side-chains with half the length of the side-chains in C742. LAOS experiments performed by Dr. S. Höfl [Höfl 06]. In all measurements and simulations γ_0 = 1.*

3.4.3 Application of LAOS flow simulation with the DCPP model on polystyrene comb-like melts

In the previous paragraph the performance of the DCPP model for predicting LAOS flow of polystyrene solutions was presented. However, for the case of polymer melts, the capability of DCPP to describe the non-linear behaviour may differ. In the absence of solvent, the entanglement number per chain increases. The effect of the topological constrains, permanent (branches), or temporary physical entanglements is more drastic. A linear monodisperse polystyrene melt of M_w = 470 kg/mol is studied in order to assess the non-linear behaviour of the DCPP model for simple topologies. The predicted intensity of the 3^{rd} harmonic, along with the corresponding relative phase and the experimental data are presented in fig. 3.28. The DCPP succeeds in describing the non-linear behaviour of a linear melt and the dependence of $I_{3/1}(\gamma_0)$ and $\Phi_3(\gamma_0)$ on the relaxation mechanism is demonstrated. The ratio λ_i/λ_{si} is the only parameter varied since q_i is set equal to 1, in order to account for the linear topology. Furthermore, a large value for λ_i/λ_{si} (= 10) is needed to account for the high molecular weight of the studied PS470, which corresponds to M_w/M_e = 26. This is also in agreement with eq. 2.19.

The modelled comb-like melts were already experimentally studied via FT-Rheology

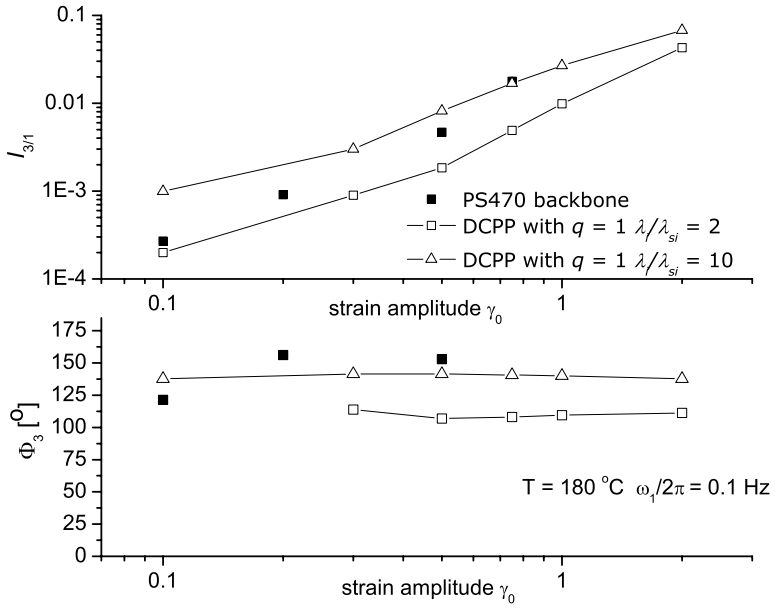

Figure 3.28: *Predicted $I_{3/1}$, Φ_3 and corresponding experimental data as a function of strain amplitude for linear polystyrene melt PS470. LAOS is performed with $\omega_1/2\pi$ = 0.1 Hz at T = 180 °C.*

[Höfl 06], namely samples C622 and C722. The study of comb melts is generally more complicated compared to solutions. Branches are more drastic as permanent obstacles in the reptation and relaxation of the backbone, according to the tube theory [Doi 79, McLeish 98]. Additionally, normal forces are prominent for the case of melts with high molecular weight ($M_{w,total}$ = 624 kg/mol and 1190 kg/mol for C622 and C722, respectively) and the flow instabilities that take place at large deformations limit the range of γ_0 and *De* that can be experimentally accessed for small sample quantities.

The DCPP model concerns the prediction of rheological behaviour for a "pom-pom" molecule. This architecture is of course different than a monodisperse comb melt and the model parameters must not be considered as real topological characteristics. However, Daniels et al. [Daniels 01] suggested that a similar time scale separation of relaxation times for the backbone and the arms can exist for the combs, as for H-shaped or pom-pom architectures. Nevertheless, the arm distribution on the backbone can produce novel and significantly different rheological response in combs, compared to pom-pom molecules. The points where the friction to the free reptation of the comb backbone (branch points) is concentrated, are distributed along the chain, rather than for a pom-pom where these obstacles are at the two backbone ends.

In this paragraph, results are presented for two polystyrene comb melts, C622 and C722. Both contain the same number of branches ($N_{arms} \approx 30$), of the same length ($M_a \approx 11.7$

kg/mol). However, C622 has a three times shorter backbone than C722, corresponding to a much higher branching density, defined as $N_{arms}M_a/M_b$ [Höfl 06]. In all cases, $M_a < 18$ kg/mol, hence the side-arms are expected to have one entanglement maximum. However, there is an effect on the dynamics of the macromolecule by the presence of branch points, statistically distributed on the backbone. In fig. 3.29 the linear rheological properties of two combs are presented, along with the fits from the multi-mode DCPP model for each case. A second relaxation process is observed at high frequencies ($\omega > 100$ rad/s) which can be attributed to the relaxation of arms [Höfl 06]. This additional relaxation of the branches can be the reason for the form of G' and G'' at the high frequencies, where both moduli increase in a parallel manner. No distinct crossover from the rubbery to the glassy zone of the linear spectrum is observed experimentally. Furthermore, the high molecular weight of C722 is the reason for the shift of the flow terminal zone (tan $\delta > 1$) at very low frequencies ($\omega < 0.01$ rad/s), where the rheological properties cannot be measured with the current experimental setup. Hence, in the studied frequency range a dominant elastic behaviour is expected from C722.

A 6-mode DCPP model is chosen to model the linear and non-linear rheological behaviour of the comb-like melts. The topology of the melts being a comb and with the conclusions derived from the study of polystyrene solutions, a low number of side arms is chosen, q_i = 4, for both cases since the N_{arms} is the same for C622 and C722. The ratio λ_i/λ_{si} is chosen considering that $\sim$30 arms are grafted in a three times longer backbone for the case of C722, in comparison with C622. Using eq. 2.19 and the suggestion by Inkson et al. [Inkson 99], a larger ratio of orientation/stretch relaxation mechanism for the backbone can be assumed for C722 than for C622, due to the lower branch density of the first. The linear rheological properties of C622 are well fitted. However, for sample C722 due to the absence of a G'-G'' crossover point the fit of the experimental data with the multi-mode DCPP model is poor and does not properly capture the dominant elastic behaviour of the material in the linear regime. Due to this problematic determination of the linear properties of the DCPP, a deviation between linear experimental and simulated properties is expected in the non-linear rheological behaviour, i.e. $I_{3/1}$ and Φ_3.

Subsequently LAOS flow is simulated for a range of strain amplitudes, $0.1 < \gamma_0 < 2.5$, and the resulting stress time signal is analyzed via FT-Rheology. The same procedure is followed for the LAOS simulations performed for the melts as for the solutions (see above paragraph). All strain sweeps are with the same excitation frequency, $\omega_1/2\pi$ = 0.1 Hz and at a temperature of 180 °C. In fig. 3.30 the resulting $I_{3/1}$ for both melts is presented as a function of strain amplitude. The relative phases for both samples are shown in fig. 3.31. The non-linearities of both comb melts are successfully predicted with the DCPP model. The predicted phases have a difference of up to 25° from the experimental Φ_3. However, the model succeeds to discriminate between the two different topologies and shows an increased $\Phi_3(\gamma_0)$ for the sample with the longer backbone and the lower branching density, in agreement to experimental results.

However, both the theoretically predicted and the experimentally measured $I_{3/1}(\gamma_0)$

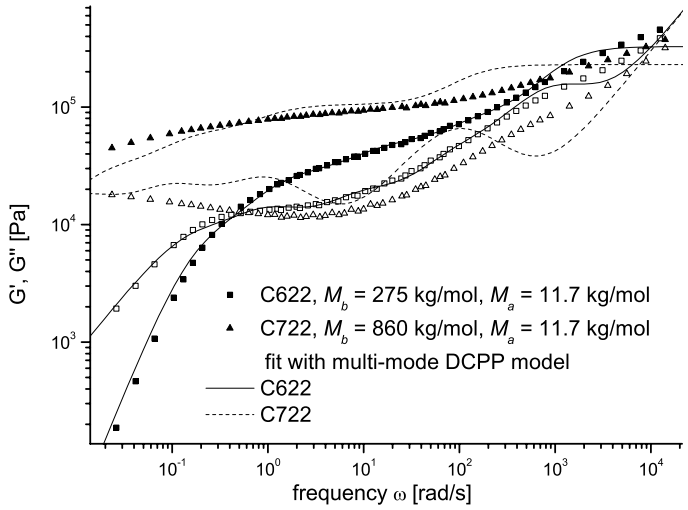

Figure 3.29: *Fit of linear rheological material properties of polystyrene comb melts C622, C722 by a 6-mode differential DCPP model. Experimental data for G', G'' and $|\eta^*(\omega)|$ obtained by dynamic oscillatory shear at a reference temperature T = 180°C [Höfl 06]. The poor fit of the moduli for C722 is due to the absence of crossoverpoints in the spectrum.*

do not significantly differ between the two samples. Sample C622 has a high branching density which can result in a highly non-linear behaviour. In particular, it contains 30 arms in a backbone of 275 kg/mol, which corresponds to ∼10 arms/1000 monomers, while for C722 a ∼4 arms/1000 monomers branching content can be estimated. Shorter relaxation times attributed to branches are found for C722 by Roovers and Graessley [Roovers 81] in comparison with C622. The authors suggested that the larger branch spacing of C722 (lower branch density) may provide greater possibility for local cooperation between backbone and branches. Daniels et al. [Daniels 01] additionally state that the effective friction of a comb, taking into account the tube model, varies with the arm number, N_{arms}, and not the backbone length (especially for combs with a high N_{arms}). If the friction can be considered as one reason for a highly non-linear rheological behaviour, then one can explain the underestimation of non-linearities for both comb melts by the DCPP model, since the friction in a pom-pom molecule is concentrated at the two branch points. This is in contrast with the case of combs with a distribution of these friction points (possibly responsible for non-linear behaviour) along the backbone.

However, sample C722 has a total M_w two times higher than C622. In the study of linear polystyrene melts, it was shown that the non-linear behaviour depends strongly on M_w and specifically, a presence of material with high M_w causes an increase in $I_{3/1}(\gamma_0)$ and $\Phi_3(\gamma_0)$ (see fig. 3.14, 3.15). A possible explanation for the similarly high non-linearity of the two

combs is that it is a result of two factors, the total molecular weight which leads to highly elastic behaviour and the number of branches per monomer, in other words the branching density. A better discrimination can possibly be achieved when comparing the samples for the same *De*, or accordingly the same tan δ, where both have the same dominantly viscous, or dominantly elastic flow behaviour.

Another important point is the length of the side-arms with respect to the entaglement molecular weight (M_e = 18 kg/mol), which corresponds to $M_a/M_e \leq 1$. This means that the specific arms are unentangled or contain maximum one entanglement. Thus, they can relax in a much faster timescale than the backbone, as described also in the Pom-pom model [McLeish 98]. The effect of these short branches on the rheological behaviour of the sample is not simple. They act as topological constrains for the reptation of the backbone due to the existence of multiple branch points in the backbone, since their length is comparable with the tube diameter. However, we can assume that due to their Rouse-like relaxation process they act also as plasticizers for the macromolecule [Inkson 99, McLeish 98].

In order to elucidate differences of the non-linear rheological behaviour of the two stud-

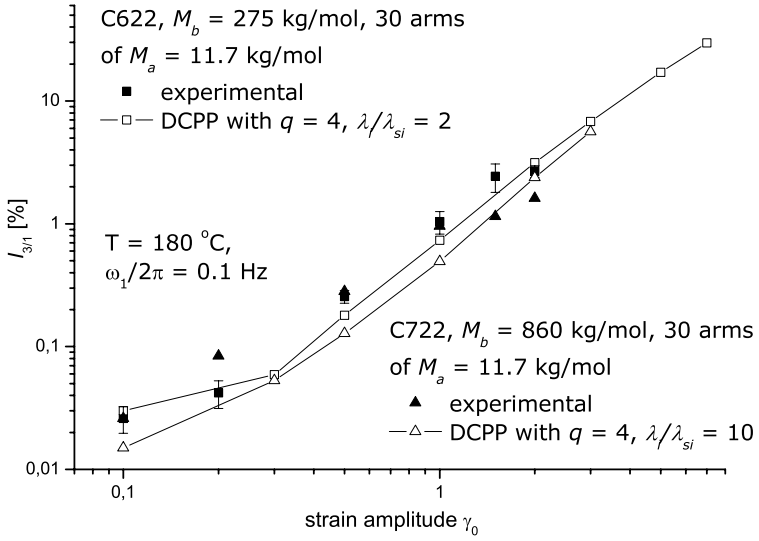

Figure 3.30: *Predicted $I_{3/1}(\gamma_0)$ for polystyrene comb melts C622, and C722. LAOS performed with $\omega_1/2\pi$ at T = 180 °C. Experimental data at the same conditions [Höfl 06].*

ied comb melts, measurement and simulations are performed for conditions corresponding to different *De* numbers. The resulting $I_{3/1}$ and Φ_3 as a function of *De* for the combs C622 and C722 are presented in fig. 3.32 and 3.33 along with the predicted values from the DCPP model.

The comb with the lower branch density and higher total M_w C722, has a relatively stable $I_{3/1}(De)$ and agreement is found between measured and predicted data. The predicted

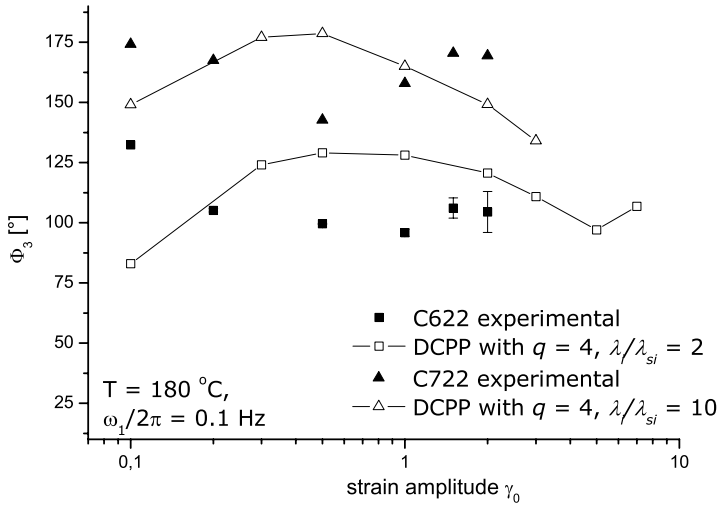

Figure 3.31: *Predicted $\Phi_3(\gamma_0)$ for polystyrene comb melts C622, and C722. LAOS performed with $\omega_1/2\pi$ at T = 180 °C. Experimental data at the same conditions [Höfl 06].*

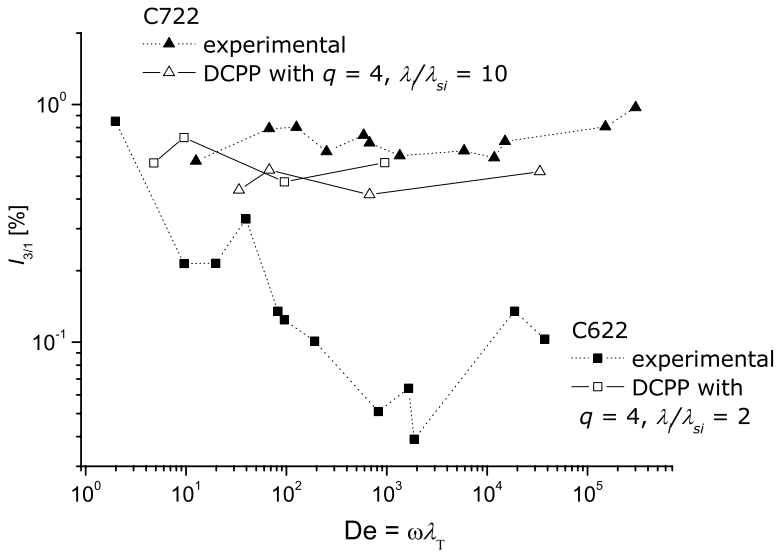

Figure 3.32: *Measured and predicted $I_{3/1}$(De) for polystyrene comb melts C622, and C722. LAOS performed with γ_0 = 1. Large differences between predictions and experimental data may be due to the utilized open-rim geometry, e.g. high normal forces, meniscus distortions [Höfl 06].*

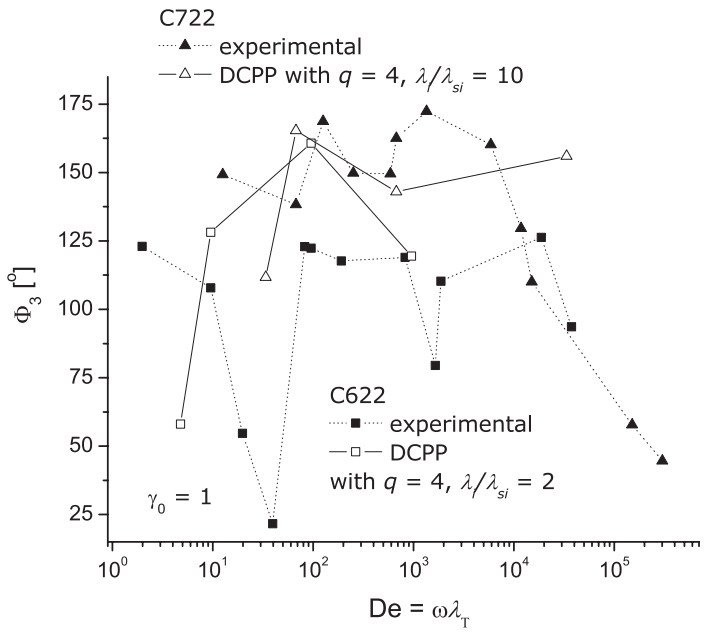

Figure 3.33: *Measured and predicted $\Phi_3(De)$ for polystyrene comb melts C622, and C722. LAOS performed with γ_0 = 1. Large differences between predictions and experimental data may be due to the utilized open-rim geometry, e.g. high normal forces, meniscus distortions [Höfl 06].*

$\Phi_3(De)$ are between 150-170°C for a broad range of Deborah numbers and close to the experimentally measured phases. Only at $De > 10^4$ a drop of the Φ_3 is experimentally observed and not captured by the DCPP model. For the case of C622 with the higher branch density, the DCPP does not fit the measured decrease of the nonlinearities for increasing elastic character of the flow (increasing *De*) and predicts a relatively stable $I_{3/1}(De)$ instead. However, the experimental data suffer from low reproducibility for the specific case of melts [Höfl 06]. This can account for the large differences between the predictions from LAOS simulation, especially in the region of dominant elastic behaviour for the C622.

It would be meaningful to study well-defined comb structures with longer side-arms, in order to elucidate the effect of arm entanglement and relaxation in the non-linear rheological behaviour of polymer melts. Samples available that could fulfill this condition are the already studied solutions, C732, C742 and C642. However, they are diluted in solvent and their number of entanglements is therefore dramatically reduced. Additionally, the interactions with the solvent may need to be taken into account. Hence, the conclusions derived from the study of model-samples in solutions are not binding for the case of melts, for which the rheological behaviour can differ significantly.

Chapter 4

Detection and quantification of long-chain branching in industrial polyethylenes

4.1 Application on industrial polydisperse polyethylene melts of different topologies

4.1.1 Long-chain branching in industrial polyethylene-short literature review

The controlled size and distribution of sparse long-chain branching (LCB) is crucial for the industrial processing of polyolefines and in particular polyethylene. Although polyethylenes with linear topology and low polydispersity posses desirable physical properties, they often suffer from poor processability [Janzen 99, Fetters 99, Read 01]. The introduction of LCB into the polymer affects its rheological behaviour and its end-use properties [Gabriel 99]. This enhanced processability originates from LCB where the side-chain length exceeds the entanglement length. Long-chain branched polyethylenes present increased melt strength and shear-thinning behaviour compared to linear low-density polyethylenes (LLDPE). Short-chain branching (SCB) dominantly affects the morphology and solid-state properties of semi-crystalline polymers, in particular crystallinity. It is well established that LCB increases viscosity and shear-thinning behaviour under shear flow (with respect to the slope of the shear-rate dependent viscosity at high shear rates) and strain hardening under elongation flow [Münstedt 98, Vega 98, Lohse 02, Malmberg 02]. Consequently, characterization techniques are needed that can detect sparse LCB content (e.g. 0.1 LCB/1000 CH_2) and distinguish short ($M_{branch} < M_e$) and long ($M_{branch} > M_e$) branched structures.

Bersted [Bersted 85] studied the effects of very low LCB levels (calculated as low as 0.01 LCB/1000 CH_2) on the rheological behaviour of high density (HDPE) and low density polyethylenes (LDPE). Long-chain branching was introduced by peroxide decomposition, thermal-mechanical degradation and free radical polymerization. The author observed large

variations of the zero-shear viscosity, η_0, with the degree of branching and related them to the relative amount of linear and branched species. An increase in η_0 with increasing branching up to a maximum of 0.25 LCB/1000 CH_2, as measured by ^{13}C nuclear magnetic resonance (NMR), was observed for PE samples with $M_w \approx$ 120-130 kg/mol. This maximum value of η_0 was rationalized as the result of two competing effects: the increase in amount of high-viscosity branched species, at low LCB content, and the reduction of the mean square gyration radius, at high LCB. The LCB content corresponding to a maximum η_0 was shifted to higher LCB/1000 CH_2 with increasing molecular weight. Vega et al. [Vega 98] used a shear thinning index (scaling exponent) from the Briedis and Faitel'son equation [Briedis 76] for quantifying the severity of the shear-rate viscosity dependence. The shear thinning parameter increases (from 0.5 for a linear PE to 0.75) with the severity of pseudoplasticity, and thus reflects the change in polydispersity, molecular weight and LCB content. Increased flow activation energy, E_a, of LCB samples up to $E_a \approx$ 40 kJ/mol was observed, while linear PE of same SCB degree had $E_a \approx$ 30 kJ/mol. It was shown that pseudoplasticity and activation energy depend on the length and concentration of branches. The distribution of branch length and LCB concentration was found to be an additional factor affecting pseudoplasticity and activation energy [Mavridis 92, Vega 98]. However, Vega et al. [Vega 98] stated that polydispersity masks the effects of LCB on the onset of shear thinning and flow activation energy. The same authors used dynamic and capillary extrusion rheometry, gel-permeation chromatography (GPC) and ^{13}C NMR for characterising metallocene-catalysed LDPE and HDPE. Lower Newtonian viscosities and higher critical shear rate $\dot{\gamma}$ (shear thinning onset) were observed for PE with high LCB, as compared to linear samples of the same molecular weight. The authors concluded that the molecular parameters as obtained by GPC and ^{13}C NMR are not sufficient to categorize samples into linear, low LCB (typically 0.1 LCB/1000 CH_2) and high LCB (typically 1 LCB/1000 CH_2), thus additional characterization is needed.

Yan et al. [Yan 99] measured rheological properties of PE with LCB as low as 0.044 LCB/1000 CH_2, as measured by ^{13}C NMR. The authors concluded that sparse branched structures resulted in higher viscosities at low shear rates, and lower viscosities at high shear rates. Additionally, increased LCB lead to longer rheological relaxation times and lower ratios of loss to storage moduli, tan $\delta = G''/G'$, at the terminal zone. Wood-Adams and Dealy [Wood-Adams 00] determined molecular weight distribution and quantified the level of branching in PE produced by a constant geometry catalyst. For this purpose, complex viscosity plotted against frequency combined with GPC and NMR were used. Results showed that an increase of the molecular weight distribution as quantified by the polydispersity index (*PDI*) and an increase of branching have similar effects on η_0.

Polyethylenes with well-defined variations in LCB and topology (linear, stars, combs, H-shaped) were investigated by Lohse et al. [Lohse 02]. The type of branched structure was described using the following variables: functionality of branching point (tri-, tetra-functional), branch length, separation between branches per backbone and the distribution of all the above. The authors concluded that polymers with a single or multiple branches

per chain show experimentally a greater degree of shear thinning than linear chains. Only multiple branched molecules exhibited extensional thickening. A small amount of comb-like molecules in the polymer on the order of 5% could induce this effect. The characterization of LCB polyethylene by creep recovery, dynamic mechanical measurements and elongation flow has been extensively investigated by Münstedt and coworkers [Laun 78, Münstedt 81, Gabriel 98, Gabriel 99, Gabriel 02, Malmberg 02, Münstedt 98]. Münstedt and Laun [Münstedt 81] already reported a strong correlation between elongational viscosity and molecular structure of LDPE, namely polydispersity and CH_3/1000 CH_2 content, following the method presented by the authors earliear [Laun 78]. Gabriel et al. [Gabriel 02] measured SCB and LCB mPE with 0.12 LCB/1000 CH_2 as determined by ^{13}C NMR. Malmberg et al. [Malmberg 02] quantified LCB degree using the fraction of LCB junction points calculated according to the method of Janzen and Colby [Janzen 99] as a branching parameter. Samples with a minimum relative LCB content of 9.7×10^{-7} (as determined by the above method) were measured in this study. Elongation experiments demonstrated the strain hardening for LCB polyethylene. Dynamic mechanical measurements were also performed from the rubbery plateau region to the transition zone. The main focus was in the use of zero shear viscosity, η_0, and the radius of gyration, as two relevant parameters to differentiate linear from branched polyethylenes. In their study radius of gyration was measured by multi-angle laser light-scattering (MALLS). Trinkle et al. [Trinkle 01, Trinkle 02] investigated the LCB content by using the so-called van Gurp-Palmen plots. This method consists of plotting the phase lag δ of the stress response in an oscillatory shear measurement plotted against the absolute values of the complex modulus $\mid G^* \mid$. This type of analysis is currently widely used for detecting LCB [Fleury 04, Lohse 02, Malmberg 02, Trinkle 01, Trinkle 02, Vega 99]. Additionally, the δ versus G^* plot was combined with the molecular weight distribution to create and algorithm that can classify polydisperse branched polymers according to their topology [Schulze 05].

From the above review, one can argue that a large part of the research on the rheological properties of LCB polyethylene focused mainly on the linear viscoelastic regime. However, non-linear mechanical conditions are most common in polymer processing. The application of large amplitude oscillatory shear (LAOS) is a simple method to characterize and quantify the non-linear regime [Cho 05, Gamota 93, Giacomin 98, Hyun 02], as already discussed in the previous chapters. Within this chapter, FT-Rheology is applied to study industrial polyethylenes. The intensity $I_{n/1}$ and phase Φ_n of the higher harmonics are afterwards correlated with structural and rheological properties. Fleury et al. [Fleury 04] used FT-Rheology for characterizing LCB in a wide set of polyethylene topologies and compared it with what they define as chain orientation/relaxation experiments and GPC. When comparing linear and branched industrial polyethylenes, distinct differences were seen between the relative intensities and phases of the higher harmonics in the FT-spectrum, indicating that FT-Rheology is sensitive to LCB.

Large amplitude oscillatory shear flow of linear HDPE melts has been investigated using

the Giesekus constitutive model by Debbaut and Burhin [Debbaut 02]. The FT-Rheology method was applied for both experimental measurements and simulations. This work demonstrated the applicability of FT-Rheology and LAOS in combination with viscoelastic simulation for the study of industrial polyethylene materials. However, as already discussed in chapter 2 and demonstrated in chapter 3, the Giesekus model does not include any parameter explicitly related to the molecular architecture, which could be appropriate for modelling polyolefines with branched topologies.

In chapter 2 and specifically in paragraph 2.2 there is an introduction to LAOS simulations and a literature review on the use of constitutive models to describe flow of polymer melts with complicated architecture. Thus, in the present chapter the results of the application of the method introduced in chapter 2 will be directly presented, concerning the finite element simulations, as for the case of PS combs studied in chapter 3.

Furthermore Schlatter et al. [Schlatter 05] utilized the Cole-Cole plots complementary to FT-Rheology to asses the polymer architecture of industrial PE. The Cole-Cole plot consists of plotting the loss viscosity, η'', against the storage viscosity η', both derived from frequency sweep measurements in the linear regime. The shape of the resulting curve is affected by the molecular weight distribution and the presence of LCB.

It must be noted that in the present thesis the work of Fleury et al. [Fleury 04] and Schlatter et al. [Schlatter 05] is extended in several ways. First, shear-strain γ_0 up to 10 is applied in two specific setups where excitation frequencies vary between 0.01 Hz and 5 Hz. In order to achieve this, the results from the two rheometers, ARES and RPA2000, are combined. The latter allows a very stable response even at very high γ_0 due to the closed double-cone geometry. Higher sensitivity is achieved for both rheometers by applying the oversampling technique in combination with a low torque transducer [Hilliou 04, Wilhelm 99]. Due to the wide range of experimental conditions, optimum measurement conditions for detecting LCB in industrial PE are evaluated. This optimisation includes excitation frequency, applied strain amplitude, temperature and geometries for LAOS. The analysis via FT-Rheology variables $I_{3/1}$, Φ_3 and the relative phase at low strains, Φ_3^0 ($lim_{\gamma_0 \to 0}\Phi_3$), with respect to the ability to differentiate between branching topologies is also included. To further extend the work of Schlatter et al. [Schlatter 05], higher molecular weight industrial polyethylene samples are investigated. The effect of normal forces which are prominent in this case, can be minimized using the closed cavity geometry of the RPA2000 rheometer. The samples vary in terms of branching topology, i.e. linear, SCB and LCB, comonomer content, molecular weight and molecular weight distribution and they consist of linear low-density (LDPE), high-density (HDPE) and metallocene-catalyzed (mLDPE) polyethylenes (see fig. 1.1 for possible topologies).

4.1.2 Investigated materials

Fifteen samples are investigated. Eleven industrial polyethylenes are supplied by TOTAL, Feluy Belgium, while four polyethylenes are provided by Prof. Münstedt, Institute of Polymer Materials, Erlangen Germany. The latter consist of two industrial samples referred to as mLLDPE and LCBmLLDPE in the present thesis, respectively correspond to mLLDPE4 and mLLDPE3 in Gabriel and Münstedt [Gabriel 99] and two linear metallocene polyethylenes L114_16 and L120_2 respectively correspond to C2 and C3 in the work of Stadler et al. [Stadler 05]. The nomenclature used consists of the topology, the M_w and the PDI of the sample.

For measurements on the ARES rheometer, melt sample disks of 13 mm diameter and 1 mm thickness are pressed, at 150 °C and 20 bars in a Weber hydraulic press under vacuum. All measurements are performed under a nitrogen atmosphere to prevent sample oxidation. Although no special sample treatment is needed for the RPA apparatus, it should be noted that 3.5 g - 4 g of sample are needed for each experiment.

4.1.3 Application of SAOS and LAOS

In order to quantify the linear regime, linear viscoelastic properties are measured for all samples, between 120 °C and 180 °C. For the investigated polyethylenes a comparison between the open-rim ARES geometry and RPA2000 shows a deviation of less than 5% for tan δ. Figures 4.1 and 4.2 show, as an example, the storage and loss moduli at T = 180 °C for two linear and three branched samples.

Subsequently, LAOS is applied in order to study the non-linear regime. Figure 4.3 illustrates a typical stress time signal for a LCB sample from LAOS experiments performed at 0.1 Hz and γ_0 = 10. Fourier transformation is then applied and the resulting spectrum is shown in fig. 4.4, where the higher odd harmonic at $9\omega_1/2\pi$ is still approximately a factor of 10 above the noise level. The measured $I_{3/1}(\gamma_0)$ and $\Phi_3(\gamma_0)$ for a linear (mLLDPE) at 0.6 Hz and 180 °C and a branched (LCBmLLDPE) at 0.012 Hz and T = 180 °C (both at tan δ = 5), are displayed in fig. 4.5. The strain amplitude range is the maximum possible applied in our experimental setup and is achieved by combining the overlapping results from ARES and RPA2000 rheometers, as demonstrated in fig. 3.12 and 3.13.

All investigated melts are induced in LAOS with strain sweep measurements undertaken for $0.5 < \gamma_0 < 10$. The results show an influence of the molecular weight and molecular weight distribution on the non-linear behaviour of the studied polyethylenes. Generally high molecular weight samples exhibit higher non-linearities, as already seen for polystyrene model systems in chapter 3. Thus, in order to see the influence of LCB on $I_{3/1}$ and Φ_3, samples of similar M_w and *PDI* are compared. Figure 4.6 depicts $I_{3/1}$ and Φ_3 for LAOS at 0.1 Hz and 180 °C, for samples with *PDI* $\approx$ 2.

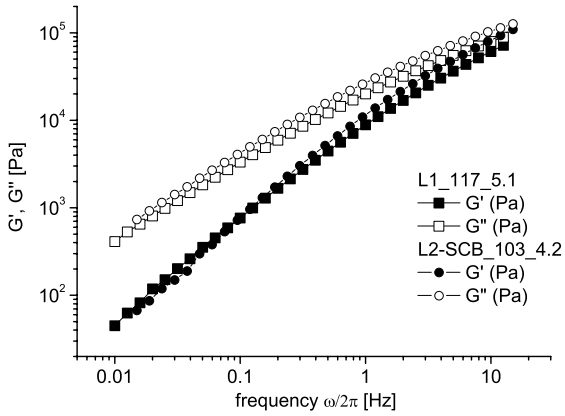

Figure 4.1: *Storage and loss moduli, G' and G'', for linear polyethylenes L1_117_5.1 and branched L2_SCB_103_4.2 at T = 180 °C.*

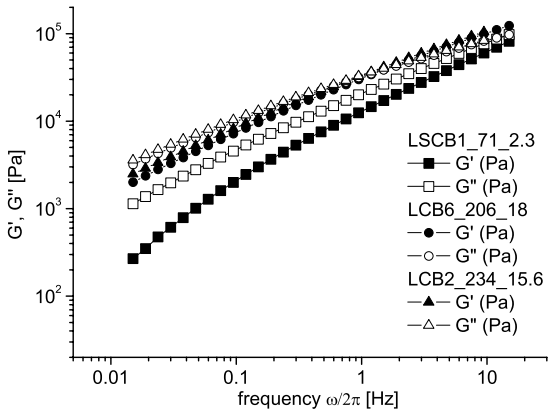

Figure 4.2: *Storage and loss moduli, G' and G'', for LCB samples LSCB1_71_2.3, LCB2_234_15.6 and LCB6_206_18 at T = 180 °C.*

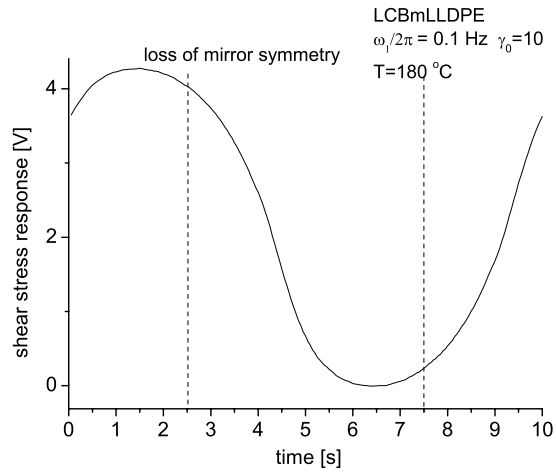

Figure 4.3: *Stress response time signal, for LCBmLLDPE under LAOS with $\omega_1/2\pi$ = 0.1 Hz, γ_0 = 10 at T = 180 °C.*

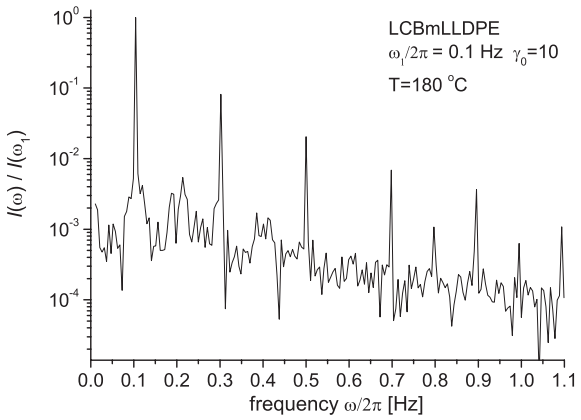

Figure 4.4: *Fourier-Transform spectrum for LCBmLLDPE under LAOS with $\omega_1/2\pi$ = 0.1 Hz, γ_0 = 10 at T = 180 °C.*

Samples top._M_w_PDI	M_w (kg/mol)	M_w/M_n	**comonomer**	**Est. topology**	**LCB+SCB** $>C_4$/1000 CH_2
L114_16	114	16.0	no	Linear	-
mLLDPE	116	1.9	butene	Linear	-
L1_117_5.1	117	5.1	no	Linear	0.0
L120_2	120	2.0	no	Linear	-
SCB2_59_2.1	59	2.1	yes	SCB	4.5
SCB1_100_2.7	100	2.7	yes	SCB	2.1
mPEmix0	135	2.0	octene	Linear-SCB	66.3
L2-SCB_103_4.2	103	4.2	butene	Linear-SCB	22.1
LSCB1_71_2.3	71	2.3	octene	LCB and SCB	18.9
LCBmLLDPE	94	2.1	octene	LCB-SCB	25.2
LCB1_123_7.1	123	7.1	no	LCB	0.2
LCB4_145_8.6	145	8.6	yes	LCB-low SCB	0.8
LCB3_199_19	199	19.0	very low	LCB-low SCB	0.5
LCB6_206_18	206	18.0	yes	LCB-low SCB	0.9
LCB5_210_20.4	210	20.4	yes	LCB- low SCB	0.6
LCB2_234_15.6	234	15.6	very low	LCB	0.5

Table 4.1: *Investigated polyethylene samples.Weight-average molecular weight, M_w and polydispersity, M_w/M_n, as given by GPC. Estimation about topology and presence of comonomer is given. Level of LCB + SCB(>C 4)/1000 CH2 is measured by melt-state ^{13}C NMR for all samples. It is the total number of all branches (SCB and LCB) of 4 carbons side-chain and longer and thus representing an upper limit of LCB. No NMR results are given for L114_16, mLLDPE and L120_2.*

The PE samples shown in fig. 4.6 have narrow and comparable molecular weight distributions. Polyethylenes containing LCB exhibit marked non-linearities ($I_{3/1}$) over the entire range of studied strain amplitude (also for $\gamma_0 < 3$, see fig. 4.7). The relative phases (Φ_3) are converging to a common plateau at high strain amplitudes. The differences observed between linear and LCB are still larger than the reproducibility range of the measurements and the same trends are found for samples of a higher *PDI* and M_w, as can be seen in fig. 4.8.

A comparison of FT-Rheology results between linear, SCB and LCB is made for samples with similar M_w but varying *PDI*. Considering the weight-average molecular weight, the samples are sorted into two groups of $M_w \approx 100$ kg/mol and of $M_w \approx 200$ kg/mol. The resulting intensities and phases of the third harmonic at 0.1 Hz and 180 °C are presented in fig. 4.9 for all samples with $M_w \approx 100$ kg/mol. All measurements are repeated at a lower temperature of 140 °C. A similar trend of separation between linear and LCB is generally observed. As an example, results for $M_w \approx 100$ kg/mol at 140 °C are presented in fig. 4.10. It can be concluded that temperature, in the range of 140 °C -180 °C, is not an important parameter for the case of PE.

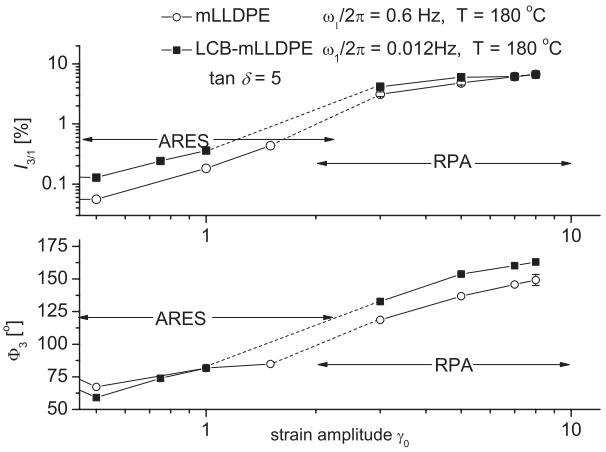

Figure 4.5: *$I_{3/1}(\gamma_0)$ and $\Phi_3(\gamma_0)$ measured at 0.6 Hz and 180 °C for mLLDPE and at 0.012 Hz and 180 °C for LCBmLLDPE, in ARES and in RPA2000. Measurement conditions correspond to tan δ = 5 in the linear regime.*

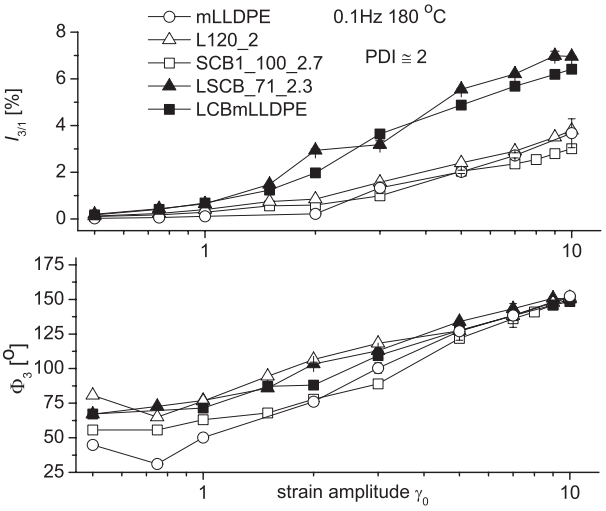

Figure 4.6: *$I_{3/1}$ and Φ_3 as a function of strain amplitude γ_0, at temperature 180 °C and frequency 0.1 Hz, for polyethylenes with PDI $\approx$ 2.*

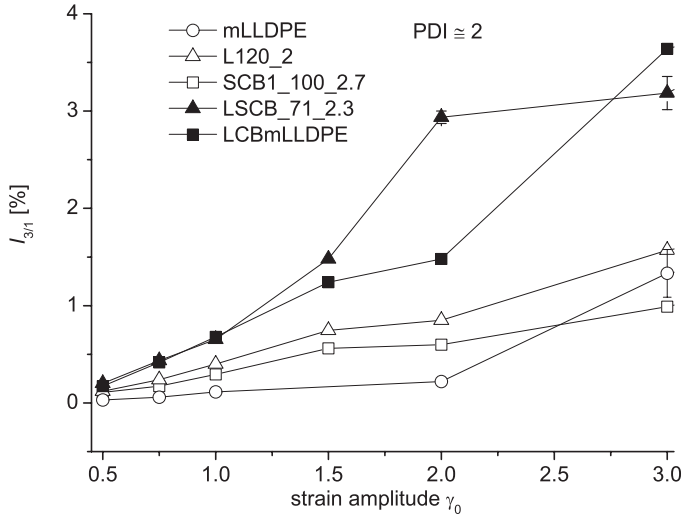

Figure 4.7: *Non-linearities for polyethylenes with PDI ≈ 2 at lower strain amplitudes.*

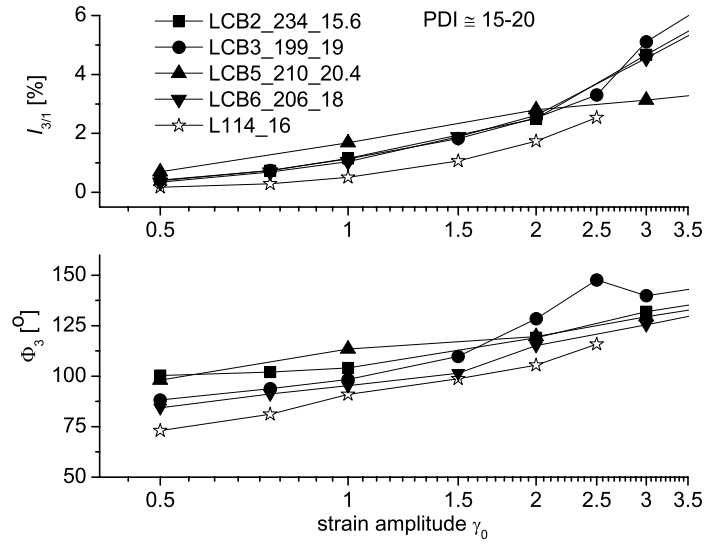

Figure 4.8: *$I_{3/1}$ and Φ_3 as a function of strain amplitude γ_0, at temperature 180 °C and frequency 0.1 Hz, for polyethylenes with PDI ≈ 15-20.*

Consequently, LCB polyethylenes are compared with respect to the detected non-

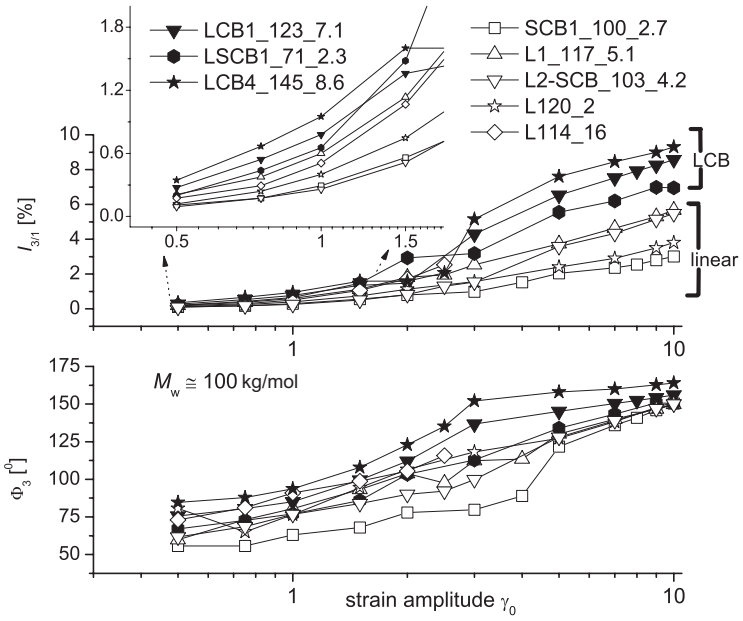

Figure 4.9: *$I_{3/1}$ and Φ_3 as a function of strain amplitude γ_0, at temperature 180 °C and frequency 0.1 Hz, for polyethylenes with $M_w \approx$ 100 kg/mol.*

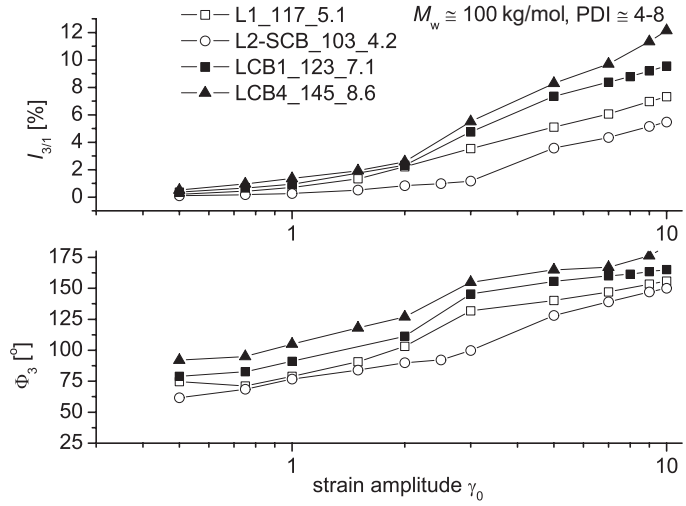

Figure 4.10: *$I_{3/1}$ and Φ_3 as a function of strain amplitude γ_0, at temperature 140 °C and frequency 0.1 Hz, for polyethylenes with PDI ≈ 4-8.*

linearities arising from a strain sweep under LAOS conditions. The goal is to categorise them according to branching level. Thus, the measured $I_{3/1}(\gamma_0)$ is correlated with ^{13}C NMR data and given in fig. 4.11 and 4.12 for a group of LCB samples with low and high *PDI*

respectively. The branching levels determined via ^{13}C NMR for these commercial samples are listed in Table 4.1. All branching quantifications are given as LCB + SCB of more than 4 carbons, LCB + SCB ($> C_4$)/1000 CH_2, and this represents the maximum possible branching content of the sample, since NMR spectroscopy cannot differentiate side-chain length of 6 and more carbons.

The effect of LCB on non-linear shear behaviour of PE is shown in fig. 4.11 and 4.12.

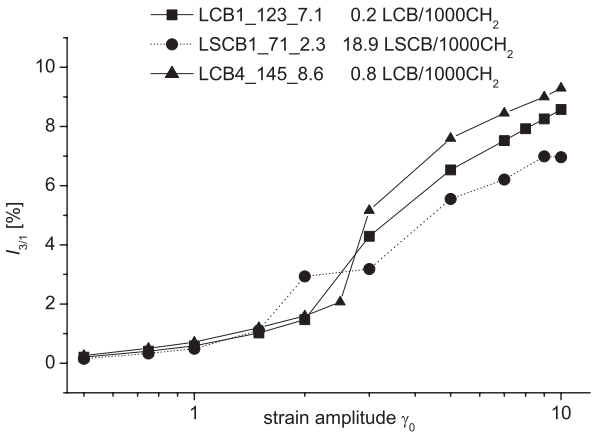

Figure 4.11: *$I_{3/1}$ as a function of strain amplitude γ_0, at temperature 180 °C and frequency 0.1 Hz, for LCB PE with low PDI.*

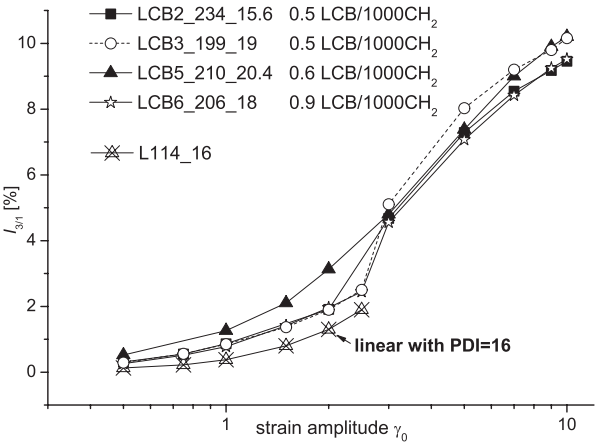

Figure 4.12: *$I_{3/1}$ at temperature 180 °C and frequency 0.1 Hz, for LCB PE with high PDI and M_w ≈ 200 kg/mol.*

When comparing LCB polyethylenes with similar polydispersity index (of low or high *PDI*), we find that higher branching level can lead to stronger non-linearity. All experimentally measured $I_{3/1}(\gamma_0)$ can be fitted with eq. 1.47. The results for parameters *A*, *B*, and *C* are listed in Table 4.2. From the limited number of samples, we see that the non-linearity plateau *A*

shows a maximum value for LCB around 0.8 LCB + SCB ($> C_4$)/1000 CH_2 for a group of materials with $M_w \approx 100$ kg/mol, as presented in fig. 4.13 for the studied PE samples. For higher molecular weights ($M_w \approx 200$ kg/mol), the maximum value of parameter *A* is found for a branching level of 0.5 LCB + SCB ($> C_4$)/1000 CH_2. At very large strain amplitudes (typically $\gamma_0 > 7$) $\Phi_3(\gamma_0)$ converges to a plateau. For the above LCB contents at 0.1 Hz and 180 °C, the maximum value of this plateau is approximately 150° -170° (see fig. 4.6, 4.8, 4.9).

In an effort to separate the effects of molecular weight, molecular weight distribution

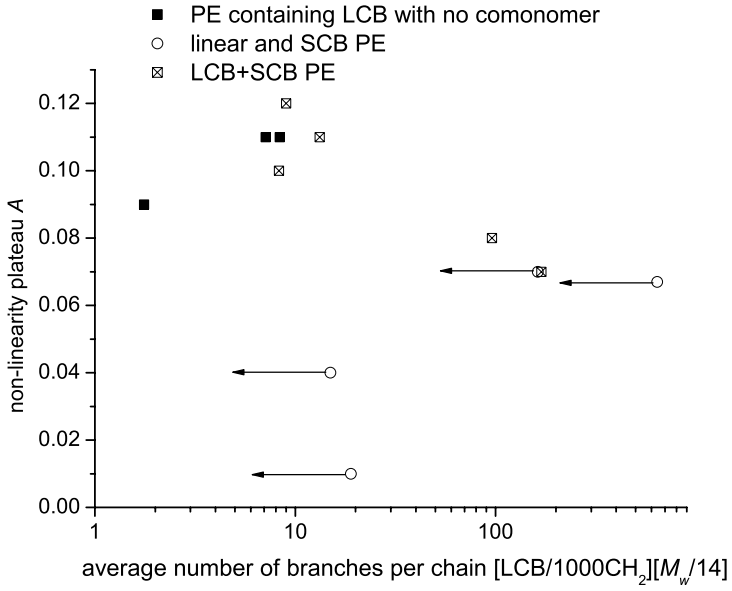

Figure 4.13: *Non-linearity plateau, A, as a function of the absolute number of LCB per polyethylene chain. Open symbols can be shifted to significantly smaller values in the x-axis, since the number of branches refers also to SCB.*

and LCB, we analyze $I_{3/1}(\gamma_0)$ fitted with eq. 1.47, for all available linear and SCB samples. Parameters *A*, *B*, and *C* are correlated to M_w and *PDI* only, since the topology is assumed to be linear. Hence the dependence of these experimental parameters with respect to molecular weight distribution can be empirically described for PE at T = 180 °C and $\omega_1/2\pi$ = 0.1 Hz as follows:

$$\begin{aligned} A &= 0.013 + 3.0 \times 10^{-4} M_w + 2.9 \times 10^{-3} PDI \\ B &= 0.08 + 8.7 \times 10^{-4} M_w + 4.6 \times 10^{-3} PDI \\ C &= 2.47 - 7.0 \times 10^{-3} M_w + 2.1 \times 10^{-2} PDI \end{aligned} \tag{4.1}$$

Samples top.-M_w-PDI	A	B	C
L114_16	0.09	0.25	2.0
mLLDPE	0.05	0.15	1.7
L1_117_5.1	0.07	0.23	1.7
L120_2	0.05	0.20	1.7
SCB2_59_2.1	0.01	0.16	2.5
SCB1_100_2.7	0.04	0.20	1.7
mPEmix0	0.07	0.24	1.75
L2-SCB_103_4.2	0.07	0.19	2.0
LSCB1_71_2.3	0.08	0.30	1.7
LCBmLLDPE	0.07	0.29	1.9
LCB1_123_7.1	0.09	0.30	2.1
LCB4_145_8.6	0.10	0.30	2.5
LCB3_199_19	0.11	0.29	2.1
LCB6_206_18	0.11	0.27	1.7
LCB5_210_20.4	0.12	0.26	1.7
LCB2_234_15.6	0.11	0.28	1.8

Table 4.2: *Parameters A, B and C for LCB samples, derived by fitting $I_{3/1}(\gamma_0)$ experimental data at T = 180 °C and $\omega_1/2\pi$ = 0.1 Hz with eq. 1.47.*

where M_w is given in kg/mol. Consequently $I_{3/1}(\gamma_0)$ of linear and SCB polyethylenes can be empirically expressed as:

$$I_{3/1}(\gamma_0) = (0.013 + 3.0 \times 10^{-4} M_w + 2.9 \times 10^{-3} PDI) \left(1 - \frac{1}{1 + ((0.08 + 8.7 \times 10^{-4} M_w + 4.6 \times 10^{-3} PDI)\gamma_0)^{(2.47 - 7.0 \times 10^{-3} M_w + 2.1 \times 10^{-2} PDI)}}\right) \quad (4.2)$$

A demonstration of this capability to fit the non-linearities of linear polydisperse PE is given in fig. 4.14, where the measured $I_{3/1}(\gamma_0)$ is presented for L120_2 and L114_16, along with predictions derived from eq. 4.2, for these specific values of M_w and *PDI*.

Furthermore, the frequency dependence of the FT-Rheology parameters is investigated. The resulting $\Phi_3(\omega)$ is depicted in fig. 4.15, at γ_0 = 3. The phase of the third harmonic is derived from the stress response at a frequency range of 0.01 Hz -1 Hz. Linear and LCB samples have similar polydispersity (*PDI* $\approx$ 2) and molecular weight ($M_w \approx$ 100 kg/mol). At lower frequencies ($\omega_1/2\pi < 0.2$ Hz) LCB results in a higher Φ_3. However, for excitation frequencies above 0.2 Hz, linear PE samples present an increasing Φ_3 which can exceed that of LCB PE. At higher excitation frequencies only minor discrimination is achieved.

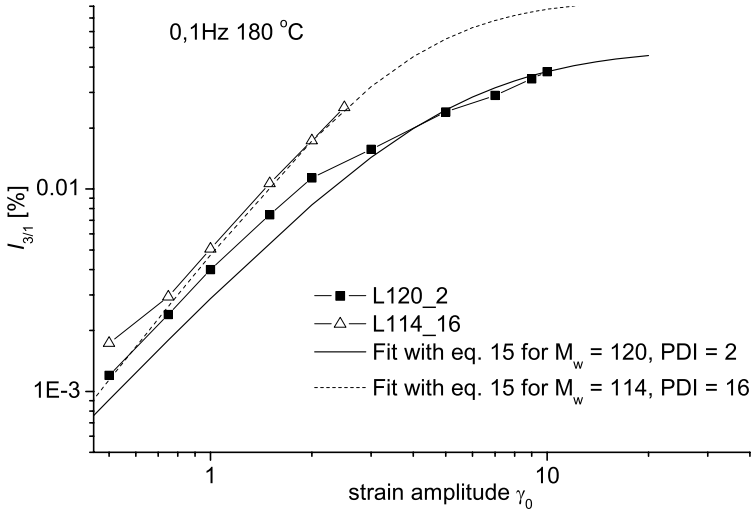

Figure 4.14: *Measured and predicted $I_{3/1}(\gamma_0)$ from eq. 4.2 for linear polyethylenes with M_w = 120 kg/mol, PDI = 2 and M_w = 114 kg/mol, PDI = 16 respectively.*

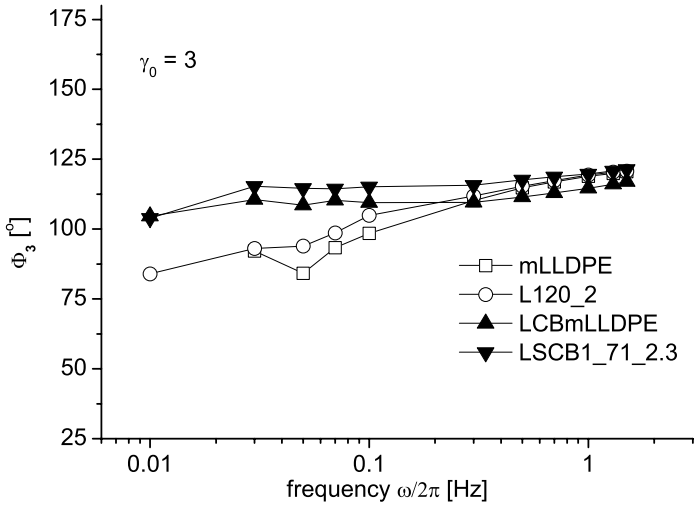

Figure 4.15: *Φ_3 as a function of excitation frequency, at temperature 180°C, γ_0 = 3 for linear and LCB polyethylenes of PDI $\approx$ 2 and $M_w \approx$ 100 kg/mol.*

4.1.4 FT-Rheology at low strain amplitudes and extension of van Gurp-Palmen method

For strain sweeps conducted at low γ_0, one can conclude that the measured $\Phi_3(\gamma_0)$ remains stable for low strain amplitudes. The relative phase Φ_3 at low strain amplitudes is sensitive to the presence of LCB. For γ_0 = 0.5, the noise level is still low enough for an accurate detection and quantification of non-linearity. This happens despite the fact that the measurement is performed approximately in the linear regime, if it is defined as the regime where G' and G'' are not yet affected beyond the reproducibility of rheological measurements, e.g. less than 10% change in moduli values. In this work we consider the measurement to be performed in the linear regime when $I_{3/1} < 1\%$. It is worth mentionning that purely linear rheology is an approximation, albeit highly accurate and in fact, materials will always respond in a non-linear fashion. FT-Rheology offers the advantage to quantify the occurring non-linearity at an early stage.

As seen in strain sweep measurements, in most cases $\Phi_3(\gamma_0)$ for polyethylenes reaches a plateau value of 150° -170° at high γ_0 when strain sweeps are preformed, as illustrated in fig. 4.6-4.10. This could suggest that Φ_3 is more appropriate for differentiating topologies at small strain amplitudes, e.g. $\gamma_0 < 1$. Furthermore, $\Phi_3(\gamma_0)$ levels off for $0.5 < \gamma_0 < 1$, where γ_0 = 0.5 is the lowest strain amplitude for which our optimised setup can still quantify reproducible non-linearities for the specific samples. Taking advantage of this lower plateau value Φ_3 measured at low strain is extrapolated to zero strain amplitude. In this limit Φ_3^0 ($lim_{\gamma_0 \to 0} \Phi_3 = \Phi_3^0$) can be an effective quantity for "fingerprinting" LCB.

The van Gurp-Palmen method consists of performing a frequency sweep in the linear regime and plotting δ (strain -stress phase lag in linear rheological regime) against the magnitude of the complex modulus, $\mid G^*(\omega) \mid$, normalized to the plateau modulus, G_N^0 [Trinkle 02]. This method is extended to include the non-linear information and the phase of the third harmonic at vanishing strain amplitude, Φ_3^0. Measurements are performed with the ARES rheometer, for a range of complex modulus $\mid G^* \mid$, and are displayed in fig. 4.16. When Φ_3^0 is plotted against $\mid G^*(\omega) \mid / G_N^0$, there is a clear discrimination between linear polyethylenes and LCB. Linear polyethylenes exhibit a Φ_3^0 lower than LCB for $\mid G^*(\omega) \mid / G_N^0$ up to 0.1. For higher moduli (or higher excitation frequencies) linear samples can exhibit a higher Φ_3^0. The same trends are shown also for samples of higher polydispersity (*PDI* of 5-8), in fig. 4.17. The measured Φ_3^0 plotted against Deborah number is displayed in fig. 4.18. Within this chapter, the Deborah number is defined as $De = \omega \lambda_T$, where ω is the angular frequency and λ_T is the characteristic relaxation time, defined by the lowest frequency where tan δ = 1. This characteristic time corresponds to the lowest inverse frequency ω_c where tan δ = 1, referred to as τ_d in chapter 1. The results are found to be reproducible (= $\pm$ 10°) for all sets of linear and branched samples.

Due to the importance of detecting LCB in PE, it is worth identifying the experimental conditions to obtain a maximum contrast between linear and LCB polyethylene towards the LAOS response. Long-chain branched polyethylenes present higher non-linearities for fre-

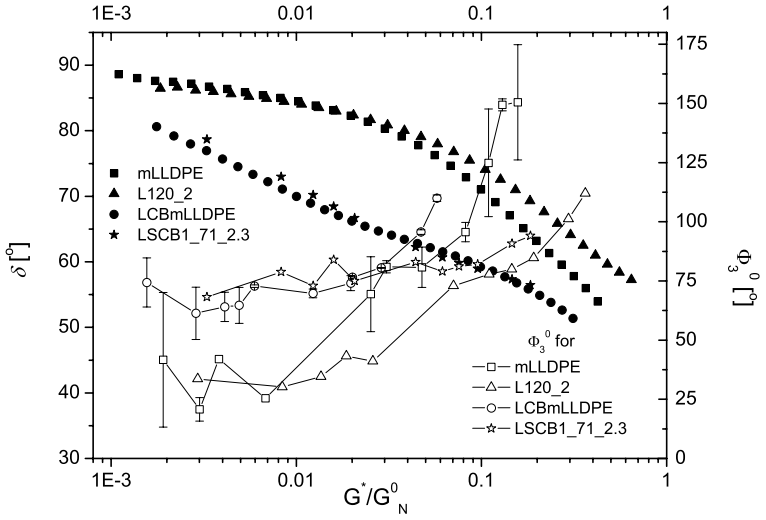

Figure 4.16: *Extended van Gurp-Palmen plot. Phase lag δ and zero-shear relative phase of 3rd harmonic, Φ_3^0, as a function of complex modulus normalized to plateau modulus, $|\ G^*\ |/G_N^0$, for LCB and linear polyethylenes of samples with PDI ≈ 2. G_N^0 values used: for mLLDPE 0.60 MPa, for L120_2 0.54 MPa, for LCBmLLDPE 0.59 MPa and for LSCB1_71_2.3 0.37 MPa.*

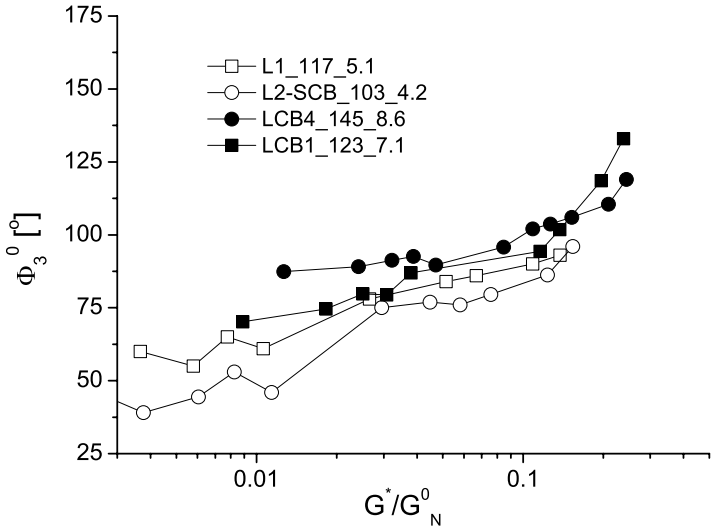

Figure 4.17: *Φ_3^0 as a function of complex modulus normalized by plateau modulus $|\ G^*\ |/G_N^0$, at T = 180 °C, for polyethylenes with PDI ≈ 5-8. G_N^0 values used: for L1_117_5.1 0.31 MPa, for L2-SCB_103_4.2 0.44 MPa, for LCB4_145_8.6 0.3 MPa and for LCB1_123_7.1 0.25MPa.*

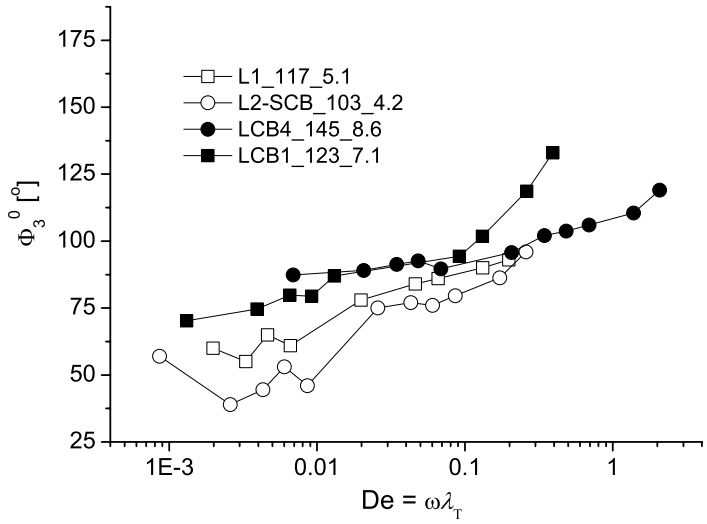

Figure 4.18: Φ_3^0 *at T = 180 °C versus Deborah number (*$De = \omega\lambda_T$*), for linear and LCB PE with PDI* $\approx$ *5-8.*

quencies and temperatures corresponding to the terminal zone of the linear spectrum as can be seen in fig. 4.19. This is also confirmed by measuring branched and linear samples at different tan δ. Results for two samples are presented in fig. 4.20. For increasing tan δ the $I_{3/1}$ of the LCB polyethylene exceeds that of the linear polymer and the difference between $I_{3/1,LCB}$ and $I_{3/1,linear}$ is larger.

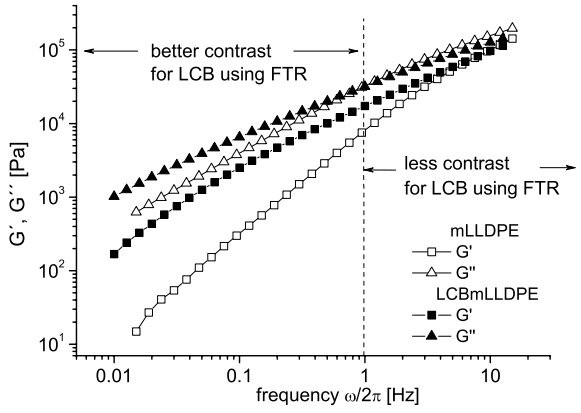

Figure 4.19: *Storage and loss moduli, G′ and G″ from dynamic mechanical measurement at T = 180 °C, for linear and branched polyethylenes, mLLDPE and LCBmLLDPE.*

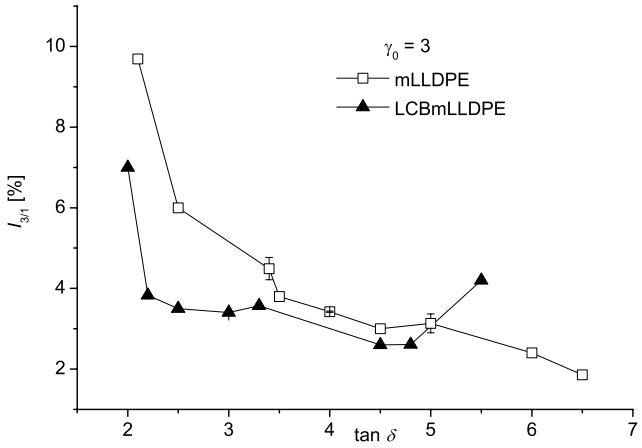

Figure 4.20: *$I_{3/1}$ for mLLDPE and LCBmLLDPE, γ_0 = 3, at different tan δ in the linear regime. Measurements performed with the RPA2000 rheometer.*

4.1.5 Influence of molecular weight and molecular weight distribution

It is well known that molecular weight and molecular weight distribution have a strong influence in the rheological properties of PE. According to Vega et al. [Vega 98] and Wood-Adams and Dealy [Wood-Adams 00], the effects of LCB on the rheological response can be masked by polydispersity and molecular weight. This statement is also true for the non-linear regime and the measured non-linearities via FT-Rheology, as already seen in chapter 3. Thus, it is crucial to separate the effects of an increased M_w and *PDI* from that of an increasing LCB content, with respect to $I_{3/1}$ and Φ_3.

Analyzing the non-linear behaviour of the linear and SCB samples, it is clear that higher M_w leads to higher non-linearity. It can also be seen that a broader molecular weight distribution (as quantified by *PDI*) leads also to an increased $I_{3/1}(\gamma_0)$ and $\Phi_3(\gamma_0)$. From eq. 4.2 with parameters M_w and *PDI* and assuming linear topology, $I_{3/1}(\gamma_0)$ can be predicted for all linear samples. The validity of this approach is demonstrated by the prediction of $I_{3/1}(\gamma_0)$ for two polydisperse linear polyethylenes (fig. 4.14).

When branching topology is introduced as a variable, the separation of the contributions of high molecular weight species and LCB structures in the non-linear behaviour becomes complicated. In order to overcome this, the samples are sorted and compared according to their *PDI* and M_w. Results show a predictable effect of M_w in the development of non-linearities (fig. 4.6-4.10). When the molecular weight and the distribution is known (i.e. M_w, *PDI*) and comparable for a set of investigated samples, LCB leads to an additional increase of $I_{3/1}(\gamma_0)$ and $\Phi_3(\gamma_0)$ at low frequencies (fig. 4.11, 4.12). The extended van Gurp-Palmen plot including Φ_3^0 can be used as another method to isolate the influences of LCB and molecular weight distribution (fig. 4.16 - 4.18). It must be noted that the experimental setup of the

RPA2000 allows reliable LAOS measurements of high molecular weight samples (up to M_w = 234 kg/mol with PDI up to ∼20 in our case) at large γ_0 where normal forces are prominent. The ability to minimize the effect of the resulting normal forces with the closed cavity in the RPA rheometer has a significant impact on the applicability of this method to high molecular weight materials.

4.1.6 Detection of LCB and correlation between NMR and FT-Rheology

The "fingerprinting" and characterization of LCB polyethylenes is a challenge which requires information obtained from several techniques and methods. For this reason, FT-Rheology results are correlated with ^{13}C melt-state NMR measurements. However, if the investigated polymer contains short-chain branches incorporated as comonomer, or formed by the catalyst, NMR may overestimate the degree of LCB. This is due to the fact that SCB of more than 6 carbons and LCB may not be distinguished in the resulting NMR spectra and their intensity sums up. Due to this inability of NMR to estimate whether a side-branch of more than 6 carbons is short ($M_{branch} < M_e$) or long ($M_{branch} > M_e$), the values obtained are related to the maximum possible degree of LCB only. This is illustrated by sample LSCB1_71_2.3 with 18.9 LCB/1000 CH_2. It is short-chain branched because of the presence of co-octene and the actual number of LCB could be significantly lower (see fig. 4.13). Another example involves samples with the same measured LCB/1000 CH_2 content (i.e. LCB2_234_15.6 and LCB3_199_19) which present different non-linear behaviour, as shown also in fig. 4.13. They have various low amounts of branching with more than 6 carbons. Thus, the actual LCB/1000 CH_2 may differ between them.

An additional parameter is the distribution and variation of branching in a LCB polyethylene, which cannot be directly measured with melt-state NMR or rheology. It is one of the key factors in the rheological behaviour [Lohse 02] and gives an additional possible explanation to differences in $I_{3/1}$ and Φ_3 observed between polyethylenes with the same measured LCB/1000 CH_2 content. Another example is L2-SCB_103_4.2 which has no rheologically detected LCB, but via NMR is found to have a high degree of co-butene incorporation (SCB). However, whether the comonomer affects the chemical reaction of LCB formation in the system is under discussion [Stadler 05].

Long-chain branching increases the non-linearity, as quantified by $I_{3/1}$ and Φ_3. However, for a branching level above a specific LCB/1000 CH_2 we can expect that non-linearities are decreasing. This could follow the behaviour described theoretically [Bersted 85] and experimentally [Vega 98, Vega 99] for the case of zero-shear viscosity. For LCB contents above a specific level, the effect from the decrease in radius of gyration becomes dominant and the side-arms act as plasticizers. In a similar way, a maximum in the non-linear behaviour for a LCB level can be observed experimentally, beyond which $I_{3/1}$ decreases. This can therefore be explained as the result from the above competing factors. It is possible that

polyethylenes of $M_w \approx 100$ kg/mol with an average LCB higher than 0.8 LCB/1000 CH_2 can exhibit a less pronounced non-linear behaviour. A similar observation is concluded for higher molecular weight LCB materials ($M_w \approx 200$ kg/mol) for an average degree of 0.5 LCB/1000 CH_2.

4.1.7 Optimized LAOS measurement conditions for differentiating LCB

Schlatter et al. [Schlatter 05] performed LAOS at constant Deborah numbers, using extremely low frequencies (ω_1 = 0.193 rad/s or $\omega_1\lambda_c$ = 0.07, where λ_c = 1/ω_c and ω_c was defined as the frequency for which the Cole-Cole diagram reaches a maximum) and at a temperature of 150 °C using solely an ARES rheometer. An open-rim cone-plate geometry was utilized, with a maximum strain amplitude of γ_0 = 4. Within this thesis, it is shown that $I_{3/1}$ of LCB polyethylenes deviates strongly from the one measured for linear and SCB samples, at strain amplitudes $3 < \gamma_0 < 7$. Above these deformations, the differences in $I_{3/1}(\gamma_0)$ and $\Phi_3(\gamma_0)$ of different topologies are not always significant (e.g. fig 4.12). For $\gamma_0 < 3$, the RPA2000 is not sensitive towards the detection of the higher harmonics, especially for low molecular weight samples. With the use of the ARES open-rim geometry, there are stability issues originating from the open plate geometry and the increasing normal forces, especially at $\gamma_0 > 2$ and $\omega_1/2\pi$ = 0.1 Hz. Within this work, we apply a strain amplitude $0.5 < \gamma_0 < 10$ by combining results from both rheometers, at two temperatures 140 °C and 180 °C, with the frequency varying between 0.01 Hz and 5 Hz, to obtain an optimised contrast between linear and LCB polyethylenes.

The zero-shear phase of the third harmonic, Φ_3^0, deduced from measurement of non-linearities at low strain amplitudes is another promising method to discriminate LCB from linear polyethylenes. This particular phase analysis is applied to compare samples of different topology separating the effect of LCB from that of molecular weight distribution on the rheological behaviour. This "fingerprint" of linear and LCB-polyethylenes can be easily presented by extending the van Gurp-Palmen plot to include the non-linear rheological behaviour (fig. 4.16, 4.17, 4.18).

Results shown in fig. 4.15 - 4.18 suggest that low frequencies are more appropriate for discriminating the non-linear rheological behaviour of LCB and linear polyethylenes. Large amplitudes are needed for a better discrimination between linear and branched polyethylenes on the basis of $I_{3/1}$. Considering all the above factors, a strain amplitude γ_0 = 2 - 4 and a typical frequency of $\omega_1/2\pi$= 0.1 Hz at 180 °C, are currently seen as the best empirical conditions towards the differentiation between LCB and linear polyethylenes using FT-Rheology.

The presented results in fig. 4.16, 4.17, 4.18 are in agreement with those shown in fig. 4.15, and suggest that the effect of LCB is more pronounced in the terminal zone (high tan δ). This can be understood if one considers that the characteristic time of the measurement should be such that the effects of branches of a macromolecule are probed. When LAOS is

applied at frequencies $\omega_1 > \omega_c$ (equivalently at low tan δ), the investigated length scale can be smaller than the distance between branches of the polyethylene macromolecules. LCB non-linearities increase with increasing tan δ. At higher tan δ values, the $I_{3/1}$ and Φ_3 curves for linear and LCB exhibit a crossover point. For tan δ larger than the crossover value (for the case in fig. 4.20 crossover tan $\delta \approx 5$), $I_{3/1,LCB}$ is higher than $I_{3/1,linear}$ as can be seen in fig. 4.15 - 4.18. Thus, the effect of LCB is reduced in this frequency range and the difference between LCB and linear polyethylenes is not pronounced. The investigated polyethylenes possess characteristic relaxation time of the order of $\tau = 1/\omega_{crossover}$ = 10^{-2} s - 10^{-3} s and exhibit a weak temperature dependence. In order to extend the study at very high Deborah numbers, high frequencies are needed. However, LAOS at frequencies $\omega_1 > 5$ Hz is not possible with the current experimental devices.

In the case of polyethylenes with no LCB detected, the molecular weight and the molecular weight distribution are considered as the only parameters affecting their non-linear behaviour. Consequently, $I_{3/1}(\gamma_0)$ for the linear and SCB polyethylenes is predicted from corresponding M_w and *PDI* using eq. 4.2. Using the molecular weight distribution, the non-linear behaviour of a polydisperse polyethylene with linear topology can be predicted (see fig. 4.14) and lead to a developement of a more elaborated equation which includes topological features of the polymer.

4.2 Application of FT-Rheology towards blends of linear and LCB industrial polyethylenes

With the use of FT-Rheology and the correlation with ^{13}C NMR results as introduced in the above paragraphs, it is shown that a "fingerprint" of the non-linear rheological behaviour of LCB PE materials can be obtained. Sparse LCB and SCB of a degree as low as $\sim$ 0.1 LCB + SCB/1000 CH_2 can be detected. However, this estimated branching degree is an average value for all the species included in the PE melt. A polydisperse industrial material may consist of macromolecular chains with topologies varying from linear to species of a high branching degree. Within this paragraph, the limits of detectable LCB PE material in a polydisperse (in molecular weight and in topology) PE melt are studied by applying FT-Rheology. For this purpose, blends of industrial polyethylene consisting of a linear and a LCB component of similar M_w and *PDI* have been specifically prepared. The concentration of the LCB containing component varies from 1.5 wt % to 94.5 wt %. As it is presented below, a very low concentration of LCB material to a linear PE melt can be detected (1-5 wt %) via the use of LAOS and FT-Rheology.

A similar approach was presented by Stange et al. [Stange 05] for quantifying LCB in polypropylene. The authors blended linear PP and LCB PP samples and applied size exclusion chromatography (SEC) coupled with multi-angle laser light scattering (MALLS)

using the mean square radius of gyration as a parameter to detect LCB. Rheological measurements where also undertaken and specifically oscillatory shear and extension experiments. A logarithmic mixing rule was applied to predict blend zero shear viscosity, η_0, as a function of the volume fractions and of η_0 of the two blend components.

Blends of linear or SCB with LCB polyethylenes have been extensively studied in the past, with respect to their thermal, rheological and mechanical properties [Yamaguchi 99]. Rheological methods, namely: Cole-Cole plots (loss viscosity, η'', versus storage viscosity, η', loss modulus, G'', versus storage modulus, G' plots and melt complex viscosity, $|\eta^*(\omega)|$, plotted against blend composition were undertaken by Kwag et al. [Kwag 00]. The authors combined the results with morphological studies and examined the miscibility of mPE and high-density polyethylene (HDPE) blends. Perez et al. [Pérez 05] applied rheological techniques to study blends of metallocene linear low-density polyethylene (mLLDPE) and low density polyethylene (LDPE), focusing in their miscibility and processing features. Thermal and rheological properties of mLLDPE/LDPE blends were also investigated by Fang et al. [Fang 05]. The authors used dynamic scanning calorimetry (DSC) and oscillatory shear measurements. The miscibility of mLLDPE materials containing different types of comonomer with LDPE of broad molecular weight distribution was determined. For this purpose, the zero shear viscosity of the blend and the complex viscosity were used, along with the calculated relaxation spectrum. The applicability of a logarithmic mixing rule was also examined. The majority of the samples followed this empirical rule, nevertheless deviations for some blends were found and were attributed to the thermo-mechanical history of the specific materials.

In the present paragraph, the quantities used to analyze the non-linear behaviour of the melt sample are the relative intensity of the 3^{rd} harmonic, $I_{3/1}$, and the relative phase of the 3^{rd} harmonic, Φ_3. A quantification of the LCB content is presented via parameters derived from fitting $I_{3/1}$ as a function of strain amplitude, γ_0, at a fixed excitation frequency, $\omega_1/2\pi$. The thermal stability of the blends is also examined. Taking into account the work of Kwag et al. [Kwag 00], as well as previous papers [Han 87, Xu 01, Hameed 02, Liu 00, Hussein 03, Hussein 04, Pérez 05], the miscibility of the two blended systems at various LCB-PE concentrations is complementary investigated using rheological techniques.

4.2.1 Investigated blends

Sixteen blends generated out of four pure components, two linear and two LCB samples, (see Table 4.1) are investigated. The first blended system is based on mPEmix0 as a linear component and LCBmLLDPE as the LCB part of varying concentration, with both samples being metallocene-catalyzed PE of similar narrow molecular weight distribution. The second blended system consists of the linear L1_117_5.1 and the LCB1_123_7.1, where the LCB

Samples	% wt. LCB-PE	Samples	% wt. LCB-PE
mPEmix0	0	Lmix0(L1_117_5.1)	0
mPEmix1	1.5	Lmix1	1.5
mPEmix2	5.5	Lmix2	5.5
mPEmix3	10	Lmix3	10
mPEmix4	30	Lmix4	30
mPEmix5	50	Lmix5	50
mPEmix6	70	Lmix6	70
mPEmix7	90	Lmix7	90
mPEmix8	94.5	Lmix8	94.5
mPEmix9(LCBmLLDPE)	100	Lmix9(LCB1_123_7.1)	100

Table 4.3: *Polyethylene blends. Samples mPEmix are blends from mLLDPE/LCBmLLDPE mixtures and Lmix are from L1_117_5.1/LCB1_123_7.1 mixtures. For each batch the % wt. content of LCB sample is given. The branching content of the pure components can be found in Table 4.1.*

PE component varies in weight fraction and both are LDPE ofsimilar broad molecular weight distribution. Details for the pure components concerning their linear and non-linear rheological behaviour, as well as their molecular weight distribution are given in Tables 4.1 and 4.2. Sample mPEmix0 corresponds to LLDPE11 in the work of Stadler et al. [Stadler 05]. It is a linear metallocene-catalysed LDPE, with M_w = 135 kg/mol, PDI = 2.0 and it contains octene as comonomer, resulting in a degree of 66.3 SCB/1000 CH_2, as determined via melt-state NMR.

The samples are blended using a Brabender Plasticizer. The chamber is cleaned before each mixing process and filled with 20 g of material. Each blend is mixed at 180 °C for 5 min. For measurements on the ARES rheometer, melt sample discs of 13 mm diameter and 1 mm thickness are pressed, at 150 °C and 20 bars in a Weber hydraulic press under vacuum. All measurements are performed under a nitrogen atmosphere to prevent sample oxidation. The names of each batch and the weight fractions are given in Table 4.3.

4.2.2 Characterization of blend components

The first set of the investigated blends consists of mPEmix0 and LCBmLLDPE varying the weight ratios. The LCB sample has been extensively investigated in previous publications using GPC and creep-recovery measurements [Gabriel 99], by FT-Rheology, melt-state NMR and simulations using the double-convected Pom-pom model (DCPP) in Vittorias et al. [Vittorias 06] and within the present thesis (paragraph 4.1.1). The linear mPEmix0 was analytically and rheologically characterized in Stadler et al. [Stadler 05]. Both samples are metallocene-catalyzed low density industrial polyethylenes. They have similar molecular

weights and distributions ($M_w \approx$ 100kg/mol and *PDI* $\approx$ 2) and both contain SCB from using octene as comonomer. Linear sample mPEmix0 has a higher degree of SCB, which is found to suppress LCB incorporation [Stadler 05]. In the case of LCBmLLDPE, no accurate number of LCB can be given. Melt-state NMR is not able to estimate whether a side-branch of more than 6 carbons is short ($M_{branch} < M_e$) or long ($M_{branch} > M_e$) and the values obtained are the sum of SCB and LCB. Thus, the value of 25.2 LCB + SCB/1000 CH_2 given for this specific sample corresponds to the sum of SCB (from co-ocetene) and LCB incorporated in the polyethylene chain.

All the above mentioned methods conclude that mPEmix0 is a linear polyethylene with SCB and LCBmLLDPE contains SCB and LCB. Following the analysis presented in this chapter and considering the measured $I_{3/1}(\gamma_0)$ and $\Phi_3(\gamma_0)$ for both species, we suggest that LCBmLLDPE has a very low degree of LCB/1000 CH_2, nevertheless detectable by FT-Rheology and approximately 0.1 LCB/1000 CH_2. This is also in qualitative agreement with the results of Gabriel et al. who studied the same material [Gabriel 98, Gabriel 99, Gabriel 02]

The Lmix blends consist of components already presented in paragraph 4.1.1. These samples are highly polydisperse (*PDI* = 5.1 for the linear and 7.1 for the LCB sample). Both have comparable M_w($\sim$ 120 kg/mol). Melt-state NMR measurements confirm the absence of comonomer and no SCB is present in both polyethylenes. Hence, the given value of 0.2 LCB/1000 CH_2 for the LCB1_123_7.1 is considered to be a good estimation for the LCB content (see Table 4.1).

4.2.3 Effect of LCB PE content in blends via SAOS and FT-Rheology

Dynamic mechanical measurements are performed at very low strain amplitudes (SAOS) in the linear regime, using typically γ_0 = 0.1, in order to obtain linear viscoelastic properties of all samples, specifically G', G'' and $|\eta^*(\omega)|$. The results are presented in fig. 4.21 and 4.22 for the mPEmix blends and in fig. 4.23 and 4.24 for the Lmix blends. In the mPEmix blends, the LCB component has a very low LCB content and M_w and PDI similar to the linear component. The LCB sample for the Lmix has a higher relative branching degree and a higher PDI compared to L1_117_5.1. This is the reason for the difference in the discrimination between the mPEmix and the Lmix blends, with respect to their moduli.

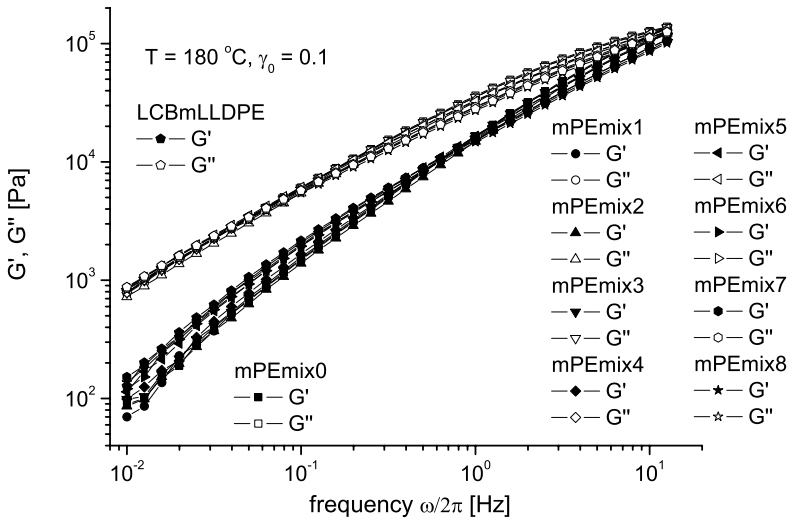

Figure 4.21: *Storage and loss moduli, G' and G'', for linear polyethylene mPEmix0, LCB sample LCBmLLDPE and the mPEmix blends at T = 180 °C with γ_0 = 0.1*

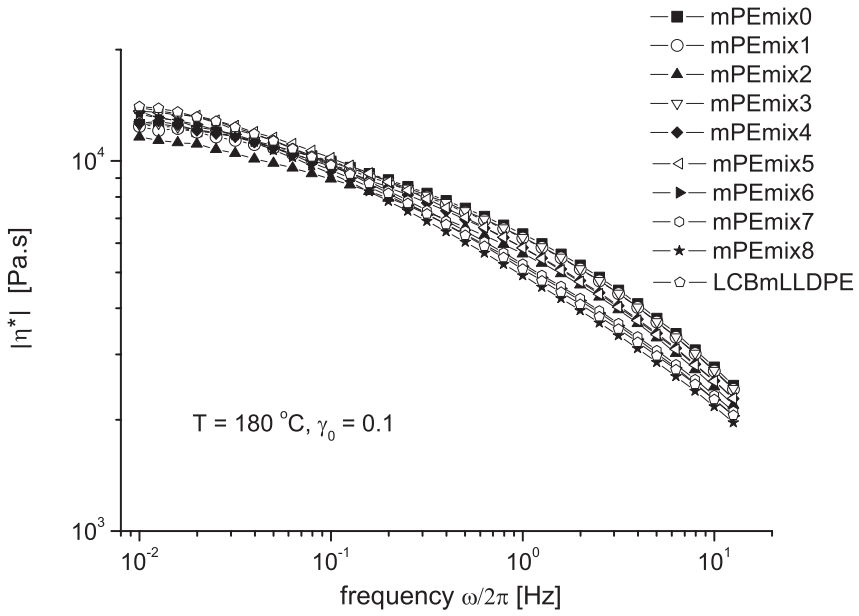

Figure 4.22: *Absolute complex viscosity, $|\eta^*(\omega)|$, at T = 180 °C with γ_0 = 0.1, for mPEmix blends (see Table 4.3).*

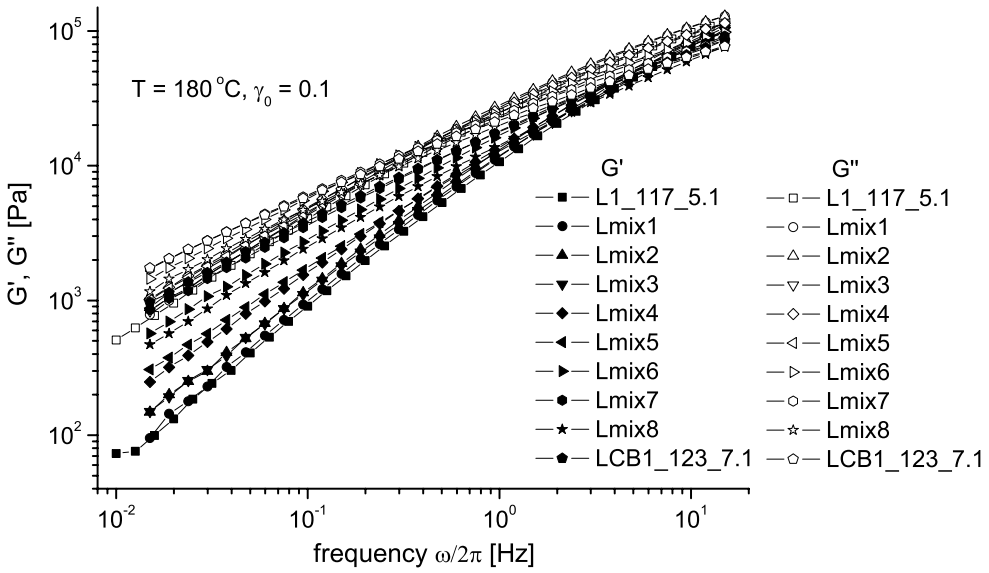

Figure 4.23: *Storage and loss moduli, G' and G'', for linear polyethylene L1_117_5.1, LCB sample LCB1_123_7.1 and the Lmix blends at T = 180 °C with γ_0 = 0.1 (see Table 4.3).*

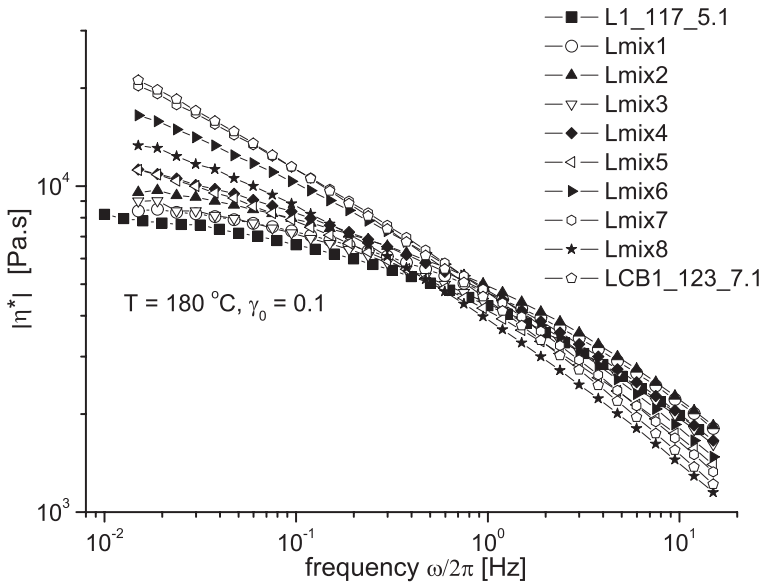

Figure 4.24: *Complex viscosity, $|\eta^*(\omega)|$, for the Lmix blends at T = 180 °C with γ_0 = 0.1.*

Large amplitude oscillatory shear is subsequently applied in order to study the non-linear rheological regime. Strain sweep measurements are performed for each sample at 0.1 Hz, 180 °C and for a strain amplitude range of $0.1 < \gamma_0 < 10$. This is achieved by combining results from measurements undertaken in the ARES and in the RPA rheometer. The resulting stress response is analyzed via FT-Rheology. The relative intensity $I_{3/1}$ and the relative phase Φ_3 as a function of strain amplitude (γ_0) of each mPEmix batch, for strain sweep measurements is presented in fig. 4.25 and fig. 4.26. The $I_{3/1}(\gamma_0)$ and $\Phi_3(\gamma_0)$ for the same LAOS measurements of the Lmix blends is depicted in fig. 4.27 and 4.28. The shape of the $\Phi_3(\gamma_0)$ curve in fig. 4.28, for γ_0 = 1.5-2.5 reflects the stability problems of the ARES geometry at these high strain amplitudes and the instabilities that occur.

As discussed in paragraph 1.5.3, the resulted $I_{3/1}(\gamma_0)$ curves are fitted using eq. 1.47

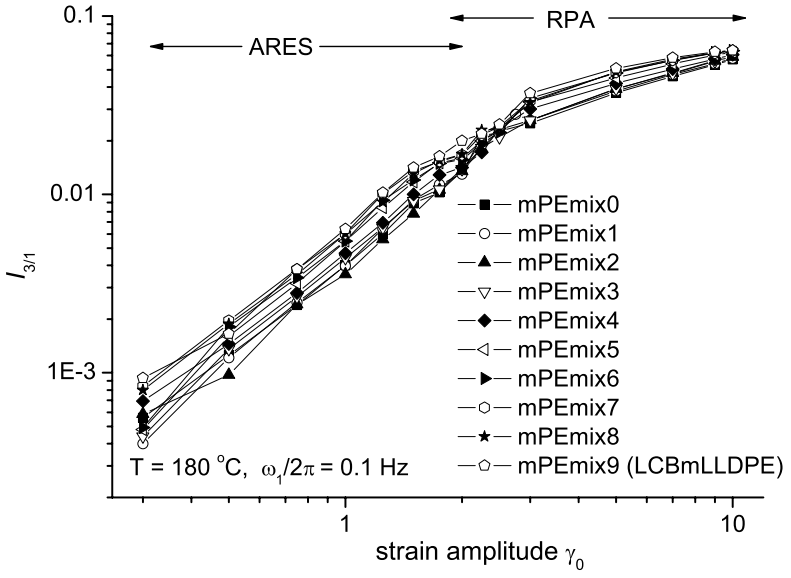

Figure 4.25: *$I_{3/1}$ as a function of strain amplitude γ_0, at T = 180 °C and $\omega_1/2\pi$ = 0.1 Hz, for mPEmix blends. $I_{3/1}$ up to γ_0 = 2.5 (ARES data) shifted to correspond to cone-plate measurements of RPA2000.*

and the parameters *A, B* and *C* derived from this fit are presented in fig. 4.29 for the mPEmix and Lmix blends. The non-linearity plateau value, *A*, and the inverse critical strain amplitude, *B* (=1/γ_0, where $I_{3/1}$ = *A*/2), are increasing with increasing LCB concentration, for both blended systems.

The use of eq. 1.47 to fit $I_{3/1}(\gamma_0)$ requires available data in a broad range of strain amplitudes. In order to have a realistic value for parameter *C*. One needs enough accurate data at low γ_0 (eq. $0.1 < \gamma_0 < 2$). Parameter *A* can be estimated by fitting data at very high strain amplitudes (for PE typically $\gamma_0 > 7$). However, these limits are not always experimentally reachable, as discussed in previous paragraphs. Hence, eq. 1.51 can be used, as for the case

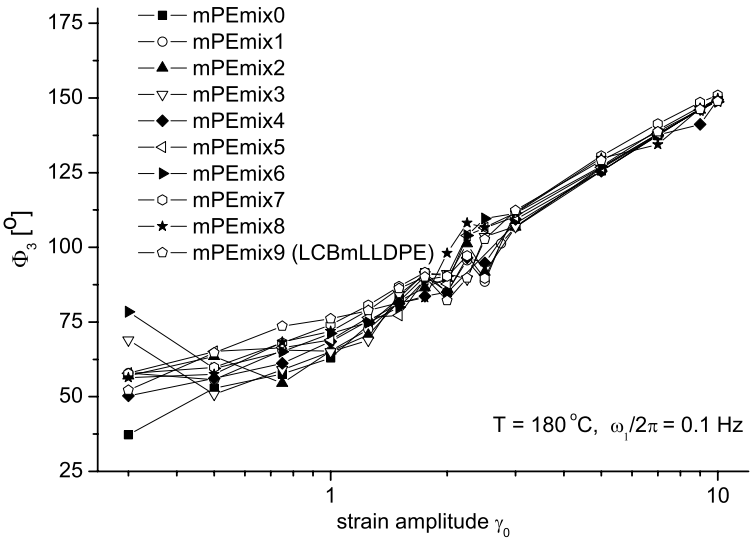

Figure 4.26: Φ_3 *as a function of strain amplitude* γ_0*, at T = 180 °C and* $\omega_1/2\pi$ *= 0.1 Hz, for mPEmix blends. For* $\gamma_0 < 0.5$*, experimental errors are significant.*

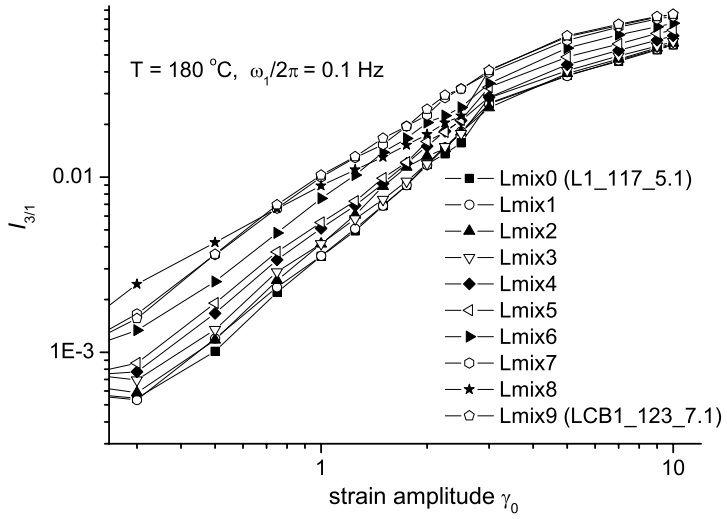

Figure 4.27: $I_{3/1}$ *as a function of strain amplitude* γ_0*, at T = 180 °C and* $\omega_1/2\pi$ *= 0.1 Hz, for Lmix blends.* $I_{3/1}$ *up to* γ_0 *= 2.5 (ARES data) shifted to correspond to cone-plate measurements of RPA2000.*

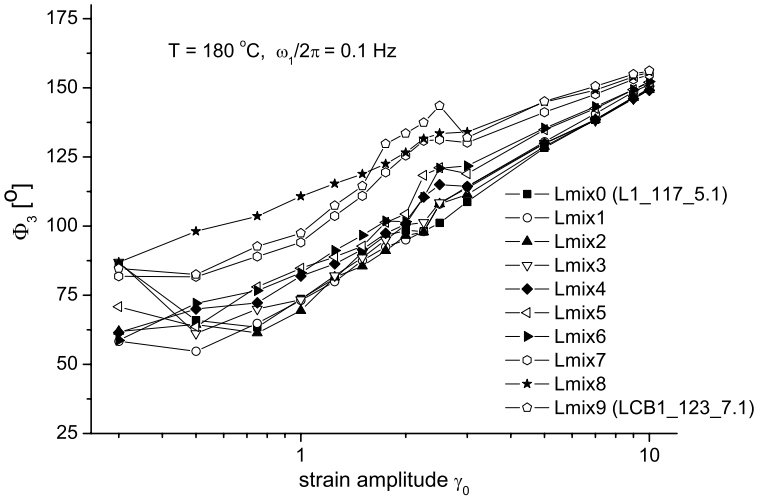

Figure 4.28: *Φ_3 as a function of strain amplitude γ_0, at T = 180 °C and $\omega_1/2\pi$ = 0.1 Hz, for Lmix blends. The shape of $\Phi_3(\gamma_0)$ for γ_0 = 1.5-2.5 is due to flow instabilities at these deformations that occur with the ARES geometry.*

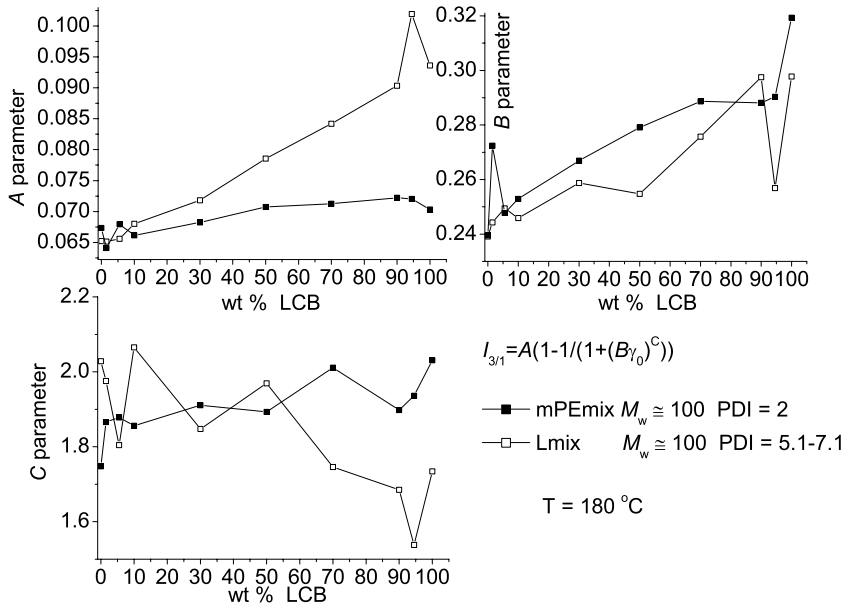

Figure 4.29: *A, B, and C values derived from fitting $I_{3/1}(\gamma_0)$ at 180 °C and 0.1 Hz with eq. 1.47, for both blended systems, as a function of wt % content of LCB sample.*

of model PS samples, for γ_0 up to 2, at 180 °C, for both blend groups. In fig. 4.30 and 4.31 parameters *D* and *C* are depicted, as a function of LCB PE weight concentration. Fittings are performed either by adjusting both parameters, or using *D* as the only adjustable parameter, and *C* as derived from eq. 1.47. Parameter *D* displays a continuous change between the two pure systems, while this is not clear for parameter *C*. The latter is however confined in fit values between the predicted values for the pure components (see table 4.2) and in any case near the theoretically expected values of 1.7-2 [Neidhöfer 03b, Pearson 82].

In both blend series one can observe that an increasing LCB species content increases

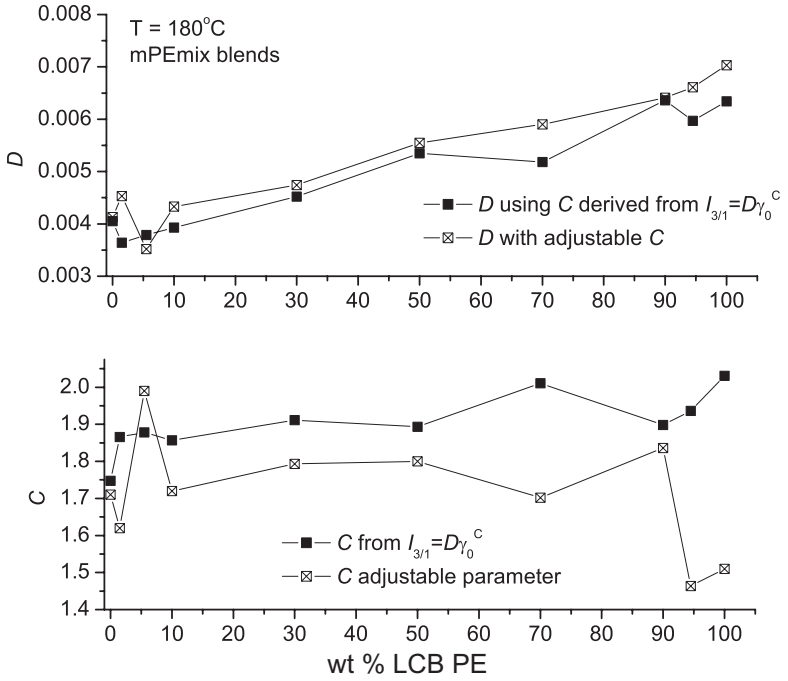

Figure 4.30: *D and C values derived from fitting $I_{3/1}(\gamma_0)$ at 180 °C and 0.1 Hz with eq. 1.51, for mPEmix systems, as a function of wt % content of LCB sample.*

monotonically the measured $I_{3/1}(\gamma_0)$ and $\Phi_3(\gamma_0)$, as reflected in parameters *A*, *B* and *D* (fig. 4.29 - 4.31). The non-linearity plateau (*A*) and the inverse critical strain (*B*) increase with increasing ratios of LCB / linear chains in the blend. The slope of $\log I_{3/1}$-$\log(\gamma_0)$ at low strains (*C*) remains between the values of the linear and the LCB polyethylene samples, and close to values theoretically predicted, *C* = 1.7-2 [Neidhöfer 03b, Pearson 82]. It should be noted that if there is enough data available at very large γ_0, one can calculate a more accurate value of *A*, thus making the determination of a *C* with less errors possible. In the absence of data near the $I_{3/1}(\gamma_0)$ plateau, the derived values of parameter *C* may vary depending on the estimation of *A*. Since there is a theoretical estimation for *C*, we can fit $I_{3/1}$ at low and medium γ_0 by adjusting only parameter *D*. This is done while keeping *C* values in a close agreement with theory, i.e. $\sim$2. The fitting procedure is also performed using both *D* and *C* as adjustable parameters and only small differences in the derived values of *D* are found

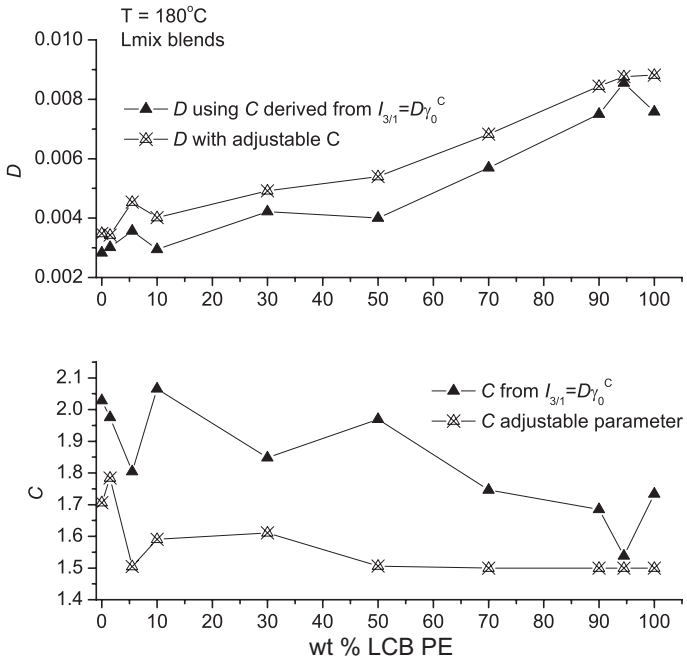

Figure 4.31: *D and C values derived from fitting $I_{3/1}(\gamma_0)$ at 180 °C and 0.1 Hz with eq. 1.51, for Lmix systems, as a function of wt % content of LCB sample.*

(fig. 4.30, 4.31). Generally, there is a weak dependence of *C* on topology and molecular weight distribution and slopes of 1.7 - 2.5 for LCB polyethylenes are expected.

4.2.4 Extended van Gurp-Palmen method for PE blends

In paragraph 4.1.4 the relative phase of the 3^{rd} harmonic at very low strain amplitudes, Φ_3^0 ($lim_{\gamma_0 \to 0}\Phi_3 := \Phi_3^0$) is introduced as a potential new parameter for LCB detection. The same method is applied to the studied polyethylene blends of known LCB PE concentration. For all samples, Φ_3^0 is measured for a frequency range of 0.01 Hz - 5 Hz, at 180 °C. First, the phase lag δ plotted against the complex modulus for all samples is depicted in fig. 4.32 and 4.33. The relative phase of the 3^{rd} harmonic at very low strain for mPEmix blends is shown in fig. 4.34. It can be concluded that an optimum discrimination between linear and LCB topologies can be achieved at low excitation frequencies (e.g. $\omega_1/2\pi$ = 0.02 Hz-0.3 Hz). For the case of mPEmix samples the the discrimination between the blends is simpler with the van-Gurp plot than with the extended Φ_3^0 at higher moduli values. Hence, results are presented from a complex modulus range corresponding to low excitation frequencies for several Lmix blends, where the differences between blends of chaging LCB component concentration is more pronounced (fig. 4.35).

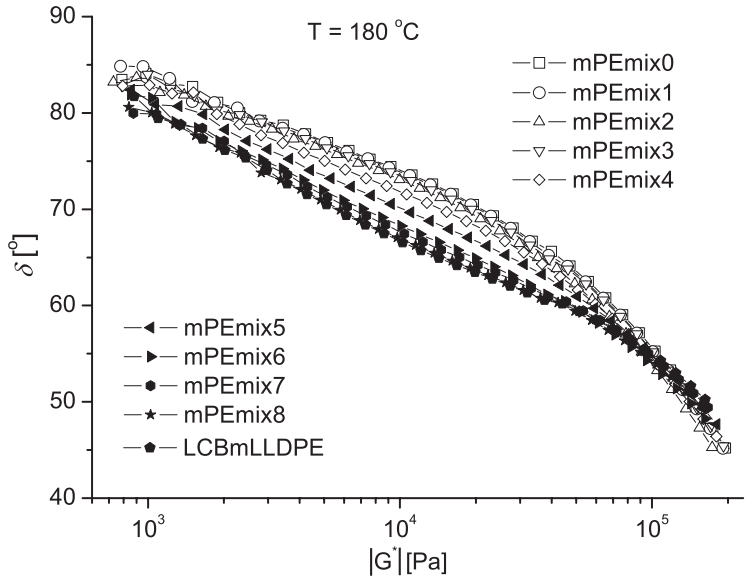

Figure 4.32: *Van Gurp-Palmen plot. Phase lag δ as a function of complex modulus, $|G^*(\omega)|$, for mPEmix blends at 180 °C.*

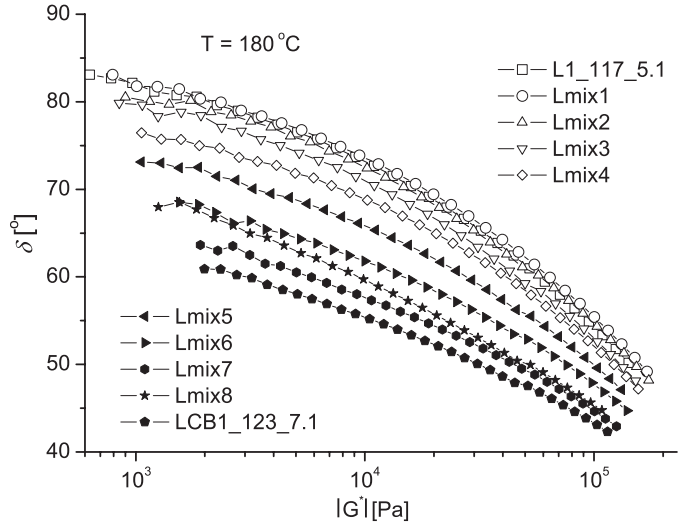

Figure 4.33: *Van Gurp-Palmen plot. Phase lag δ as a function of complex modulus, $|G^*(\omega)|$, for Lmix blends at 180 °C.*

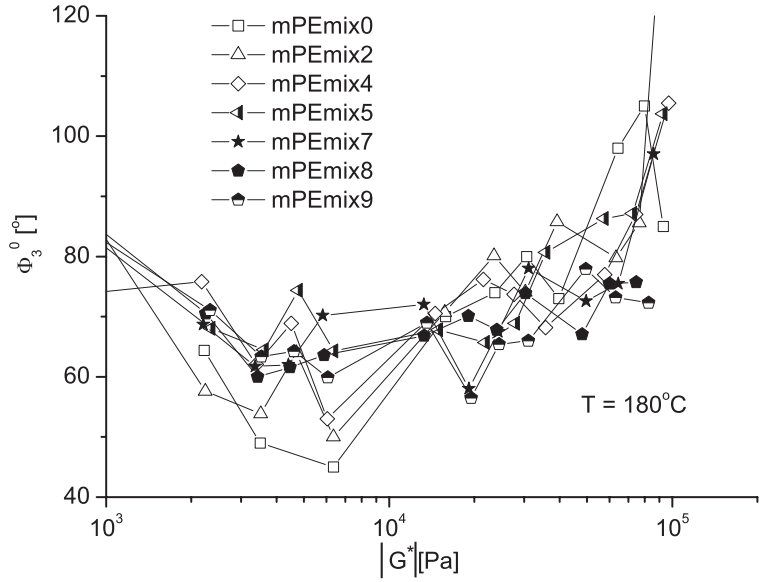

Figure 4.34: *Extended Van Gurp-Palmen plot. Relative phase of 3rd harmonic at low strains (γ_0=0.5), Φ_3^0, as a function of complex modulus, $|G^*(\omega)|$, for mPEmix blends at 180 °C. For $|G^*(\omega)| > 2{\times}10^4$, no discrimination can be achieved between the specific blends.*

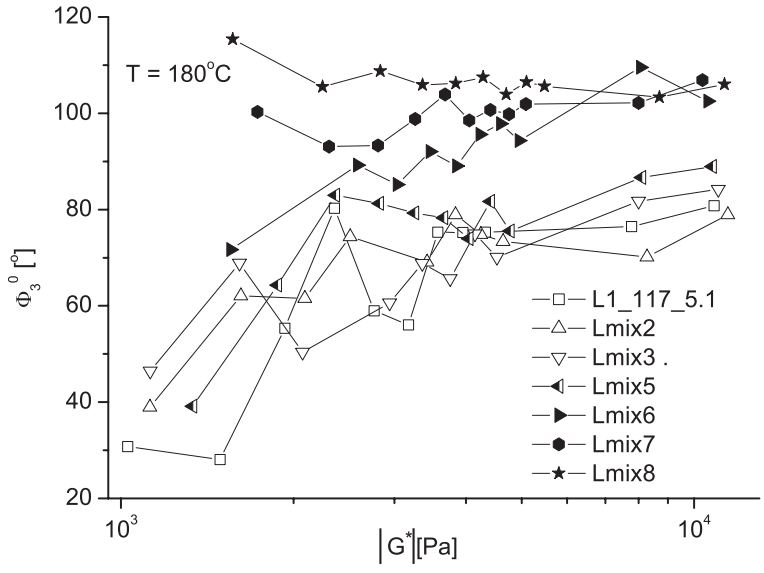

Figure 4.35: Φ_3^0 *as a function of* $|G^*(\omega)|$*, measured at low frequencies,* $\omega_1/2\pi$ *= 0.02 Hz - 0.3 Hz, for Lmix blends at 180 °C.*

4.2.5 Mixing rules for predicting non-linearity of linear/LCB blends

Stange et al. [Stange 05] studied the rheological behaviour of blends with linear and LCB polypropylene. The authors applied a logarithmic mixing rule between the two blend components to follow the zero-shear viscosity. In our case a linear mixing rule is applied to predict $I_{3/1}(\gamma_0)$ of each blend:

$$I_{3/1,blend}(\gamma_0) = \phi_{(1)} I^{(1)}_{3/1}(\gamma_0) + \phi_{(2)} I^{(2)}_{3/1}(\gamma_0) \tag{4.3}$$

where ϕ is the mass fraction of each component. A second effort is also presented for predicting the non-linear behaviour of the binary blends by a logarithmic mixing rule [Stange 05]:

$$log(I_{3/1,blend}(\gamma_0)) = \sum_{i=1}^{n^{th}component} \phi_{(i)} log(I^{(i)}_{3/1}) \tag{4.4}$$

and specifically for the studied binary blends:

$$log(I_{3/1,blend}(\gamma_0)) = \phi_{(1)} log(I^{(1)}_{3/1}(\gamma_0)) + \phi_{(2)} log(I^{(2)}_{3/1}(\gamma_0)) \tag{4.5}$$

Results for LCB concentrations of 10 wt %, 50 wt % and 90 wt % are shown in fig. 4.36 for mPEmix blends. In fig. 4.37 the results for all Lmix blends are depicted. For the majority of the blends, both mixing rules describe in a satisfactory way the blend $I_{3/1}(\gamma_0)$. However for some cases, e.g. for very large LCB PE weight fractions, the linear mixing rule is in slightly better agreement with experimental data. In fig. 4.36 the small difference between the predicted $I_{3/1}$ with eq. 4.3 and 4.5, is not clear due to the small difference of the non-linearities between the two components and the logarithmic scale used.

The non-linear behaviour as quantified by $I_{3/1}$ is a function of the LCB concentration. Thus, it can be expected to be described by a blend mixing rule. An empirical mixing rule is supposed to predict the blend non-linearity from the known $I_{3/1}(\gamma_0)$ of the pure components and the weight fractions, since they have similar molecular weight distribution (see eq. 4.3 and 4.5). The logarithmic rule gives better predictions for the Lmix blends and for some cases of the mPEmix. The linear mixing equation performs better for blends with high LCB PE weight fractions. However, both mixing rules do not describe successfully the non-linearities of all the investigated blends. In previous works this has been interpreted

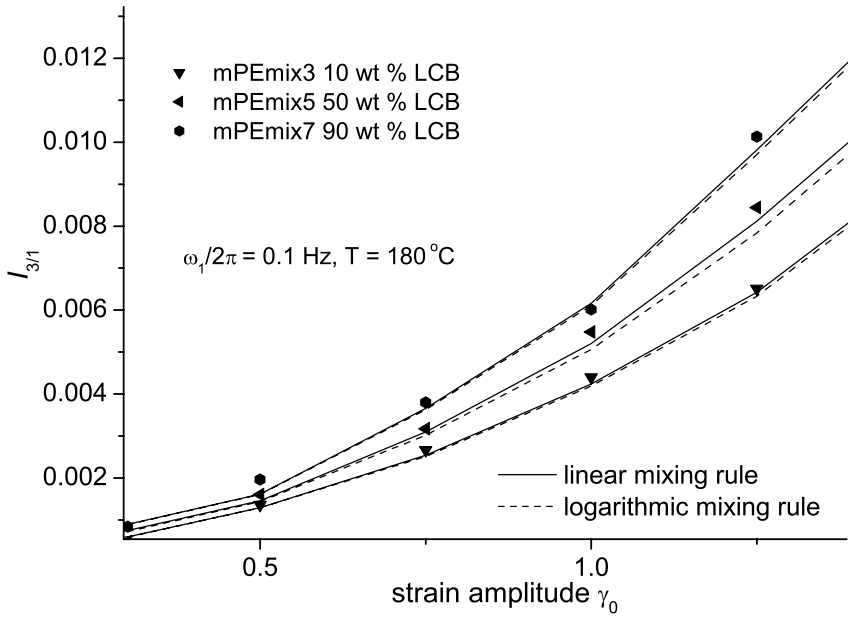

Figure 4.36: *Comparison of experimental $I_{3/1}(\gamma_0)$ and predicted from linear and logarithmic rule, for mPEmix blends at 180 °C at low and medium strain amplitudes.*

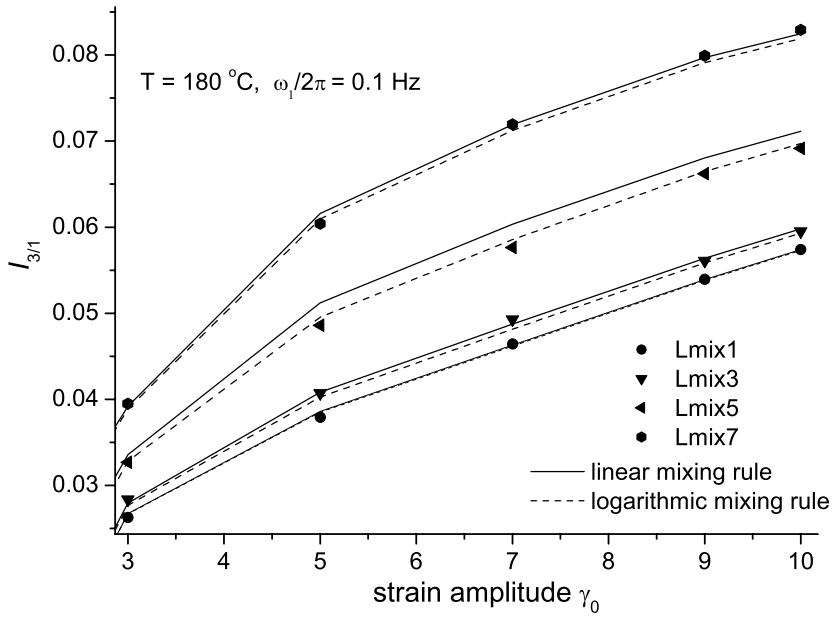

Figure 4.37: *Comparison of experimental $I_{3/1}(\gamma_0)$ and predicted from linear and logarithmic rule, for Lmix blends at 180 °C. Results for $\gamma_0 > 3$.*

as an indication of blend immiscibility [Kwag 00]. However, one must be aware that these are empirical rules with no theoretical basis and thus, they cannot support stringent conclusions about material behaviour. The failure to describe rheological properties (linear and non-linear) could be overcome with the use of more elaborated and theory based mixing rules.

4.2.6 Limits of LCB PE content detectable via FT-Rheology

Polyethylenes of the mPEmix group with an LCB sample mass fraction lower than 10 wt % do not present significant differences in the linear spectrum. However, for large strain amplitudes ($\gamma_0 > 3$) even sample mPEmix1 (1.5 wt % LCBmLLDPE) presents a slightly higher $I_{3/1}$. For example at γ_0 = 5, mPEmix1 has a slightly higher non-linearity value compared to that of the linear pure component, mPEmix0 ($I_{3/1}$ = 3.8% and 3.7% respectively). Such small differences in the non-linear behaviour are close to the limits of the reproducibility of the measurement, nevertheless it can be detected and quantified with the optimized experimental setup at large amplitudes (see chapter 2). Concerning the LCB sample, an addition of 5.5 wt % of linear chains, is adequate to change the non-linear behaviour from that of a 100 wt % LCBmLLDPE. This is also reflected in the parameters *A, B, C,* and *D* (fig. 4.29 - 4.31).

For the Lmix blends the lowest detectable LCB component concentration is 5.5 wt % and the lowest detectable linear component weight fraction is also found to be 5.5 wt %. The higher sensitivity of FT-Rheology for the Lmix series can also be explained by the different and high polydispersity between the two blend components. Higher polydispersity generally results in higher $I_{3/1}(\gamma_0)$ and $\Phi_3(\gamma_0)$ values (see chapter 3 and paragraph 4.1.1). Hence, adding a very small weight fraction (e.g. 1-5 wt %) of a sample with a higher PDI into a linear PE will cause an additional increase of non-linearity, via the broadening of the molecular weight distribution. This increase of $I_{3/1}(\gamma_0)$ and $\Phi_3(\gamma_0)$ is thus attributed not only in the presence of more LCB chains but also in the presence of larger macromolecules, as discussed in the paragraph 4.1.1 and in chapter 3. One additional factor may be that the chains in the high molecular weight tail ($M > 300$ kg/mol) of the distribution for the LCB1_123_7.1 can contain a higher relative branching degree. Hence, a relatively small amount of this component (1-5 wt %) is enough to induce a different non-linear rheological behaviour under LAOS conditions as recorded by FT-Rheology. as a comparison, the analysis of the moduli measured in the linear regime with SAOS is sensitive to LCB PE for concentrations higher than 30 wt % for mPEmix and higher than 10 wt % for the Lmix blends.

4.2.7 Melt stability and miscibility of the studied blends

Within the blend analysis, only rheological techniques are used in order to check the miscibility and stability of the blends. Anaylisis via differential scanning calorimetry (DSC) [Fang 05] or scanning electron microscopy (SEM) [Kwag 00] is not presented. It has to be taken into consideration that all four blend pure components are industrial samples and contain stabilizers and no degradation is observed during the experiments. Large amplitude oscillatory shear tests performed at low frequencies $\omega_1/2\pi$ = 0.01 Hz and at test temperature of 180 °C show that the samples mPEmix0, mPEmix9, Lmix0 and Lmix9 are stable towards their moduli and non-linear properties ($I_{3/1}$, Φ_3), for more than 2h (typical duration of LAOS measurements).

The homogeneity of the blends is initially examined by monitoring the resulting torque in the Brabender mixer as a function of time. In fig. 4.38 the torque is plotted against the mixing time for two blends, mPEmix5 and Lmix5. We can conclude that the mixing time is adequate to achieve a homogeneous blend.

Furthermore, linear properties (G', G'', tan δ) of each blend are measured with frequency

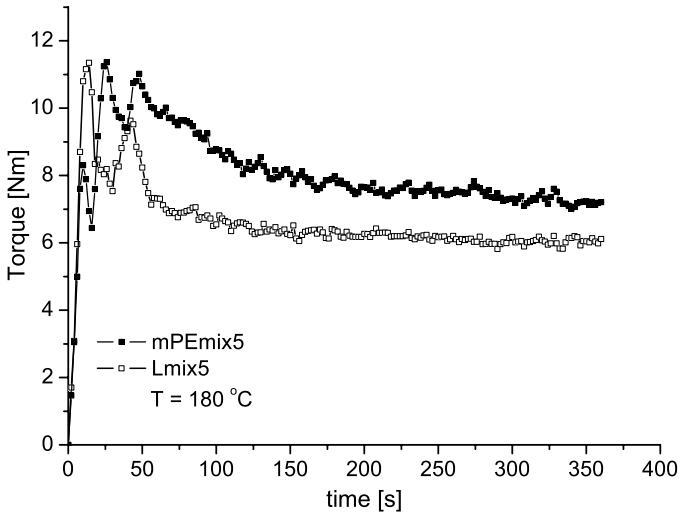

Figure 4.38: *Torque measured in the Brabender plasticizer as a function of mixing time, for blends mPEmix5 and Lmix5 at 180 °C.*

sweeps using low strain amplitudes (typically γ_0 = 0.1) before and after each non-linear measurement and within reproducibility no differences are found in the linear rheological spectrum, which is a strong evidence of blend stability at the specific experimental conditions. Finally, for each strain sweep at LAOS conditions ($I_{3/1}(\gamma_0)$ and $\Phi_3(\gamma_0)$ measurements) and for each frequency sweep for $\Phi_3^0(\omega)$ measurements, new samples are used.

The miscibility of the blends is investigated by applying LAOS for more than 2h, at T = 180 °C, $\omega_1/2\pi$ = 0.1 Hz, with γ_0 = 0.5. The complex modulus, $|G^*(\omega)|$, normalized to the

initial complex modulus $|G^*(\omega)|_0$ (at t = 0 sec) and $I_{3/1}$ recorded is presented in fig. 4.39 for sample Lmix5. The increase of $|G^*(\omega)|$ is negligible ($< 5\%$) and the relative intensity of the 3^{rd} harmonic is also quite stable ($0.16 \pm 0.01\%$). This suggests that no phase separation takes place, at least during the time needed for a series of SAOS (measurement of G', G'', tan δ), LAOS strain and frequency sweep measurements. The studied blends are stable at the specific conditions [Stange 05].

In order to further verify the miscibility of all blends via rheological techniques in

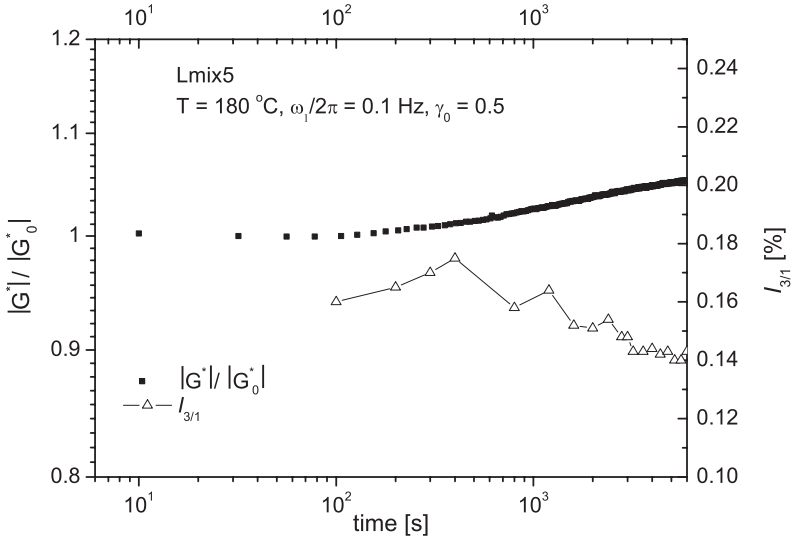

Figure 4.39: *Blend stability. Complex modulus normalized to complex modulus at time t = 0, $|G^*(\omega)|$ / $|G^*(\omega)|_0$ and relative intensity $I_{3/1}$ as a function of time for LAOS at 180 °C, $\omega_1/2\pi$ = 0.1 Hz and γ_0 = 0.5.*

fig. 4.40 and 4.41, the Cole-Cole plots and the G'' plotted against G', for all blends are presented, following the approach of Kwag et al. [Kwag 00]. The mPE blends show a semi-circular relationship and the same slope of G'' versus G', which according to Kwag et al. [Kwag 00] and Han and Kim [Han 87] indicate miscibility. The Lmix blends show deviations from this behaviour. For the case of the mPEmix blends, the resulting Cole-Cole and G'' against G' plots reinforce the argument of miscibility for these specific mixtures. The loss viscosity, η'', plotted against the storage viscosity, η'', presents a semi-circular pattern for all mPEmix blends. The shift of the curve maximum can be attributed solely to the presence of LCB, since the components mPEmix0 and LCBmLLDPE have similar molecular weight distributions [Schlatter 05]. Immiscibility could be considered for the case of the Lmix blends by solely observing their specific Cole-Cole and G'' versus G' curves (fig. 4.42 and 4.43). However, Kwag et al. [Kwag 00] and Schlatter et al. [Schlatter 05] suggest that this can also be attributed to the combination of high polydispersity and the presence of LCB.

Furthermore, taking into account the monitored moduli and non-linearity of fig. 4.39, the spread of the curves observed in fig. 4.42 and 4.43, can be attributed to the combined

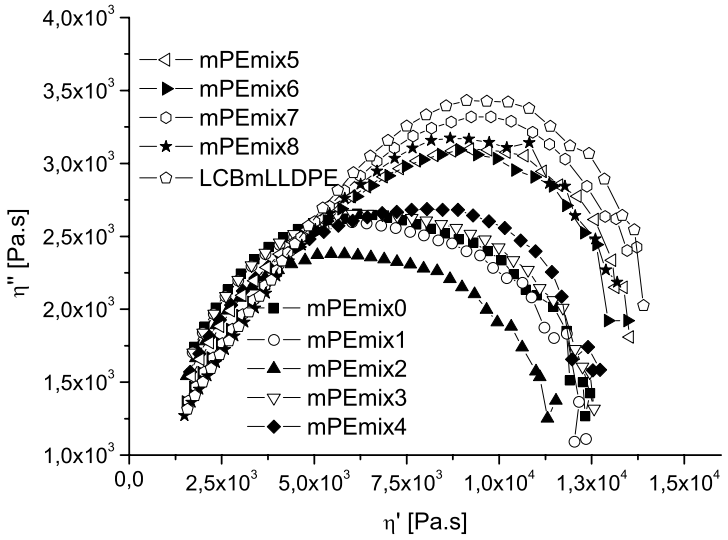

Figure 4.40: *Cole-Cole plot for mPEmix blends at 180 °C.*

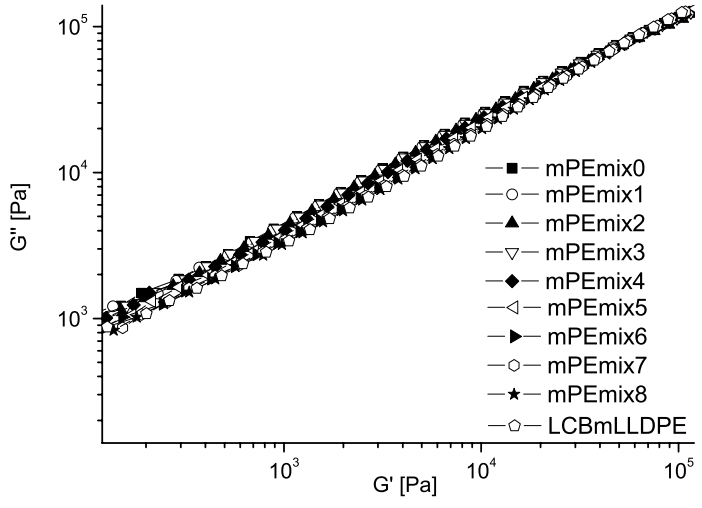

Figure 4.41: *Loss modulus versus storage modulus for the mPEmix at 180°C.*

high polydispersity and higher branching degree (LCB/1000 CH_2) of the samples (PDI $\approx$ 5-7). Additionally, the blend components have predominantly identical chemical structure and similar molecular weight distribution. Both mPEmix0 and LCBmLLDPE are produced with metallocene catalysts and contain co-octene. Samples L1_117_5.1 and LCB1_123_7.1 are homopolymers with no SCB. Linear L1_117_5.1 is produced by Ziegler-Natta method and LCB1_123_7.1 is synthesized with Cr as catalyst. Components of each blend system mainly differ only in the polymer topology (and small differences in M_w and *PDI*) and specifically in the existence of LCB (the SCB type is similar for each component pair). Hence, no separation between the two phases is expected, due to the similar Van der Waals interactions.

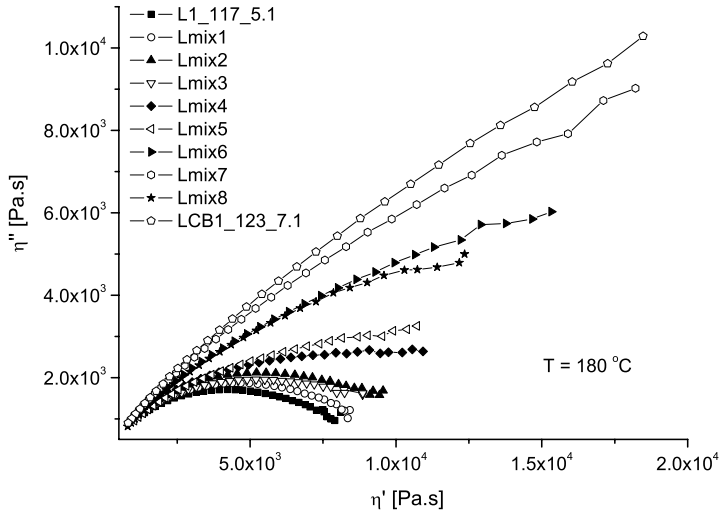

Figure 4.42: *Cole-Cole plot for Lmix blends at 180°C.*

4.3 LAOS simulations with the DCPP model for LCB industrial polyethylenes

4.3.1 Prediction of shear stress and non-linearities during LAOS

Large amplitude oscillatory shear flow is simulated for some of the investigated polyethylene melts, according to the method introduced in chapter 2 and already applied on PS branched model systems in chapter 3. The resulting stress response is analysed in the same way as the experimental torque signals, via FT-Rheology analysis. The linear parameters of the DCPP model, i.e. the relaxation time λ_i and the shear modulus of each mode G_i of each

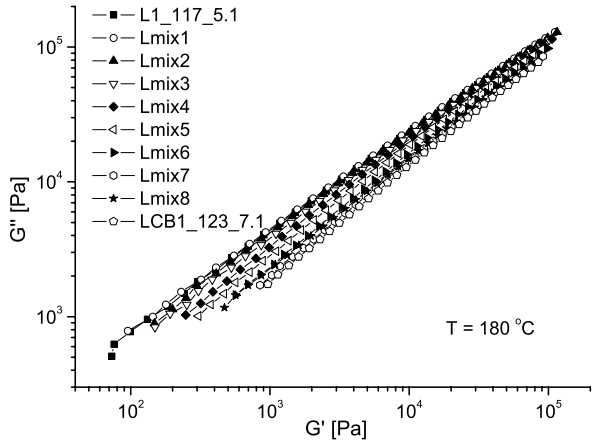

Figure 4.43: *Loss modulus versus storage modulus for the Lmix at 180°C.*

mode are identified by fitting experimental data of G', G'' and complex viscosity, $|\eta^*(\omega)|$. As an example, the fit of LCBmLLDPE with a 4-mode DCPP model is presented in fig. 4.44. Inkson et al. [Inkson 99] and Graham et al. [Graham 01] have indeed proposed the use of a multi-mode model to account for the complex architecture of a branched LDPE. The superposed "pom-pom macromolecules" of different relaxation times and arm number will account for the relaxation processes of the polydisperse macromolecules studied, that contain multiple irregularly spaced long-chain branches (see Table 4.1).

Simulations are performed at conditions corresponding to various tan δ as measured in the linear regime. In fig. 4.45 the relative intensities, $I_{3/1}(\gamma_0)$, predicted for both polyethylenes for selected values of non-linear parameters, q_i and λ_i/λ_{si} are displayed. Strain sweeps are simulated at conditions corresponding to tan δ = 2. In fig. 4.46 the predicted $I_{3/1}$ for mLLDPE and LCBmLLDPE for LAOS with γ_0 = 3, for a range of tan δ between 1.5 and 6.5 are presented. The predicted crossover between $I_{3/1,LCB}$ and $I_{3/1,linear}$ is close to the one measured experimentally.

An analysis of the effects of non-linear model parameters on the resulting non-linearity, i.e $I_{3/1}(\gamma_0)$ and $\Phi_3(\gamma_0)$, is performed. This correlation is needed for understanding the behaviour of different "pom-pom molecule blends" in the non-linear regime. Both non-linear parameters, *q* and λ_s, are found to affect the shape of the resulting $I_{3/1}(\gamma_0)$ and $\Phi_3(\gamma_0)$ curves. Simulation results of $I_{3/1}$ and Φ_3 for LCBmLLDPE at 0.04 Hz and 180 °C (where tan δ = 3.5 in the linear regime) are shown in fig. 4.47 and 4.48. Each curve corresponds to a different "blend of pom-pom molecules" chosen to decouple the non-linear behaviour of this LCBmLLDPE grade [Inkson 99].

The predicted $I_{3/1}(\gamma_0)$ is fitted by eq. 1.47. Parameters *A*, *B* and *C*, defining the shape of the resulting sigmoidal curve, are correlated to the non-linear parameters *q* and λ/λ_s. Equation 1.47 exhibits a good fit between experimental and predicted $I_{3/1}(\gamma_0)$ data for all

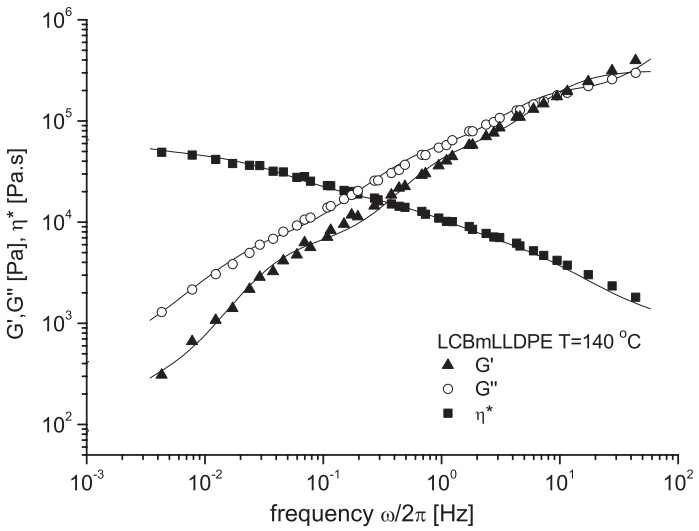

Figure 4.44: *Fit of linear rheological material properties of LCBmLLDPE, by a 4-mode differential DCPP model. Experimental data for G', G'' and $|\eta^*(\omega)|$ obtained by dynamic oscillatory shear at T = 140 °C.*

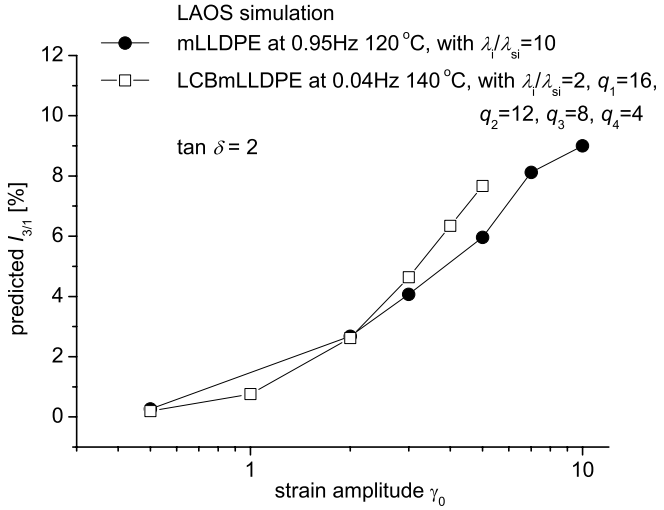

Figure 4.45: *Predicted $I_{3/1}(\gamma_0)$ from DCPP model, for mLLDPE and LCBmLLDPE samples at tan δ = 2.*

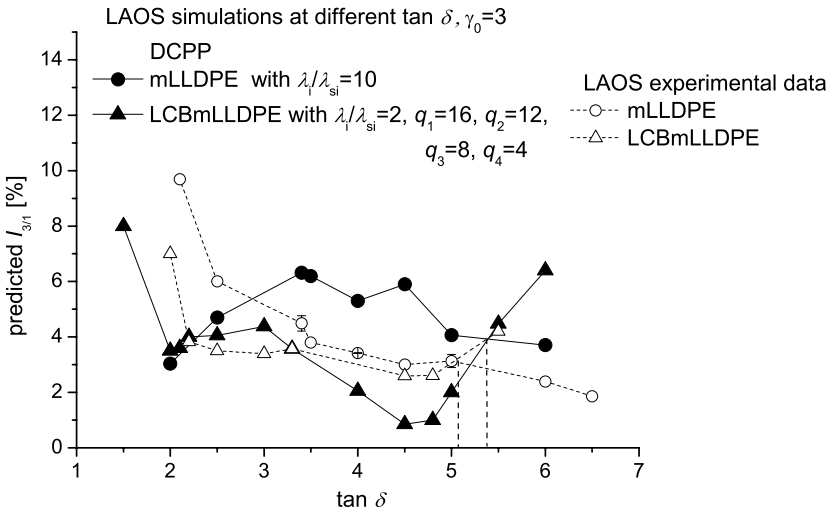

Figure 4.46: *Predicted $I_{3/1}$ using DCPP at conditions corresponding to different tan δ in the linear regime.*

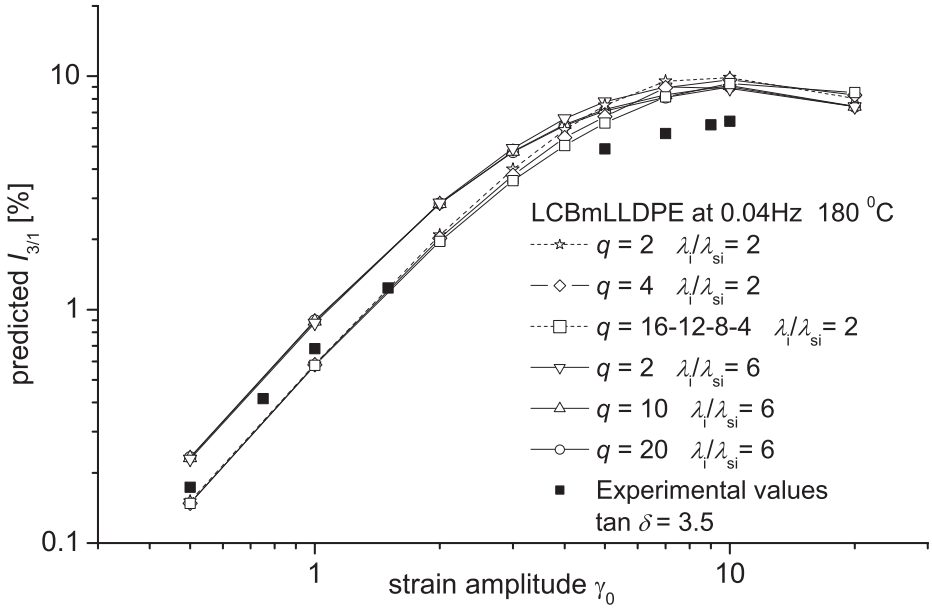

Figure 4.47: *Effect of non-linear parameters q_i and λ_i/λ_{si} on predicted $I_{3/1}$ for LCBmLLDPE at tan δ = 3.5*

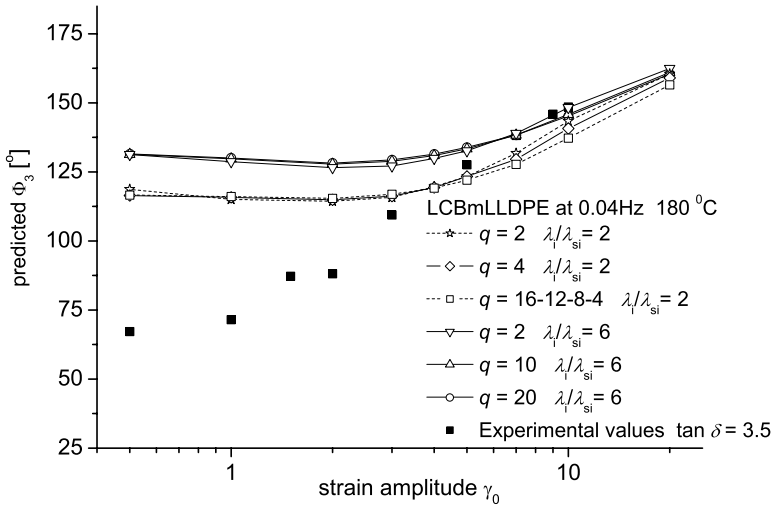

Figure 4.48: *Effect of non-linear parameters q_i and λ_i/λ_{si} on predicted Φ_3 for tan δ = 3.5 in the linear regime.*

cases in fig. 4.47, as demonstrated for an example in fig. 4.49.

Predictions for different combinations of q_i and λ_i/λ_{si} are fitted. We find that parameter *A* exhibits a very weak dependence on both non-linear parameters (A = 0.10 - 0.0002q - 0.0023λ/λ_s). Parameter *B* is very weakly dependent on number of side-arms (B = 0.25 - 0.00078q + 0.023λ/λ_s). Thus, to simplify our approach we neglect the q-dependent terms. The dependence of *A*, *B* and *C* with respect to molecular architecture for the DCPP model can be then described empirically as follows:

$$\begin{aligned} A &= 0.1 - 0.0023\lambda/\lambda_s \\ B &= 0.25 + 0.023\lambda/\lambda_s \\ C &= 2.92 - 0.02q + 0.018\lambda/\lambda_s \end{aligned} \tag{4.6}$$

An increasing number of arms causes a slight reduction on the non-linearity plateau (*A*), which can be considered as a dynamic dilution of the pom-pom molecule from its arms. Furthermore, a pom-pom with a large q has a small inverse critical strain, *B*, which means that higher deformations are needed to have $I_{3/1}$ = *A*/2 for this material. The parameter *C* is also reduced when increasing the number of arms. The ratio λ/λ_s is proportional to the number of entanglements (consequently to the total length) of the backbone chain in a pom-pom molecule (see eq. 2.19). Thus, one can conclude that pom-poms with large backbones (and hence short arms since the total molecular weight is constant) present low non-linearity plateau, high inverse critical strain and large log($I_{3/1}$)-log(γ_0) slopes. The non-linearity in a LAOS flow of the pom-pom chain with large λ/λ_s increases at smaller

deformations but reaches a lower plateau, compared with pom-poms with the same number of arms but of shorter backbone. Consequently $I_{3/1}$, as predicted from the DCPP model and the non-linearity of LCBmLLDPE can be empirically expressed as:

$$I_{3/1}(\gamma_0) = (0.1 - 0.0023\lambda/\lambda_s) \times (1 - \frac{1}{1 + ((0.25 + 0.023\lambda/\lambda_s)\gamma_0)^{(2.92-0.02q+0.018\lambda/\lambda_s)}}) \quad (4.7)$$

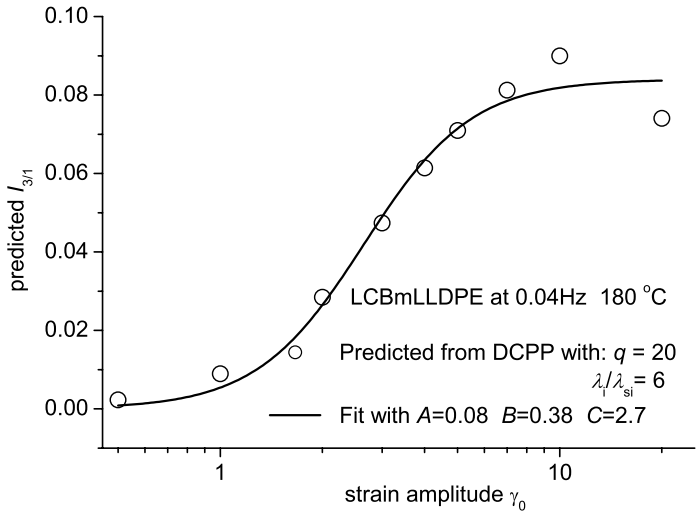

Figure 4.49: *Predicted $I_{3/1}$ for different strain amplitudes from DCPP with q_i = 20 and λ_i/λ_{si} = 6, and $I_{3/1}(\gamma_0)$ from eq. 1.47 for parameters A = 0.08, B = 0.38 and C = 2.7.*

A comparison between the *A, B* and *C* parameters derived from fitting the predicted $I_{3/1}(\gamma_0)$ and those calculated by eq. 4.6 is depicted in fig. 4.50, 4.51, and 4.52 respectively.

It is worth mentioning that the parameters *A* and *B* show a minor dependence with respect to *q* as compared to parameter *C*. However, although the rheology of the melt is described with a 4-mode model, it is remarkable that the predictions show a quite low deviation with respect to the experimentally estimated values.

In order to estimate the effect of the DCPP molecular parameters on $I_{3/1}(\gamma_0)$ and $\Phi_3(\gamma_0)$, a broad range of deformations is needed in the LAOS simulations. Within the present paragraph, LAOS with strain amplitudes $0.5 < \gamma_0 < 20$ is studied. Experimental results shown in fig. 4.11, 4.12 suggest that a correlation is not easily identified between increasing $I_{3/1}(\gamma_0)$ and branching levels. Thus, it is expected that a higher number of arms or a higher ratio of orientation/stretching relaxation times λ_i/λ_{si} do not result in monotonically

increasing intensities and phases for LCB polyethylene in the whole range of simulated γ_0.

The above conclusion is in contrast with Schlatter et al. [Schlatter 05]. However, in the present work LAOS flow is predicted using the DCPP model for a broader range of applied strain amplitudes and frequencies, while Schlatter could only apply strain amplitudes of up to γ_0 = 4. For most simulation cases, $I_{3/1}$ and Φ_3, are not sensitive with respect to *q* at low strain amplitudes ($\gamma_0 < 3$). Generally, at constant number of arms q_i, an increased ratio of λ_i/λ_{si} leads to a higher $I_{3/1}$. This ratio is proportional to the backbone length as suggested by McLeish and Larson [McLeish 98], and Inkson et al. [Inkson 99], who suggested that $\lambda \propto {M_b}^3$, $\lambda_s \propto {M_b}^2$ hence $\lambda/\lambda_s \propto M_b$. Consequently, higher non-linearity for a broad range of shear deformations suggests that the polymer melt behaves like a "blend of pom-poms" with longer backbones. Hence, the time-determining step of the stress relaxation is the orientation process (since $\lambda >> \lambda_s$). Furthermore, simulations show the same trend as the experimental FT-Rheology results. Under conditions corresponding to high tan δ in the linear spectrum, LCBmLLDPE has a higher predicted non-linear behaviour than mLLDPE. This result agrees qualitatively with experimental data for the whole range of investigated tan δ (fig. 4.46).

The relative phase Φ_3 is mainly affected by molecular architecture (*q*, λ_s), for LAOS simulation with strain amplitudes $\gamma_0 > 3$ (fig. 4.48). The DCPP model overestimates Φ_3 at low strains ($\gamma_0 < 2$) for this specific sample, which increases with increasing λ/λ_s and levels off for $\gamma_0 < 3$. This could suggest that a longer backbone introduces higher non-linearities ($I_{3/1}$), but with a higher phase value Φ_3 as compared to the main material response. Furthermore, higher number of side-arms results in lower Φ_3 for the same λ/λ_s ratios.

The behaviour of this "pom-pom material" in the non-linear regime depends on branching level and relaxation mechanism. From eq. 4.7 we could suggest that the plateau *A* of the non-linearity of a material (see eq. 1.47) has a weak dependence on both number of arms and relaxation mechanism. The inverse critical strain amplitude 1/*B* depends strongly only on the backbone length and consequently on the length of the arms (since M_{total} = $M_{backbone}$ + 2qM_{arms}). Parameter *C* depends on *q* and λ/λ_s and decreases with increasing number of arms and decreasing backbone length. Parameter *A* has a typical value of 0.1 $\pm$ 0.05 for LCB PE. For LCBmLLDPE modelled by DCPP, we find values of *A* between 0.08-0.1. Parameter *B* is typically 0.2, suggesting that a polyethylene "pom-pom" blend reaches the half-maximum non-linearity at around $\gamma_0 \approx 5$. Parameter *C* is generally approximately 2 [Neidhöfer 03b, Helfland 82, Pearson 82]. The DCPP model overestimates *C*, and predicts typical values around 2.9. In order to obtain a lower value of *C* we suggest that the LCBmLLDPE structure can be decoupled into a blend of "pom-pom" macromolecules with a high number of branches and shorter backbones. For the specific case of LCBmLLDPE, in order to minimize the deviation between experimental and predicted values of parameters *A*, *B*, *C*, we choose: λ_i/λ_{si} = 3, q_i = 30. In addition, Φ_3 will be lower for a large q_i and lower λ_i/λ_{si}, thus reducing the deviation between experimental FT-Rheology data and LAOS simulation results.

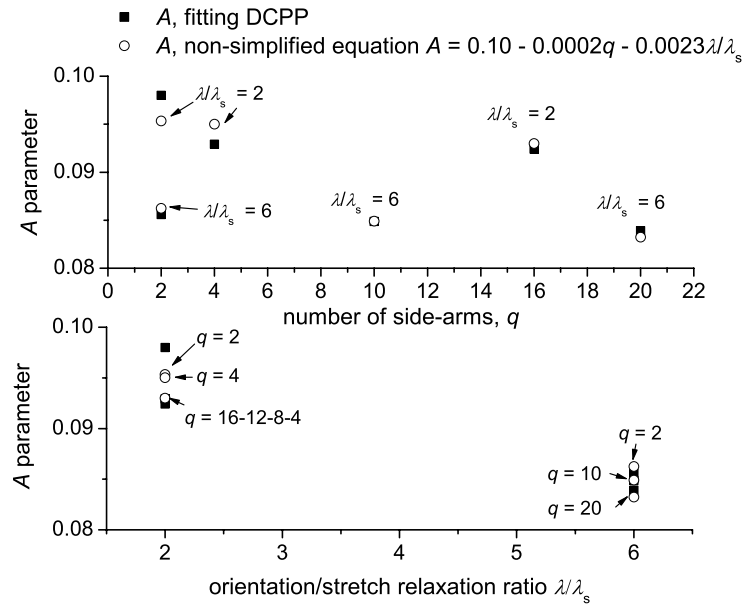

Figure 4.50: *Comparison between parameter A values derived from fitting predicted $I_{3/1}(\gamma_0)$ and empirical descriptive eq. 4.6. Both q_i and λ_i/λ_{si} are varied in all cases.*

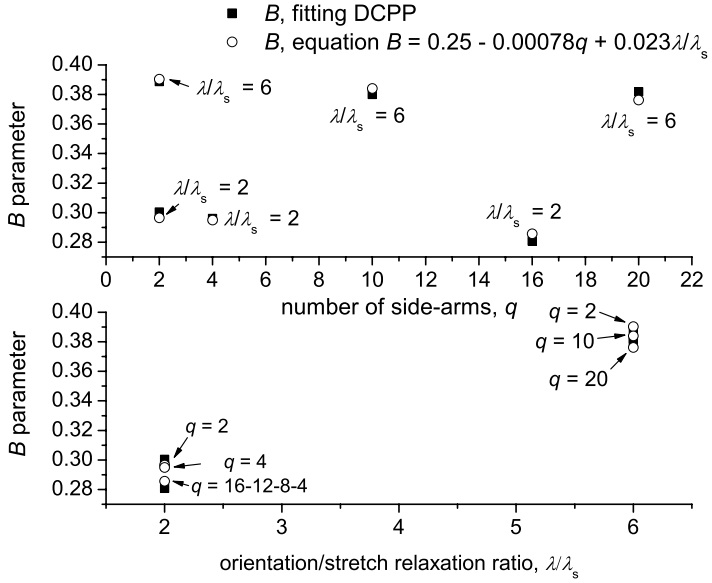

Figure 4.51: *Comparison between parameter B values derived from fitting predicted $I_{3/1}(\gamma_0)$ and empirical descriptive eq. 4.6. Both q_i and λ_i/λ_{si} are varied in all cases.*

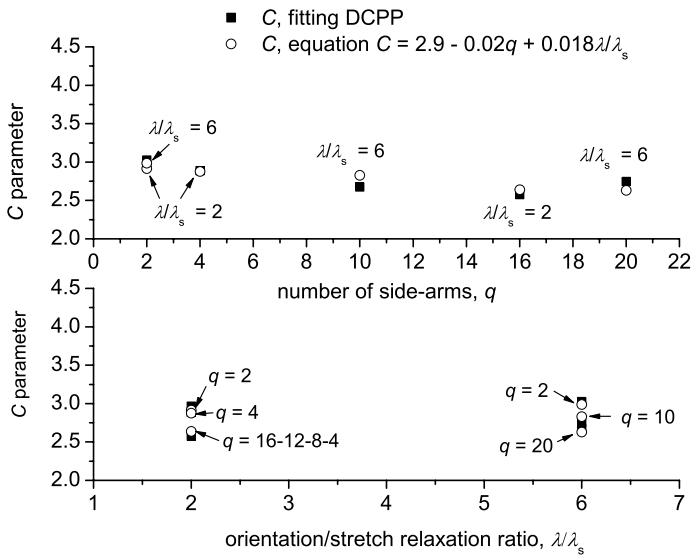

Figure 4.52: *Comparison between parameter C values derived from fitting predicted $I_{3/1}(\gamma_0)$ and empirical descriptive eq. 4.6. Both q_i and λ_i/λ_{si} are varied in all cases.*

4.3.2 Normal forces in LAOS flow simulation

As discussed above, from the LAOS flow simulation using the DCPP model the extra-stress tensor components can be predicted for the modelled polyethylenes. From T_{11} - T_{22} (or T_{xx} - T_{yy}) the first normal stress difference, N_1 is calculated. The predicted (and measured if experimentally possible) N_1 can be a promising quantity for discriminating branched topologies [Graham 01] and is investigated within this chapter. An example of the predicted N_1 during LAOS, for two LCB polyethylenes modeled via the DCPP, is shown in fig. 4.53.

The predicted shear stress is also shown in fig. 4.53 for both polyethylenes. The discrimination between the two LCB samples modeled via DCPP is more pronounced when studying the normal forces, even for a small change of the side-arms parameter q. One can differentiate between the two topologies using the N_1 time data, or the intensity of the higher harmonics from the corresponding FT spectrum. Three spectra for the studied samples are given in fig. 4.54, with a peak at 0 Hz (as expected due to the time data offset) and the highest harmonic at $2\omega_1/2\pi$ as predicted for normal forces in LAOS flow [Owens 02]. The intensity of the peaks at even multiples of the excitation frequency is similar for the two LCB materials modelled by DCPP. However, the intensities for the case of a linear PE as modelled with the DCPP are significantly lower, demonstrating the applicability of N_1 time data from LAOS

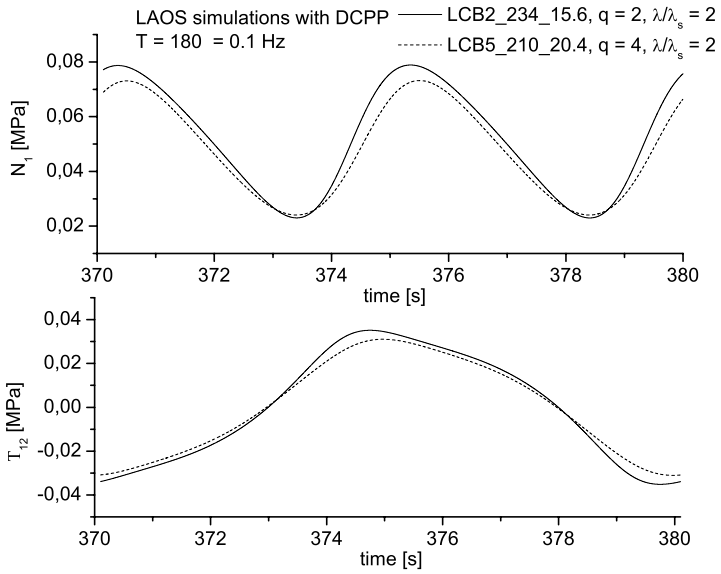

Figure 4.53: *Predicted first normal stress difference for two LCB PE with different q_i and λ_i/λ_{si} DCPP parameters. LAOS flow simulation is with $\omega_1/2\pi$ = 0.1 Hz, γ_0 = 5 and T = 180 °C. Predicted shear stress T_{12} also shown.*

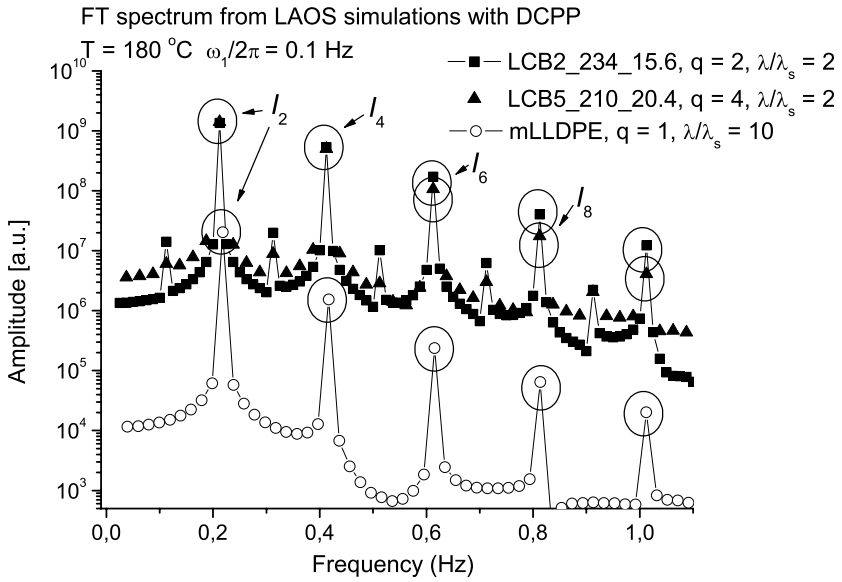

Figure 4.54: *FT-spectra for the first normal stress difference, predicted for two LCB PE with different q_i and λ_i/λ_{si} and a linear PE as modelled via the DCPP. LAOS flow simulation is for γ_0 = 10.*

as a potential parameter for discriminating linear and branched polyethylenes, in agreement with Graham et al. [Graham 01].

4.4 Summary on experimental FT-Rheology and LAOS simulations for linear and LCB industrial PE

Within this chapter, the rheological behaviour of linear and long-chain branched polyethylenes in the non-linear rheological regime is investigated for the case of pure materials and linear/LCB PE blends and for a broad range of deformations via FT-Rheology. The effects of topology, molecular weight and molecular weight distribution are correlated to the relative intensity $I_{3/1}$ and phase, Φ_3 of the resulting third harmonic obtained in LAOS experiments. Long-chain branched polyethylenes exhibit higher non-linearities than linear polyethylenes of similar molecular weight and molecular weight distribution. In the case of linear topology, $I_{3/1}$ is found to increase with increasing M_w and *PDI*. The van Gurp-Palmen method is extended by including the phase of the third harmonic, Φ_3^0, extrapolated at zero strain amplitude. The quantity Φ_3^0 is found to be sensitive to the presence of LCB. Consequently, the samples are categorized into linear and LCB using the measured Φ_3^0 in the extended van Gurp-Palmen plot. With this phase analysis a separation between the effects of LCB and molecular weight distribution in the non-linear rheological response is achieved.

Additionally, the optimum experimental conditions for differentiating linear and branched polyethylenes using LAOS and FT-Rheology are investigated. Polyethylenes have low activation energy and therefore a rather weak temperature-dependence. Thus, strain sweep is a more appropriate test method for studying the non-linear rheological behaviour of these samples, with the current experimental setup. Experimental FT-Rheology is optimized with respect to the sensitivity towards LCB. The optimum conditions are found to be around: T = 180 °C, $\omega_1/2\pi$ = 0.1 Hz, with γ_0 = 0.5 and γ_0 = 3. Polyethylenes containing LCB are found to produce higher non-linear behaviour at low frequencies and at conditions corresponding to higher tan δ values in the linear spectrum (flow region).

Although the minimum detected LCB and SCB degree via FT-Rheology is quite low, 0.1 LCB + SCB /1000 CH_2 as estimated from ^{13}C melt-state NMR, the information about the structure of the industrial PE samples is not complete. The above estimation is an average of the branching of all chains in the melt. However, one needs to know what fraction of the macromolecules are branched in a melt, which is polydisperse with respect to molecular weight and topology. Additionally, it is useful to determine at which minimum amount the LCB chains influence the rheological properties of PE. Thus, the limits and sensitivity of FT-Rheology towards presence of LCB chains in a material need to be investigated. Since no monodisperse model polyethylene sample with known LCB/1000 CH_2 and type of LCB (combs, H-shaped, pom-pom, tree-like branching) is available, well-characterized industrial

linear PE blended with LCB PE, of known branching content, at different known ratios are studied. The blended components have either similar narrow (mPEmix) or similar broad (Lmix) molecular weight distribution and a similar SCB type. Thus, by applying LAOS and FT-Rheology the effect increasing concentration of the LCB component, specifically the ratio of LCB to linear chains in the polydisperse melt, is probed.

From oscillatory shear measurements in the linear regime one can clearly detect the presence of LCB in the melt for LCB polyethylene concentrations $>$ 30 wt %. However, the goal is not only to present a more sensitive method for detecting LCB, but additionally to obtain information about the non-linear behaviour of PE with varying topology. Hence, LAOS is applied with strain sweeps in a fixed excitation frequency (0.1 Hz) and temperature (180 °C), along with frequency sweeps at low strain amplitude (γ_0 = 0.5) for studying $\Phi_3^0(\omega)$. The analysis with FT-Rheology shows that LCB PE component of a concentration as low as 5.5 wt % in a linear melt and a linear component of weight fraction as low as 5.5 wt % in a LCB polyethylene sample, can be clearly differentiated and are adequate to change effectively the non-linear rheological properties of the material.

Furthermore, the quantities used to quantify the non-linear behaviour of the polyethylenes, $I_{3/1}(\gamma_0)$, $\Phi_3(\gamma_0)$, Φ_3^0, as well as the parameters derived from fitting the sigmoidal $I_{3/1}(\gamma_0)$ (*A*, *B*, *C*, *D* in eq. 1.47 and 1.51), increase monotonically with increasing concentration of LCB species, demonstrating the dependency of the non-linearity on the topology of polymers, specifically polyethylene. Parameters *A*, *B* and *D* are found to increase monotonically with increasing LCB content, which confirms the fact that they are functions of topology and i.e. relative branching degree (per chain) as well as relative amount of branched species in a melt with linear PE, molecular weight and molecular weight distribution.

Finally, the miscibility and stability of the blends is investigated by means of rheological techniques, already presented by other authors [Kwag 00, Han 87]. The storage and loss viscosity, as well as the storage and loss moduli, as measured in the linear regime, are analyzed for the purpose of assessing the miscibility of the studied blends. Additionally the complex modulus and the non-linearity of the blends under LAOS for more than 2h are recorded. Taking into consideration the results from rheological tests of miscibility of the blends (Cole-cole plots, G'' vs. G' plots and mixing rules), we are confident that they are miscible. No phase separation takes place. The only property that varies in the blends and results in increasing non-linearity ($I_{3/1}(\gamma_0)$) with higher phases ($\Phi_3(\gamma_0)$, Φ_3^0) is the LCB/linear chains ratio.

The non-linearity change with increasing deformation is correlated to the molecular parameters of a “pom-pom” blend, specifically the number of arms and the ratio of orientation-to-stretch relaxation times. We achieve this by performing LAOS simulations with the DCPP model. In order to extend our study of LAOS flows for different polymer topologies with the DCPP, model samples such as H-shaped, combs, or tailor-made “pom-pom” polyolefines are needed in combination with blended linear and branched structures. However, FT-Rheology using a constitutive equation based on molecular architecture enables

the qualitative prediction of non-linear behaviour for LCB polymers.

Graham et al. [Graham 01] state that extensional flows are more discriminating for nonlinear stretch characteristics and a more sensitive way to determine stretch characteristic times in Pom-pom model. This difference from shear flows lies in the measured stress tensor component and the orientation way of molecules. The authors suggest that the first normal stress difference in exponential shear could be a more sensitive quantity to use for stretch and orientation of the pom-pom macromolecule determination. This motivates numerical simulations of polymers with varying topology, as quantified by the molecular structure related parameters of the DCPP model, on the resulting normal stress difference, N_1, during a modelled LAOS flow. This promising method can be extended experimentally by accurately measure the normal forces during a LAOS experiment, especially for the samples studied in chapters 3 and 4, for which normal forces are already observed to be prominent due to their high molecular weight. However, the experimental equipment needed to conduct these type of measurements are not yet available.

Chapter 5

Investigation of flow instabilities via FT-Rheology

5.1 Experimental and theoretical studies of flow instabilities in polymers-short literature review

Flow instabilities are time-dependent phenomena occuring in flows which are supposed to be in steady-state. For example, a time-dependent shear stress response of a material under application of a steady shear strain, or oscillations in pressure drop of a polymer melt during capillary flow under constat inflow rate. Instabilities in viscoelastic flows are of great practical importance and therefore a subject of significant and growing interest for rheologists in the last decades [Graham 95, Hatzikiriakos 91, Larson 92]. Industrial important materials such as polyethylene (LDPE and HDPE), present flow distortions and surface features like sharkskin (small irregular distortions on surface, roughness), or more extreme, for example gross fracture and helical extrudate distortions, during capillary flow or extrusion (see fig. 5.1). The above occurring flow distortions are not only distinguished and quantified by the appearance of the extrudate (both amplitude and periodicity of surface oscillations), but additionally by the critical conditions for the onset of these instabilities and the flow characteristics, e.g. critical shear rate for sharkskin or stick-slip during capillary flow.

The investigation of such phenomena that occur during polymer flow can lead to the development of a robust method to control the quality of extruded products. Additionally, understanding the mechanisms behind the onset and development of flow instabilities can provide us with a valuable insight in the polymer melt dynamics and allow further polymer processing optimization. Whether these flow distortions are constitutive, or driven by melt elasticity, molecular structure, surface properties, flow geometry or a combination of the above is yet to be fully understood and answered. Explanations proposed for extrudate distortions include concepts of adhesion failure of the polymer to the die wall, referred

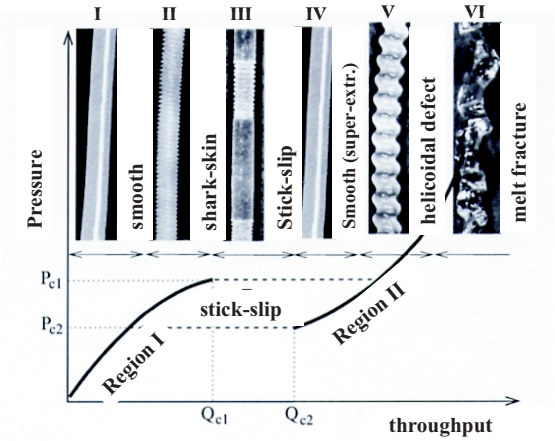

Figure 5.1: *Typical flow curve for a polyethylene melt and regions of instabilities.*

to as wall slip, and/or mechanical failure of the material itself, referred to as constitutive instabilities [Larson 92, Wang 96b]. The first phenomenon can be modeled by replacing the boundary condition of a vanishing wall velocity (no-slip condition) with a finite value that depends on wall shear stress and/or strain history of the fluid [Pearson 68]. On the other hand, a constitutive instability occurs when the relationship between shear stress and shear-rate is non-monotonic [Larson 92]. However, it is difficult to distinguish experimentally between the two origins of the instabilities, due to the fact that both result in the same macroscopically observed effects.

Capillary and extrusion flows are not the only cases where instabilities might occur. It is generally accepted that instabilities may occur in parallel plate or cone-plate shear flow [Larson 92], for example meniscus distortions as seen in fig. 5.2. This phenomenon is often observed for polymers even at low Reynolds numbers (*Re*) with negligible inertia effects. Larson actually separated the distortions into irregular non-axisymmetric “vortexes” and axisymmetric indentations of the meniscus or edge fracture [Larson 92]. One different abnormality that can possibly occur is the elastic instability, in which a meniscus distortion is not an essential feature. This instability is generally observed in Boger fluids, i.e. dilute or moderately concentrated solutions of high molecular weight polymers. There are evidence that the instability phenomena are related to a radial driving force created by the first normal stress difference (N_1) in a curvilinear shearing flow [Larson 92].

Since polymer melts subjected to LAOS may exhibit complicated nonlinear periodic responses related to meniscus distortions and wall slip [Chen 94, Larson 92], this flow presents a practical way for studying the dynamics of instabilities and the effect of rheological properties with high sensitivity. Additionally, LAOS experiments can provide predictions for the performance of the investigated melts in a capillary flow and can connect structure to processability. Henson and Mackay [Henson 95] studied slip effects of monodisperse polystyrene melts (with M_w = 49 kg/mol, 104 kg/mol, 198 kg/mol and 392 kg/mol) and found that all

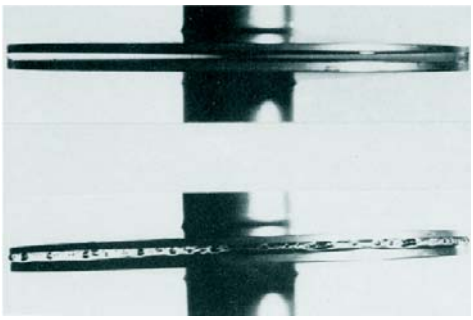

Figure 5.2: *Photographs of polymer solution at two shear rates in a cone-plate rheometer with radius = 50 mm and angle 2.3°. For $\dot{\gamma}$ = 1.58 s^{-1} the fluid surface is smooth and for $\dot{\gamma}$ = 158 s^{-1} meniscus distortions are observed. Adapted from Kulicke et al. [Kulicke 79]*

exhibit slip behaviour. They discussed three possible models to describe slipping of polymer chains: (1) the adsorbed layer, (2) the disentangled layer and (3) the true slip model, and used a parameter *b*, introduced by de Gennes [deGennes 85] to quantify the slip phenomenon. This parameter corresponds to the extrapolated distance to zero velocity in a parallel plate flow and is comparable to the average thickness of a polymer melt droplet during spreading on a smooth wall. According to this model, a liquid flowing over a smooth solid wall will display a length b comparable to the molecular size, d [deGennes 85]. The slip velocity is then given by:

$$v_s = \frac{d}{\eta_M}\sigma_w \tag{5.1}$$

where *d* is a length of molecular dimensions, η_M is the shear viscosity of a liquid of monomers (with the same interactions, but no entanglements) [deGennes 85]. The wall shear stress is given by σ_w. For the linear viscoelastic regime eq. 5.1 can be written as follows:

$$v_s = \frac{d}{\eta_M}\eta_0\ \dot{\gamma}_w \equiv b\ \dot{\gamma}_w \tag{5.2}$$

where η_0 is the zero-shear viscosity of the polymer. From the reptation theory, the relation between monomeric liquid viscosity, η_M, and polymer melt viscosity is, $\eta_0 = \eta_M \frac{N^3}{N_e^3}$, where N is the number of monomers per chain and N_e the number of monomers between two entanglements. The true wall shear rate is $\dot{\gamma}_w$. This true wall shear rate in a parallel plate geometry with a gap of *H*, and the upper plate moving with a velocity ωR is given by [Henson 95]:

$$\dot{\gamma}_w = \frac{\omega R}{H + 2b} \tag{5.3}$$

The torque for a shear flow between to parallel moving plates of radius *r* is known:

$$M = 2\pi\eta_0 \int_0^R \dot{\gamma}_w \, r^2 dr \tag{5.4}$$

where *R* is the maximum plate radius. Combining eq. 5.3 and 5.4 and integrating we obtain the nominal wall shear stresses ($2M/\pi R^3$) at the gap *H* and at infinite gap, σ_N and $\sigma_{N\infty}$, respectively. Hence the ratio of the stresses will be as follows:

$$\frac{\sigma_N}{\sigma_{N\infty}} = 1 + \frac{2b}{H} \tag{5.5}$$

Henson and Mackay [Henson 95] used eq. 5.5 to quantify slip in the monodisperse polymer melts and made the needed adjustments and approximations to import in this model the three different concepts mentioned above. All studied melts were found to exhibit slip behaviour during oscillatory shear in parallel plate geometry. In the linear regime, the slip velocity was found to be proportional to the shear rate. This proportionality was related to the molecular weight with a power index of ∼1.1. This experimental result is not consistent with the theory of de Gennes since $b \propto \eta_0 \propto M_w^3$. The authors attributed this deviation to lack of data (only three PS melts studied) which may have caused errors in determining b. A study of wall slip for concentrated high molecular weight PS (M_w = 109×10^3 kg/mol and 289×10^3 kg/mol) was presented by Reimers and Dealy [Reimers 98]. The authors quantified nonlinear viscoelasticity using step-strain experiments, LAOS, FT-Rheology and birefringence measurements. Although they state that the instable behaviour at a high shear stress is due to wall slip, it was suggested that the polymer does not loose adhesion. A more plausible hypothesis according to the authors, is a change in interaction between adsorbed molecules and bulk polymer chains of the solution above a critical stress value. Large amplitude oscillatory shear was indeed used, to reveal the dynamics of slip, since stress exceeds the critical slip value for brief periods of time. High non-linearities were observed in the LAOS response and quantified via FT-Rheology. The results demonstrated the dynamic nature of slip and the resulting intensities and phases of the higher harmonics were found to be sensitive to molecular weight. Chen et al. [Chen 94] investigated fracture and flow instabilities in a parallel plate rheometer for PS melts (with M_w = 10 kg/mol, 13 kg/mol, 32 kg/mol, 184 kg/mol and 233 kg/mol) and solutions by LAOS, and discussed three possible reasons for the recorded wave forms, namely: (1) viscous heating, (2) constitutive instability and (3) cohesive/adhesive failure. They conclude that high non-linearities in LAOS signals cannot be caused by viscous heating, however they can be attributed to a combination of both constitutive instabilities and polymer-surface adhesive failure. Graham [Graham 95] modelled the nonlinear dynamics of LAOS and suggested that both viscoelasticity and

dynamic slip are necessary to explain the instabilities of polymer melts under oscillatory shear. The author related complicated non-periodic response in LAOS with exhibited wall slip and suggested that both fluid elasticity and a dynamic slip (or a certain memory in the instability), are necessary for a non-periodic stress response to be observed.

The wall slip of HDPE melts in sliding plate and capillary geometries was extensively investigated by Hatzikiriakos and Dealy [Hatzikiriakos 91, Hatzikiriakos 92a, Hatzikiriakos 92b]. A sliding plate rheometer has the advantage of absence of pressure gradient and entrance effects from the flow, as well as the convenient modification and control of the polymer-wall interface. Utilizing capillary flow measurements, the critical shear stress for slip occurrence of the particular HDPE resin (M_w = 177.8 kg/mol, *PDI* = 9.4) was found to be 0.09 MPa. They observed a clear dependence of slip velocity on shear stress using the Mooney method [Mooney 31]. By repeating the measurements at different temperatures a dependence of the slip velocity on temperature was revealed. From the analysis of the slip velocity as a function of shear stress in a capillary flow, the following relation was extracted to describe the phenomenon:

$$\begin{aligned} v_s &= 0, \quad \sigma < \sigma_c \\ v_s &= \alpha\sigma^m, \ \sigma > \sigma_c \end{aligned} \tag{5.6}$$

where σ_c is the critical shear stress defined as the onset of melt slip. For stresses lower than σ_c, the slip velocities, as determined by extrapolating eq. 5.6 to lower stress values, were found to be approximately zero. The slip coefficient, α, was found to be a function of temperature. The derived values for the exponent *m* were ~ 3 [Hatzikiriakos 91]. The authors repeated the experiment with surfaces coated with fluorocarbon spray, used the $v_s = \alpha\sigma^m$ equation to fit the resulting stress and a dependence of α was found on the interface conditions. However, no changes were recorded for the exponent *m* (the slope of v_s versus σ in the log-log plot was not significantly changed).

The polyethylenes were additionally exposed to LAOS flow and the resulting shear stress was analyzed. The stress overcame the critical value for short periods of time in every cycle and since a relaxation time is involved in the melt slip process, several cycles were needed for the polymer to slip. Wall slip became apparent by the decrease of the stress amplitude after some cycles. Finally a quasi-steady state was reached after the gradual decrease of maximum stress. The complex stress waveforms were attributed to slip by the following interpretation: Above a critical stress, the polymer looses adhesion with the wall, slip occurs and the stress is decreasing. This nominal stress decrease causes a periodic regain of adhesion and stress increases again. The authors separated the different types of LAOS signals into four categories for increasing number of cycles: (a) non-sinusoidal due to non-linear viscoelasticity of the melt, (b) decrease in stress amplitude due to slip presence

for non-sinusoidal signals, (c) increasing non-sinusoidal and asymmetric character of the stress as for an elastic Bingham fluid in Yoshimura and Prud'homme [Yoshimura 87] and finally, (d), further distorted signals resembling chaotic systems, where stress exhibits an aperiodic deterministic behavior which is very sensitive to initial conditions [Thompson 87]. The LAOS stress waveforms were correlated also with the deformation history and rest time between experiments and a strong dependence on the initial conditions is found for the recieved waveforms. The slip phenomenon is often empirically modelled by an algebraic relationship between slip velocity, v_s (non-vanishing fluid velocity at the wall), and shear stress, σ [Graham 95, Hatzikiriakos 91, Henson 95, Larson 92]:

$$v_s = f(\sigma) \tag{5.7}$$

Equation 5.6 is valid under the assumption that the slip velocity adjusts instantaneously to the wall shear stress. However, Lim and Schowalter [Lim 89] suggested that the transition from the slip to the stick condition was gradual and showed characteristics of a relaxation process. Thus, to account for this experimental observation a "memory slip model" was introduced by Hatzikiriakos and Dealy and [Hatzikiriakos 92a]:

$$v_s + \lambda_{slip}\, \dot{v}_s = f(\sigma) \tag{5.8}$$

where λ_{slip} is a relaxation time for slip and the slip velocity is a nonlinear function f of the stress history. Combining eq. 5.8 with 5.6 one derives a phenomenological equation used to study also exponential and oscillatory shear [Hatzikiriakos 91]:

$$v_s + \lambda_{slip}\frac{dv_s}{dt} = \alpha\sigma^m \tag{5.9}$$

For steady shear the second term on the left hand of the eq. 5.9 is zero and eq. 5.6 is recovered. The validity of the above equation was examined by observing slip in exponential shear flow. In this particular study [Hatzikiriakos 91], the "slip relaxation time", λ_{slip}, was determined from exponential shear experiments between 0.20 s and 0.25 s.

Furthermore, the resulting stress time signal from LAOS experiments was compared to the one theoretically predicted via the combination of eq. 5.9 with a constitutive model, in particular a Maxwell model. For the eq. 5.9, slip parameter, α, was taken as a simple time function (assumption of a linear proportionality, α = 0.0625*t*) to cope for the time-evolution

of the slip with increasing number of deformation periods. This empirical model was found to qualitatively predict stress signals observed in LAOS experiments. Finally, a dependence of the critical shear rate for unstable LAOS flow on excitation frequency was found. In a later study [Hatzikiriakos 92b] the same authors used the following function to determine α:

$$\alpha = \xi f_1(T) f_2(\sigma_n/\sigma_w) \tag{5.10}$$

where ξ is a constant depending on polymer molecular structure. The function f_1 including the temperature dependence was found to be well approximated by the WLF equation (eq. 1.19). Finally f_2 is a function of σ_n and σ_w, which are the normal and wall stresses respectively. From modeling capillary flow of HDPE/LDPE blends, the authors concluded that the critical wall stress for slip, σ_c, depends on the average molecular weight of the polymer and the polydispersity [Hatzikiriakos 92a]. The above model for slip using eq. 5.8 can be combined with any constitutive equation relating shear stress and deformation. Graham [Graham 95] applied the Maxwell model and the White-Metzner. For the latter model, the viscosity as a function of shear-rate is given by the Carreau equation. Equation 5.8 combined with a constitutive equation for stress consist a system with two dependent variables, σ_s and v_s. If however, in eq. 5.8 the relaxation process is neglected, the above equation takes an algebraic form and periodic behaviour can be predicted. This is not the case for a Newtonian fluid, thus both fluid elasticity and dynamic slip are necessary for non-periodic response [Chen 94, Graham 95]. Graham indeed predicted LAOS signals for various combinations of *De* and parameters for the function f(σ) [Graham 95]. At high strains harmonics at even multiples of the excitation frequency ($2\omega_1$, $4\omega_1$,...etc.) were predicted in the FT-spectrum. Finally it was stated that quantitative reproducibility of particular chaotic behaviour in LAOS is impossible, due to the sensitivity towards the initial conditions, which is in agreement to the experimental findings in the present work (e.g. fig. 3.7 and 3.11).

The concept of a relation between molecular structure and sharkskin was discussed by Allal et al. [Allal 06] following the work of Wang et al. [Wang 96b]. Several models were discussed for the formation and propagation of surface flow distortions during capillary extrusion of molten polymers. Most relevant to the present work is the concept of an existing critical shear rate for the onset of sharkskin formation, which has a temperature dependence that can be described by the WLF shift factors and increase with increasing polydispersity and/or temperature. Allal et al. assumed a critical shear rate inversely proportional to a characteristic relaxation time for extrudate distortions. Wang et al. suggested that this characteristic time is of the same order of magnitude with the terminal relaxation time. Subsequently, Allal et al. suggested that this time can correspond to the tube renewal time, as determined by Graessley [Graessley 82] and using this time they derived an equation for the critical shear rate for sharkskin onset of the following type: $1/\ \dot{\gamma}_c = d[M_w/M_e]^n$, with n = 4.3 for polydisperse PE. The prefactor d was determined in terms of molecular characteristics,

however no further explanation is provided on the theoretical background of this equation.

5.2 Motivation for studying flow instabilities via FT-Rheology

From the analysis of LAOS flow for the studied PS and PE melts in chapters 3 and 4, evidence of slip and flow instabilities are observed at large strain amplitudes. The recorded stress signals at γ_0 above a critical value present a decaying amplitude or lost periodicity, where the non-linear contributions become a function of time (e.g. fig. 3.16, 3.11). Thus, it is important to detect instabilities during polymer LAOS and discriminate their effect on FT-Rheology results from the non-linearity of the material due to structural properties (e.g. LCB). In the following paragraphs the validity of the above considerations is examined for polystyrene and polyethylene melts of various molecular weights and distributions (see Tables 3.1 and 4.1). The effect of M_w, PDI and branching content on $\gamma_{0,critical}$ for slip onset in LAOS is examined and additionally, the influence of surface type and geometry on $I_{3/1}$, $I_{2/1}$ and Φ_3 is studied. The relation of topology and specifically of branching with the onset and development of extrudate distortions during capillary flow for the PE samples is also derived, along with the correlation with FT-Rheology results for the material non-linearity. Simulations are also performed for LAOS including slip boundary conditions and some preliminary results for capillary flow simulation are presented. In this numerical study of flow instabilities, the slip equation proposed by Hatzikiriakos and Dealy [Hatzikiriakos 91] as given in eq. 5.9, is incorporated in the LAOS flow model and the resulting non-linear rheological behaviour is analyzed via FT-Rheology.

5.3 Flow instabilities in LAOS for polystyrene linear melts

Experimental examples of decaying stress amplitude are already presented for a polystyrene melt (chapter 3, fig. 3.16). The majority of the studied samples present LAOS signals for γ_0 larger than $\gamma_{0,critical}$, that can belong to the four categories mentioned by Hatzikiriakos and Dealy [Hatzikiriakos 91] (decaying amplitude, loss of periodicity). However, it must be noted that for samples of low molecular weight, typically $M_w < 100$ kg/mol for monodisperse melts, the torque signal starts to decay or looses its periodicity for large strain amplitudes which are inaccessible with the ARES rheometer. In fig. 5.3 and 5.4 the regions of non-linear viscoelastic unstable behaviour are presented for two polystyrenes, as monitored via $I_{3/1}(\gamma_0)$ and $\Phi_3(\gamma_0)$.

As a result of asymmetry in the stress signal, even harmonics may occur indicating unstable flow, in agreement with Graham [Graham 95]. Specifically, the relative intensity of

the 2^{nd} harmonic, $I_{2/1}$, is well above the noise level for deformations where instabilities take place, as seen in fig. 5.5 for the two linear polystyrene melts at 180 °C.

The 2^{nd} harmonic is reproducible and its presence is attributed to the instabilities oc-

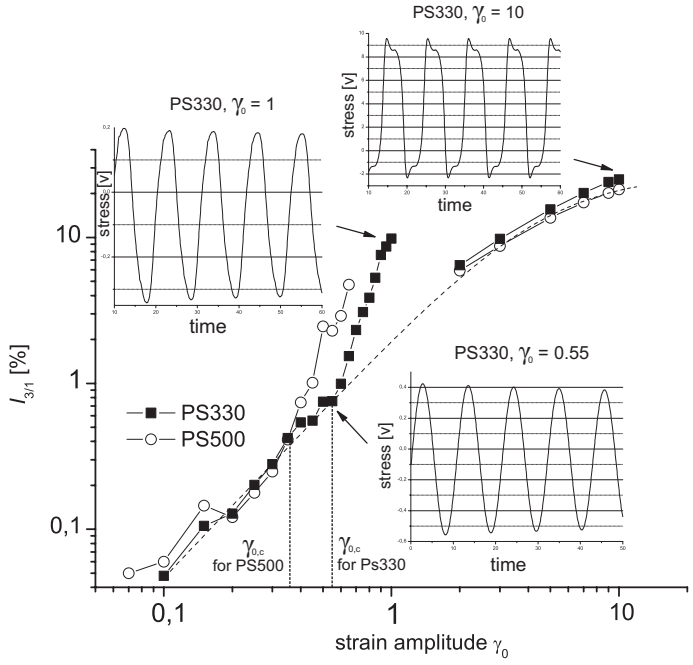

Figure 5.3: *Observed types of LAOS stress signals and $I_{3/1}(\gamma_0)$ for linear polystyrenes PS330 and PS500. Measurements with strain amplitude $\gamma_0 \geq 2$ are performed with the RPA2000. $I_{3/1}$ up to γ_0 = 1 (ARES data) shifted to correspond to cone-plate measurements of RPA2000. Dashed-line represents a fit of $I_{3/1}(\gamma_0)$ with eq. 1.47.*

curring during the LAOS flow. There is a possibility that even harmonics result from an imperfectly applied sinusoidal strain, due to inaccurate motor control. However, within this work, this factor is insignificant since FT analysis on the applied strain signal reveals no higher harmonics in the spectrum of the applied strain (intensities are below noise level).

An increased polydispersity has a significant effect in the resulting instabilities as monitored via $I_{2/1}$. The results from the linear binary blends are presented in 5.6. The relative intensity of the 2^{nd} harmonic increases dramatically with an increase in polydispersity. The presence of large macromolecules in a melt influences the even harmonics, in a way similar to $I_{3/1}$ (e.g. fig. 3.8). This outcome reinforces the argument that large macromolecules in a melt dominate the non-linear response, as demonstrated in chapters 3 and 4. The critical strain amplitude for the instabilities onset is lower and the resulting $I_{2/1}$ is larger for high molecular weight materials.

The temperature dependence of the flow instabilities is studied by repeating the experiments at higher and lower temperatures, i.e. T = 200 °C and T = 140 °C. High temperatures are already found to suppress the flow distortions in capillary flow [Allal 06, Hatzikiriakos 92a,

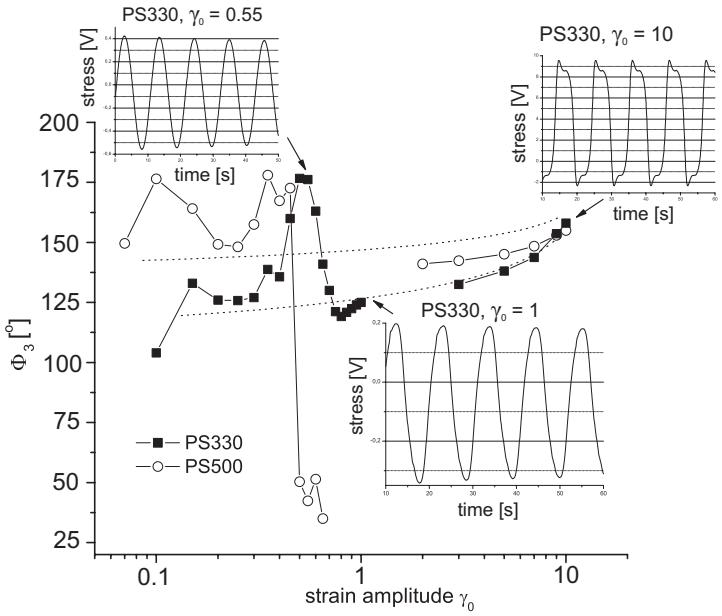

Figure 5.4: *Stress signals and $\Phi_3(\gamma_0)$ obtained for linear polystyrenes PS330 and PS500. The resulting $\Phi_3(\gamma_0)$ is sensitive to the onset of stress amplitude decay and asymmetry. Measurements at strain amplitude $\gamma_0 \geq 2$ are performed with the RPA2000. Lines are guides to the eyes.*

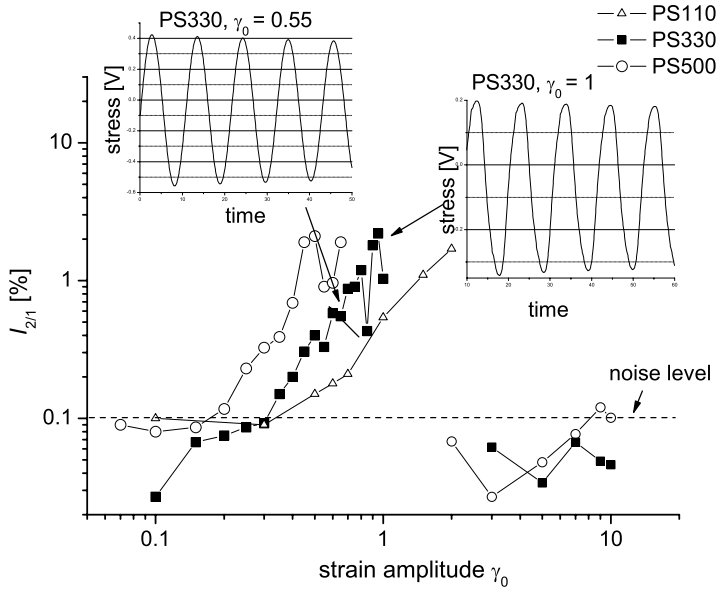

Figure 5.5: *Experimentally detected $I_{2/1}(\gamma_0)$ for PS110, PS330 and PS500, at T = 180 °C and $\omega_1/2\pi$ = 0.1 Hz. Measurements with strain amplitude $\gamma_0 \geq 2$ are performed with the RPA2000.*

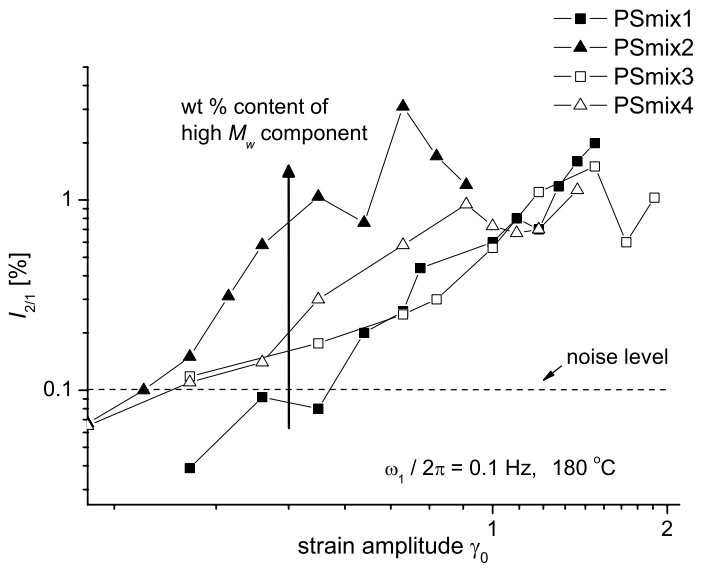

Figure 5.6: *Experimental $I_{2/1}(\gamma_0)$ for binary blends. Occurring instabilities are higher for blends with increased content of high molecular weight samples. Blend composition can be seen in Table 3.2*

Hatzikiriakos 92b]. If the argument that slip parameters have a WLF dependence on temperature is accepted, as suggested by Hatzikiriakos and Dealy [Hatzikiriakos 92b], then the recorded non-linearities in LAOS should be lower for a higher temperature. However, both the odd and even higher harmonics decrease with increasing temperature and increase with molecular weight. In fig. 5.7 the resulting intensity of the 3^{rd} harmonic is depicted for several linear polystyrene melts at 200 °C. A clear decrease of the resulting higher harmonics is indeed observed when increasing the temperature. Furthermore, if the sample is subsequently cooled down to 180 °C and the test is repeated, the material recovers its non-linear character and the resulting intensities are close to the values initially recorded. As expected, the dependence of the $I_{3/1}$ on the molecular weight distribution is conserved also at higher temperatures, where higher $I_{3/1}(\gamma_0)$ are found for linear melts of higher M_w and *PDI*.

5.3.1 Effect of flow geometry and surface type on LAOS instabilities

In this paragraph, the correlation between the onset and development of flow instabilities and the conditions of LAOS flow is examined, i.e. the surface type (steel, aluminium, fluorocarbon coated, grooved surface) and the geometry used (plate diameter and gap). The sample used is PS330, a linear polystyrene melt. Large amplitude oscillatory shear strain sweep tests are performed for PS330 using steel parallel plates with diameters of 8 mm, 13 mm and 25 mm

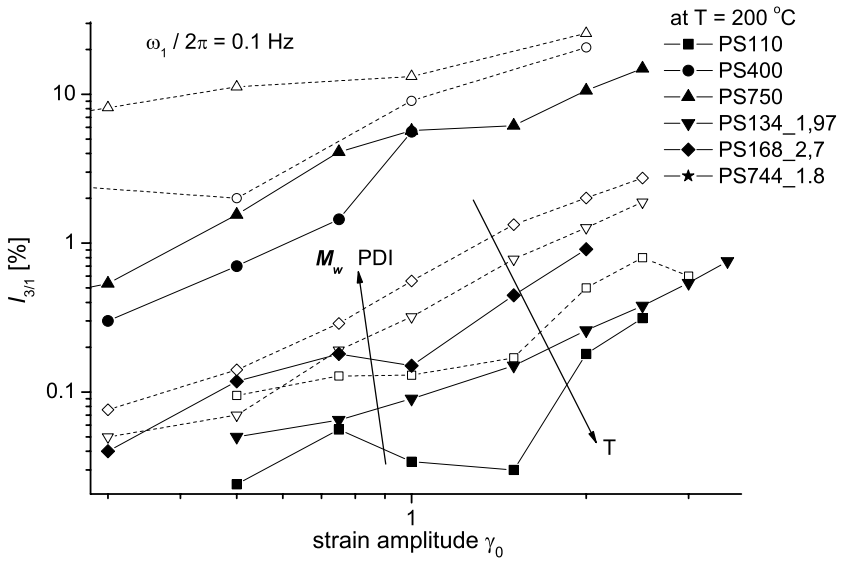

Figure 5.7: *Resulting $I_{3/1}(\gamma_0)$ for several linear polystyrene melts at T = 200 °C. Comparison with results for T = 180 °C (open-symbols with dashed lines).*

and the resulting non-linear response is analyzed with respect to the relative intensities of the 2^{nd} and 3^{rd} harmonic and the relative phase, Φ_3. As mentioned in chapter 3, all disk samples are prepared with the same procedure and no detectable degradation takes place during the measurement.

In fig. 5.8 it is shown that the plate diameter has no significant effect on the onset and development of unstable LAOS flow. However, by changing the plate material from steel to aluminium, the onset of slip is observed at lower critical strain amplitude, $I_{3/1}$ is slightly higher and $I_{2/1}$ is significantly increased. When the gap between the plates is approximately doubled, the sample behaves highly non-linear at lower strain amplitudes, in comparison with the case of a 1 mm gap. Highly asymmetric stress signals are recorded, due to the onset of secondary flows, outflow, edge fractures and generally meniscus distortions even for relatively small deformations, as indicated from the resulting FT-spectrum data (fig. 5.9).

Subsequently, the surface type is altered. In order to reinforce the slip effect, a layer of polyfluoro-1,3-dimethylcyclohexane (PFDMCH) is created on the surface of aluminium plates by chemical vapor deposition. The estimated thickness of the polymerized substance is in the order of 0.1 μm. In this altered surface the polymer melt is supposed to loose adhesion at smaller strain amplitudes, compared to a metal plate surface. Indeed, higher non-linearities are observed for strain sweeps of PS330 using these fluorocarbonated surfaces. The evidence of flow instability onset, namely a sudden slope change in $I_{3/1}(\gamma_0)$ (deviation from predicted sigmoidal curve), an increased $I_{2/1}(\gamma_0)$ above the noise level and a local maximum in the

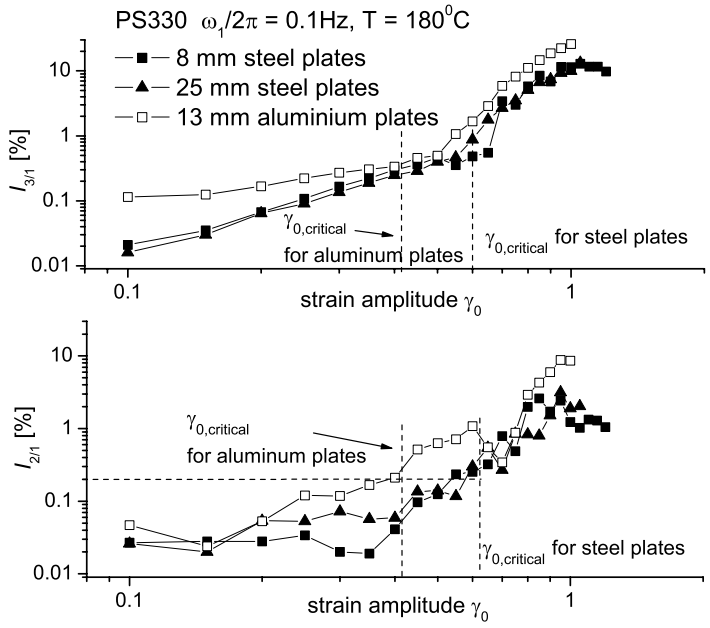

Figure 5.8: *Effect of plate diameter and material on flow instabilities as monitored via FT-Rheology at T = 180 °C, for a linear monodisperse polystyrene melt with M_w = 330 kg/mol.*

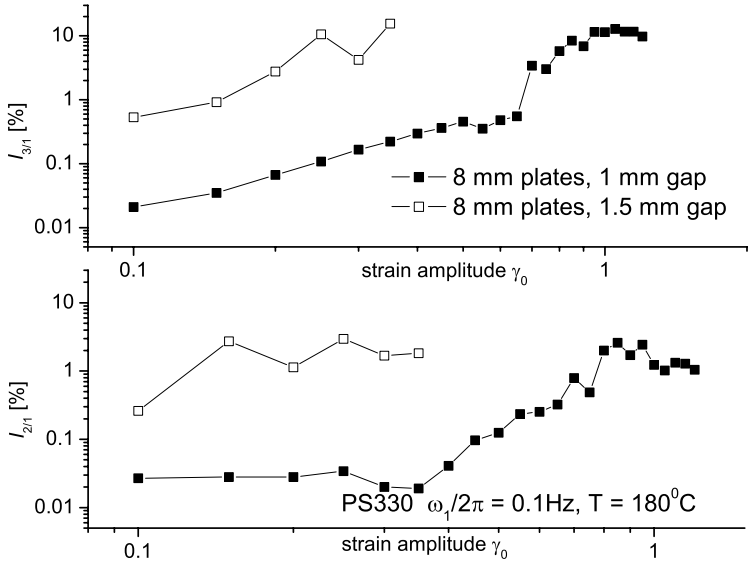

Figure 5.9: *Effect of sample thickness on flow instabilities as monitored via FT-Rheology at T = 180 °C, for a linear monodisperse polystyrene melt with M_w = 330 kg/mol, measured with steel plates.*

$\Phi_3(\gamma_0)$, are observed at lower strain amplitudes ($\gamma_{0,c} \approx 0.4$) for the specific experimental conditions. Furthermore, the resulting non-linearities for $\gamma_0 > \gamma_{0,critical}$ are higher. The measured $I_{2/1}$ for fluorocarbonated surface can be 10 times higher compared to $I_{2/1}$ recorded during strain sweep tests with normal steel surface (see fig. 5.11). One can suggest that the observed non-linear rheological behaviour is the sum of the non-linear viscoelastic character of the material (inherent non-linearity, constitutive instabilities) due to molecular characteristics and the non-linearities caused by the flow type, i.e. non-vanishing wall velocities (wall slip).

A complementary way to modify the flow pattern in order to "fingerprint" the non-linear rheological behaviour of the melts during instable flows is to create grooves, or anomalies on the metal surface, in a controlled manner. A pattern used is shown in fig. 5.10 and compared with the die design of the RPA. In the latter apparatus no decay of the stress time signal amplitude is observed, even at large amplitudes where the non-linearities are extremely high. By applying LAOS in the ARES with a grooved surface geometry it is observed that, on the contrary, the non-linear behaviour is significantly enhanced. One can conclude that grooved surfaces are not sufficient to suppress slippage. However, the flow pattern in an open-rim geometry with large grooves may contain secondary flows and the inherent complexity of the flow can be the reason for the increased $I_{3/1}(\gamma_0)$ and $I_{2/1}(\gamma_0)$, even with the absence of slip. The second factor that is different in the RPA2000 and can lead to a suppression of slippage and flow instabilities is the closed-rim feature and the high pressure applied between the biconical dies (6 MPa). White et al. indeed investigate the effect of pressure in flow instabilities and concluded that high pressure is an effective way to reduce wall slip [White 91].

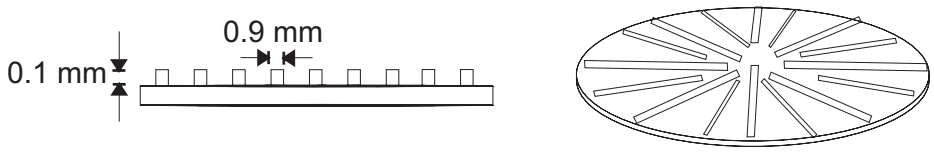

Figure 5.10: *Typical form of grooved plate open-rim geometries. Diameter can be 8 mm or 25 mm and the gap between the plates 1-1.5 mm.*

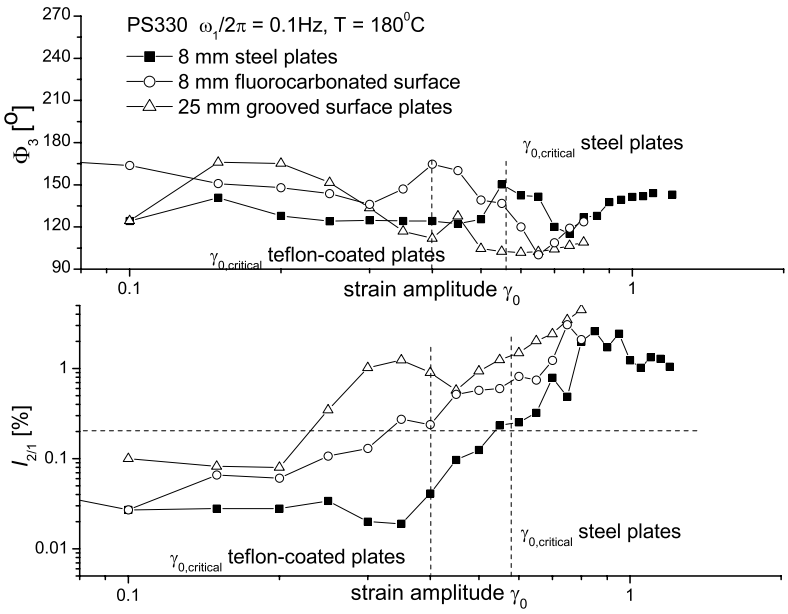

Figure 5.11: *Effect of surface treatment on flow instabilities as monitored via FT-Rheology at T = 180 °C, for a linear monodisperse polystyrene melt with M_w = 330 kg/mol.*

5.3.2 Monitoring the time evolution of slip during LAOS via FT-Rheology

Since the phenomenon of wall slip can possess a time-dependent character, the time evolution can be monitored and analyzed via FT-Rheology. The material is exposed to constant strain amplitude and frequency for a long time. Typically 100 to 200 recorded cycles are adequate. In a strain sweep at T = 180 °C, for the large γ_0, in the case of PS330 ($\gamma_0 > 0.8$), the signal is significantly distorted and extremely high non-linearities are recorded. Afterwards, the sample is subjected in a strain sweep for γ_0 = 0.01 - 2, using the fluorocarbonated surfaces, LAOS is applied with a constant γ_0 = 0.9 and excitation frequency $\omega_1/2\pi$ = 0.1 Hz for $\sim$ 30 min. The recorded $I_{3/1}$, $I_{2/1}$ and Φ_3 reveal the dynamic character of the slip and the large effect of deformation time on the flow properties. In fig. 5.12 the time signals after 100 s, 700 s and 1300 s of measurement are presented. The observed distortions of the signal result in the intensities and phases shown in fig. 5.13. One cannot deduct stringent characteristic times for slip because the flow characteristics in this case are extremely sensitive to initial conditions and deformation history. Additionally, the surface characteristics may change depending on the quality of the fluorocarbon coating (depth, surface coverage) which may be sensitive at high temperatures and increasing time under large deformations. However, it is clearly demonstrated that the non-linearities and especially the appearing 2^{nd} harmonic, can be used to monitor phenomena like slip onset and evolution. With the analysis of the FT-Rheology

spectrum one can quantify the departure of a flow from a periodic non-linear viscoelastic type to a time-dependent non-linear rheological behaviour.

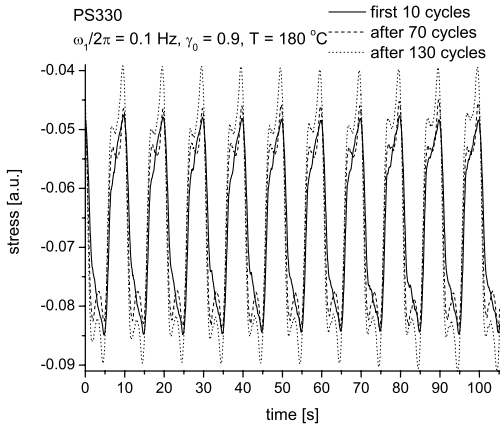

Figure 5.12: *Time signals recorded for LAOS of PS330 at different time points, at T = 180°C, using 8 mm diameter plates with fluorocarbonated surfaces and a 1 mm gap.*

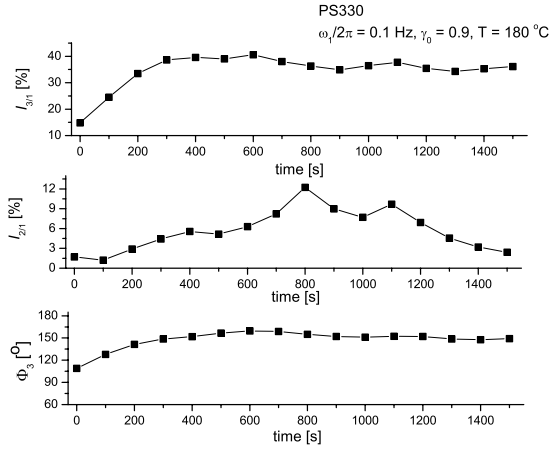

Figure 5.13: *Time evolution of slip monitored via FT-Rheology spectrum at T = 180°C for γ_0 = 0.9, with the ARES rheometer. Time t = 0 s corresponds to the initiation of LAOS after a strain sweep test and a delay time of 5 min. Plates of 8 mm diameter with a 1 mm gap and fluorocarbon-coated surfaces are used.*

5.3.3 Correlation of flow instabilities and molecular weight distribution

The critical strain amplitude for the slip onset as a function of molecular weight is presented in fig. 5.14 for linear polystyrene. For $\gamma_{0,c}$, the stress signal exhibits an amplitude decay, typically after 5 cycles the stress amplitude is 10% reduced. In literature slope values for critical shear rate for slip onset during capillary flow versus M_w/M_e of ~ 4 are reported [Allal 06]. However, for LAOS flows using steel plates the results presented in fig. 5.14 are found, where two molecular weight ranges can be distinguished. The first is of low molecular weight samples corresponding to $M_w/M_e \leq 6$, where a small dependence of the $\gamma_{0,critical}$ is found on molecular weight and $\gamma_{0,c} \propto (M_w/M_e)^{0.2}$. For an average number of entanglement per chain $N_e >$ 6-7, the power index is increased up to a value of $\sim$ 2. However, when fitting a scaling law of a $\gamma_{0,c}$ = a$(M_w/M_e)^n$ type, the determination of the exponent n can contain errors. This is demonstrated by the slight difference on the fit quality for the dashed lines in fig. 5.14, which correspond to slopes of 3 and 4. Nevertheless, a correlation of molecular weight and topological constrains (entanglements) with the onset of flow instabilities is revealed for the studied materials, wich are of linear topology and cover a wide range of molecular weight.

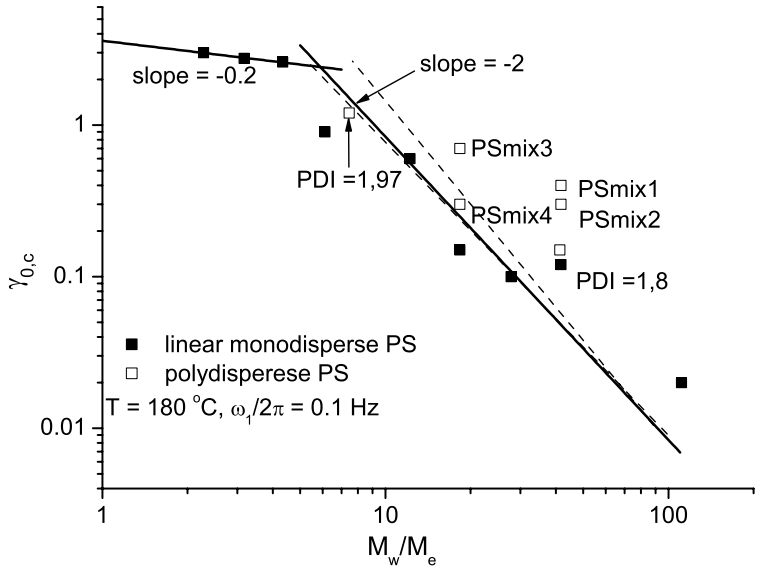

Figure 5.14: *Critical strain amplitude for stress signal amplitude decay as a function of number of entanglements per chain at T = 180°C, for LAOS with $\omega_1/2\pi$ = 0.1 Hz. Samples are linear polystyrene melts (Tables 3.1 and 3.2). Open symbols correspond to polydisperse samples. M_w for PSmix corresponds to the value of the high molecular weight component.The error in $\gamma_{0,c}$ is typically the size of the data points.*

5.3.4 Experimental procedure for determination of material inherent non-linearity with suppressed flow instabilities

It is obvious that flow instabilities are prominent when studying polymer melts via LAOS. In order to estimate the material non-linearity, especially of high molecular weight melts (typically $M_w > 100$), the contribution to the torque signal and the corresponding FT-spectrum of phenomena like wall slip must be suppressed. While the plate diameter is irrelevant, small gaps in the order of 1 mm are appropriate. The surface material is an important factor and a choice of steel plates is recommended. By using alumium as plate material, wall slip is enhanced and $I_{2/1}$ can be significantly higher (up to an order of magnitude for $\gamma_0 \approx \gamma_{0,critical}$). As expected, flow instabilities are maximized when fluorocarbon-coated plates are used, thus confirming the relation between increased non-linearities as quantified by the FT-spectrum ($I_{2/1}$, $I_{3/1}$ and Φ_3) and wall slip. Furthermore, by measuring at high temperatures, e.g. T = 200 °C for PS, the non-linearities and the occurring instabilities can be reduced. Additionally, the problem of overflow and large normal forces for an open-rim geometry (ARES) at large deformations (typically $\gamma_0 > 2$, for $\omega_1/2\pi$ = 0.1 Hz), can be controlled by using the closed-cavity geometry of the RPA2000. Since eq. 1.47 fits satisfactory the resulting $I_{3/1}$, it can be used to fit data at large γ_0 from RPA2000 ($2 < \gamma_0 < 10$), at small strain amplitudes in ARES (typically $0.1 < \gamma_0 < 0.5$) and predict the non-linearity for the range of deformations where the effect of normal forces and wall slip is prominent, $\gamma_0 > \gamma_{0,critical}$ (as demonstrated for PS330 and PS500 in fig. 5.3). With this method, the non-linear rheological behaviour of polymer melts can be quantified via $I_{3/1}(\gamma_0)$, for the whole range of applicable deformations.

5.4 Flow distortions in polyethylene melts-correlation with topology

The flow instabilities during LAOS flow are studied for the case of industrial polyethylene samples (see Table 4.1). The resulting non-linearities present a similar dependence on molecular weight as discussed for polystyrene melts. Polyethylene melts of higher molecular weight and/or higher polydispersity present higher $I_{3/1}(\gamma_0)$ and $I_{2/1}(\gamma_0)$ and the critical strain for slip onset, $\gamma_{0,critical}$ is lower. Laun has already reported lower critical shear rates for slip of HDPE of higher M_w, as detected from capillary flow, cone-plate and sandwich rheometer studies [Laun 82]. However, the specific samples have a smaller molecular weight range, namely 71 kg/mol $< M_w <$ 234 kg/mol, and they are highly polydisperse with *PDI* ranging from 1.9 to 20.4. Thus, deviations from a scaling behaviour as the one shown in fig. 5.14 are expected. The low entanglement molecular weight of polyethylene, M_e = 1.45 kg/mol [Seitz 93], results in a high N_e for the specific samples. Furthermore, the most important feature in these melts is the variation of topology, which may influence the onset and evolution of flow instabilities. The dependence of phenomena like slip on topological chain constrains is revealed through

this study. The critical strain amplitudes for the onset this decay, $\gamma_{0,c}$, is depicted in fig. 5.15 for all studied PE as a function of M_w/M_e.

From the plot of $\gamma_{0,critical}$ (critical shear rate for onset of stress time signal amplitude decay) versus entanglement number, it is obvious that no simple relation can be extracted between slip onset and molecular weight, due to the broadened molecular weight distribution and the significant difference in branching between the investigated samples. The critical deformation for slip decreases with increasing molecular weight, however no simple scaling law, $\gamma_{0,c}$ = a(M_w/M_e)^n, can be derived to describe this dependence. The difference from the case of linear monodisperse polystyrene melts (see paragraph 5.3) is the topological complexity of the samples. In the case of Wang and Drda [Wang 96a] where HDPE was studied, only three linear melts were used differing only in M_w (130.5 kg/mol, 225.6 kg/mol and 316.6 kg/mol). In Allal et al. [Allal 06] the extracted exponent from a similar plot has a value of 4.3 for three polyethylenes, however it is a fit parameter and deviations from this function are also seen in the particular work.

The critical strain amplitude for slip onset in LAOS is clearly reduced by the presence of LCB. Furthermore, for the case of the linear samples, the effect of a high polydispersity is clearly observed. Large macromolecules induce instabilities at relatively low deformations and dominate the non-linear rheological behaviour, whether the non-linearities and instabilities originate from material inherent non-linearity or due to flow characteristics. Presence of LCB increases the number of topological constrains for a polymer chain. Consequently branching affects the slip onset and development for a melt, either the latter is related to elasticity and constitutive material properties, or to an entanglement/disentanglement process of bulk chains with chains adsorbed on the wall [Barone 98, Wang 96b].

5.4.1 LAOS simulations including slip

The effect of changing the boundary conditions in a LAOS flow is studied numerically by combining the dynamic slip model from eq. 5.9 with the DCPP constitutive model, in a LAOS flow simulation performed according to chapter 2. A non-vanishing wall velocity is introduced for the lower boundary of the calculation domain (see fig. 2.3) which is time and stress dependent, according to Hatzikiriakos and Dealy [Hatzikiriakos 91, Hatzikiriakos 92a]. The introduction of a slip velocity which changes with time and is coupled with the calculated shear stress at the wall leads to LAOS signals with a decaying stress amplitude. This predicted stress time signal is in agreement with experimental LAOS results as depicted for a polydisperse LCB polyethylene in fig. 5.16. A parameter optimization is needed for an improved fitting of the stress in LAOS, however it is remarkable that this simple model can be easily coupled with a constitutive equation for the stress calculation and capture the effect of slip onset and development in a finite element simulation.

Slip parameter α is taken simply proportional to time, i.e. α= k·t and highly non-linear

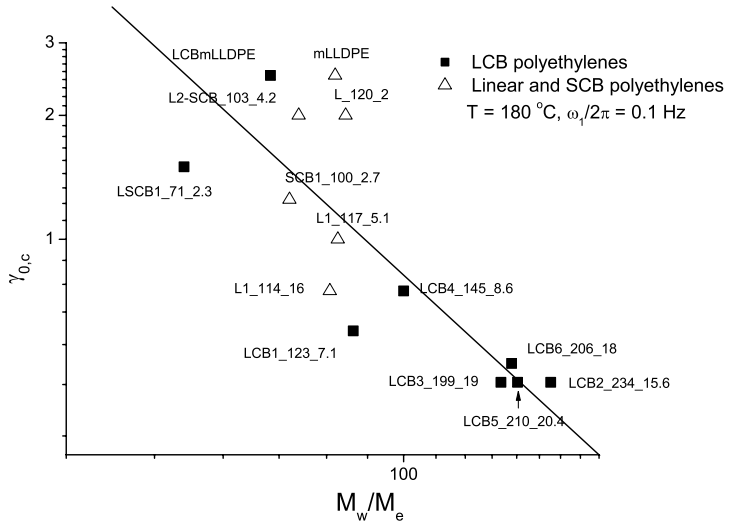

Figure 5.15: *Critical strain amplitude for stress signal amplitude decay for PE of Table refTable 1 as a function of number of entanglements per chain. T = 180°C, for LAOS with $\omega_1/2\pi$ = 0.1 Hz. Open symbols correspond to linear and SCB samples. Line of slope -2 is guide to the eyes. The error in determining $\gamma_{0,c}$ is typically the size of the data points.*

signals are calculated for a polyethylene modelled with the DCPP. When a higher slip velocity is calculated by increasing parameter *k*, the stress amplitude decay is larger, as seen in fig. 5.16. Such a highly distorted signal results from coupling wall shear stress with the non-vanishing wall velocity v_s (slip velocity). As an example, a predicted signal at theoretical extreme slip conditions is presented in fig. 5.17 and corresponds to a $I_{2/1}$ = 0.4% and a $I_{3/1}$ = 20% with a relative phase $\Phi_3 = 176°$. The calculated stress components of the DCPP model are reffered to as T_{11}, T_{12}, T_{22}, corresponding to the normal and shear stress components of the extra-stress tensor **T**, T_{xx}, T_{yy} and T_{xy}, respectively (see fig. 2.3). The FT-Rheology results from predicting a strain sweep with slip model and DCPP are shown in fig. 5.18. A change of $I_{3/1}(\gamma_0)\ \Phi_3(\gamma_0)$ is predicted in the evolution of the non-linearities with increasing strain amplitude, from the use of a slip model as a boundary condition.

The calculated velocity profile for LCB2_234_15.6 is presented in fig. 5.19 for a LAOS simulation with the DCPP model, including slip condition in the lower plate. A non-vanishing velocity in the lower wall is indeed predicted and has a value $\sim$ 10% of the maximum velocity (which corresponds to the wall velocity of the upper moving plate). One can extrapolate the velocity profile and extract the length parameter *b* (see eq. 5.3) which in this case it is caclulated to $\sim$ 0.07 mm, for a gap of 1 mm between the plates.

As demonstrated in paragraph 4.3.2, the normal stress difference can be determined for a LAOS flow simulation using the DCPP model. This quantity shows a dependence on topological parameters of the model and can further be analyzed via Fourier transformations.

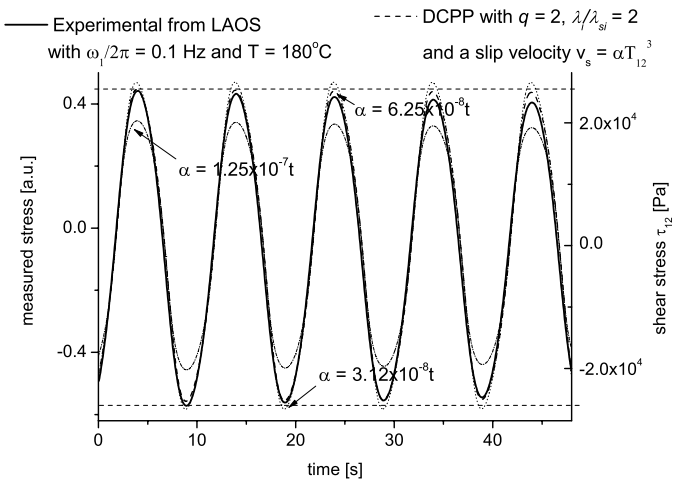

Figure 5.16: *LAOS stress time signal experimentally measured at T = 180 °C, with $\omega_1/2\pi$ = 0.1 Hz and γ_0 = 3 and predicted by DCPP model coupled with a dynamic slip model. Modelled sample is LCB2_234_15.6, LCB polydisperse polyethylene melt. The stress amplitude decay is larger for large values of α.*

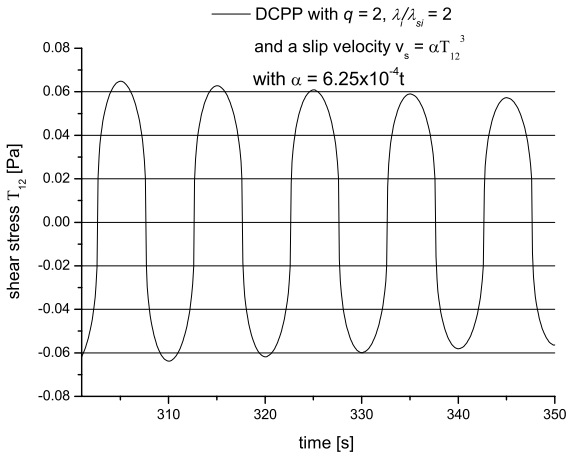

Figure 5.17: *Prediction of a LAOS stress time signal for modelled sample LCB2_234_15.6 at T = 180 °C, with $\omega_1/2\pi$ = 0.1 Hz and γ_0 = 3, increasing parameter α by 10^4, thus predicting large slip velocities.*

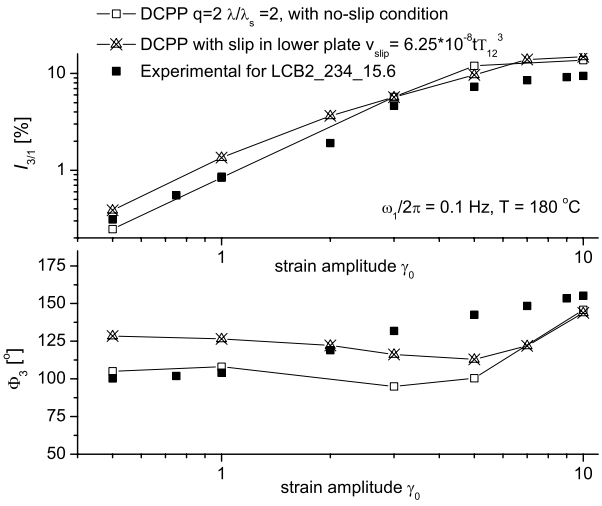

Figure 5.18: *Predicted $I_{3/1}(\gamma_0)$ and $\Phi_3(\gamma_0)$ for modelled sample LCB2_234_15.6 at T = 180 °C and $\omega_1/2\pi$ = 0.1 Hz. The DCPP model is coupled with a slip equation.*

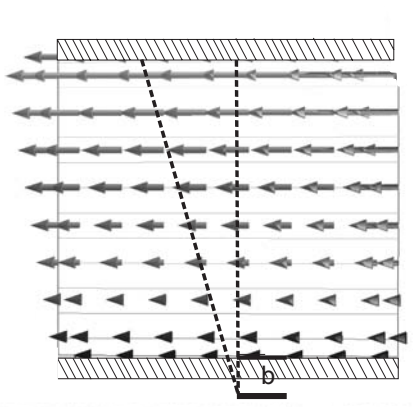

Figure 5.19: *Predicted velocity profile for a LAOS flow with $\omega_1/2\pi$ = 0.1 Hz, γ_0 = 10 and T = 180 °C for a modelled polyethylene LCB2_234_15.6. The DCPP model is coupled with a slip equation for the lower plate and a non-vanishing velocity is calculated at the lower plate.*

The resulting intensities of the higher harmonics, at odd multiples of the excitation frequency ($2\omega_1$, $4\omega_1$,...e.t.c.) can be used for the quantification of the normal forces in LAOS. Since, the normal forces are crucial to the occurrence and evolution of flow instabilities [Larson 92], one can analyze the "fingerprint" of N_1 for a simulated flow including wall slip. As an example the resulting normal stress difference for the LAOS flow with a slip law is calculated for several strain amplitudes n fig. 5.20. The resulting stress components in the normal direction can differ significantly when slip takes place from the case of non-slip condition, as depicted in fig. 5.21.

Furthermore, it is proposed that the ratio between shear and normal stresses may be the

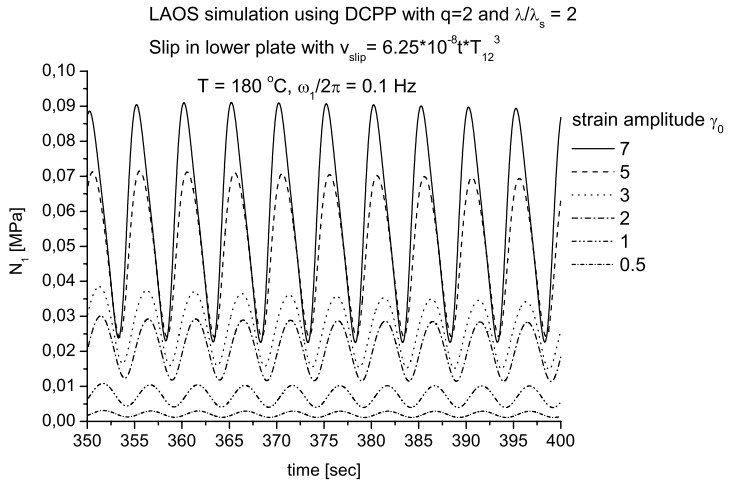

Figure 5.20: *N_1 for a simulated strain sweep with the DCPP model coupled with a slip equation for the lower plate. The modelled sample is LCB_234_15.6.*

critical quantity controlling the concurrence of flow instabilities in LAOS flows [Larson 92]. Thus, this ratio is predicted and shown in fig. 5.22 for the case of no-slip boundary conditions and for the simulation with a DCPP modelled coupled with the slip law. The existence of a critical point during the LAOS flow is evident, where the wall shear stress is close to its maximum value. The contribution of the normal forces becomes significant and increases the non-linearity of the response. This can be the onset of instabilities and flow distortions. A change in the ratio of shear to normal stresses is observed when slip takes place. In that case, the normal stress difference is smaller (as seen also in fig. 5.21) and the shear stress has a higher contribution in the predicted stress response of the polymer, which may be directly connected to the non-vanishing tagential velocity at the lower plate and the slip occurrence. Nevertheless, experimental data for N_1 are needed for deriving conclusions about the onset and development of flow instabilities in LAOS flow.

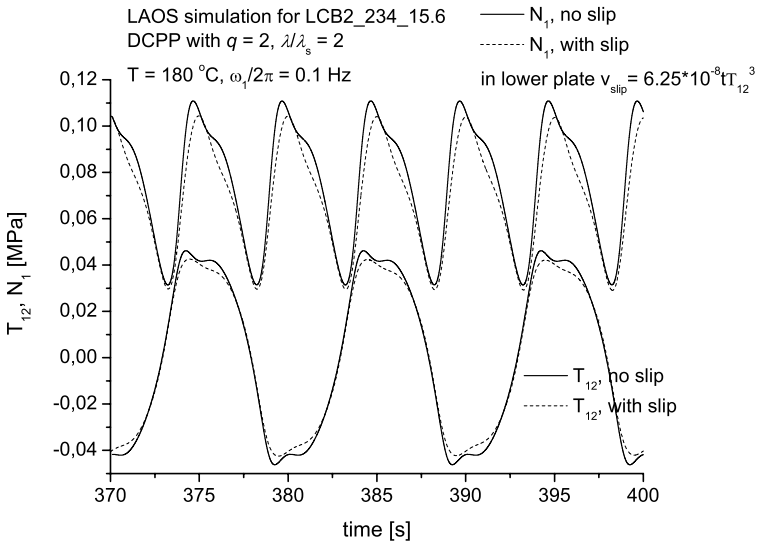

Figure 5.21: *Normal stress difference, N_1 and wall shear stress, T_{12} for LCB_234_15.6, at γ_0 = 5, for no-slip boundary conditions and for slip law imposed at the lower plate.*

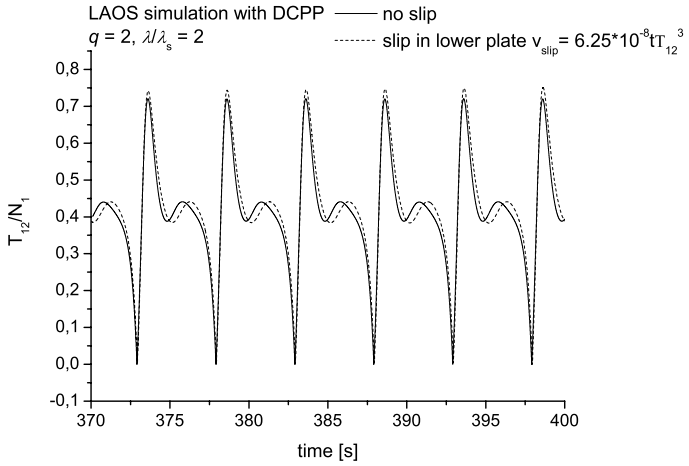

Figure 5.22: *Ratio of shear stress to normal stress difference for modelled LCB PE, at γ_0 = 5, for no-slip boundary conditions and for slip law imposed at the lower plate.*

5.4.2 Correlation between LAOS non-linearities and capillary flow distortions

The industrial polyethylene samples (see Table4.1) are tested in capillary flow. To achieve capillary flow, a piston is used to generate pressure on the test polymer melt in a reservoir, which is thus forced through a die (capillary tube) of a specific diameter, *D* and length, *L* [Macosko 94]. The shear viscosity is determined by relation between wall shear stress and wall shear rate. By measuring the pressure drop, p_c, and flow rate, Q, of the melt through the die are used to determine the viscosity, using the following equations [Macosko 94] for apparent flow (no corrections for slip):
Wall shear stress:

$$T_{12,w} = \frac{Dp_c}{4L} \tag{5.11}$$

Wall shear rate:

$$\dot{\gamma}_{a,w} = \frac{32Q}{\pi D} \tag{5.12}$$

Additionally, the pressure on the walls is recorded and the extrudate is studied with respect to its surface distortions. This process is similar to extrusion and allows access to rheological properties at high deformations. However, partial wall slip influences the results and must be taken into consideration [Laun 04]. The experimental setup is modified with the used of sensitive pressure transducers and is presented in more details by Filipe et al. [Filipe 06]. Measurements are performed under constant pressure and also under constant piston velocity using two different dies, a cylindrical with: *L* = 30 mm and *D* = 1 mm and a slit die with: *L* = 30 mm and crossection of 0.3 mm $\times$ 3 mm. During the measurement of the apparent shear stress, pressure oscillations are recorded in three different points along the die, namely: 3 mm, 15 mm and 27 mm after die entrance named tr1, tr2, tr3 respectively. A schematic representation of the capillary geometry is shown in fig. 5.23.

In fig. 5.24 and 5.25 the apparent flow results are shown for linear and LCB polyethylene melts respectively. The measurements are performed at T = 180 °C with one cylindrical die. The critical shear rate or stress for the onset of slip is of interest at this point and it can be determined by a change in the slope of shear rate plotted against stress.

For the linear polyethylene samples a proportionality between the critical stress for slippage in capillary flow and the critical strain amplitude in LAOS flow, $\gamma_{0,c}$ is determined within this work. The latter critical strain amplitude is defined (as described in paragraph 5.3 and 5.4) by the lowest strain amplitude where stress time signal decay is observed. However, this critical deformation depends on several factors, as discussed in paragraph 5.3. Within this analysis for the PE samples, steel parallel plates of 13 mm diameter with a 1 mm gap are used, for strain sweeps conducted at T = 180 °C and $\omega_1/2\pi$ = 0.1 Hz. Results are presented in fig. 5.26 and an increase of both the critical capillary wall stress and $\gamma_{0,c}$ is found for increasing SCB content. Although SCB is not considered to have a significant effect on the rheological properties, the results show that by incorporating SCB in polyethylene the

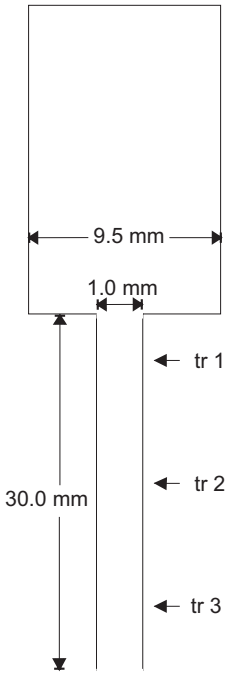

Figure 5.23: *Schematic representation of the capillary reservoir and the die. The three pressure transducers, tr1, tr2 and tr3 are at 3 mm, 15 mm and 27 mm from the die entry respectively.*

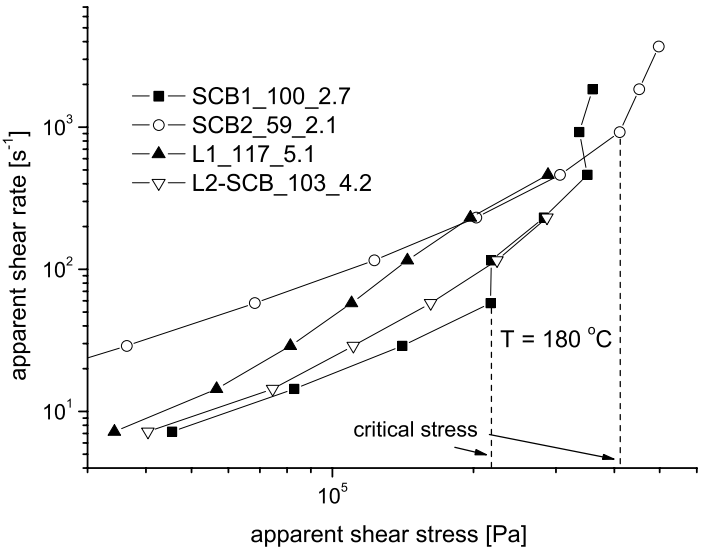

Figure 5.24: *Apparent capillary flow data for linear and SCB polyethylenes at T = 180°C. Die aspect ratio is L/D = 90. Measurements were conducted by S. Filipe. Critical stresses are indicated as determined by a change of the slope of the flow curve.*

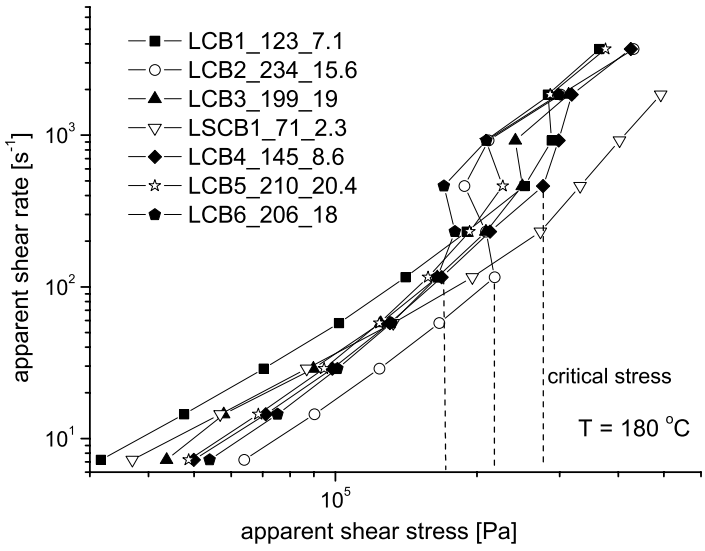

Figure 5.25: *Apparent capillary flow data for LCB polyethylenes at T = 180°C. Die aspect ratio is L/D = 90. Measurements were conducted by S. Filipe. Several critical stresses are indicated as determined by a change of the slope of the flow curve.*

flow can be more stable. In SCB materials the slippage onset is delayed and the instabilities suppressed, as shown from the slopes of the corresponding apparent shear-rate versus stress curves (see fig. 5.24). Additionally, for linear polyethylene samples with similar content of SCB, larger M_w and broad molecular weight distributions (increased *PDI*) result in an onset of slip at lower strain amplitudes and wall stresses.

Polyethylenes containing LCB chains show flow instabilities at significantly lower critical deformations, as depicted in fig. 5.27. The plateau nonlinearity in LAOS flow, as quantified by parameter A (see eq. 1.47), or in other words the maximum possible deviation from linear viscoelastic behaviour, as quantified by FT-Rheology, is generally higher for melts that tend to slip at lower critical stresses. Furthermore, these highly non-linear materials are more likely to flow in an instable manner. This is presented in fig. 5.28, nevertheless no simple $\gamma_0 = a(M_w/M_e)^b$ proportionality can be derived. An explanation about this deviation is that, A is a fitting derived parameter of the non-linear behaviour as quantified via $I_{3/1}(\gamma_0)$ and is a result of non-linear viscoelasticity . One cannot easily discriminate the factors affecting the non-linear behaviour of melts. However, results from capillary and LAOS flows for macromolecules with different topologies show that instabilities can originate from material structure, since for example for the case of RPA2000 non-linearities due to wall slip are insignificant. These material non-linearities can be suppressed or reinforced by the flow type, i.e. large deformations, flow geometry and surface type.

In order illustrate the different occurring instabilities of samples with varying topol-

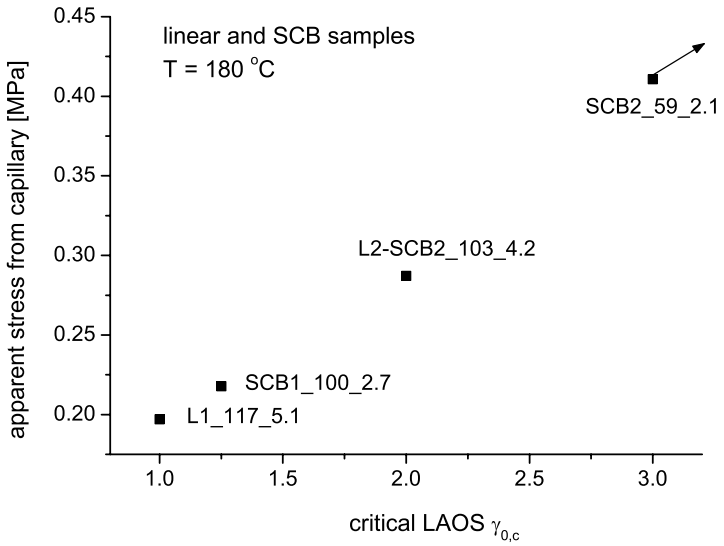

Figure 5.26: *Correlation between apparent wall capillary stress and critical strain amplitude in LAOS flows, for linear and SCB samples at T = 180 °C. Sample SCB2_59_2.1 presents instabilities for higher deformations, not experimentally reachable with ARES.*

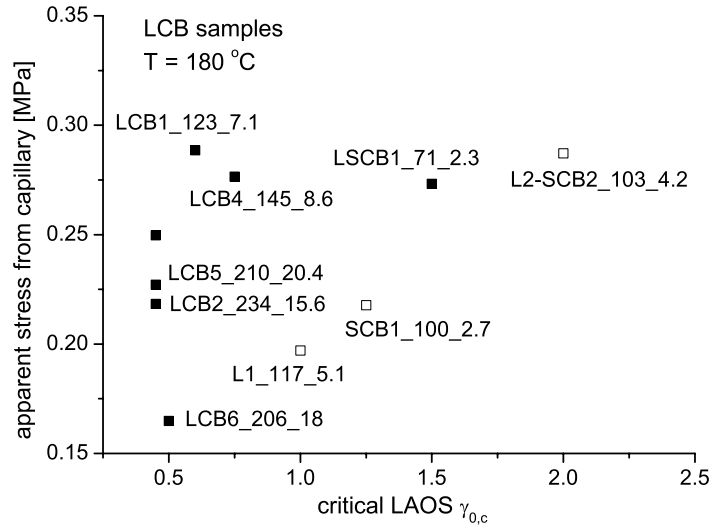

Figure 5.27: *Correlation between apparent wall capillary stress and critical strain amplitude in LAOS flows, for LCB polyethylenes at T = 180 °C (filled symbols). Results for linear PE are given in open-symbols for comparison.*

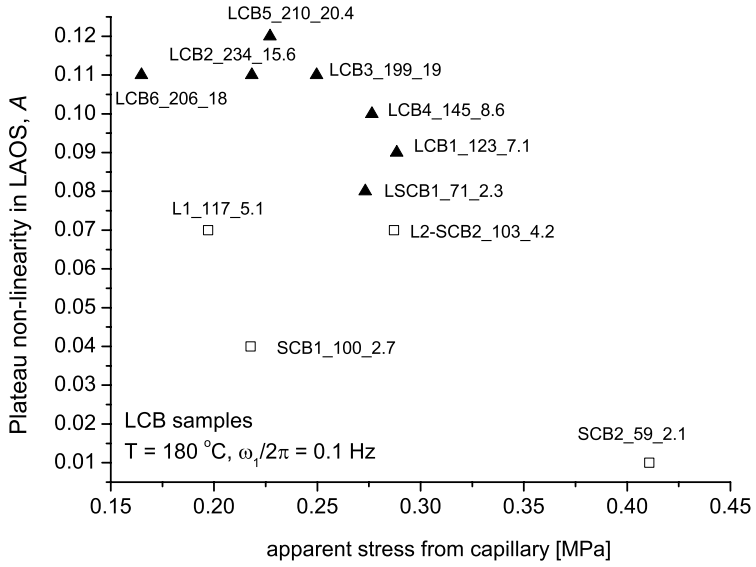

Figure 5.28: *Non-linearity plateau of LAOS flow for polyethylenes with different measured critical stresses for slip in capillary flow, as defined by slope change of apparent flow plots, at T = 180°C. Open-symbols are used for linear and SCB PE.*

ogy and non-linearity, photographs of the extrudates are presented in fig. 5.29 and 5.30. The first figure depicts two melts, LCB2_234_15.6 and LCB6_206_18, which present stick-slip instability. This is recognized by the interchanging regions of smooth extrudate and periodic surface distortions. Both samples present highly nonlinear rheological behaviour under LAOS flow with A = 0.11. On the contrary, sample SCB1_100_2.7 which is linear with 4.5 SCB / 1000 CH_2, presents low non-linearities with A = 0.04 even at higher apparent shear-rates, while exhibits only sharkskin type extrudate distortions (see fig. 5.30).

The observed extrudate distortions, such as sharkskin (see fig. 5.30) stick-slip (see fig. 5.29) and melt fracture are correlated, with respect to their periodicity and intensity, to the measured pressure deviation, σ_P and the pressure oscillation period [Filipe 06]. These distortions on the extrudate surface are of great importance and a method to predict these occurring instabilities at large deformations is needed. The measured average σ_P is subsequently correlated to the non-linearities in LAOS flow and FT-Rheology data of the studied materials.

Results reveal a strong relation between the plateau non-linearity measured in a LAOS flow via FT-Rheology and the pressure deviation measured by the pressure transducers in the capillary, as presented in fig. 5.32. The pressure oscillations are recorded for capillary flow of melts under constant piston velocity. An example of measured pressure from the three different transducers in the slit die for LCB2_234_15.6 is presented in fig. 5.31. A similar setup was used by Laun [Laun 83], however due to the low transducer sensitivity, the pressure

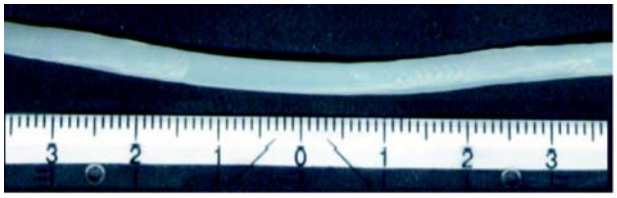

Figure 5.29: *Stick-slip instabilities for two LCB polydisperse polyethylene melts, for the slit die. Experiments were performed by S. Filipe.*

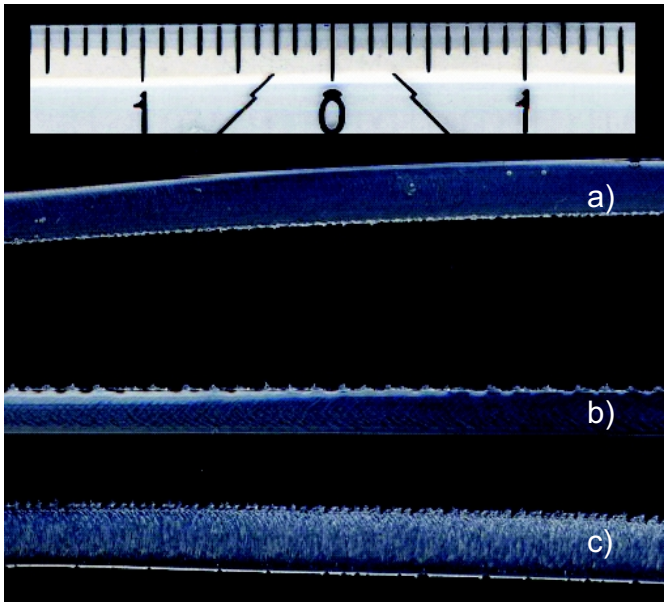

Figure 5.30: *Sharkskin surface distortion of SCB1_100_2.7, at 180 °C, for 230 s^{-1} (a), 920 s^{-1} (b) and 1420 s^{-1} (c) apparent shear rate. Measurements were performed by S. Filipe.*

oscillations could not be accurately measured.

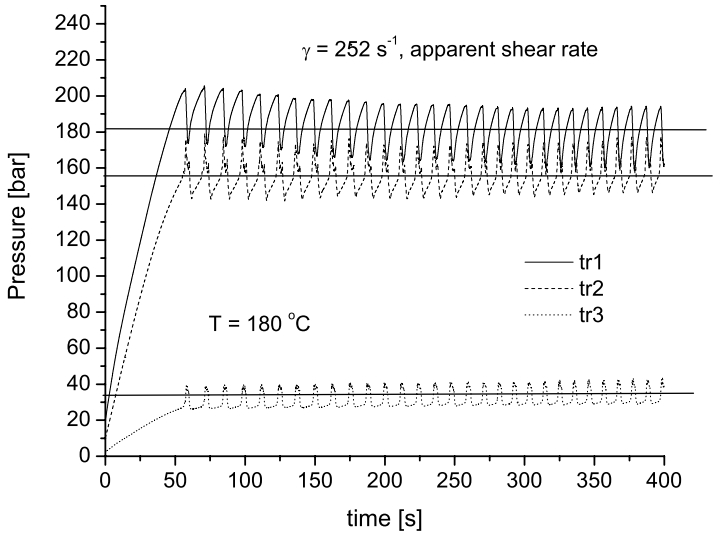

Figure 5.31: *Example of recorded pressure oscillations from the transducers in a slit die of L = 30 mm and a crossection of 0.3 mm × 3 mm. Sample is LCB2_234_15.6. The average pressure is 180 bar, 155 bar and 30 bar for tr1, tr2 and tr3, respectively. Measurements were performed by S. Filipe.*

5.4.3 Capillary flow simulations and prediction of extrudate distortions

Modelling the capillary flow of molten polyethylene and predicting the occurring flow instabilities has been a subject of interest in the past [Achilleos 02, Georgiou 94, Rutgers 01]. A numerical simulation with the capability of capturing the free surface extrudate distortions as well as predicting the experimentally measured pressure oscillations can relate instabilities with structure and predict the performance of materials during capillary flow or extrusion. In this paragraph some preliminary results are presented for the case of an LCB PE. The DCPP model is mainly used in order to capture the dependence of the instabilities on topological characteristics of the material. The model is coupled with a slip equation to describe the correlation between wall shear stress and slip velocity. In order to simplify the problem the flow is additionally modeled with a simpler shear-rate dependent viscosity equation, and specifically the Carreau-Yassuda model [Carreau 97]:

$$\eta = \eta_\infty + (\eta_0 - \eta_\infty)(1 + (\lambda\,\dot{\gamma})^{a_c})^{\frac{n-1}{a_c}} \tag{5.13}$$

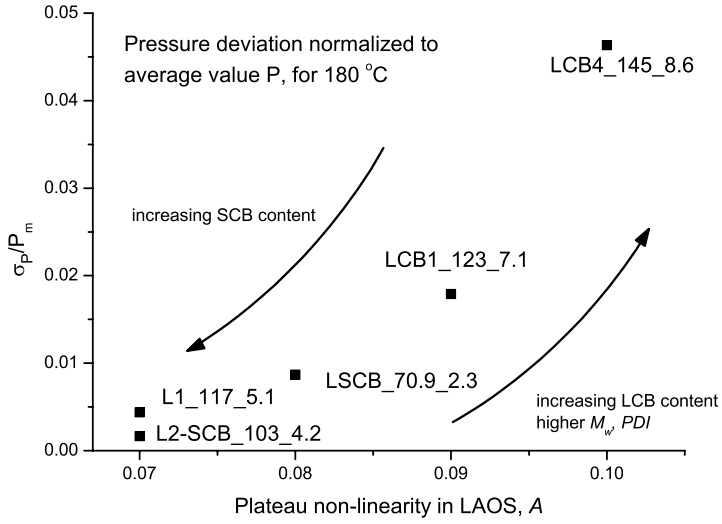

Figure 5.32: *Standard deviation of the pressure normalized to mean pressure value for polyethylenes with different non-linearity plateau of LAOS flow. All measurements are at T = 180°C and the pressure measurements correspond to an apparent shear-rate of 800 s^{-1} in a slit die.*

where η_0 is the zero-shear rate viscosity, η_∞ is the infinite shear-rate viscosity (lower Newtonian plateau), λ is the inverse of the critical shear-rate, or the pivot point, for transition from Newtonian to non-Newtonian fluid behaviour. The parameter a_c controls how abrupt this transition is. If it is lower $a_c > 1$, a longer transition regime is predicted. If $a_c > 1$ an abrupt transition is calculated for the viscosity. Finally, parameter *n* is the power-law index [Polyflow 03].

For the simulations performed using the DCPP model, the parameters are identified as mentioned in chapter 2. The flow of polyethylene in the whole capillary (reservoir and die) is simulated and also the case where only the die is considered. The calculation domains with the boundary conditions are described in fig. 5.33.

Simulations with no-slip boundary condition for the die walls predict a stress distribution for the die entry in qualitative agreement to literature [Baaijens 97, Clemeur 04]. The predicted stress distribution at the exit is also in qualitative agreement to numerical studies in literature [Rutgers 00, Rutgers 01]. A die swell is predicted for the extrudate with no surface instabilities, even at high shear rates, where experimentally sharkskin or stick-slip instabilities are observed for the specific polyethylene melt. The stress distributions for the die exit are depicted in fig. 5.34, using the DCPP model. High wall shear stresses are calculated near the exit, reflecting the absence of slip.

Additionally, the scalar stretch variable Λ (see eq. 2.16), which describes the stretching of the pom-pom backbone, can be calculated for the entry and the exit of the modelled

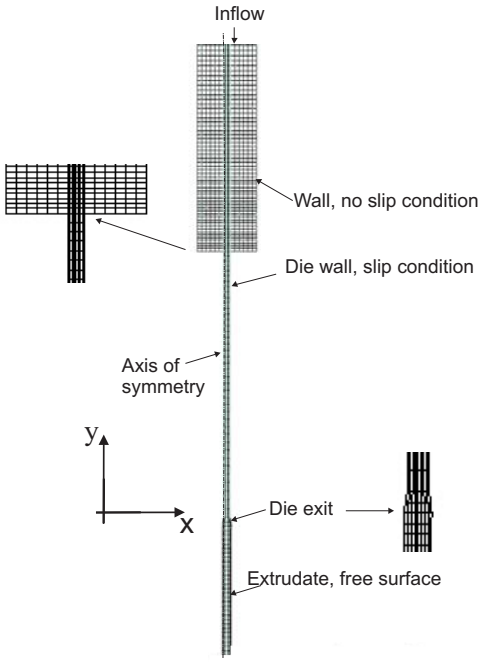

Figure 5.33: *Calculation domain for capillary flow with a cylindrical die of L = 30 mm and D = 1 mm. The contraction ratio in the die entry is 9.5. Mesh consists of 2400 elements.*

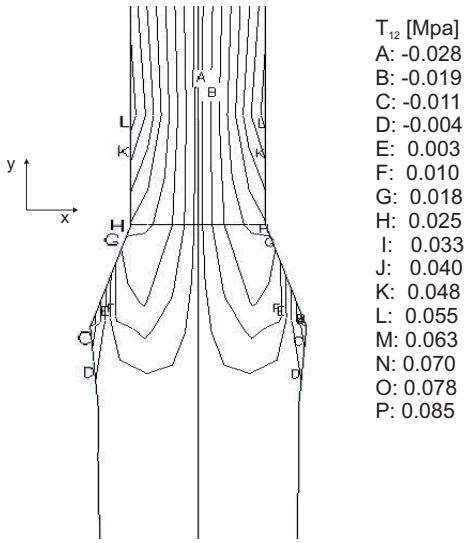

Figure 5.34: *Shear stress T_{12} for LCB2_234_15.6 at low apparent shear rate ($\sim$4 s^{-1}) in the die exit.*

melt. It represents the backbone length after the deformation normalized to the initial backbone length. The large stretching that the pom-pom molecules undergo, especially in the axis-center of the flow, is reflected in fig. 5.35. After a short distance from the entry, the distribution of Λ shows a relatively homogenous stretching of the pom-pom molecules.

Simulations are additionally performed for flow rates corresponding to experimental

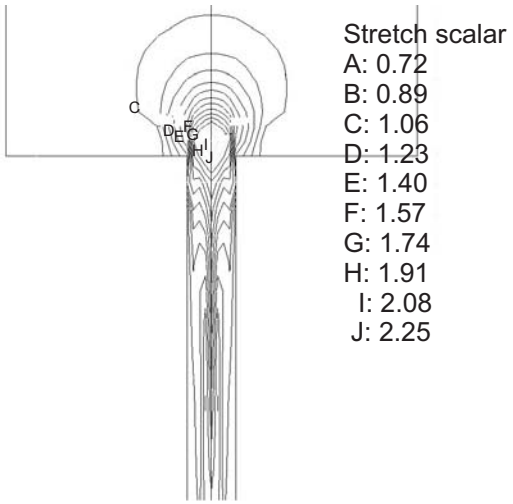

Figure 5.35: *Stretch variable Λ calculated for the DCPP model with q = 2, λ/λ_s = 2, at the die entry. Apparent shear rate $\approx$ 4 s^{-1}. Larger stretching of the pom-pom backbone is predicted near the flow axis at the die contraction.*

apparent shear rates larger than the critical shear rate for instabilities onset (which is 100 s^{-1} for LCB_234_15.6). Significantly larger stresses are predicted for both the entry and the die exit. As an example in fig. 5.36 the normal stress T_{11} is depicted which takes large values at the wall near the exit and is eventually responsible for the swelling of the polymer after the exit. The significantly larger stretching of the pom-pom molecules near the axis of the die is reflected on the higher Λ for this case, as shown in fig. 5.37.

The die is long enough for the entry effects to be insignificant with respect to the stresses at the exit and the resulting extrudate swell for this case, as shown from the stress distribution in the die entrance. Thus, the focus is to predict the flow inside the die and the phenomena taking place at the exit, considering the entrance effects irrelevant to the extrudate distortions for this specific geometry. The calculation domain is restricted to the die and the extrudate, as presented in fig. 5.38. A constant inflow rate is imposed (to model the constant piston velocity), corresponding to high apparent shear rates ($\dot{\gamma}_{apparent} >> 250^{-1}$), i.e. in the flow regime where stick slip is experimentally observed for the specific sample in the studied capillary flow.

By introducing a wall-slip condition for the die, instabilities are predicted in the extrudate surface. However, from the numerical calculation point of view, non-vanishing wall velocities reduce convergence problems since the velocity profile has no singularities at the

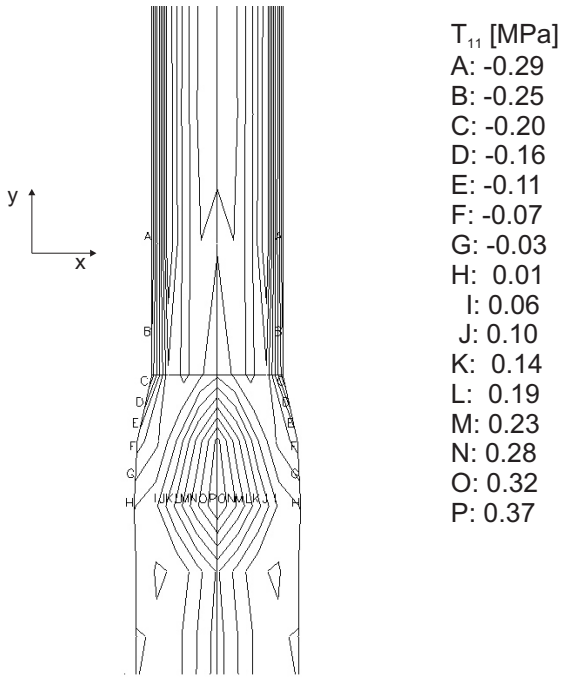

Figure 5.36: *Normal stress T_{11} for modelled LCB2_234_15.6, at flow rate corresponding to critical apparent shear rate (100 s^{-1}), for the die exit and extrudate. High normal stresses are predicted at the wall region in the die and near to the exit.*

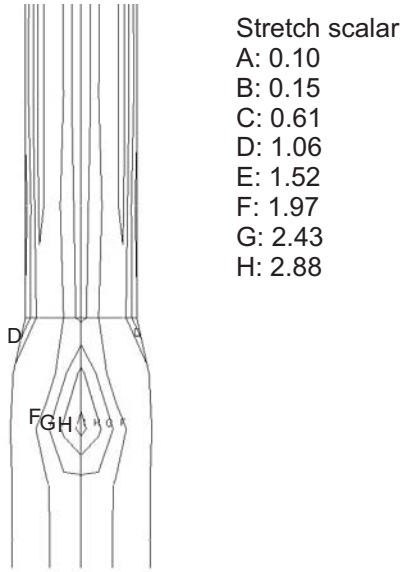

Figure 5.37: *Stretch variable Λ for modelled sample LCB2_234_15.6. Prediction with the DCPP model at the die exit. Apparent shear rate is approximately 100 s^{-1}. The predicted extrudate is highly stretched.*

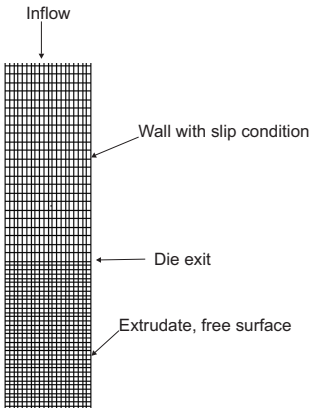

Figure 5.38: *Part of the calculation domain for simulation of polymer flow through the capillary die, including the extrudate. The set of boundary conditions is also given. The specific mesh consists of 5000 elements and the density of the mesh is increased in the extrudate.*

wall. Thus, it is possible to simulate flows of higher Weissenberg numbers, $W_i = \lambda\ \dot{\gamma}$, for which convergence difficulties are encountered when imposing a non-slip condition. The slip law used is in agreement with eq. 5.9.

A dependence is revealed for the flow instabilities on the slip parameters. Slip parameter α can be a constant or a function of time (the problem is isothermal and no temperature dependence of α is considered, as in Hatzikiriakos and Dealy [Hatzikiriakos 92b]). By coupling the slip equation with the Carreau-Yassuda model (see eq. 5.13), one can predict the developement of distortions on the extrudate free surface. In fig. 5.39 results from two time-steps are depicted. The predicted time evolution of surface distortions is presented as reflected in the normal stress distribution at the die exit. These sets of T_{11} contours correspond to time-steps of the calculation during the build-up of normal stresses and the appearance of flow distortions approximately 4 s later. The normal stress is significantly lower in comparison with flow under no-slip conditions. However, T_{11} increases periodicaly near the exit and contributes to the formation of instability effects on the free surface.

Furthermore, the pressure, P, and the first normal stress difference, N_1 as a function of time can be derived, at the same points along the die, where the pressure transducers are installed in the experimental setup. However, the predicted P and N_1 time signals are decaying, in contrast to experimental data where pressure oscillations of constant amplitude are recorded during stick slip occurrence (see fig. 5.31). This may be improved by the use of a more elaborated slip equation.

With the use of a large value for the slip velocity in the simulation a stable flow may be predicted (no extrudate surface distortions). However, for unrealistically high slip velocities a plug flow is predicted and the expected die swell phenomenon vanishes. Generally the slip law parameters are adjusted in order to result in a realistic slip velocity $v_{slip} \leq 0.1$ v_{max} [Polyflow 03]. It must also be noted that the used slip models are phenomenological

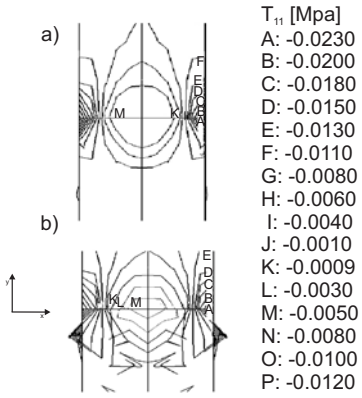

Figure 5.39: *Normal stress T_{11} for modelled sample LCB2_234_15.6 at die exit for apparent shear rate corresponding to the region of experimentally observed stick-slip. a) During stress build-up, t = 1.5 s. b) After the occurrence of flow instabilities and extrudate distortions, t = 5 s.*

and empirical with no solid physical background that correlates the slip phenomenon with structural properties of the polymer material. Nevertheless, the applicability of a slip law in combination with a simple non-linear viscosity model (like Carreau-Yassuda) or a more complicated constitutive equation (DCPP) in order to describe the capillary flow of a polymer melt and model the occurring flow instabilities is remarkable. At this stage no quantitative results can be derived. However, it is demonstrated that using slip parameters to calculate a realistic slip velocity, for example using eq. 5.9, one can predict surface distortions in qualitative agreement with the experimental observations (see fig. 5.39). These parameters are however not universal and they must be defined for each material and wall surface characteristics.

5.5 Summary on the study of flow instabilities of polymer melts via FT-Rheology

In the present chapter the occurring flow instabilities of polymers under LAOS flow are investigated via FT-Rheology and simulations. The experimental setup allows the recording of stress as a function of time with a high sensitivity. Hence, phenomena like stress signal

amplitude decay, or appearance of even harmonics in the FT-spectrum can be analyzed and correlated to the occurring flow instabilities with increased sensitivity and for samples well-characterized with respect to their topology and molecular weight distribution.

The evolution of the non-linearity in a strain sweep experiment depends strongly on molecular weight, molecular weight distributions and topology of the studied polymer. Additionally the onset of flow instabilities, as quantified by the critical strain amplitude for stress signal decay, is decreasing for increasing molecular weight and LCB content. It is possible to predict LAOS instable flow by simulations using the DCPP model coupled with a slip equation, which relates slip velocity with wall shear stress. Shear stress of decaying amplitude can be predicted and fitted to experimental time and FT data for LCB polyethylenes.

All investigated polyethylene melts are complementary measured in a capillary using a cylindrical and a slit die. The observed flow instabilities and distortions, such as sharkskin effect, stick-slip, gross fracture, are recorded along with the critical apparent shear rate for their occurrence and the oscillations of the normal pressure in the die. The results show a strong relation with the LAOS flow. This demonstrates that FT-Rheology is a promising method to investigate flow instabilities (e.g. constitutive instabilities, slip) and predict the occurring flow distortions in a capillary extrusion. The standard deviation of the pressure on the die wall is proportional to the plateau non-linearity, *A*, of the material, as measured in a parallel plate geometry by FT-Rheology. Additionally the critical strain amplitude, $\gamma_{0,critical}$ for instabilities in LAOS shows a similar dependence on molecular weight, molecular weight distribution and topology, with the critical apparent shear rate (or critical stress) for capillary flow distortions. Furthermore simulations of the capillary flow using simple viscosity models (like Carreau-Yassuda) or a more complex constitutive equation (DCPP), can predict flow instabilities and pressure oscillations in the capillary die, when coupled with an appropriate slip model.

Finally, results from both flow types, LAOS and capillary, can be used to correlate flow distortions and material non-linearity with molecular weight distribution and molecular architecture (type of branching). It is found that materials with high non-linearity plateau, *A*, as determined by FT-Rheology, present large pressure deviations in a capillary flow and consequently extrudate distortions like stick-slip, while materials of low *A* (eq. 1.47) present low instabilities and sharkskin for the same shear rates. The first is the case for LCB PE and materials of high molecular weight (as quantified by M_w, *PDI*) and the latter behaviour is observed for PE with lower non-linearity, namely linear of low M_w and SCB. However, one should also investigate more intensively the effect of the normal stress differences in the onset and evolution of flow instabilities. Specifically, the term N_1/T_{12} may be a more effective variable to be correlated to the slip velocity. Larson further suggested that the above ratio of normal stress difference to shear stress may be the critical parameter controlling the surface distortion phenomenon in cone-plate and plate-plate flows [Larson 92].

By studying the non-linear rheological behaviour of materials under LAOS with the

high sensitivity that FT-Rheology provides, one can predict occurring instabilities in capillary flows. These flow distortions are partially due to constitutive instabilities, or in this work mentioned as inherent material non-linearity, which is quantified via FT-Rheology according to chapters 3 and 4. The results from this analysis are strongly connected with structural properties of the studied melts, i.e. molecular weight, molecular weight distribution and topology (SCB, LCB), while additional factors such as temperature, pressure and deformation history have an additional influence on the non-linear behaviour in both LAOS and capillary flow.

Chapter 6

Conclusion and summary

The detection and characterization of polymer architectures is an extremely important subject for the polymer industry and especially for the polyolefine production and processing. The knowledge of the rheological properties which result from incorporated long- (LCB) and short-chain branching (SCB) on a polymer chain and the information about the effect of the permanent (branches) and non-permanent (entanglements) topological constrains, can be used to optimize the processing and end-use properties of polymer products. Large amplitude oscillatory shear (LAOS) combined with FT-Rheology is established as a method to probe structural characteristics and quantify the non-linear rheological behaviour of different polymer topologies in both solutions and melts [Höfl 06, Neidhöfer 03a, Neidhöfer 03b, Neidhöfer 04, Schlatter 05].

A systematic study of well-characterized polymers with FT-Rheology provides the "fingerprints" of linear, short-chain branched (SCB) and long-chain branched (LCB) macromolecules in the non-linear regime. This rheological regime is the most often encountered in polymer processing industry. The resulting intensity of the 3^{rd} harmonic as a function of strain amplitude, $I_{3/1}(\gamma_0)$, can be described by empirical equations (eq. 1.47 and eq. 1.51). The derived non-linear parameters, A (non-linearity plateau), B (inverse critical strain), C (slope of log$I_{3/1}$ vs. logγ_0 at low strains) and D (non-linearity at low and medium strain amplitudes), are used to quantify the material non-linear rheological behaviour.

Measurements performed for monodisperse polystyrene (PS) linear melts of a wide range of molecular weights with M_w = 41 kg/mol - 4530 kg/mol, reveal a strong correlation between molecular weight and mechanical non-linearities, as quantified via FT-Rheology with the relative intensity of the 3^{rd} harmonic, $I_{3/1}$, and the relative phase, Φ_3. Parameter D is found to be proportional to $M_w^{2.5}$. In a polydisperse melt, the non-linear rheological behaviour is dominated by the large macromolecules, however the effect of this high molecular weight can be reduced by diluting the melt with smaller chains. An increase of polydispersity index (PDI) up to 2, for a PS melt with $M_w \approx$ 100 kg/mol, can result to a 5 times larger $I_{3/1}$. Additionally, if a PS of high molecular weight (e.g. M_w = 750 kg/mol) is "diluted" to

70 wt % with a PS of low M_w (e.g. M_w = 41 kg/mol) the derived parameter D for the blend is found to be 1/6 of the value for high M_w component (e.g. M_w = 750 kg/mol). Combining the results from LAOS flow measurements of polydisperse linear polystyrene melts and binary blends, one can conclude that the non-linearities increase with increasing chain length, or equivalently with increasing number of entanglements per macromolecule. The non-linear response becomes more complicated when branches are incorporated in a linear chain. Finite element simulations are performed to predict linear and non-linear rheological properties of polystyrene comb-like architectures in melt or solution, using the Pom-pom model in the DCPP formulation (double-convected Pom-pom model [Clemeur 03]). The resulting intensities and phases of the higher harmonic contributions are in relatively good agreement with experimental data, taking into account that the rheological properties of a comb-like polymer are described by a multi-mode model for a pom-pom topology. For linear polymers the Giesekus model performs as good as the DCPP in predicting FT-Rheology data. However, when simulating LAOS flows for H-shaped and generally branched PS melts, the DCPP model is found to satisfactory capture the non-linear rheological behaviour. An increased number of relatively short branches (containing 1-2 entanglements per arm) can act as a "solvent" for the polymer backbone, thus reducing the non-linearity, as measured experimentally and predicted by the DCPP model. The effect from the presence of branches of various lengths and quantities on the non-linear rheological behaviour of polymers is demonstrated. Thus, it is experimentally and theoretically supported that FT-Rheology is sensitive towards molecular structure, i.e. branching, molecular weight and molecular weight distribution.

Samples of well-defined topology (mainly anionically synthesized) are good candidates to be used for studying the effects of branching on the polymer shear flow. However, they are mainly produced in a laboratory scale and their purity, monodispersity and stability may differ significantly from that of industrial samples. Therefore, the method of combined experimental FT-Rheology with complementary NMR spectroscopy analysis and finite element LAOS flow simulations is extended to industrial polyolefines, specifically polyethylene (PE) of varying molecular weight, molecular weight distribution, branching type and content. A dependence of the resulting non-linearities on M_w and *PDI* is also determined, in consistency with the results from model polystyrene samples. The non-linear parameters A and B can be predicted as a function of molecular weight distribution with a linear equation, $a + bM_w + cPDI$, for linear and SCB polyethylenes. Additionally, an incorporation of a small amount of LCB increases significantly the non-linearity of the stress response for the whole range of applied deformations, as well as the Φ_3. As an example, a LCB PE sample with M_w = 123 kg/mol and PDI = 7.1 contains 0.2 LCB/1000CH_2, which result in increased values for A and B (9 % and 0.3 respectively) in comparison with a linear PE of similar molecular weight distribution, with M_w = 117 kg/mol and PDI = 5.1 (with A = 7 % and B = 0.23). Hence, the FT-Rheology parameters introduced show a great potential in quantifying branching content. The correlation between LCB and resulting $I_{3/1}$ and Φ_3 is confirmed by coupling

the non-linear rheological results with melt-state NMR and LAOS simulations using the DCPP model. Large values of the branching parameter q in this model are found to decrease the non-linearity plateau the inverse critical strain, B and the slope C, hence acting as "solvents" for the backbone. Furthermore, when the pom-pom molecule relaxes mainly by orientation and less by stretching (quantified via λ/λ_s) the parameter A decreases, however the non-linearities increase at lower γ_0 (larger B values) and with a larger slope (as given by C). Additionally results from measuring blends of linear and LCB industrial polyethylenes of similar molecular weight distribution reveal a monotonic dependence of the intensities and phases of the FT-spectrum on LCB sample content and prove the high sensitivity of FT-Rheology on small concentrations of branched species in a miscible homogeneous polyethylene melt, as low as 1-5 wt % of branched PE added in linear PE, while linear rheology can detect concentrations higher than 10-30 wt % for these materials. For the specific miscible linear/LCB PE blends, the non-linear parameters A, B and D are found to increase linearly with the concentration of the LCB PE component. An additional potential quantity to discriminate LCB and linear polyethylenes is the zero-shear extrapolated phase of the 3^{rd} harmonic, Φ_3^0. At the onset of non-linearity (at relatively low strain amplitudes) this particular relative phase can be measured reproducibly and is found to be significantly large for PE containing LCB than for linear PE. Finally, the optimum conditions for probing LCB in industrial polyethylene are investigated and are found to be T = 180 °C in combination with large strain amplitudes, i.e. γ_0 = 3 in a closed-cavity geometry with grooved surfaces to avoid slippage (e.g. RPA2000) and low excitation frequencies, typically $\omega_1/2\pi$ = 0.1 Hz.

A factor of great importance in polymer industry along with molecular architecture is the occurring flow instabilities during processing of commercial products and especially in industrial polyethylene. FT-Rheology is a useful robust tool to quantify the resulting stress response in LAOS flows including instabilities. Combining results from a rheometer sensitive at low strain amplitudes (ARES) and an apparatus where large deformations can be applied with suppressed slippage (RPA2000) one can derive the "mastercurve" for the $I_{3/1}$ and Φ_3 as a function of γ_0, for a specific excitation frequency and at constant temperature, which will correspond only to the material inherent non-linearity. When flow instabilities take place at an open-rim geometry, the resulting non-linearities depart significantly from the expected non-linear response of the material, which within this work is referred to as material inherent non-linearity. The relative intensity, $I_{3/1}(\gamma_0)$, shows a sudden change in slope departing from the predicted behaviour ($A(1 - \frac{1}{1-(B\gamma_0)^C})$), the phase $\Phi_3(\gamma_0)$ exhibits a local maximum and even harmonics appear, i.e. $I_{2/1}(\gamma_0)$ larger than the noise level being typically 0.2%. Typically for the critical strain $\gamma_{0,c}$, $I_{2/1} > 0.1$ %. This additional intensity of the odd higher harmonics, as well as the appearance of even harmonics and the change in corresponding relative phases, is attributed to the wall slip of the sample in the parallel plate flow configuration.

The onset of slip can be quantified and correlated with molecular weight and polymer topology. The non-linearities quantified via FT-Rheology can be significantly changed by a

surface modification of the plates. Using fluorocarbonated coating on steel plates, four times large values for $I_{2/1}$ and $I_{3/1}$ are found and the critical strain for slip onset is reduced to 3/4 of the value for steel plates. The non-linear rheological behaviour depends generally in all factors which influence the onset and development of flow instabilities, namely surface material type, geometry of flow domain (e.g. sample thickness, grooved surfaces) and deformation history. By using a sample of double thickness, or grooved surfaces in the ARES open-rim geometry, the intensities can increase up to an order of magnitude, thus indicating the occurrence of secondary flow and instabilities, such as meniscus distortions. The test or process temperature is another important factor [Hatzikiriakos 92a, Larson 92]. An increase in the temperature from 180 °C to 200 °C, $I_{3/1}$ for the case of PS can be reduced up to 1/3 of its value and the flow is stable for a wider range of deformations (increase of $\gamma_{0,critical}$). The highly non-linear and in some cases asymmetric stress signals are qualitatively predicted via finite element LAOS simulations with the DCPP model and the slip model which couples the slip velocity with the wall shear stress. Finally, the FT-Rheology results from LAOS flow can be correlated to sample behaviour during capillary extrusion. Thus, the combination of FT-Rheology combined with capillary rheometry can be used to predict extrudate distortions like sharkskin, stick-slip, gross fracture in polyethylene. The study of a specific set of industrial polyethylenes leads to the following conclusions. Low molecular weight polyethylenes exhibit less flow instabilities and especially by increasing the amount of incorporated SCB, a shift of instabilities onset at higher critical deformations, or even a suppression of stick-slip and generally of intense extrudate distortions, is observed. On the other hand, samples containing LCB and accordingly high values of $I_{3/1}$ during LAOS flow present instabilities at lower critical stresses and of higher pressure deviations, consequently higher extrudate surface distortion amplitudes.

As already pointed out that the normal forces and especially the first normal stress difference N_1 = T $_{xx}$ - T $_{yy}$ (or N_1 = T $_{11}$ - T $_{22}$ within chapters 2 and 5) can be considered to strongly affect the onset of slip and the occurring flow non-linearities. In LAOS flow this parameter can be used for differentiating topologies in the non-linear regime. Furthermore, the potential of the stress ratio, N_1/σ_{xy} [Larson 92], to be the critical parameter controlling the onset of flow instabilities is preliminary examined. Within this work, this is evaluated in numerical simulations for LAOS and capillary flows and the results reveal a correlation between the normal stresses and topological characterization, as well as flow instabilities.

Appendix

A Dimensionless numbers

The Reynolds number, Re describes the ratio of the kinetic energy, or inertia, to the energy lost due to viscous forces in a flow.

$$Re = \frac{dv\rho}{\eta} \tag{A.1}$$

where d is a characteristic distance for the flow, e.g. capillary diameter. The characteristic velocity for the fluid is v and ρ and η are the fluid density and the absolute dynamic viscosity, respectively. The Re can be defined for a couette flow [Tanner 00]:

$$Re = \frac{\rho\omega h^2}{\eta} \tag{A.2}$$

where ω is the excitation frequency of the moving cup, η is calculated from $\sigma_{xy}/\ \dot{\gamma}$ and h is the gap between the walls.

The Deborah number corresponds to the ratio of the characteristic relaxation time, e.g. τ of the material to the characteristic observation time of the flow process, e.g. T_0 [Owens 02]. For an oscillatory shear with an excitation frequency $\omega = 1/T_0$ it can be expressed as:

$$De = \frac{\tau}{T_0} = \tau\omega \tag{A.3}$$

The Deborah number is zero for a Newtonian fluid and infinite for an ideal Hookean elastic solid. However, in general the Deborah number associated with a material takes not a single value. If the characteristic time of the flow process is small, e.g. large ω in a oscillatory shear

rheometric flow, a material with a non-zero τ will behave in a solid-like way. Conversely, a material which appears solid, will behave fluid-like if the observation time is sufficiently increased.

An alternative definition used to provide a quantitative measure for the viscoelasticity of non-Newtonian fluids is the Weissenberg number, W_i (or W_s in literature). It is defined as:

$$W_i = \tau \frac{v}{h} \tag{A.4}$$

where v and h are the characteristic process velocity and process length [Nassehi 02]. It can be used to decide whether viscoelastic effects are significant in a certain flow problem or not.

B Tensor analysis

The tensor quantities and calculus relations used in the models presented within this work are presented here.
The gradient of a scalar $\phi(x, y, z)$ is defined as:

$$\nabla(\phi) \equiv \frac{\partial \phi}{\partial x}\mathbf{i} + \frac{\partial \phi}{\partial y}\mathbf{j} + \frac{\partial \phi}{\partial z}\mathbf{k} \tag{B.1}$$

where **i**, **j**, **k** are the unit vectors in a Cartesian coordinate system. The divergence of a vector **V(**x, y, z**)** is defined as:

$$\nabla \cdot \mathbf{V} = (\frac{\partial}{\partial x}\mathbf{i} + \frac{\partial}{\partial y}\mathbf{j} + \frac{\partial}{\partial z}\mathbf{k}) \cdot (V_1\mathbf{i} + V_2\mathbf{j} + V_3\mathbf{k}) = \frac{\partial V_1}{\partial x} + \frac{\partial V_2}{\partial y} + \frac{\partial V_3}{\partial z} \tag{B.2}$$

$\overset{\triangle}{\mathbf{T}}_{\mathbf{1}}$ is the lower-convected derivative of the viscoelastic extra stress, which is defined as follows:

$$\overset{\triangle}{\mathbf{T}} = \frac{D\mathbf{T}}{Dt} + \mathbf{T} \cdot \nabla \mathbf{v}^T + \nabla \mathbf{v} \cdot \mathbf{T} \tag{B.3}$$

$\overset{\nabla}{\mathbf{T}}$ is the upper-convected derivative of a tensor **T** defined as:

$$\overset{\nabla}{\mathbf{T}} = \frac{D\mathbf{T}}{Dt} - \mathbf{T} \cdot \nabla\mathbf{v} - \nabla\mathbf{v}^T \cdot \mathbf{T} \tag{B.4}$$

where **v** is the velocity vector and $\frac{D}{Dt}$ is the material time derivative:

$$\frac{D}{Dt} = \frac{\partial}{\partial t} + \mathbf{v} \cdot \nabla \tag{B.5}$$

C Maxwell model for oscillatory shear

The Maxwell model can be used as shown below. in order to describe an oscillatory shear flow. The applied sinusoidal shear strain, $\gamma(t) = \gamma_0 sin\omega t$ can be described by the following complex expression [Tanner 00]:

$$\begin{aligned} &\gamma(t) = \gamma_0 exp(i\omega t), \\ &\dot{\gamma} = \gamma_0(i\omega)exp(i\omega t) = i\omega\gamma(t) \end{aligned} \tag{C.1}$$

In the dynamic steady-state:

$$\begin{aligned} &\sigma(t) = \sigma_0 exp(i(\omega t + \delta)), \\ &\dot{\sigma} = \sigma_0(i\omega)exp(i(\omega t + \delta)) = i\omega\sigma(t) \end{aligned} \tag{C.2}$$

In the Maxwell model, the total shear rate is the sum of the shear rate of the elastic part (spring) and the shear rate of the viscous component (dash-pot):

$$\begin{aligned} &\dot{\gamma} = \frac{\dot{\sigma}}{G} + \frac{\sigma}{\eta} \Rightarrow i\omega\gamma(t) = \frac{i\omega\sigma(t)}{G} + \frac{\sigma}{\eta}, \\ &[i\omega\gamma(t)]\frac{G}{i\omega\sigma(t)} = [\frac{i\omega\sigma(t)}{G} + \frac{\sigma}{\eta}]\frac{G}{i\omega\sigma(t)}, \\ &\frac{G\gamma(t)}{\sigma(t)} = 1 + \frac{G}{i\omega\eta} \end{aligned} \tag{C.3}$$

where the ratio of strain to stress is defined as:

$$\frac{\gamma(t)}{\sigma(t)} = \frac{1}{G^*(\omega)} \tag{C.4}$$

and η/G is the relaxation time τ. Hence, eq. C.3 is expressed as follows:

$$\frac{G}{G^*(\omega)} = 1 + \frac{1}{i\omega\tau}, G^*(\omega) = G\frac{i\omega\tau}{1+i\omega\tau} \tag{C.5}$$

The resulting expression for the complex modulus is separated into a real and an imaginary part:

$$G^*(\omega) = G'(\omega) + iG''(\omega) = G(\frac{\omega^2\tau^2}{1+\omega^2\tau^2} + i\frac{\omega\tau}{1+\omega^2\tau^2}) \tag{C.6}$$

thus, from the above equations one can derive the expression for the storage and the loss modulus as a function of frequency:

$$\begin{aligned} G'(\omega) &= G\frac{\omega^2\tau^2}{1+\omega^2\tau^2} \\ G''(\omega) &= G\frac{\omega\tau}{1+\omega^2\tau^2} \end{aligned} \tag{C.7}$$

From the above equation one can easily observe that for low excitation frequencies ($\omega \to 0$), $G' \propto \omega^2$ and $G'' \propto \omega$.

D Calculation of plateau modulus, G_N^0

Below are presented different ways to derive the plateau modulus, G_N^0, from a measurement of $G'(\omega)$, $G''(\omega)$ and tan δ.

G_N^0 can be determined from the value of $G'(\omega)$ at the lower frequency where tan δ is minimum:

$$G_N^0 = [G']_{tan\delta \to minimum} \tag{D.1}$$

Another method is by integrating G'' in the flow transition region [Fetters 94].

$$G_N^0 = \frac{2}{\pi} \int_{-\infty}^{+\infty} G''_{FT}(\omega) dln\omega \tag{D.2}$$

E ^{13}C melt-state NMR spectrum and carbon site assignments

A schematic representation of a polyethylene chain with LCB is presented in fig. E.1, with the several carbon cites detected by ^{13}C. Below a typical NMR melt-state spectrum is shown with the peaks assigned to the specific carbons in the polyethylene branched chain.

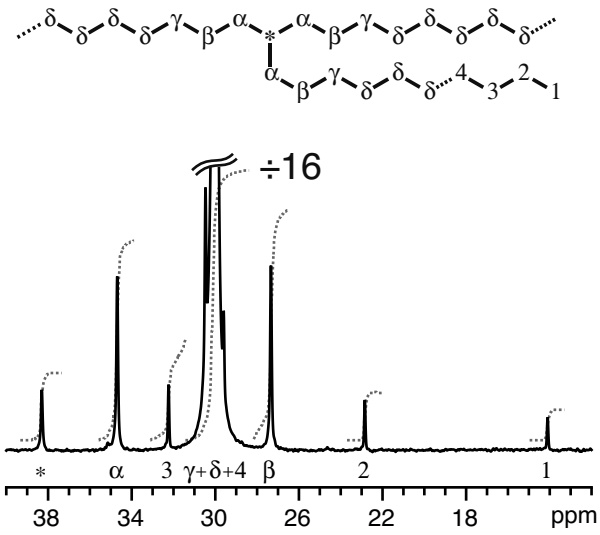

Figure E.1: *Typical melt-state ^{13}C NMR spectrum of a polyethylene containing branches of seven carbons in length or longer [Klimke 06].*

F Pom-pom model

The Pom-pom model is described below at its initial configuration [McLeish 98]. The approximation of the model to a differential form is additionally provided [Inkson 99] and the transformation to its DCPP formulation is given by Rutgers et al. [Rutgers 02], which is the formulation used in the present thesis. For a polymer molecule with a pom-pom topology (see fig. 2.4), M_b, M_a and q are the backbone molecular weight, the arms molecular weight and the number of arms attached to each backbone end, respectively. The dimensionless

partial molecular weights are defined as $s_a = M_a/M_e$ and $s_b = M_b/M_e$, where M_e is the entanglement molecular weight. The relaxation process of a pom-pom molecule cannot be fully described by the Doi-Edwards tube theory. This is due to the existence of branch points at the backbone ends, which act as topological constrains for the reptation of the backbone.

F.1 Branch point withdrawal

The resistance to the reptation of the backbone due to the branch points cannot be unlimited. The Doi-Edwards type tube, in which the backbone is reptating to relax, has a diameter a. Taking a linear chain into account, in order to maintain Gaussian chain statistics in equilibrium, a net Brownian force on every free chain end of magnitude kT/a would tend to maintain the curvilinear path of the chain segment within the tube. Hence, the pom-pom backbone may be stretched by the q free ends until it sustains a curvilinear tension of qkT/a. Beyond this tension, the free ends are withdrawn into the tube. The path length of an arm forced to adopt a configuration set by backbone orientation due to arm withdrawal is in units of tube diameter, s_c with $0 < s_c < M_a/M_e$.

F.2 Linear stress relaxation

The free arms in a pom-pom melt relax as if they were in a star polymer melt, except for one aspect, the backbones remain effective network parts throughout the relaxation process and exhibit a spectrum of relaxation times. The relaxation time spectrum for an arm, $\tau_a(x)$ is given by [Milner 97]:

$$\tau_a(x) = \tau_0 exp[\frac{15}{4} s_a \frac{(1-x)^2}{2} - (1-\phi_b)\frac{(1-x)^3}{3}] \tag{F.1}$$

where ϕ_b is the effectively fixed backbone material and x is a fraction of the tube segment from the branch point to the free end (retracted chain part). The constant τ_0 is an attempt time for deep retractions of the entangled dangling arm [McLeish 98]. The modulus has a quadratic dependence on concentration of oriented polymer segments and for these timescales [McLeish 98]:

$$G(t) = G_0(\phi_b + (1-\phi_b)\int_0^1 e^{-t/\tau_a(x)} dx)^2 \tag{F.2}$$

The effective friction for the reptation of the backbone with a curvilinear motion is found at the branch points. A branch point moved within the tube for a distance equal to the tube diameter, a after a time $\tau_a(0)$ has a diffusion constant $D_c = a^2/2\tau_a(0)$. Thus, using Einstein's equation and requiring that the drag on a branch point increases linearly with q, the branch point friction constant, ζ_b is given by:

$$\zeta_b = \frac{kT}{D_c} = 2kT\frac{\tau_a(0)}{a^2}q \tag{F.3}$$

The characteristic time for orientational relaxation of the backbone, τ_b, is the diffusion time of a one-dimensional walker with a diffusion constant, $D_c/2$, to move along a mean square distance of the dilated primitive path between the branch points, L^2. Assuming $M_e \propto 1/\phi_b$ (ϕ_b in this case is the concentration of entangled segments), the dilated tube diameter has an effective value $a_{eff} = a\phi_b^{-1/2}$ and $s_{b,eff} = s_b\phi_b$. Thus, $L^2 = s_{b,eff}^2 a_{eff}^2 = a^2\phi_b s_b^2$. Finally, the backbone relaxation time via orientation is given:

$$\tau_b = \frac{4}{\pi^2}s_b^2\phi_b\tau_a(0)q \tag{F.4}$$

By assigning a single relaxation time to the backbone material, the full relaxation modulus becomes:

$$G(t) = G_0(\phi_b e^{-t/\tau_b} + (1-\phi_b)\int_0^1 e^{-t/\tau_a(x)}dx)^2 \tag{F.5}$$

The stress is assumed to be calculated as a function of molecular orientation, and that in turn as in the tube-model theory [Doi 86], may be calculated by the orientation distribution of occupied tube segments, **u**. For linear polymers with known **u**, when are not stretched beyond equilibrium contour length of chain per tube segment, the stress tensor may be written:

$$\sigma = \frac{15}{4}G_0\langle\mathbf{uu}\rangle \tag{F.6}$$

Hence, a modified stress expression in terms of the high-frequency plateau modulus, arising from the backbone alone (the arms relax in a much faster timescale) is:

$$\sigma = \frac{15}{4} G_0 \phi_b^2 \langle \mathbf{uu} \rangle \tag{F.7}$$
$$\phi_b = \frac{s_b}{s_b + 2qs_a}$$

The factor ϕ_b is accounting for the number of elastically active segments and multiplied by another ϕ_b factor accounting for the dependence of the tube diameter, a, on concentration. Assuming that the orientation distribution is a weak function of position along the backbone, the unique measure of orientation also imposed upon the withdrawn material is the tensor **S** = $\langle \mathbf{uu} \rangle$. Finally, the stress can be expressed as:

$$\sigma = \frac{15}{4} G_0 \phi_b (\phi_b \Lambda^2(t) + \frac{2qs_c(t)}{2qs_a + s_b}) \mathbf{S}(\mathbf{t}) \tag{F.8}$$
$$\phi_b = \frac{s_b}{s_b + 2qs_a}$$

where Λ is the dimensionless stretch ratio of the backbone path length to its equilibrium length.

F.3 Dynamic equations

The orientation tensor **S** measures the distribution of the unit vectors describing the orientation of tube segments in the deforming melt. A dynamical system of evolution equations is used for **S**(t), Λ(t) and $s_c(t)$, which are used to construct the stress. For a flow with $s_c > 0$, the orientation characteristic time can be generalized as follows:

$$\tau_b = \frac{4}{\pi^2} s_b^2 \phi_b \tau_a(x_c(t)) q \tag{F.9}$$

where $x_c(t) = s_c/s_a$. Tube segments are created at a rate t_b^{-1} and afterwards extended during the flow. A segment created with orientation **u** at time t', has an orientation $\mathbf{E}(t,t') \cdot \mathbf{u}/|\mathbf{E}(t,t') \cdot \mathbf{u}|$ at time t, where $\mathbf{E}(t,t')$ is the local deformation gradient tensor between these times [McLeish 98]. Segments created at time t' with orientation **u** carry a relative weight of $|\mathbf{E}(t,t') \cdot \mathbf{u}|/\langle|\mathbf{E}(t,t') \cdot \mathbf{u}|\rangle$ in the distribution at time t, since a segment will increase in length and therefore in the amount of chain it carries by $|\mathbf{E}(t,t') \cdot \mathbf{u}|$. The surviving probability itself is the exponential of the time integral of destruction rates $\tau_b^{-1}(t'')$ in the interval $t' < t < t''$. The resulting expression for **S**(t) is then:

$$\mathbf{S}(t) = \int_{-\infty}^{t} \frac{dt'}{\tau_b(t')} exp(-\int_{t'}^{t} \frac{dt''}{\tau_b(t'')}) \frac{1}{\langle|\mathbf{E}(t,t')\cdot\mathbf{u}|\rangle} \langle \frac{\mathbf{E}(t,t')\cdot\mathbf{u}\mathbf{E}(t,t')\cdot\mathbf{u}}{|\mathbf{E}(t,t')\cdot\mathbf{u}|} \rangle \tag{F.10}$$

If we define the deformation rate tensor **K** such that $\partial\mathbf{E}(t,t')/\partial t$=**K.E**$(t,t')$ then the average increase in backbone length per unit length of tube is **K:S** and the relative curvilinear tube velocity is L**K.S**, where $L(t)$ is the curvilinear distance of separation between two branch points along the tube. By setting the frictional drag force from the relative velocity equal to the elastic force restoring L to its equilibrium length, we obtain:

$$\zeta_b(\mathbf{K}.\mathbf{S} - \frac{\partial L}{\partial t}) = \frac{kT}{s_b a^2}(L - s_b a) \tag{F.11}$$

for ζ_b in eq. F.3 and introducing Λ we obtain:

$$\frac{\partial \Lambda}{\partial t} = \Lambda(\mathbf{K} : \mathbf{S}) - \frac{1}{\tau_s}(\Lambda - 1) \tag{F.12}$$

where $\Lambda < q$.

The stretch relaxation timescale, τ_s, which appears only in non-linear deformations is given by:

$$\tau_s = s_b \tau_a(0) q \tag{F.13}$$

For the branch point withdrawal dynamic equation, we balance the drag and elastic tension and cancel the dimensional factors of the tube diameter obtaining the following for s_c:

$$\frac{\partial s_c}{\partial t} = (q\frac{s_b}{2} + s_c)\mathbf{K} : \mathbf{S} - \frac{1}{2\tau_a(s_c)} \tag{F.14}$$

For the above equation, Λ= q.

The eq. F.10, F.12 and F.14, with the expressions for the variable timescales, eq. F.9 and F.13, along with the equation for stress F.8 construct the simplified constitutive formulation for the pom-pom material [Inkson 99, McLeish 98].

F.4 Approximate differential model

For the evolution of a tensor of unit trace in a flow, we can have the following differential equation:

$$\frac{\partial \mathbf{S}(t)}{\partial t} = \mathbf{K}.\mathbf{S} + \mathbf{S}.\mathbf{K}^T - 2(\mathbf{S} : \mathbf{K})\mathbf{S} - \frac{1}{\tau_b}(\mathbf{S} - \frac{1}{3}\mathbf{I}) \tag{F.15}$$

In order to retain the simplicity of the above equation and obtain stable solutions, the calculation of **S**(t) is performed as:

$$\begin{aligned} \frac{\partial \mathbf{A}(t)}{\partial t} &= \mathbf{K} \cdot \mathbf{A} + \mathbf{A} \cdot \mathbf{K}^T - \frac{1}{\tau_b}(\mathbf{A} - \frac{1}{3}\mathbf{I}), \\ \mathbf{S}(t) &= \frac{\mathbf{A}(t)}{trace[\mathbf{A}(t)]} \end{aligned} \tag{F.16}$$

In a later paper for the Pom-pom model [Inkson 99] the evolution of **A**(t) is expressed as:

$$\frac{\partial \mathbf{A}(t)}{\partial t} + \mathbf{u} \cdot \nabla \mathbf{A} = \mathbf{K} \cdot \mathbf{A} + \mathbf{A} \cdot \mathbf{K}^T - \frac{1}{\tau_b}(\mathbf{A} - \mathbf{I}) \tag{F.17}$$

where $\mathbf{K} = \nabla \mathbf{u}$. The multi-mode model is introduced by adding the stress contribution of all n modes (from eq. F.8. Equation F.17 can be rewritten using the definition of the upper-convective derivative :

$$\overset{\nabla}{\mathbf{A}}_i\,(t) + \frac{1}{\tau_{bi}}(\mathbf{A}_i(t) - \mathbf{I}) = \mathbf{0} \tag{F.18}$$

where i is the number of each individual mode. A correction is introduced in the equation for the stretch [Rutgers 02], eq. F.12 which is given by:

$$\frac{D\Lambda_i(t)}{Dt} = \Lambda_i(t)(\nabla \mathbf{u} : \mathbf{S}_i(t)) - \frac{1}{\tau_{si}}(\Lambda_i(t) - 1)e^{\frac{2}{q_i}(\Lambda_i(t)-1)} \tag{F.19}$$

which is strictly for $\Lambda_i(t) < q$, otherwise $\Lambda_i(t) = q$. In this multi-mode version of the model the total stress is given by:

$$\sigma(t) = \sum_i 3G_i\Lambda_i^2(t)\mathbf{S}_i(t) \tag{F.20}$$

In the extended and the double-convected (DCPP) formulation, the relaxation time for orientation is denoted as λ and the stretching characteristic time, λ_s, refers to the above mention τ_b and τ_s, respectively. In order to introduce a non-vanishing second normal stress difference and derive a constitutive equation in terms of a viscoelastic extra-stress tensor, $\mathbf{T}$ a closure approximation is introduced [Clemeur 03]:

$$trace[\mathbf{A}(t)] = \Lambda^2 \tag{F.21}$$

The extended Pom-pom model (SXPP) can be written as follows:

$$\overset{\nabla}{\mathbf{T}} + \lambda(\mathbf{T})^{-1} \cdot \mathbf{T} = 2G\mathbf{D} \tag{F.22}$$

$$\lambda(\mathbf{T})^{-1} = \frac{1}{\lambda}[\frac{\alpha}{G}\mathbf{T} + f(\mathbf{T})^{-1}\mathbf{I} + G(f(\mathbf{T})^{-1} - 1)\mathbf{T}^{-1}] \tag{F.23}$$

$$\frac{1}{\lambda}f(\mathbf{T})^{-1} = \frac{2}{\lambda_s}e^{\frac{2}{q}(\Lambda_B - 1)}(1 - \frac{1}{\Lambda_B}) + \frac{1}{\lambda\Lambda_B^2}(1 - \frac{atrace(\mathbf{T}\cdot\mathbf{T}}{3G^2}) \tag{F.24}$$

$$\Lambda_B = \sqrt{}(1 + \frac{trace\mathbf{T}}{3G}) \tag{F.25}$$

where a is a "Giesekus-like" non-linear parameter. The above model is referred to as DXPP. To circumvent singularity problems that occur the model is further modified [Clemeur 03]. An additional parameter is introduced, ξ, which controls the ratio of the second to the first normal stress difference.

$$\mathbf{A} + \lambda[(1 - \frac{\xi}{2})\overset{\nabla}{\mathbf{A}} + \frac{\xi}{2}\overset{\triangle}{\mathbf{A}}] - \frac{\mathbf{I}}{3} = \mathbf{0} \tag{F.26}$$

Thus, the orientation equation in the DCPP formulation is given by:

$$\lambda[(1 - \frac{\xi}{2})\overset{\nabla}{\mathbf{S}} + \frac{\xi}{2}\overset{\triangle}{\mathbf{S}}] + \lambda(1 - \xi)[2\mathbf{D} : \mathbf{S}]\mathbf{S} + \frac{1}{\Lambda^2}[\mathbf{S} - \frac{\mathbf{I}}{3}] = \mathbf{0} \tag{F.27}$$

The unknowns $\mathbf{S}$ and Λ obey also the equation:

$$\lambda_s \frac{D\Lambda}{Dt} - \lambda_s(\mathbf{D} : \mathbf{S})\Lambda + (\Lambda - 1)e^{2(\Lambda-1)/q} = \mathbf{0} \tag{F.28}$$

Finally, the viscoelastic extra stress tensor in a single-mode DCPP (for a multi-mode the stress contributions are simply added) is given by the following equation:

$$\mathbf{T} = \frac{G}{1-\xi}(3\Lambda^2\mathbf{S} - \mathbf{I}) \tag{F.29}$$

Bibliography

[Achilleos 02] E. Achilleos, G. C. Georgiou, S. G. Hatzikiriakos. On numerical simulations of polymer extrusion instabilities. *App. Rheol.* **12**, 88–104 (2002).

[Allal 06] A. Allal, A. Lavernhe, B. Vergnes, G. Martin. Relationships between molecular structure and sharkskin defect for linear polymers. *J. Non-Newton. Fluid Mech.* **134**, 127–135 (2006).

[Baaijens 97] F. P. T. Baaijens, S. H. A. Selen, H. P. W. Baaijens, G. W. M. Peters, H. E. H. Meijer. Viscoelastic flow past a confined cylinder of a low density polyethylene melt. *J. Non-Newton. Fluid Mech.* **68**, 173–203 (1997).

[Barone 98] J. R. Barone, N. Plucktaveesak, S. Q. Wang. Interfacial molecular instability mechanism for sharkskin phenomenon in capillary extrusion of linear polyethylenes. *J. Rheol.* **42**, 813–832 (1998).

[Bartsch 74] H. J. Bartsch. Handbook of mathematical formulas. Academic Press New York, New York (1974).

[Bersted 85] B. H. Bersted. On the effects of very low long chain branching in rheological behaviour of polyethylene. *J. App. Polym. Sci.* **30**, 3751–3765 (1985).

[Bicerano 02] J. Bicerano. Prediction of polymer properties. Marcel Dekker Inc., New York (2002).

[Briedis 76] I. P. Briedis, L. A. Faitel'son. Rheology and molecular structure of a polyethylene melt. 3. Relaxation spectra and characteristic relaxation time. *Mekh. Polim.* **2**, 322–330 (1976).

[Carreau 97] P. J. Carreau, D. De Kee, R. P. Chhabra. Rheology of Polymeric Systems: Principle and Application. Hanser Publishers, Munich (1997).

[Chen 94] Y. L. Chen, R. G. Larson, S. S. Patel. On Shear fracture of polystyrene melts and solutions. *Rheol. Acta* **33**, 243–256 (1994).

[Cho 05] K. S. Cho, K. Hyn, K. H. Ahn, S. J. Lee. A geometrical interpretation of large amplitude oscillatory shear response. *J. Rheol.* **49**, 747–758 (2005).

[Clemeur 03] N. Clemeur, R. P. G. Rutgers, B. Debbaut. On the evaluation of some differential formulations for the pom-pom constitutive model. *Rheol. Acta* **42**, 217–231 (2003).

[Clemeur 04] N. Clemeur, R. P. G. Rutgers, B. Debbaut. Numerical simulation of abrupt contraction flows using the double convected pom-pom model. *J. Non-Newton. Fluid. Mech.* **117**, 193–209 (2004).

[Cox 58] W. P. Cox, E. H. Merz. Correlation of Dynamic and Steady Flow Viscosities. *J. Polym. Sci.* **28**, 619–622 (1958).

[Crochet 92] M. J. Crochet, B. Debbaut, R. Keunings, J. M. Marchal. POLYFLOW, a multipurpose finite element program for continuous polymer flows. Applications of CAE in extrusion and other continuous processes. Carl Hanser Verlag, München (1992).

[Daniels 01] D. R. Daniels, T. C. B. McLeish, B. J. Crosby, R. N. Young, C. M. Fernyhough. Molecular Rheology of Comb Polymer Melts. 1. Linear Viscoelastic Response. *Macromolecules* **34**, 7025–7033 (2001).

[Debbaut 02] B. Debbaut, H. Burhin. Large amplitude oscillatory shear and Fourier-transform rheology for a high-density polyethylene: Experiments and numerical simulation. *J. Rheol.* **46**, 1155–1176 (2002).

[deGennes 71] P. G. deGennes. Reptation of a polymer chain in the presence of fixed obstacles. *J. Chem. Phys.* **55**, 572–579 (1971).

[deGennes 85] P. G. deGennes. Wetting: statics and dynamics. *Rev. Modern Phys.* **57**, 827–863 (1985).

[Doi 78a] M. Doi, S. F. Edwards. Dynamics of concentrated polymer systems. 1. Brownian-motion in equilibrium state. *J. Chem. Soc., Faraday Transactions II* **74**, 1789–1801 (1978).

[Doi 78b] M. Doi, S. F. Edwards. Dynamics of concentrated polymer systems. 2. Molecular-motion under flow. *J. Chem. Soc., Faraday Transactions II* **74**, 1802–1817 (1978).

[Doi 78c] M. Doi, S. F. Edwards. Dynamics of concentrated polymer systems. 3. Constitutive equation. *J. Chem. Soc., Faraday Transactions II* **74**, 1818–1832 (1978).

[Doi 79] M. Doi, S. F. Edwards. Dynamics of concentrated polymer systems. 4. Rheological properties. *J. Chem. Soc., Faraday Transactions II* **75**, 38–54 (1979).

[Doi 86] M. Doi, S. F. Edwards. The theory of polymer dynamics. Oxford University Press, Oxford (1986).

[Dusschoten 01] D. van Dusschoten, M. Wilhelm. Increased torque transducer sensitivity via oversampling. *Rheol. Acta* **40**, 395–399 (2001).

[Ernst 90] R. R. Ernst, G. Bodenhausen, A. Wokaun. Principles of nuclear magnetic resonance in one and two dimensions. Clarendon Press, Oxford (1990).

[Fang 05] Y. Fang, P. J. Carreau, P. G. Lafleur. Thermal and rheological properties of mLLDPE/LDPE blends. *Polym. Eng. Sci.* **45**, 1254–1264 (2005).

[Fetters 94] L. J. Fetters, D. J. Lohse, D. Richter, T. A. Witten, A. Zirkel. Connection between polymer molecular weight, density, chain dimensions, and melt viscoelastic properties. *Macromolecules* **27**, 4639–4647 (1994).

[Fetters 99] L. J. Fetters, D. J. Lohse, S. T. Milner, W. W. Graessley. Packing length influence in linear polymer melts on the entanglement, critical and reptation molecular weights. *Macromolecules* **32**, 6847 (1999).

[Filipe 06] S. Filipe, A. Becker, M. Wilhelm. Optimized pressure detection and analysis of melt flow instabilities in polymer melts using capillary rheometry. *J. Rheol.* **50**, 1–30 (2006).

[Fleury 04] G. Fleury, G. Schlatter, R. Muller. Non linear rheology for long chain branching characterization, comparison of two methodologies: Fourier transform rheology and relaxation. *Rheol. Acta* **44**, 174–187 (2004).

[Gabriel 98] C. Gabriel, J. Kaschta, H. Münstedt. Influence of molecular structure on rheological properties of polyethylenes I. Creep recovery measurements in shear. *Rheol. Acta* **37**, 7–20 (1998).

[Gabriel 99] C. Gabriel, H. Münstedt. Creep recovery behaviour of metallocene linear low-density polyethylenes. *Rheol. Acta* **38**, 393–403 (1999).

[Gabriel 02] C. Gabriel, H. Münstedt. Analytical and rheological characterization of long-chain branched metallocene-catalyzed ethylene homopolymers. *Polymer* **43**, 6383–6390 (2002).

[Gahleitner 01] M. Gahleitner. Melt rheology of polyolefines. *Prog. Polym. Sci.* **26**, 895–944 (2001).

[Gamota 93] D. R. Gamota, A. S. Wineman, F. E. Filisko. Fourier transform analysis: Nonlinear dynamic response of an electrorheological material. *J. Rheol.* **37**, 919–933 (1993).

[Georgiou 94] G. C. Georgiou, M. J. Crochet. Time-dependent compressible extrudate-swell problem with slip at the wall. *J. Rheol.* **38**, 1745–1755 (1994).

[Giacomin 98] A. J. Giacomin, J. M. Dealy. Large amplitude oscillatory shear. In A. A. Collyer, D. W. Clegg (eds.), Rheological measurements. Chapman Hall, London (1998).

[Graessley 82] W. W. Graessley. Entangled linear, branched and network polymer systems-Molecular theories. *Adv. Polym. Sci.* **47**, 67–117 (1982).

[Graham 95] M. D. Graham. Wall slip and the nonlinear dynamics of large amplitude oscillatory shear flows. *J. Rheol.* **39**, 697–712 (1995).

[Graham 01] R. S. Graham, T. C. B. McLeish, O. G. Harlen. Using the pom-pom equations to analyze polymer melts in exponential shear. *J. Rheol.* **45**, 275–290 (2001).

[Griskey 95] R. Griskey. Polymer process engineering. Chapman and Hall, New York (1995).

[Gröhn 06] F. Gröhn, H. Frey, A. Kilbinger. Makromolekulare Chemie 2005. *Nachrichten aus der Chemie* **3**, 292–300 (2006).

[Hadjichristid 00] N. Hadjichristidis, H. Iatrou, S. Pispas, M. Pitsikalis. Anionic polymerization: High vacuum techniques. *J. Polym. Sci. Polym. Chem.* **38**, 3211–3234 (2000).

[Hameed 02] T. Hameed, I. A. Hussein. Rheological study of the influence of M_w and comonomer type on the miscibility of mLLDPE and LDPE blends. *Polymer* **43**, 6911–6929 (2002).

[Hamielec 96] A. E. Hamielec, J.P.B. Soares. Polymer reaction engineering-Metallocene catalysts. *Prog. Polym. Sci.* **21**, 651–706 (1996).

[Han 87] C. D. Han, J. Kim. Rheological technique for determining the order-disorder transition of block-copolymers. *J. Polym. Sci., Polym. Phys.* **25**, 1741–1764 (1987).

[Hatzikiriakos 91] S. G. Hatzikiriakos, J. M. Dealy. Wall slip of molten high density polyethylenes. I. Sliding plate rheometer studies. *J. Rheol.* **35**, 497–523 (1991).

[Hatzikiriakos 92a] S. G. Hatzikiriakos, J. M. Dealy. Role of slip and fracture in oscillating flow of HDPE in a capillary. *J. Rheol.* **36**, 845–884 (1992).

[Hatzikiriakos 92b] S. G. Hatzikiriakos, J. M. Dealy. Wall slip of molten high density polyethylenes. II. Capillary rheometer studies. *J. Rheol.* **36**, 703–740 (1992).

[Helfland 82] E. Helfland, D. S. Pearson. Calculation of the non-linear stress of polymers in oscillatory shear fields. *J. Polym. Sci. Polym. Phys.* **20**, 1249–1258 (1982).

[Henson 95] D. J. Henson, M. E. Mackay. Effect of gap on the viscosity of monodisperse polystyrene melts: Slip effects. *J. Rheol.* **39**, 359–373 (1995).

[Hilliou 04] L. Hilliou, D. van Dusschoten, M. Wilhelm. Increasing the force torque transducer sensitivity of an RPA2000 by a factor of 5-10 via advanced data acquisition. *Rubber. Chem. Technol.* **77**, 192–200 (2004).

[Höfl 06] S. Höfl. Einfluss von Topologie und Verscherung auf Dynamik und mechanische Parameter bei Homopolymeren. Johannes Gutenberg-Universtität Mainz (2006).

[Hussein 03] I. A. Hussein, T. Hameed, B. F. A. Sharkh, K. Mezghani. Miscibility of hexene-LLDPE and LDPE blends: Influence of branch content and composition distribution. *Polymer* **44**, 4665–4672 (2003).

[Hussein 04] I. A. Hussein, M. C. Williams. Rheological study of the influence of branch content on the miscibility of octene-mLLDPE and Zn-LLDPE in LDPE. *Polym. Eng. Sci.* **44**, 660–672 (2004).

[Hyun 02] K. Hyun, S. H. Kim, K. H. Ahn, S. J. Lee. Large amplitude oscillatory shear as a way to classify complex fluids. *J. Non-Newton. Fluid Mech.* **107**, 51–65 (2002).

[Inkson 99] N. J. Inkson, T. C. B. McLeish, O. G.Harlen, D. J. Groves. Predicting low density polyethylene melt rheology in elongational and shear flows with "pom-pom" constitutive equations. *J. Rheol.* **43**, 873–896 (1999).

[Janzen 99] J. Janzen, R. H. Colby. Diagnosing long chain branching in polyethylenes. *J. Mol. Struct.* **485**, 569–584 (1999).

[Kallus 01] S. Kallus, N. Willenbacher, S. Kirsch, D. Distler, T. Neidhöfer, M. Wilhelm, H.-W. Spiess. Characterization of polymer dispersion by Fourier transform rheology. *Rheol. Acta* **40**, 552–559 (2001).

[Kauppinen 01] J. Kauppinen, J. Partanen. Fourier Transforms in Spectroscopy. Wiley-VCH, Berlin (2001).

[Klein 05] C. Klein. Rheology and Fourier-Transform Rheology on water-based systems. Johannes Gutenberg-Universität Mainz (2005).

[Klimke 06] K. Klimke, M. Parkinson, C. Piel, W. Kaminsky, H. W. Spiess, M. Wilhelm. Optimized polyolefin branch quantification by melt-state ^{13}C NMR spectroscopy. *Macrom. Chem. Phys.* **207**, 382–395 (2006).

[Krieger 73] I. M. Krieger, T. F. Niu. A rheometer for oscillatory studies of nonlinear fluids. *Rheol. Acta* **12**, 567–571 (1973).

[Kulicke 79] W. M. Kulicke, H. E. Jeberien, H. Kiss, R. S. Porter. Visual observation of flow irregularities in polymer solutions at theta-conditions. *Rheol. Acta* **18**, 711–716 (1979).

[Kwag 00] H. Kwag, D. Rana, K. Cho, J. Rhee, T. Woo, B. H. Lee. Binary blends of metallocene polyethylene with conventional polyolefines: Rheological and morphological properties. *Polym. Eng. Sci.* **40**, 1672–1681 (2000).

[Larson 92] R. G. Larson. Instabilities in viscoelastic flows. *Rheol. Acta* **31**, 213–263 (1992).

[Larson 99] R. G. Larson. The structure and rheology of complex fluids. Oxford University Press, Inc., Oxford (1999).

[Laun 78] H. M. Laun, H. Münstedt. Elongational behaviour of a low density polyethylene melt. *Rheol. Acta* **17**, 415–425 (1978).

[Laun 82] H. M. Laun. Elastic properties of polyethylene melts at high shear rates with respect to extrusion. *Rheol. Acta* **21**, 464–469 (1982).

[Laun 83] H. M. Laun. Polymer melt rheology with a slit die. *Rheol. Acta* **22**, 171–185 (1983).

[Laun 04] H. M. Laun. Capillary rheometry for polymer melts revisited. *Rheol. Acta* **43**, 509–528 (2004).

[Leblanc 03] J. L. Leblanc. Fourier transform rheology on gum elastomers. *J. App. Polym. Sci.* **89**, 1101–1115 (2003).

[Lim 89] F. J. Lim, W. R. Schowalter. Wall slip of narrow molecular weight distribution polybutadienes. *J. Rheol.* **33**, 1359–1382 (1989).

[Liu 00] S. Liu, A. Sen. Synthesis of syndiotactic-polystyrene-graft-poly(methyl methacrylate), syndiotactic-polystyrene-graft-poly(methyl acrylate) and syndiotactic-polystyrene-graft-atactic-polystyrene with defined structures by atom transfer radical polymerization. *Macromolecules* **33**, 5106–5110 (2000).

[Lohse 02] D. J. Lohse, S. T. Milner, L. J. Fetters, M. Xenidou, N. Hadjichristidis, R. A. Mendelson, C. A. Garca-Franco, M. K. Lyon. Well-defined, model long chain branched polyethylene. 2. Melt rheological behaviour. *Macromolecules* **35**, 3066–3075 (2002).

[Macosko 94] C. W. Macosko. Rheology, principles, measurements, and applications. Wiley-VCH, Inc., New York (1994).

[Malmberg 02] A. Malmberg, C. Gabriel, T. Stefl, H. Münstedt, B. Löfgren. Long-chain branching in metallocene-catalyzed polyethylenes investigated by low oscillatory shear and uniaxial extensional rheometry. *Macromolecules* **35**, 1038–1048 (2002).

[Marrucci 93] G. Marrucci, F. Greco. Flow behavior of liquid crystalline polymers. *Adv. Chem. Phys.* **86**, 331–404 (1993).

[Marrucci 94] G. Marrucci. Non-linearities in polymer rheology. *J. Phys. Condens. Matter* **6**, A305–A309 (1994).

[Mavridis 92] H. Mavridis, R. N. Schroff. Temperature dependence of polyolefin melt rheology. *Polym. Eng. Sci.* **32**, 1778–1791 (1992).

[McLeish 97] T. C. B. McLeish. Polymer architecture influence on rheology. *Curr. Op. Solid State Mater. Sci.* **2**, 678–682 (1997).

[McLeish 98] T. C. B. McLeish, R. G. Larson. Molecular constitutive equations for a class of branched polymers: The pom-pom polymer. *J. Rheol.* **42**, 81–110 (1998).

[Milner 97] S. T. Milner, T. C. B. McLeish. Parameter-free theory for stress relaxation in star polymer melts. *Macromolecules* **30**, 2159–2166 (1997).

[Mooney 31] M. J. Mooney. Explicit formulas for slip and fluidity. *J. Rheol.* **2**, 210–222 (1931).

[Morawetz 85] H. Morawetz. Polymers, the origin and growth of a science. Courier Dover Pub., New York (1985).

[Münstedt 81] H. Münstedt, H. M. Laun. Elongational properties and molecular structure of polyethylene melts. *Rheol. Acta* **17**, 415–425 (1981).

[Münstedt 98] H. Münstedt, S. Kurzbeck, L. Egersdörfer. Influence of molecular structure on rheological properties of polyethylenes. Part II: Elongational behaviour. *Rheol. Acta* **37**, 21–29 (1998).

[Nassehi 02] V. Nassehi. Practical Aspects of Finite Element Modelling of Polymer Processing. Wiley & Sons, West Sassex (2002).

[Natta 60] G. Natta. Stereospecific polymerizations. *J. Polym. Sci.* **48**, 219–239 (1960).

[Neidhöfer 01] T. Neidhöfer, M. Wilhelm, H. W. Spiess. Fourier-transform rheology on linear polystyrene melts. *Appl. Rheol.* **11**, 126–133 (2001).

[Neidhöfer 03a] T. Neidhöfer. Fourier-transform rheology on anionically synthesised polymer melts and solutions of various topology. Johannes Gutenberg-Universität Mainz (2003).

[Neidhöfer 03b] T. Neidhöfer, M. Wilhelm, B. Debbaut. Fourier-transform rheology experiments and finite-element simulations on linear polystyrene solutions. *J. Rheol.* **47**, 1351–1371 (2003).

[Neidhöfer 04] T. Neidhöfer, S. Sioula, N. Hadjichristidis, M. Wilhelm. Distinguishing linear from star-branched polystyrene solutions with Fourier-transform rheology. *Macromol. Rapid Commun.* **25**, 1921–1926 (2004).

[Owens 02] R.G. Owens, T.N. Phillips. Computational rheology. Imperial college press, London (2002).

[Peacock 00] A. J. Peacock. Handbook of polyethylene. Structures, properties and applications. Marcel Dekker, New York (2000).

[Pearson 68] J. R. A. Pearson, C. J. S. Petrie. On melt flow instability of extrudated polymers. In R. E. Wetton, R. H. Whorlow (eds.), Polymer systems: Deformation and flow, pp. 163–187. Macmillian, London (1968).

[Pearson 82] D. S. Pearson, W. E. Rochefort. Behaviour of concentrated polystyrene solutions in large amplitude oscillatory shear fields. *J. Polym. Sci.* **20**, 83–98 (1982).

[Pérez 05] R. Pérez, E. Rojo, M. Fernadez, V. Leal, P. Lafuente, A. Santamaria. Basic and applied rheology of mLLDPE/LDPE blends: Miscibility and processing features. *Polymer* **46**, 8045–8053 (2005).

[Pino 80] P. Pino, R. Mühlhaupt. Stereospecific polymerization of propylene: An outlook 25 years after its discovery. *Angew. Chem. Inter.* **19**, 857–875 (1980).

[Pollard 04] M. Pollard, K. Klimke, R. Graf, H. W. Spiess, M. Wilhelm, O. Sperber, C. Piel, W. Kaminsky. Observation of chain branching in polyethylene in the solid state and melt via ^{13}C NMR spectroscopy and melt NMR relaxation time measurements. *Macromolecules* **37**, 813–825 (2004).

[Polyflow 03] Benelux Polyflow. POLYFLOW User Guide. Fluent Inc., Lebanon, NH (2003).

[Ramirez 85] R. W. Ramirez. The FFT fundamentals and concepts. PH PTR, Enlewood Cliffs, New Jersey (1985).

[Read 01] D. J. Read, T. C. B. McLeish. Molecular rheology and statistics of long-chain branched metallocene-catalyzed polyolefines. *Macromolecules* **34**, 1928–1945 (2001).

[Reimers 98] M. J. Reimers, J. M. Dealy. Sliding plate rheometer studies of concentrated polystyrene solutions: Non-linear viscoelasticity and wall slip of two high molecular weight polymers in tricresyl phosphate. *J. Rheol.* **42**, 527–548 (1998).

[Roovers 79a] J. Roovers. Melt rheology of model branched polystyrenes. *Polym. Prepr. (Am. Chem. Soc., Div. Polym. Chem.)* **20**, 144–148 (1979).

[Roovers 79b] J. Roovers. Synthesis and dilute characterization of comb polystyrenes. *Polymer* **20**, 843–849 (1979).

[Roovers 81] J. Roovers, W. W. Graessley. Melt rheology of some model comb polystyrenes. *Macromolecules* **14**, 766–773 (1981).

[Roovers 87] J. Roovers, P. M. Poporowski. Relaxation by constraint release in combs and star-combs. *Macromolecules* **20**, 2300–2306 (1987).

[Rubinstein 03] M. Rubinstein, R. H. Colby. Polymer physics. Oxford University Press, New York (2003).

[Rutgers 00] R. P. G. Rutgers, M. R. Mackley. The correlation of experimental extrusion surface instabilities with numerically predicted exit surface stress concentrations and melt strength for linear low density polyethylene. *J. Rheol.* **44**, 1319–1334 (2000).

[Rutgers 01] R. P. G. Rutgers, M. R. Mackley. The effect of channel geometry and boundary conditions on the formation of extrusion surface instabilities for LLDPE. *J. Non-Newton. Fluid Mech.* **98**, 185–199 (2001).

[Rutgers 02] R. P. G. Rutgers, N. Clemeur, S. Muke, B. Debbaut. Polyethylene flow prediction with a differential multi-mode pom-pom model. *Korea-Australia Rheology Journal* **14**, 25–32 (2002).

[Schlatter 05] G. Schlatter, G. Fleury, R. Muller. Fourier transform rheology of branched polyethylene: experiments and models for assessing the macromolecular architecture. *Macromolecules* **38**, 6492–6503 (2005).

[Schmidt-Rohr 94] K. Schmidt-Rohr, H. W. Spiess. Multi-dimensional solid-state NMR and polymers. Academic press, London (1994).

[Schulze 05] D. Schulze, T. Roths, C. Friedrich. Classification of model topologies using the δ versus G^* plot. *Rheol. Acta* **44**, 485–494 (2005).

[Seitz 93] J. T. Seitz. The estimation of mechanical properties of polymers from molecular structure. *J. App. Polym. Sci.* **49**, 1331–1351 (1993).

[Skoog 96] D. A. Skoog, J. J. Leary. Principles of instrumental analysis. Saunders College Publications, New York (1996).

[Sperling 92] L. H. Sperling. Introduction to physical polymer science. Wiley-Interscience, New York (1992).

[Stadler 05] F. J. Stadler, C. Piel, K. Klimke, J. Kaschta, M. Parkinson, M. Wilhelm, W. Kaminsky, H. Münstedt. Influence of type and content of very long comonomers on long-chain branching of ethane-/α-olefine copolymers. *Macromolecules* (2005).

[Stange 05] J. Stange, C. Uhl, H. Münstedt. Rheological behaviour of blends from a linear and a long chain branched polypropylene. *J. Rheol.* **49**, 1059–1079 (2005).

[Strunglinski 88] M. J. Strunglinski, W. W. Graessley, L.J. Fetters. Effects of polydispersity on the linear viscoelastic properties of entangled polymers. 3. Experimental observations on binary mixtures of linear and star polybutadienes. *Macromolecules* **21**, 783–789 (1988).

[Tanner 00] R. I. Tanner. Engineering Rheology. Oxford University Press, Inc., Oxford (2000).

[Thompson 87] J. M. T. Thompson, H. B. Stewart. Nonlinear dynamics and chaos. Wiley, New York (1987).

[Trinkle 01] S. Trinkle, C. Friedrich. Van Gurp-Palmen Plot: a way to characterize polydispersity of linear polymers. *Rheol. Acta* **40**, 322–328 (2001).

[Trinkle 02] S. Trinkle, P. Walter, C. Friedrich. VanGurp-Palmen-plot II - classification of long chain branched polymers by their topology. *Rheol. Acta* **41**, 103–113 (2002).

[Vega 98] J. F. Vega, A. Santamaria, A. Munoz-Escalona, P. Lafuente. Small amplitude oscillatory shear flow measurements as a tool to detect very low amounts of long-chain branching in polyethylene. *Macromolecules* **31**, 3639–3647 (1998).

[Vega 99] J. F. Vega, A. Santamaria, A. Munoz-Escalona, P. Lafuente. Rheological criteria to characterize metallocene catalyzed polyethylenes. *Macromol. Chem. Phys.* **200**, 2257–2268 (1999).

[Verbeeten 04] W. M. H. Verbeeten, G. W. M. Peters, F. P. T. Baajens. Numerical simulations of the planar contraction flow for a polymer melt using the XPP model. *J. Non-Newton. Fluid Mech.* **117**, 73–84 (2004).

[Vittorias 06] I. Vittorias, M. Parkinson, K. Klimke, B. Debbaut, M. Wilhelm. Detection and quantification of polyethylene branching topologies via Fourier-transform rheology, NMR, and finite element simulation, using the pom-pom model. *Rheol. Acta* (2006). Online.

[Wang 96a] S. Q. Wang, P. A. Drda. Stick-slip transition in capillary flow of polyethylene. 2. A molecular weight dependence and low-temperature anomaly. *Macromolecules* **29**, 4115–4119 (1996).

[Wang 96b] S. Q. Wang, P. A. Drda, Y. W. Inn. Exploring molecular origins of sharkskin, partial slip and slope change in flow curves of linear low-density polyethylene. *J. Rheol.* **40**, 875–898 (1996).

[Ward 04] I. M. Ward, J. Sweeney. An introduction to the mechanical properties of solid polymers. Wiley, West Sussex (2004).

[White 91] J. L. White, M. H. Han, N. Nakajima, R. Brzoskowski. The influence of materials of construction on biconical rotor and capillary measurements of shear viscosity of rubber and its compounds and consideration of slippage. *J. Rheol.* **35**, 167–189 (1991).

[Wilhelm 98] M. Wilhelm, D. Maring, H. W. Spiess. Fourier-transform rheology. *Rheol. Acta* **37**, 399–405 (1998).

[Wilhelm 99] M. Wilhelm, P. Reinheimer, M. Ortseifer. High sensitivity Fourier-transform rheology. *Rheol. Acta* **38**, 349–356 (1999).

[Wilhelm 00] M. Wilhelm, P. Reinheimer, M. Ortseifer, T. Neidhöfer, H. W. Spiess. The crossover between linear and non-linear mechanical behaviour in polymer solutions as detected by Fourier-transform rheology. *Rheol. Acta* **39**, 241–246 (2000).

[Wilhelm 02] M. Wilhelm. Fourier-Transform Rheology. *Macromol. Mater. Eng.* **287**, 83–105 (2002).

[Williams 55] M. L. Williams, R. F. Landel, J. D. Ferry. The temperature dependence of relaxation mechanisms in amorphous polymers and other glass-forming liquids. *J. Am. Chem. Soc.* **77**, 3701–3707 (1855).

[Wood-Adams 00] P. M. Wood-Adams, J. M. Dealy. Using rheological data to determine the branching level in metallocene polyethylenes). *Macromolecules* **33**, 7481–7488 (2000).

[Xu 01] J. Xu, X. Xu, L. Chen, L. Feng, W. Chen. Effect of composition distribution on miscibility and co-crystallization phenomena in the blends of low density polyethylene with conventional and metallocene-based ethylene-butene copolymers. *Polymer* **42**, 3867–3874 (2001).

[Yamaguchi 99] M. Yamaguchi, S. Abe. LLDPE/LDPE blends. I. Rheological, thermal and mechanical properties. *J. App. Polym. Sci.* **74**, 3153–3159 (1999).

[Yan 99] D. Yan, W.-J. Wang, S. Zhu. Effect of long-chain branching on rheological properties of metallocene polyethylene. *Polymer* **40**, 1737–1744 (1999).

[Yoshimura 87] A. S. Yoshimura, R. K. Prud'homme. Response of an elastic Bingham fluid to oscillatory shear. *Rheol. Acta* **26**, 428–436 (1987).

[Young 91] R. J. Young. Introduction to Polymers. Chapman and Hall, London (1991).

[Zachmann 94] H. G. Zachmann. Mathematik für Chemiker. VCH, Weinheim (1994).

[Ziegler 55] K. Ziegler, E. Holzkamp, H. Breil, H. Martin. The Mühlheim low-pressure polyethylene process. *Angew. Chem. Internat. Ed.* **67**, 541–547 (1955).

Acknowledgments

I would like to thank:

- Prof. M. Wilhelm for the chance he gave me to work for my Ph.D. at the MPI-P, the direct supervision of my work all these years, the guidelines and helpful comments always kindly provided and the whole fruitful and friendly cooperation. I am also grateful to him, for providing the opportunity and organising my visit in MacDiarmid Institute, in Wellington New Zealand.
- Prof. H. W. Spiess for accepting me in his group and contributing to my work with his helpful and always valuable suggestions.
- Prof. P. Callaghan for giving me the opportunity to work in his group at MacDiarmid Institute in Wellington New Zealand and for his helpful comments and suggestions.
- Prof. H. Münstedt, F. Stadler, Dr. D. Auhl, and J. Kaschta from the Institute of Polymer Materials, Friedrich-Alexander-University of Erlangen-Nurmberg, Erlangen, Germany, for supplying with polyethylene samples, associated analytical data and for fruitful discussions.
- Dr. Debbaut for sharing his valuable experience in the field of viscoelastic flow simulations and C. Gomez, both from Polyflow s.a./Fluent Benelux, for continuous support and assistance with anything concerning the simulation part of the thesis.
- Dr. C. Lamotte and Dr. J. Michel from TOTAL, Feluy Belgium, for providing with polyethylene samples and corresponding analytical data.
- Dr. K. Knoll from BASF AG, Ludwigshafen Germany, for kindly providing us with several polystyrene samples.
- T. Wagner and J. Thiel from MPI-P for providing me with polystyrene samples.
- Dr. V. Maus and M. Drechsler from MPI-P, for providing polystyrene samples and blends, as well as demanded analytical measurements, anytime and for any sample. Additionally, the help of S. Seywald from Polymeranalytik group in MPIP with the GPC measurements on all studied materials is deeply acknowledged.
- Dr. R. Wäber, G. Vulpius and H. Dörr for preparing the polyethylene blends at the Deutsches Kunstoff Institut, Darmstadt, Germany.

- The whole group of Prof. Spiess, for the friendly atmosphere during my three years in MPIP, the nice cooperation and the help, always provided to me whenever I needed it.
- Especially the FT-Rheology group: Dr. V. Barroso, A. Becker, Dr. S. Filipe, Dr. S. Höfl, Dr. K. Hyun, Dr. C. Klein, Dr. K. Klimke, Dr. P. Minkin, R. Musampa, Dr. T. Neidhöfer, Dr. C. Oelschlaeger and Dr. M. Parkinson, for introducing me to the mysteries of polymers and FT-Rheology, the wonderful cooperation all these years, the kind knowledge exchange and generally the warm group working atmosphere in the office and for being the best lab partners. From these people, I am especially tankful to Dr. S. Höfl for helping me integrate in Germany (secretarial-bureaucratic duties undertaken), for providing with experimental results for the PS combs and correcting my thesis and any manuscript I wrote during the last years. Furthermore, I am grateful to Dr. S. Filipe for the capillary measurements on my polyethylene samples and the promising fruitful cooperation. Special thanks also to Dr. M. Parkinson and Dr. K. Klimke for the NMR measurements on the polyethylenes, the helpful suggestions and their valuable corrections on my manuscripts. To all my colleagues, special thanks for tolerating my comments and annoying jokes all this time (like football related photos, comments and videos to my Portuguese and French friends).
- I. Naue and K. Riazi, students at the TU Darmstadt, for keeping up with me as their supervisor during their practice in MPIP. Their measurements were extremely valuable to the well-timed completion of the present thesis (although Ingo never learnt to make me a decent coffee!!).
- The group of Prof. Callaghan in Wellington New Zealand, especially my office and lab colleagues: B. Douglas, S. Rogers, A. Lutti, Dr. M. Hunter, Dr. P. Hubbard, Dr. P. Galvosas and Dr. R. Lopez, for helping me integrate in the institute and also getting to know the life “down under”.
- My family for their continuous support all these years in any possible way. Without them I wouldn’t have achieved anything.
- My Ewa for being my partner in every aspect of my life. For helping me with small arrangements at work up to checking my manuscript and from psychologically supporting me up to tolerating my temper the last years. Above all, for giving me the best and most important of all, my son.

CV

Personal

Iakovos Vittorias

born in 13. September 1980 in Rhodos, Greece

School education

Elementary school in Rhodos, Greece

Gymnasium in Rhodos, Greece

1995-1998	Lyceum in Rhodos, Greece

Studies

10.1998-07.2003	Diploma in Chemical engineering, Engineering school, Aristotle University in Thessaloniki, Greece
10.2002-07.2003	Diploma thesis in Chemical engineering, Engineering school, Aristotle University in Thessaloniki, in group of Prof. K. Kiparissides, LPRE Institute (Thesis title: Dynamic simulation of styrene polymerization)

Postgraduate studies

Since 11.2003	Ph.D. studies in Max-Planck Institute for Polymer Research in Mainz, Germany, in the group of Prof. Spiess and in Mechanical Engineering department, TU Darmstadt, Germany, in the group of Prof. M. Wilhelm.
11.2003-10.2005	Marie Curie research fellow in Max-Planck Institute for Polymer Research in Mainz, Germany.
05.2004-07.2004	Visiting scientist in MacDiarmid Institute for Advanced Materials and Nanotechnology in Wellington, New Zealand, in the group of Prof. P. Callaghan.

Occupation

Since 11.2004	Scientific staff in Max-Planck Institute for Polymer Research in Mainz, Germany.
07.2002-08.2002	Practice in BASF AG in Ludwigshafen, Germany, Polymer Reaction Engineering department.